Leveraging Open Microfluidics for Platform Development and Cell-Signaling Studies *In Vitro*

Samuel Berry

A dissertation

submitted in partial fulfillment of the

requirements for the degree of

Doctor of Philosophy

University of Washington

2020

Reading Committee:

Ashleigh Theberge, Chair

Paul Yager

Jesse Zalatan

Program Authorized to Offer Degree:

Chemistry

University of Washington

Abstract

Leveraging Open Microfluidics for Platform Development and Cell-Signaling Studies *In Vitro*

Samuel Berry

Chair of the Supervisory Committee

Ashleigh Theberge, Ph.D.

Department of Chemistry

This dissertation discusses the fundamentals, development, validation, and application of open microfluidic technologies as a research tool in biological studies. Open microfluidics is a rapidly evolving and expanding field, characterized by the study of fluid behavior in channels with dimensions < 1 mm and containing at least one interface that is open to the air (*i.e.*, not enclosed). While still a relatively new field, advances in the mathematical theory describing the fluidics in open channels, the fabrication process and resolution, and the creation of application-driven platforms are supporting the use of open microfluidics in biological and chemical studies. The work presented in this dissertation can be broadly separated into two sections: the first, exploring the fundamental mechanics underlying fluid flow in open systems, such as U-shaped channels and rails, to build up general functionalities and toolboxes that include droplet manipulation and hydrogel patterning; and the second, demonstrating the creation and validation of analytical systems to study cell-cell signaling *in vitro* with customizable cell-targeting beads and a microscale mycobacterial infection model.

Through the elucidation of the theory governing fluid behavior in our systems, we can describe the limitations of our open microfluidic systems and incorporate customizable functionalities for various experimental needs, ultimately improving the transferability of the systems to collaborators and other

researchers (Chapters 2 and 3). We couple this fundamental design approach with applications in cell-cell signaling, a vital biological phenomenon that plays important roles in immune response, homeostasis, organ development and function, and tissue repair. However, the microenvironments where these complex intercellular signaling processes occur are difficult to study and prevent researchers from deciphering the role of important cellular communication, illustrating a need for new technologies and approaches to better model and probe these systems (Chapter 4). To partially address this need, we present the development and validation of two novel approaches to study intercellular signaling that can be easily adapted and customized for use in different settings (Chapter 5 and 6). Ultimately, the techniques and technologies described here represent foundational analytical and modeling approaches and warrant further development to increase their potential impact.

TABLE OF CONTENTS

List of Figures

Additional figures in Appendices A-E.

Acknowledgements

Nothing exists or occurs in isolation, and completing a PhD is no exception, making this section the most difficult part to write for this thesis. There are many people who have been involved in accomplishing this, and I just want to broadly say thank you to everyone who was been here along the way.

First, thank you to all my colleagues and lab mates in the Theberge Lab. Tianzi and Dostie for all the support, baked goods, guidance, and encouragement from the day I joined the lab; Jing, for all your support and drive that permeated your work and that of those around you; Tammi and Ulri for all the divergent tangents in the group office, tea breaks, early instrument times, and conference travel over the years; Amanda for your inquisitive and unique insights and humor; Xiaojing, for your patient, gentle, and caring guidance from my first day; Yun, for your passion, excitement, and wealth of experience on all things biology and sailing; John, for your innate curiosity and passion for science coupled with your stupendous work ethic and drive; and Maia, for all your help, patience, crazy time points, hard work ethic, Swedish discussions, and diverse interests to occupy the imaging time. Thank you.

To Ashleigh, I cannot express how you have made my graduate career what it is, through the freedom, independence, trust, advice, guidance, patience, and encouragement to pursue my own interests and ideas while grounding them and pushing me forward. You have provided a wonderful environment to grow and learn through your leadership and understanding, and have been looking out for me and my interests since the day I started; thank you. To Erwin, for your inspiring and myriad ideas to try out everything and push the limits on my thinking and scope, and not to be limited by what has been done before or what is even possible.

To my committee, Dr. Daniel Chiu, Dr. Chetan Seshadri, Dr. Paul Yager, and Dr. Jesse Zalatan; thank you for your guidance, advice, and belief in my work and myself. You have all encouraged me to be the best scientist I can and to look at my work in the correct contexts and scales; thank you for taking

the time to go through my work with a fine-tooth comb, to sit with me and provide insight and advice on career paths and research ideas, and for so willingly connecting me and introducing me to collaborators within Seattle. To the Seattle TB community, thank you for your inclusion, training, and feedback on my work.

To the rest of my cohort, Wing, Daniele, and Calvin; from having to actually do homework in classes to getting through the research slumps and highs, thanks for going through all of this together and supporting me and each other to get through this journey together.

To the Mace Lab, who started my research career at Tufts, and who have still offered valuable advice, mentorship, and guidance through my graduate career and beyond. Thank you Charlie and Syrena for always being there for me and helping me every step along the way.

Outside of lab, to all my friends to whom I could always rely on for whatever I needed; the endless dinners, climbing shenanigans, outdoor adventures, culinary explorations, and Golden Gardens sunset fires, you have made Seattle a home and this entire PhD much more enjoyable and manageable through all the ups and downs. Thank you for dealing with my crazy work schedule and my always having to leave early; Austin, Andy, Danny, Jarrid, Emma, Josh, Chris, Calvin, Kade, James, Max, Summer, Foris, Elif, Gabe, and Zabir. To the Wilridge family, for allowing me to be a part of Wilridge and get out of lab to pursue my passion in wine here in the PNW. And to my friends back out East, thank you for your support, continued friendship, trust, and advice at all hours and times on what I am doing out on the West Coast: Kit, Sydney, Monil, Jon, Cam, Eric, Jake, Nitin, Barbara, and Ben.

To everyone in Sweden, who made Stockholm a familiar and fantastic place to live and made it home through the seasons and science. Thank you Mattias, for responding to my cold email and allowing me to come and work with everyone at CIM and have a transformative experience, and to Puran, Magda, Egle, and Sanna for your patience, understanding, training, warmth, and welcome into a new environment and making it really feel like home. To the rest of CIM, and Caroline, Tiphaine, and Alvaro, thank you so much for your friendship, all the dinners, late nights out, inclusion, and making Stockholm truly feel like home. You all made my time there one of the best parts of my graduate career.

Lastly, thank you to my family for supporting me in all of this. Mom and Dad, thank you for all your love and support through the years and pushing me to make the most of this and every opportunity, and to always find a place to call home. To David, I literally could not have done any of this without your guidance, advice, insight, experience, and encouragement; to Barbara, for always injecting excitement and joy into my life and highlighting the positives of every situation; and to Zeynep, for always supporting me through the ups, downs, near, and far, reminding me to leave lab and go out to find enjoyment in life, and for your patience, understanding, and love throughout the years.

Dedication

I would like to dedicate this dissertation to my family who always push me to do my best and work my hardest to achieve my goals in whatever I do. The work presented here would not have happened without your support.

Chapter 1. Introduction

The content of this dissertation spans the topics of fluid behavior in microfluidics, technology development and implementation, analytical and modeling approaches in cell-signaling, and infectious disease mechanisms of pathogenesis and communication. This chapter serves as a broad introduction to these research areas in the context of this dissertation and is not meant to serve as an in-depth exploration or background of each field.

1.1 Introduction to Microfluidics and Fundamentals

The field of microfluidics, characterized by the analysis, manipulation, and characterization of fluids on length scales less than 1 mm, emerged as a highly promising research area in the early 2000s.[1,2] Microfluidics utilizes volumes much smaller than conventional methods (on the order of $\leq 10^{-6}$ liters) and enables precise control over experimental factors such as flow, mixing, environmental conditions, reagent consumption, and sample size[1,2]; these characteristics make it an attractive tool for applications in a wide range of fields including pharmaceuticals, chemical synthesis, environmental sampling, industrial processes, and biomedical research.[3–7] Platforms relying on microfluidic functionalities offer numerous advantages over comparable macroscale systems, such as low reagent and sample consumption, control over environmental conditions, small laboratory footprints, compatibility with high-throughput screening, and a fluidic regime governed by separate clearly defined physical principles.[1,2,8]

Fluid behavior in microfluidic platforms is governed by a different set of physical parameters than macroscale systems because the effect of gravity on the fluid is minimized compared to the effect of interfacial and viscous forces (among others).[8] Physical parameters of note to the work presented in this dissertation are the Laplace pressure, contact angle, and the dimensionless numbers Re (Reynold's number) and Ca (Capillary number). The Laplace pressure can be defined as the pressure difference across a curved interface resulting from the surface tension of the interface, and the contact angle is the

angle at the triple point of the solid-gas, solid-liquid, and liquid-solid interface of a droplet on a surface (Figure 1). These physical parameters are valuable for describing the behavior of fluids within open-air channels and at the interfaces between different phases and substrates. The Reynold's number (Equation 1) defines the relationship between viscous forces and inertial forces within a system and the Capillary number (Equation 2) illustrates the importance of interfacial tension. The Re and Ca are described as:

$$Re = \frac{\rho UL}{\mu} \quad \text{(Eq. 1)}$$

$$Ca = \frac{\mu U}{\gamma} \quad \text{(Eq. 2)}$$

where ρ is the fluid density, U is the fluid velocity, L is the length scale of the system, μ is the viscosity of the fluid, and γ is the surface tension. Within microfluidic systems, fluids tend to fall under a low Re regime (< 1), indicating that viscous forces are dominant over inertial forces; this is evident in the presence of diffusive mixing as opposed to turbulent mixing in microfluidic channels. Depending on the system, Ca, which describes the contribution of interfacial forces over viscous forces, can vary, as users often design channels and platforms with different flow requirements (*i.e.*, capillary driven or pump driven).

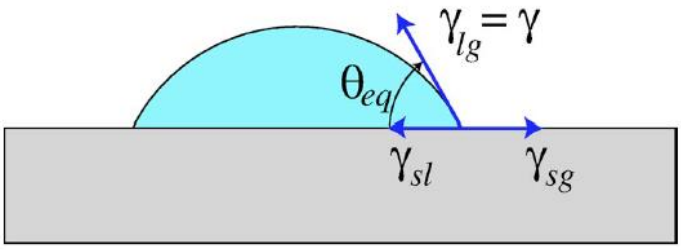

Figure 1.1: Equilibrium contact angle (θ_{eq}) is the angle of the triple point between the balanced solid-liquid (γ_{sl}), solid-gas (γ_{sg}), and liquid-gas (γ_{lg}) interfacial tensions of a droplet on a surface. Reproduced from Squires and Quake.[8]

1.2 Open Microfluidics and Development of the Field

The topics described herein utilize a subset of microfluidics, known as open or capillary microfluidics, as a key component in their functionalities. Open microfluidics, broadly described as the study of fluid behavior in a microscale channel with at least one surface exposed to air, encompasses a wide range of microfluidic systems including paper microfluidics, thread-based microfluidics, suspended microfluidics, and open channel microfluidics.[9] Within open microfluidic systems, capillary forces and interfacial tension forces govern much of the fluid behavior and system functionality. For example, flow within an open capillary system can be achieved through the use of spontaneous capillary flow (SCF), which occurs as a result of a negative Laplace pressure at the advancing fluid front and a relative zero Laplace pressure at the back. While not unique to only open microfluidic channels, it can be leveraged as a source of flow in place of mechanical or pneumatic pumps, and is mathematically described by the SCF equation[10] (Equation 3):

$$\frac{P_f}{P_w} < \cos(\theta) \qquad \text{(Eq. 3)}$$

where P_f and P_w are the free and wetted perimeter, respectively, and θ is the contact angle of the fluid on the surface (Figure 1). Additional functionalities can be obtained within open microfluidic systems through the manipulation of surface characteristics to induce a hydrophilic or hydrophobic character or inclusion of microfabricated structures to generate pinning ridges that are permissive or restrictive of fluid flow.[11,12]

Open microfluidic systems offer numerous user advantages such as pipette accessibility, ease of fabrication with biocompatible materials, and capillary-driven flow. Pipette accessibility enables straightforward user access to the system while capillary-driven flow removes the need for external flow generators (*e.g.*, syringe pumps). Fabrication *via* 3D printing, computer numerical control (CNC) micromilling, and injection molding removes the need for highly specialized fabrication facilities (*e.g.*, clean rooms) and bonding steps.[13,14] Due to these advantages, the field of open microfluidics is constantly evolving and expanding, with applications in biological, chemical, physical, medical, and environmental research.[10,13,15–17]

1.3 Biological Relevance and Importance of Cell-Cell Signaling

The exchange of cell-secreted chemical signals (*e.g.*, growth factors, cytokines) between cells plays a vital role in the induction of cellular functions and systemic physiological processes including cellular differentiation, maintenance of homeostasis, and immune response.[18] These signaling mechanisms include various signaling embodiments: paracrine signaling (secreted soluble factors from one cell are exchanged over short distances with neighboring cells); juxtacrine signaling (where physical cues derived from cell-cell contact induce intracellular signaling mechanisms and functions); autocrine signaling (where soluble factors secreted from one cell are received by the same cell); and volatile signaling (where gas-phase volatile factors are secreted and received by different cellular populations).[18] The careful coordination of these myriad signaling pathways enables higher-order organ function and host immunity, and deciphering these complex cellular communication networks provide valuable insight into which factors are driving important biological functions.

The importance of elucidating key signaling pathways can be highlighted in many recent scientific advances, such as the development of checkpoint inhibitor therapies targeting the programmed cell death protein 1/ligand (PD-1/PD-L1) signaling axis[19–21], the understanding of tumor necrosis factor (TNF) signaling and blockers in infectious diseases such as tuberculosis [22,23], and the harnessing of host immune components as potential treatments for autoimmune diseases.[24,25] However, these signaling processes are rarely driven by a single factor, relying on the interplay between various signals originating from different cellular populations.[26] In order to better understand the intricate signaling milieu, researchers are utilizing a wide range of techniques and platforms that enable precise manipulation and probing of signaling environments, ultimately allowing them to decipher the roles of many signals in important physiological processes and provide a foundation for advances in the biomedical research fields.

1.4 Microfluidics as Tools for Studying Cell-Signaling Phenomena

Adapting microfluidic platforms for biological studies offers several benefits over macroscale systems, such as biomimetic length scales, diffusive mixing (resulting from a low Re), precise control

over microenvironment conditions (*e.g.*, flow, surface topography, gas gradients), and low reagent consumption[1,6,7], enabling studies in the fields of genetics, tissue engineering, cell development, biomechanics, single-cell "omics", and cell signaling. Through leveraging these advantages, researchers have developed systems that enabled micrometer-resolution of cell patterning for quorum signaling studies[27], segregated coculture with discrete microscale culture chambers to probe paracrine signaling-induced cancer drug resistance[28], creation of clearly defined diffusion gradients for cell chemotaxis assays[29,30], high-throughput screening of host pathogen interactions and drug resistance in infectious disease[31,32], and recapitulation of higher order organ functions *in vitro*.[33–35] It is important to note that applying microfluidic technologies to all biological systems is not always advantageous, as microfluidic platforms are often incompatible with large volume samples, require the establishment of new standards and controls, and utilize different techniques and instrumentation for fabrication and use.[6] However, the development of microfluidic tools to probe complex biological systems has provided important insight across a wide range of applications and fields when successfully developed and implemented.

Open microfluidic platforms have not been adopted as ubiquitously as conventional closed channel systems, however the number and type of tools available to study biological systems and cell-cell signaling are increasing. A push towards creating open microfluidic systems that integrate with existing biological materials (*e.g.*, well plates, petri dishes) and the pipette accessibility to add, remove, or manipulate cells in culture eases the translation of these technologies into biological studies.[36–38] Additionally, creation of arrays of these open microfluidic platforms permits screening of multiple conditions in parallel while maintaining discrete culture systems.[15,39,40] Among other applications, these beneficial characteristics of open microfluidic platforms have been implemented to create organotypic models of angiogenesis and endothelial-fibroblast signaling[38], to facilitate coculture of prostate cancer cells and adipocytes for lipogenesis studies[37], to enable microbial metabolomic studies of the communication amongst both human and plant pathogens[15], and to spatially and temporally manipulate conditioned immune cells to recapitulate cancer-immune cell signaling.[40] For open microfluidic fields, the advancement of the underlying mathematical theory behind the functionality of these platforms, the

fabrication methods and resolution, and the creation of application-driven platforms will improve the transferability and adaptation of these technologies to biological and chemical studies and foster valuable insights into cell-signaling phenomena and other physiological processes.

1.5 References

1. Sackmann EK, Fulton AL, Beebe DJ. The present and future role of microfluidics in biomedical research. *Nature*. 2014;507(7491):181-189. doi:10.1038/nature13118
2. Whitesides GM. The origins and the future of microfluidics. *Nature*. 2006;442(7101):368-373. doi:10.1038/nature05058
3. Weibel DB, Whitesides GM. Applications of microfluidics in chemical biology. *Curr Opin Chem Biol*. 2006;10(6):584-591. doi:10.1016/j.cbpa.2006.10.016
4. Shang L, Cheng Y, Zhao Y. Emerging Droplet Microfluidics. *Chem Rev*. 2017;117(12):7964-8040. doi:10.1021/acs.chemrev.6b00848
5. Bai Y, Gao M, Wen L, *et al*. Applications of Microfluidics in Quantitative Biology. *Biotechnol J*. 2018;13(5). doi:10.1002/biot.201700170
6. Duncombe TA, Tentori AM, Herr AE. Microfluidics: Reframing biological enquiry. *Nat Rev Mol Cell Biol*. 2015;16(9):554-567. doi:10.1038/nrm4041
7. Sonnen KF, Merten CA. Microfluidics as an Emerging Precision Tool in Developmental Biology. *Dev Cell*. 2019;48(3):293-311. doi:10.1016/j.devcel.2019.01.015
8. Squires T, Quake S. Microluidics: Fluid Physics at the nanoliter scale. *Rev Mod Phys*. 2005;77(977). https://journals.aps.org/rmp/pdf/10.1103/RevModPhys.77.977.
9. Berthier J, Brakke K, Berthier E. *Open Microfluidics*. Wiley; 2016.
10. Casavant BP, Berthier E, Theberge AB, *et al*. Suspended microfluidics. *PNAS*. 2013;110(25):10111-10116. doi:10.1073/pnas.1302566110
11. Berthier J, Loe-Mie F, Tran VM, *et al.* On the pinning of interfaces on micropillar edges. *J Colloid Interface Sci*. 2009;338(1):296-303. doi:10.1016/j.jcis.2009.06.007
12. Berthier J, Brakke K. *The Physics of Microdroplets*. Wiley; 2012.
13. Berry SB, Zhang T, Day JH, *et al.* Upgrading well plates using open microfluidic patterning. *Lab Chip*. 2017;17(24):4253-4264. doi:10.1039/c7lc00878c
14. Lee UN, Su X, Guckenberger DJ, *et al.* Fundamentals of rapid injection molding for microfluidic cell-based assays. *Lab Chip*. 2018;18(3):496-504. doi:10.1039/c7lc01052d
15. Barkal LJ, Theberge AB, Guo C-J, *et al.* Microbial metabolomics in open microscale platforms. *Nat Commun*. 2016. doi:10.1038/ncomms10610
16. Lee UN, Berthier J, Yu J, Berthier E, Theberge AB. Stable biphasic interfaces for open microfluidic platforms. *Biomed Microdevices*. 2019;21(1). doi:10.1007/s10544-019-0367-z
17. Berthier E, Dostie AM, Lee UN, Berthier J, Theberge AB. Open Microfluidic Capillary Systems. *Anal Chem*. 2019;91(14):8739-8750. doi:10.1021/acs.analchem.9b01429
18. Cooper G. Signaling Molecules and Their Receptors. In: *The Cell: A Molecular Approach*. 2nd ed. Sunderland, SInauer Associates; 2000.
19. Smith DC, Mcdermott DF, Powderly JD, *et al.* Safety, Activity, and Immune Correlates of Anti-PD-1 antibody in cancer. *N Engl J Med*. 2012;366(26):2443-2454.
20. Brahmer JR, Tykodi SS, Chow LQM, *et al.* Safety and activity of anti-PD-L1 antibody in patients with advanced cancer. *N Engl J Med*. 2012;366(26):2455-2465. doi:10.1056/NEJMoa1200694
21. Akinleye A, Rasool Z. Immune checkpoint inhibitors of PD-L1 as cancer therapeutics. *J Hematol Oncol*. 2019;12(1):1-13. doi:10.1186/s13045-019-0779-5
22. Harris J, Keane J. How tumour necrosis factor blockers interfere with tuberculosis immunity. *Clin Exp Immunol*. 2010;161(1):1-9. doi:10.1111/j.1365-2249.2010.04146.x
23. Domingo-Gonzalez R, Prince O, Cooper A, Khader SA. Cytokines and Chemokines in Mycobacterium tuberculosis Infection. *Microbiol Spectr*. 2016;4(5):1-37. doi:10.1128/microbiolspec.tbtb2-0018-2016
24. Romano M, Fanelli G, Albany CJ, Giganti G, Lombardi G. Past, present, and future of regulatory T cell therapy in transplantation and autoimmunity. *Front Immunol*. 2019;10(JAN).

doi:10.3389/fimmu.2019.00043
25. Ferreira LMR, Muller YD, Bluestone JA, Tang Q. Next-generation regulatory T cell therapy. *Nat Rev Drug Discov*. 2019;18(10):749-769. doi:10.1038/s41573-019-0041-4
26. Berry S, Haack A, Theberge A, Brighenti S, Svensson M. Host and pathogen communication in the respiratory tract: mechanisms and models of a complex signaling environment. *Front Med*.
27. Lee SH, Helnz AJ, Shln S, *et al.* Capillary based patterning of cellular communities in laterally open channels. *Anal Chem*. 2010;82(7):2900-2906. doi:10.1021/ac902903q
28. Patel D, Gao Y, Son K, *et al.* Microfluidic co-cultures with hydrogel-based ligand trap to study paracrine signals giving rise to cancer drug resistance. *Lab Chip*. 2015;15(24):4614-4624. doi:10.1039/c5lc00948k
29. Berthier E, Beebe DJ. Gradient generation platforms: New directions for an established microfluidic technology. *Lab Chip*. 2014;14(17):3241-3247. doi:10.1039/c4lc00448e
30. Berthier E, Surfus J, Verbsky J, Huttenlocher A, Beebe D. An arrayed high-content chemotaxis assay for patient diagnosis. *Integr Biol*. 2010;2(11-12):630-638. doi:10.1039/c0ib00030b
31. Tezera LB, Bielecka MK, Chancellor A, *et al.* Dissection of the host-pathogen interaction in human tuberculosis using a bioengineered 3-dimensional model. *Elife*. 2017;6:1-19. doi:10.7554/eLife.21283
32. Bielecka MK, Tezera LB, Zmijan R, *et al.* A bioengineered three-dimensional cell culture platform integrated with microfluidics to address antimicrobial resistance in tuberculosis. *MBio*. 2017;8(1). doi:10.1128/mBio.02073-16
33. Zhang B, Korolj A, Lai BFL, Radisic M. Advances in organ-on-a-chip engineering. *Nat Rev Mater*. 2018;3(8):257-278. doi:10.1038/s41578-018-0034-7
34. Bein A, Shin W, Jalili-Firoozinezhad S, *et al.* Microfluidic Organ-on-a-Chip Models of Human Intestine. *Cmgh*. 2018;5(4):659-668. doi:10.1016/j.jcmgh.2017.12.010
35. Benam K, Villenave R, Lucchesi C, *et al.* Small airway-on-a-chip enables analysis of human lung inflammation and drug responses in vitro. *Nat Methods*. 2016;13(2):151-157. doi:10.1038/Nmeth.3697
36. Álvarez-García YR, Ramos-Cruz KP, Agostini-Infanzón RJ, *et al.* Open multi-culture platform for simple and flexible study of multi-cell type interactions. *Lab Chip*. 2018;18(20):3184-3195. doi:10.1039/c8lc00560e
37. Day JH, Nicholson TM, Su X, *et al.* Injection molded open microfluidic well plate inserts for user-friendly coculture and microscopy. *Lab Chip*. 2019;20(1):107-119. doi:10.1039/c9lc00706g
38. Lee Y, Choi JW, Yu J, *et al.* Microfluidics within a well: An injection-molded plastic array 3D culture platform. *Lab Chip*. 2018;18(16):2433-2440. doi:10.1039/c8lc00336j
39. Humayun M, Chow CW, Young EWK. Microfluidic lung airway-on-a-chip with arrayable suspended gels for studying epithelial and smooth muscle cell interactions. *Lab Chip*. 2018;18(9):1298-1309. doi:10.1039/c7lc01357d
40. Yu J, Berthier E, Craig A, *et al.* Reconfigurable open microfluidics for studying the spatiotemporal dynamics of paracrine signalling. *Nat Biomed Eng*. 2019;3(10):830-841. doi:10.1038/s41551-019-0421-4

Chapter 2. Droplet Manipulation and Behavior in Open Microfluidic Channels

Reproduced in part with permission from Berry, S.B.*; Lee, J.J.*; Berthier, J.; Berthier, E.; Theberge, A.B. "Droplet incubation and splitting in open microfluidic channels". *Anal. Methods*, 2019, 11, 4528-4536.

*denotes co-authorship

Abstract:

Droplet-based microfluidics enables compartmentalization and controlled manipulation of small volumes. Open microfluidics provides increased accessibility, adaptability, and ease of manufacturing compared to closed microfluidic platforms. Here, we begin to build a toolbox for the emerging field of open channel droplet-based microfluidics, combining the ease of use associated with open microfluidic platforms with the benefits of compartmentalization afforded by droplet-based microfluidics. We develop fundamental microfluidic features to control droplets flowing in an immiscible carrier fluid within open microfluidic systems. Our systems use capillary flow to move droplets and carrier fluid through open channels and are easily fabricated through 3D printing, micromilling, or injection molding; further, droplet generation can be accomplished by simply pipetting an aqueous droplet into an empty open channel. We demonstrate on-chip incubation of multiple droplets within an open channel and subsequent transport (using an immiscible carrier phase) for downstream experimentation. We also present a method for tunable droplet splitting in open channels driven by capillary flow. Additional future applications of our toolbox for droplet manipulation in open channels include cell culture and analysis, on-chip microscale reactions, and reagent delivery.

2.1 Introduction

Open microfluidic systems offer many advantages for conducting life science experimentation including pipette accessibility, simple fabrication techniques with biocompatible materials, independence from pumps and external flow generators, and customizability.[1] Here, we describe a biphasic system driven by capillary forces that enables the control and manipulation of multiple droplets within an open

channel devoid of any electrical or pneumatic actuation systems, in a fully open, pipette-accessible platform. We demonstrate a new open channel system for prolonged static droplet incubation in channel followed by capillary-driven translation of discrete droplets for downstream analysis, as well as tunable droplet splitting in open channels.

Droplet-based microfluidics advances the capabilities of traditional single-phase microfluidic platforms through compartmentalization of reaction components into discrete micro- to picoliter volumes, enabling decreased reagent consumption and use of valuable, low-volume samples that may otherwise be expensive or difficult to obtain.[2,3] Translation of assays to droplet-based platforms allows users to precisely form, manipulate, and transport small volumes for use in cell-based assays, chemical synthesis, and biochemical analyses.[2] Droplet-based systems for an extensive range of functions have been described[3], and droplet manipulation methods such as incubation[4,5], reagent addition[6], and splitting[7,8] have been developed. However, most current droplet-based microfluidic approaches rely on complex designs and multistep fabrication methods (*e.g.*, photolithography, bonding) to create closed-channel platforms and often use external pumps and actuators to manipulate flow, allowing them to perform specialized functions but limiting their wide-spread adoption beyond engineering and physical science laboratories.[3] Recent work by Li *et al.*[9] overcomes some of the fabrication challenges of traditional droplet systems by using an open paper-based device, but the flow still requires external syringe pumps.

Systems utilizing open fluidic channels (*e.g.*, channels devoid of a ceiling, devoid of a ceiling and floor, or devoid of lateral walls) and surface tension-driven flow have emerged as alternatives to closed channel, pump-driven microfluidic platforms due to their relative ease of design, fabrication, and use.[1,10] Open channel platforms do not require bonding and can be fabricated in a single step using micromilling[11-13] or high-volume fabrication techniques such as injection molding.[14,15] Open platforms provide improved accessibility (*e.g.*, pipette, automated reagent delivery systems) to users to manipulate experimental conditions through direct addition or removal of reagents at any point on the platform.[16] Additionally, open channel systems can be driven by capillary flow in a manner similar to that of closed capillary systems. Capillary flow removes the need for external flow drivers and improves the robustness

and functionality of the platform, as the mechanism for flow is built into the device.[10] Recently, an analytical model, numerical simulations, and experimental validation that described the behavioral modes of a single immiscible droplet placed in an open channel where a carrier flow occurs was published[17]; it was found that an immiscible droplet can behave in a number of fundamentally different ways (remain static in the channel, translate at the leading edge of the carrier fluid, or detach from the walls of the channel and flow with the carrier fluid).

In prior work[17], it also was demonstrated that multiple aqueous droplets can be created and transported by pipetting the aqueous phase into an oil carrier phase that is already flowing through the device based on capillary flow. In the present manuscript, we developed a new capability, which enables extended incubation of droplets within the channel in the absence of the carrier phase, followed by introduction of the carrier phase in the channel using spontaneous capillary flow, and subsequent movement of the droplets. In contrast to our prior work, the present manuscript enables longer residence times of the droplets within the channels since they can be incubated for multiple hours before the carrier phase is added. Pipetting multiple aqueous droplets directly into an empty channel, incubating them, and *then* translating the train of droplets using a capillary-driven immiscible phase presents further challenges, as conditions such as surface wetting, evaporation, droplet merging, and satellite droplet formation all must be accounted for.

Here, we build a toolbox of droplet manipulation capabilities for open channel droplet-based microfluidics. We describe new open channel systems in which multiple discrete droplets can be placed into an open channel, incubated *in situ*, and then translated downstream either with droplet merging or without droplet merging, depending on the desired application. We also demonstrate an open microfluidic droplet splitting method to enable a parent droplet to be aliquoted into tailored smaller droplets (equal or unequal volumes) for multiplexed processing and readouts. Our open microfluidic systems rely on the surface interactions between the aqueous droplets, organic carrier phase, and channel surface which can be altered to fit various experimental needs; additionally, reliance on capillary-driven flow in an open channel removes the need for flow-generation devices and enables direct user access to the system at any

time point. These platform functionalities (*i.e.*, merging/splitting, incubation, user access) can help streamline large and cumbersome screening experiments that rely on manual pipetting, mixing, and splitting for sample generation, where manual processing can negatively contribute to assay time, sample loss, and costs associated with instrument usage. In future applications, these functionalities can be adapted and applied to array generation, sample preparation, and multiplexing.

2.2 Capillary-driven flow of droplets in open channels

While the dynamics and behavior of single phase capillary flow within an open system have been well characterized[18-21], the interaction and behavior of multiple phases within an open channel has been less extensively studied. Previously, in an open two-phase system driven by spontaneous capillary flow (SCF), it was found that a single aqueous droplet within an open channel demonstrates different behavioral modes (*e.g.*, translation, displacement, remaining stationary) largely governed by the interfacial tension between the droplet and the carrier phase, the contact angle of the droplet and carrier phase on the channel surface, and the velocity of the carrier phase.[17] In the present manuscript, we use two of these behavioral modes (Figure A1) to create open channel manipulation modules driven by capillary flow: "shift mode", in which an aqueous droplet wets all sides of the open channel and is translated downstream by the carrier phase (Figure A1i-ii), and "raft mode", in which an aqueous droplet completely detaches from the channel and is displaced downstream by the carrier phase (Figure A1iii-iv).[17] Shift mode occurs when an aqueous droplet in the channel precedes the advancing front of the carrier fluid, and the carrier fluid does not pass in front of the droplet; alternatively, raft mode occurs when the carrier fluid surrounds the droplet and simultaneously flows in front of and behind the droplet. Notably, in the case of both behavioral modes, the carrier fluid governs the overall dynamics of the system, as the pipetted droplets are entrained by the carrier fluid and transported downstream.

Within our open-channel platforms, we designed channel dimensions to fall within the flow regime governed by SCF[1,10] to ensure capillary-driven flow, and incorporated a rounded channel geometry to negate flow along a wedge (*i.e.*, Concus-Finn flow)[22](Figure 2.1). Further, we fabricated our platform

with poly (methyl methacrylate) (PMMA) to provide the desired wettability between droplets, the carrier phase, and the channel surface; specifically, with contact angles of 78° between PMMA and the aqueous droplet, ≈ 12.5° between PMMA and the organic carrier phase, and 146.14° ± 0.9° between the PMMA and the aqueous droplet when submerged in the organic carrier phase (pentanol). Additionally, we did not use any surfactants in our platform. To prevent evaporation of droplets from within the channels during prolonged incubation times (*i.e.*, hours), we enclosed our open channel platform within a humidified Omnitray™ (rectangular petri dish) surrounded by sacrificial water (1.5 mL in ≈ 50 µL droplets). Our open channel system offers advantages to closed systems as we can add droplets directly to the channel with a pipette and initiate flow of the carrier phase through simple pipetting into the inlet reservoir (Figure 2.1).

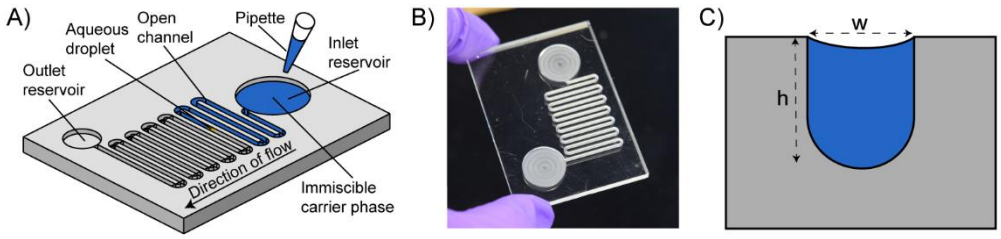

Figure 2.1: General platform design and modes of operation for translating aqueous droplets *via* capillary flow of an organic carrier phase. A) Schematic representation of open channel platform illustrating addition of organic carrier fluid (blue) with aqueous droplets (yellow) present in the channel; B) image of open channel platform; C) cross sectional schematic of channel (w = 0.90 mm and h = 1.0 mm).

2.3 Droplet incubation and transport

Inputting fluids into a typical microfluidic channel commonly requires dedicated ports and connectors. Addition of droplets into an open microfluidic channel, on the other hand, can be performed directly and at any location in the channel. Delivering small droplets (0.5-2.0 µL) with a pipette is a common approach available to most laboratories; alternatively, smaller droplets can be inputted through other approaches such as Acoustic Droplet Ejection methods.[23,24] While depositing droplets on a surface is straightforward, removal or transfer of small droplets from a surface at subsequent time points is

challenging; for example, pipetting is unreliable and tedious, as part of the droplet often remains behind on the surface. Digital microfluidics, also referred to as Electrowetting on Dielectric (EWOD), provides a method to move small droplets, but requires the use of electrical components.[25-27] There is a need for simple systems in which droplets can be pipetted onto an unmodified surface, incubated *in situ* for a desired period, and then passively manipulated or transferred.

Previously, addition of droplets to an organic carrier phase as the carrier fluid was flowing downstream, enabling droplet transport but limiting the incubation time of the pipetted droplets to the time required to reach the outlet.[17] Here, we present a different and adaptable platform where we pipette multiple discrete droplets into an open channel (in the absence of the organic carrier phase), incubate the droplets for a desired time, and then passively transport the droplets to a different location on chip *via* capillary-driven flow of an organic carrier phase (Figure 2.2). When multiple droplets are placed in series within an empty single open channel, translation of the droplets in shift mode leads to coalescence, as they merge with each subsequent droplet in the channel (Figure 2.2A). This functionality can be beneficial for analyses requiring pooling of multiple samples (*e.g.*, discovery assays). For applications where droplet coalescence is not desired, we designed a separate flow path that we refer to as a 'bypass channel'. The bypass channel enables the immiscible carrier fluid to separate each discrete droplet (thereby preventing coalescence) and transport the droplets downstream *via* raft mode (Figure 2.2B-C). When the carrier phase reaches the bypass, which is positioned upstream of the droplet, part of the flow of the carrier fluid diverts through the bypass, while the remainder of the carrier phase continues in the main channel; the diverted flow fills the space between each droplet, while the nondiverted flow continues to drive the droplets through the main channel (Figure 2.2B-C). Initially, we observed droplet disruption (*e.g.*, droplet breakup and/or flow through the bypass) and an increased flow rate through the bypass, which resulted in stagnation of the carrier phase flow in the bends of the main channel and prevented droplets from reaching the outlet (Figure 2.2B). To mitigate this droplet disruption, we designed the bypass channels with a step (Figure 2.2C-D) to increase the hydrodynamic resistance (and therefore

decrease the flux) through the bypass and maintain a sufficient flow rate in the main channel, ensuring that the droplets reached the outlet without breaking apart.

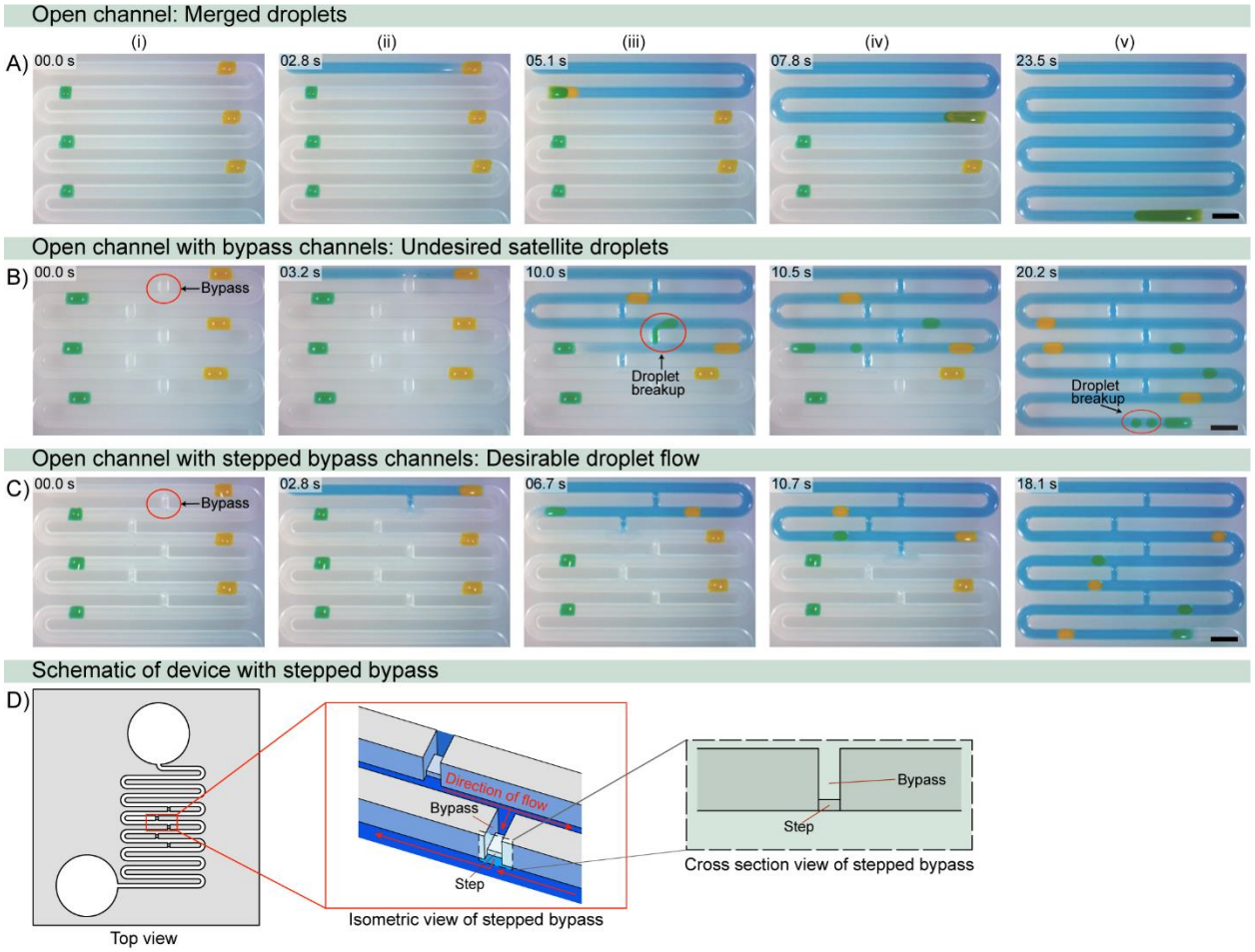

Figure 2.2: Open channel droplet incubation and transport. Droplets (alternating yellow and green for visualization) are incubated in an open channel without (A) or with (B-C) bypass channels (red circles); i-v) carrier fluid (blue) is pipetted in the inlet and flows down the channel *via* capillary flow, translating the droplets down the channel to the outlet reservoir. Bypass channels (B-C) prevent coalescence of preincubated droplets by inserting immiscible carrier fluid between aqueous droplets as they flow downstream. C) Incorporation of stepped bypass improves flow in the main channel and prevents formation of satellite droplets and droplet stagnation. D) Schematic of stepped bypass showing an isometric and cross-sectional view of the step in the bypass. Scale bar: 2 mm. Timestamps correspond to the addition of the carrier fluid (0.0 s) and not total droplet incubation time.

It is important to have a generalizable set of rules for designing bypass channels, to enable extension of our method to channels of different dimensions and geometries. We generated an analytical model that describes the ratio of fluid fluxes through the main channel relative to the bypass with respect

to the fluidic resistance associated with each flow path. Deriving a model from a generalized Lucas-Washburn-Rideal law for open channels[18] (Appendix A), we found the relationship between the fluidic resistances and flux to be:

$$\Delta P = P_1 - P_2 \approx \tilde{R}_1 Q_1 \approx \tilde{R}_2 Q_2 \quad (1)$$

where P is the pressure drop across our bypass system (P_1 and P_2 refer to the pressure drops at the nodes before and after the bypass, respectively), R_1 and R_2 are the resistances in the main channel and bypass channel, respectively, and Q_1 and Q_2 are the flux through the main channel and the bypass channel, respectively (Appendix A). The fluidic resistance of the capillary-driven flow in our system can be described by Equation 2:

$$\mu \frac{p}{\lambda S^2} L = R \quad (2)$$

where S is the cross-sectional area, L is the channel length, μ is the liquid viscosity, p is the total perimeter, and λ is the friction length.[28] The resistance in our system inversely correlates to the cross-sectional area and the flux of fluid through the channel (Appendix A). Solving for the ratio of the fluxes between the main channel and the bypass channel and then inserting the physical dimensions of our system into Equation 2 (as detailed in Appendix A) yielded a flux ratio of $Q_2/Q_1 = 3.18$ wherein the flux through the bypass channel (Q_2) is greater than the flux through the main channel (Q_1). However, through incorporation of a step, we are able to increase the resistance through the bypass channel and ensure less diversion of flow from the main channel, altering the flux ratio to $Q_2/Q_1 = 2.68$. This relation demonstrates that the resistance through the bypass can be manipulated by altering the geometry of the step (*i.e.*, larger step, increased resistance and decreased flux), enabling adaptation for different geometries and channel lengths. With different manufacturing techniques, even greater ratios can be designed. Further, while the flux is still greater in the bypass than the main channel, the decrease in the flux through the bypass afforded by the step enabled sufficient flow in the main channel to drive droplets towards the outlet and prevent stagnation of the carrier fluid in the channel curves (Figure 2.2C). The

derived model provides a framework for adapting the bypass system with different geometries and acts as a useful tool for quantification of flow and hydrodynamic resistance in open channels, as well as for guiding optimization of droplet flow in open channel systems.

The ability to transport small volumes with SCF lays the foundation for future open-channel platforms that integrate processes such as cell culture or biochemical reactions with small-volume readouts such as mass spectrometry and immunoassays. Overall, the bypass system is designed to incubate and manipulate droplets without extensive user interaction or difficult pipetting steps. Ease of use is demonstrated through a simple two-step process (droplet addition followed by carrier fluid addition) without the need for adjusting flow rates and flow directions for droplet manipulation. Due to the fabrication and droplet addition methods used, this technique is currently limited to low-throughput applications and droplet volumes compatible with micropipettes (≥ 0.2 μL). Additionally, droplet number is determined by the device footprint and friction forces between the carrier phase and the channel (resulting in decreased flow rate with an increased channel length) which restrict us from significantly extending the channel length; however, the bypass platform can be expanded to include more droplets through the creation of arrays of different geometries.

To demonstrate the expansion of this platform to incorporate more droplets, we fabricated an array of 8 devices with aligned inlet reservoirs, channels, and outlet reservoirs that enables sample loading, manipulation, and removal with a multichannel pipette. We present a potential workflow for this platform by conducting a model colorimetric assay[29] that consists of the combination of potassium thiocyanate (KSCN) and ferric nitrate ($Fe(NO_3)_3$) to form the colored complex $Fe(SCN^-)_x^{(3-x)+}$ (Figure 2.3). We pipetted 64 droplets (1 μL in volume) containing KSCN, $Fe(NO_3)_3$, or H_2O (negative control) into the channel and allowed the droplets to incubate for 30 min. at room temperature. Following incubation, we added a second 1 μL droplet containing KSCN, $Fe(NO_3)_3$, or H_2O to the first droplet and then initiated flow with undyed carrier fluid, coalescing the droplets within a single device and collecting them at each outlet reservoir. Once flow ceased, the droplets were removed using a multichannel pipette and transferred to a 96 well plate, where the absorbance of each combination was measured (Figure 2.3). Due

to the formation of the $Fe(SCN^-)_x^{(3-x)+}$ complex and the movement of the droplet in shift mode, some droplet residue was observed in the channel after the addition of the carrier fluid. The ability to pipette droplets into a channel, incubate them for a desired period of time, and then supplement those droplets or manipulate them with flow through an open channel highlights the benefits of this open platform for assays where access to reagents or samples at specific time points with minimal user interaction is important. Further, compatibility of this platform with multichannel pipettes enables handling of larger volumes of liquid and simple integration with established laboratory materials (*i.e.*, well plates) and readouts (*i.e.*, plate reader). Oftentimes, researchers want to be able to screen multiple conditions in an assay but then pool the samples together prior to analysis[30-32]; we envision that this platform can fulfill this need in a simple and easily implemented manner.

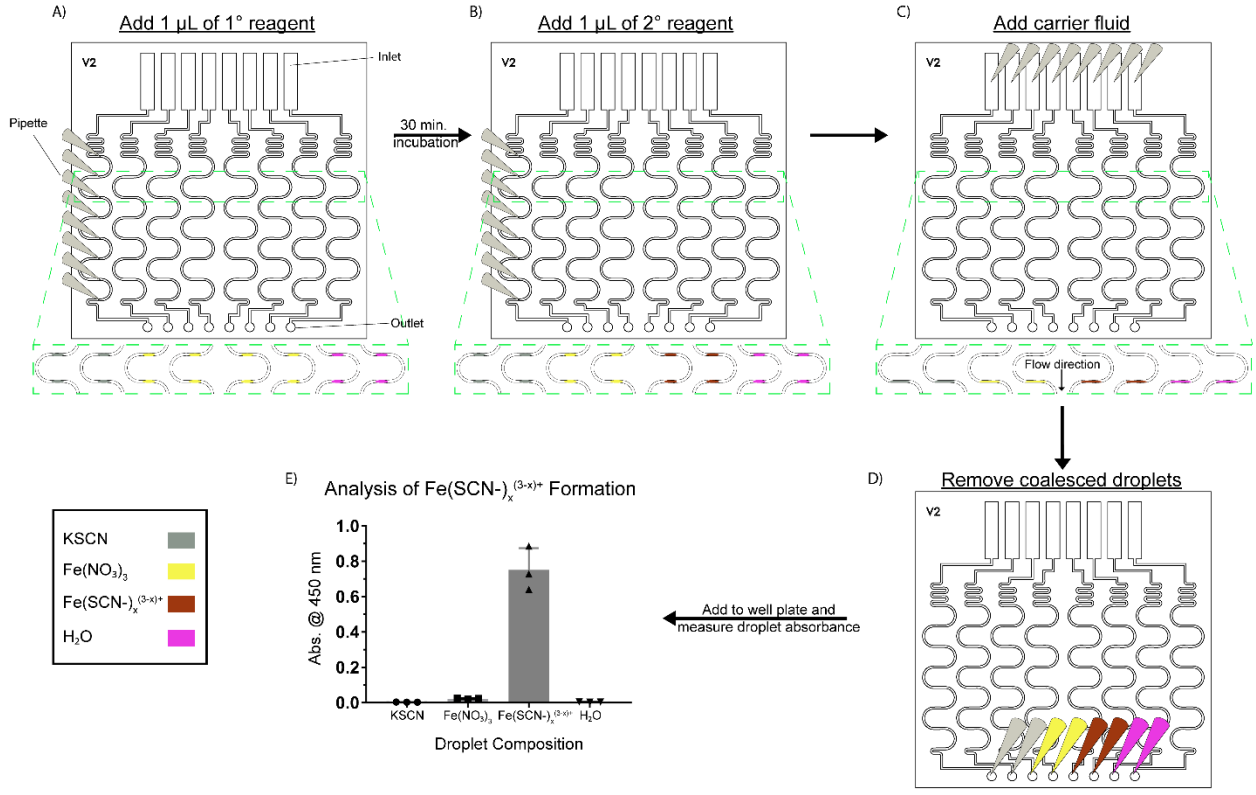

Figure 2.3: Workflow schematic and results for model colorimetric assay. A) Using a multichannel pipette, eight 1 µL droplets of KSCN (first and second channel), $Fe(NO_3)_3$ (third through sixth channel) or H_2O (seventh and eighth channel) are added to their respective open channel in each device of the array and allowed to incubate for 30 minutes at room temperature. B) After incubation, 1 µL droplets of KSCN, $Fe(NO_3)_3$, or H_2O are added to the incubating droplets with the following combinations: KSCN + KSCN, $Fe(NO_3)_3$ + $Fe(NO_3)_3$, KSCN + $Fe(NO_3)_3$, and H_2O + H_2O (negative

control). C) Colorless carrier fluid was then added to the inlet to coalesce and flow all the droplets to the outlet. D) Droplets are removed from the outlet reservoir using a multichannel pipette and transferred to a 96 well plate. E) The absorbance of the droplets is measured at 450 nm and a color change is observed in the droplet containing KSCN + $Fe(NO_3)_3$, indicating the presence of the colored compound $Fe(SCN^-)_x^{(3-x)+}$.

2.4 Controlled and adjustable droplet splitting

Building upon the droplet handling capabilities described for incubation and transport of multiple droplets, we demonstrate the ability to controllably split droplets within an open channel. Droplet splitting is an important feature that can extend the use of valuable or small volume samples by generating identical replicates and creating arrays for multiplexing. Using traditional droplet splitting geometries previously developed for closed-channel droplet-based microfluidics[7,8], we designed T junctions to split incoming droplets, where a droplet entering the junction fills each branch of the junction until it is slowed down by an expansion in the geometry of the channel (Figure 2.4A)[33,34]; once the junction is filled, the droplet splits relative to the length of each branch (Figure 2.4B). By tuning the lengths of the left and right branches of the T junction, we can generate symmetric or asymmetric droplets (Figure 2.4B-C), enabling users to generate variable volume aliquots from an original sample simply by changing the device dimensions. Further, the splitting of symmetric and asymmetric droplets was reproducible between devices within an array (Figure 2.4D). Some variability was observed between multiple arrays due to manual micromilling artifacts, but inter-array variability can be alleviated through fabrication with more consistent methods such as injection molding and advanced automated milling.[11,14] Currently, the platform is capable of splitting a single droplet in shift mode; devices can also be reused following washing and drying with reproducible results (Figure A5).

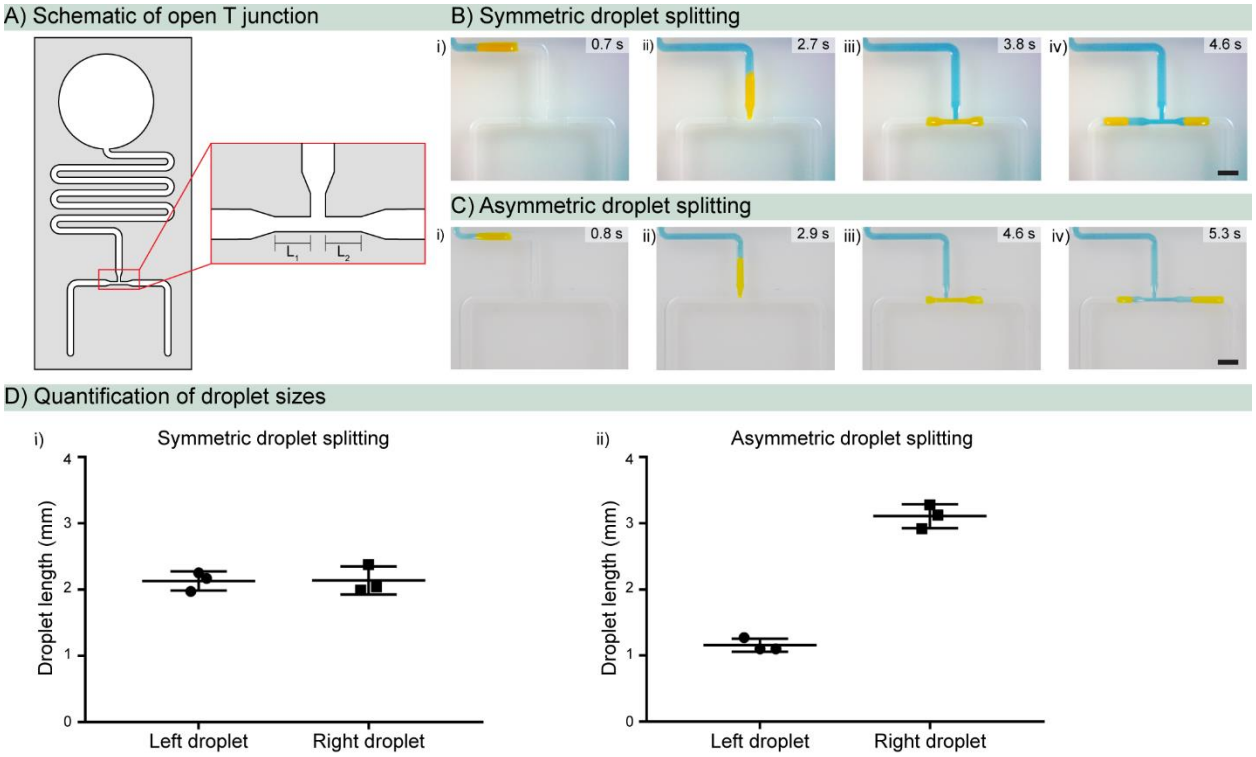

Figure 2.4: Controlled and adjustable droplet splitting in open channels with SCF. A) Schematic of T junction showing branches (L_1 and L_2) within the junction; B-C) i-ii) a droplet in the channel above a T junction with symmetric (B) or asymmetric (C) branch lengths is translated toward the junction *via* SCF; iii) the droplet fills both branches in the junction and slows upon reaching the channel expansion after the junction due to temporary pinning; iv) the droplet splits into two discrete droplets dependent upon the branch length; D) quantification of daughter droplet sizes after splitting in T junctions with symmetric (i) or asymmetric (ii) branch ratios (data points represent a single droplet split in three different devices within an array of devices, mean and standard deviation are indicated). For images and measurement of droplets at the end of the channel, please refer to Figure A4. Scale bar: 2 mm.

To demonstrate the workflow for a potential application of the open channel droplet splitting platform, we present a model experimental system for on-chip reagent delivery and reactions. We pipetted aqueous droplets tinted with yellow dye (to model primary reagents) upstream of a T junction and aqueous droplets tinted with green dye (to model secondary reagents) downstream of the T junction. We then loaded the inlet reservoir with carrier fluid to initiate flow. The carrier fluid flow drove the yellow droplet through the T junction, wherein the droplet split and its components were delivered to multiple samples (green droplets) downstream of the junction (Figure 2.5). The ability to preload the platform with reaction reagents allows users to generate multiplexed arrays for subsequent passive reagent delivery with

minimal user handling; additionally, altering the channel distance and geometry after mixing can be used to adjust the incubation time of the reaction.[8]

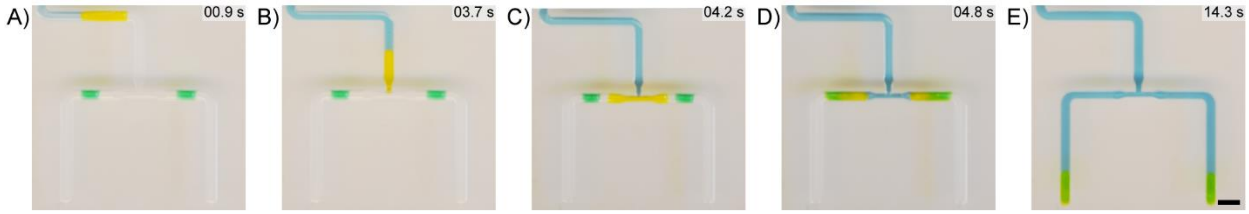

Figure 2.5: Workflow for droplet splitting and merging with downstream droplets to model reagent delivery. A yellow droplet (representing a primary reagent) was pipetted above the T junction while green droplets (representing secondary reagents) were added after the junction. A-B) Carrier fluid translates the yellow droplet *via* SCF into the junction; C) the droplet splits equally and is delivered (D) to the secondary reagents in the channel; E) the droplet and reagent mix as the droplet flows down the channel. Scale bar: 2 mm.

2.5 Conclusion

In this work, we develop essential features for immiscible droplet manipulation in capillary-driven open systems. Open channels offer several advantages over closed channels including pipette accessibility, manufacturability, customizability, and ease of use. Using these features, we created a generalized open channel platform for addition, incubation, and translation of multiple droplets and an open channel platform for droplet splitting and delivery. These platforms build upon prior work describing the fundamental behavior of single droplets in open biphasic systems by providing previously unavailable user functionalities (*e.g.*, incubation of multiple droplets within a channel, droplet splitting) and creating foundational systems that can be customized and adapted for a range of experimental needs. Traditional closed-channel droplet microfluidics provides high throughput capabilities that can accommodate $>10^7$ samples with droplet volumes reaching 10^{-15} L and can integrate with large-capacity screening instrumentation (LC/MS, high speed microscopy, *etc.*), greatly increasing the abilities of researchers to perform high throughput experimentation.[3] Open-channel droplet microfluidics aims to address a different scale and set of experimental applications for researchers performing smaller screening studies (tens or hundreds of samples) with higher volumes (µL-nL) that do not require the extensive infrastructure nor cost associated with high throughput droplet microfluidics; further, we anticipate that

our platform offers increased user accessibility, tractability, streamlining, and ease of use that allows for easy integration with existing experimental protocols and sample generation tools (*e.g.*, pipettes, liquid handling robot). Future work with these platforms will include increasing the capacity of the bypass system for larger droplet arrays, expanding the droplet splitting capabilities to accommodate a wider range of splitting ratios, and studying the dynamics of mixing in open channels. Further, in future investigations our platforms could be extended to smaller scales with the use of high resolution fabrication techniques and lower-volume liquid handlers or dispensers. In the future, we envision adaptation of these foundational platforms will enable users to expand and customize their current experimental toolbox for studies relating to drug screening, microscale reactions, and the "-omics" fields (*e.g.*, metabolomics, proteomics).

2.6 Materials and Methods

Materials

Droplets were created with deionized (DI) water (Type II, Harleco; Fisher Scientific, Hampton, NH) tinted with either yellow or green dye (Spice Supreme; Gel Spice Company, Bayonne, NJ) at a concentration of 10% or 1% (v/v), respectively. The carrier fluids were: toluene (Fisher Scientific, Figure 2.1) or 1-pentanol (Acros Organics, Thermo Fisher Scientific, Waltham, MA, Figures 2.1, 2.2, 2.3, 2.4, and 2.5). All carrier fluids solvents were tinted with Solvent Green 3 (Sigma-Aldrich, St. Louis, MO) at a concentration of 0.50 mg/mL.

Device fabrication

Devices were designed with Solidworks 2017 (Solidworks, Waltham, MA) and converted to .TAP files with SprutCam 10 (SprutCam, Naberezhnye Chelny, Russia). The devices were milled on poly(methyl methacrylate) (PMMA) sheets of 3.175 mm thickness (McMaster-Carr, Santa Fe Springs, CA) using a Tormach PCNC 770 mill (Tormach, Waunakee, WI). All device channels were milled with ball endmills (Performance Micro Tool, Janesville, WI) with a cutter diameter of 1/32" (TR-2-0313-BN) or 1/64" (TR-2-0150-BN) to create round-bottom channels. After milling, the devices were rinsed with DI

water, sonicated in 70% (v/v) ethanol, and rinsed again with DI water. The devices were then dried with compressed air prior to use.

Device design and testing

The main device dimensions are a channel width of 0.90 mm and a channel depth of 1.0 mm, with smaller channels included for carrier fluid bypass (0.5 mm wide, 1.0 mm length, 0.2 mm step height) (Figure 2.2D) and splitting (1.0 mm branch length, 0.45 mm channel width); the detailed dimensions of the devices and features are included in Appendix A (Figure A2). Aqueous droplets with a volume of 1.0 μL (Figures 2.1 and 2.2) or 3.0 μL (Figures 2.3 and 2.4) were generated in the channel with a pipette. Carrier fluids with a volume of 240 μL were dispensed in the inlet reservoir of the channel. Droplets were imaged and analyzed with ImageJ (National Institutes of Health, MD) for quantification (Figure 2.3 and A3). To prevent evaporation, devices were placed inside of a humidified Nunc™ Omnitray™ (Thermo Fisher, Frederick, MD) surrounded by 1.5 mL of sacrificial water droplets (≈ 50 μL/droplet), and the Omnitray was then placed inside a secondary humidified bioassay dish (#240835, Thermo Fisher) containing 100 mL of sacrificial water for extended incubations.

For the arrayed colorimetric analysis system, 1 μL droplets containing 0.1 N potassium thiocyanate (KSCN) (Fisher Scientific), 0.067 M ferric nitrate ($Fe(NO_3)_3$) (Fisher Scientific), or DI water were added to the open channel device (Figure 2.3) and allowed to incubate at room temperature for 30 minutes. Following incubation, a second 1 μL droplet containing KSCN, $Fe(NO_3)_3$, or H_2O was added directly to the incubating droplet for a final volume of 2 μL. 150 μL of undyed 1-pentanol was then added to the inlet reservoir to initiate flow. Once the coalesced droplets reached the outlet reservoir, they were removed using a multichannel pipette (16 μL) and added to a 96 well plate; each sample was diluted with DI water up to 50 μL to ensure accurate absorbance measurements. The absorbance of the plate was then measured at 450 nm using a Multiskan Spectrum UV/visible Microplate Reader (Thermo Labsystems, Waltham, MA). The experiment was repeated three times using three independent arrays of devices; each array contained two replicate devices per condition. Plotted points represent the average of the two

replicate devices. All images were analyzed using ImageJ and visualized using Prism (GraphPad Software, San Diego, CA).

Imaging

Images and videos were acquired using a MU1403B High Speed Microscope Camera mounted on an Amscope SM-3TZ-80S stereoscope (Amscope, Irvine, CA) unless otherwise noted. For Figure 2.1B, 2.4C and 2.5, images and videos were obtained with a Nikon-D5300 ultra-high resolution SLR camera (Tokyo, Japan).

2.7 References

1. Berthier, J.; Brakke, K.A.; Berthier, E. Open Microfluidics. Wiley, **2016**.
2. Teh, S.Y.;Lin, R.; Hung, L.H.; Lee, A.P. Droplet microfluidics. *Lab Chip*, **2008**, 8, 198-220.
3. Shang, L.; Cheng, Y.; Zhao, Y. Emerging Droplet Microfluidics. *Chem. Rev.*, **2017**, 117, 7964-8040.
4. Frenz, L.; Blank, K.; Brouzes, E.; Griffiths, A.D. Reliable microfluidic on-chip incubation of droplets in delay-lines. *Lab Chip*, **2009**, 9, 10, 1344-1348.
5. Boukellal, H.;Selimovic, S.; Jia, Y.; Cristobal, G.; Fraden, S. Simple, robust storage of drops and fluids in a microfluidic device. *Lab Chip*, **2009**, 9, 331-338.
6. Abate, A.R.; Hung, T.; Mary, P.; Agresti, J.J.; Weitz, D.A. High-throughput injection with microfluidics using picoinjectors. *PNAS*, **2010**, 107, 45, 19163-19166.
7. Link, D.R.; Anna, S.L.; Weitz, D.A; Stone, H.A. Geometrically mediated breakup of drops in microfluidic device. *Phys. Rev. Lett.*, **2004**, 92, 054503.
8. Song, H.; Chen, D.L.; Ismagilov, R.F. Reactions in droplets in microfluidic channels. *Angew. Chem. Int. Ed. Engl.*, **2006**, 45, 44, 7336-7356.
9. Li, C.; Boban, M.; Tuteja, A. Open-channel, water-in-oil emulsification in paper-based microfluidic devices. *Lab Chip*, **2017**, 1436.
10. Casavant, B.P.; Berthier, E.; Theberge, A.B.; Berthier, J.; Montanez-Sauri, S.I.; Bischel, L.L.; *et al.* Suspended Microfluidics. *PNAS*, **2016**, 110, 10111–10116.
11. Guckenberger, D.J.; de Groot, T.E.; Wan, A.M.D.; Beebe, D.J.; Young, E.W.K. Micromilling: A method for ultra-rapid prototyping of plastic microfluidic devices. *Lab Chip*, **2015**, 15, 11, 2364-2378.
12. de Groot, T.E.; Veserat, K.S.; Berthier, E.; Beebe, D.J.; Theberge, A.B. Surface-tension drive open microfluidic platform for hanging droplet culture. *Lab Chip*, **2016**, 16, 334.
13. Barkal, L.J.; Theberge, A.B.; Guo, C.J.; Spraker, J.; Rappert, L.; Berthier, J.; *et al.* Microbial metabolomics in open microscale platforms. *Nature Communications*, **2016**, 7, 10610.
14. Lee, U.N.; Su, X.; Guckenberger, D.J., Dostie, A.M.; Zhang, T.; Berthier, E.; *et al.* Fundamentals of rapid injection molding for microfluidic cell-based assays. *Lab Chip*, **2018**, 18, 496-504.
15. Lee, Y.; Choi, J.W.; Yu, J.; Park, D.; Ha, J.; Son, K.; *et al.* Microfluidics within a well: an injection-molded plastic array 3D culture platform. *Lab Chip*, **2018**, 18, 2433-2440.
16. Huemmer, D.; Bachler, S.; Kohler, M.; Blank, L.M.; Zenobi, R.; Dittrich, P.S.; Microfluidic platform for multimodal analysis of enzyme secretion in nanoliter droplet arrays. *Anal. Chem.*, **2019**, 91, 3, 2066-2073.
17. Lee, J.J.; Berthier, J.; Brakke, K.A.; Dostie, A.M.; Theberge, A.B.; Berthier, E. Droplet behavior in Open Biphasic Microfluidics. *Langmuir*, **2018**, 34, 18, 5358-5366.
18. Berthier, J.; Gosselin, D.; Berthier, E. A generalization of the Lucas-Washburn-Rideal law to composite microchannels of arbitrary cross section. *Microfluid. Nanofluid.*, **2015**, 19, 3, 497-507.
19. Chen, Y.F.; Tseng, F.G.; Chein, S.Y.C.; Chen, M.H.; Yu, R.J.; Chieng, C.C. Surface tension driven flow for open microchannels with different turning angles. *Microfluid Nanofluid,* **2008**, 5, 193-203.

20. Lade Jr., R.K.; Jochem, K.S.; Macosko, C.W.; Francis, L.F. Capillary Coatings: Flow and Drying Dynamics in Open Microchannels. *Langmuir*, **2018**, 34, 7624-7639.
21. Yang, D.; Krasowska, M.; Priest, C.; Popescu, M.N.; Ralston, J. Dynamics of capillary-driven flow in open microchannels. *J. Phys. Chem. C.*, **2011**, 115, 18761-18769.
22. Concus, P.; Finn, R. On the behavior of a capillary surface in a wedge. *PNAS*, **1969**, 2, 63, 292–299.
23. Hadimioglu, B.; Stearns, R.; Ellson, R. Moving Liquids with Sound: The Physics of Acoustic Droplet Ejection for Robust Laboratory Automation in Life Sciences. *Journal of Laboratory Automation*, **2016**, 21, 1, 4-18.
24. Demirci, U. Acoustic Picoliter Droplets for Emerging Applications in Semiconductor Industry and Biotechnology. *Journal of Microelectromechanical Systems*, **2006**, 15, 4, 957-966.
25. Choi, K.; Ng, A.H.C.; Fobel, R.; Wheeler, A.R. Digital Microfluidics. *Annu. Rev. Anal. Chem.*, **2012**, 5, 413-440.
26. Ng, A.H.C.; Li, B.B.; Chamberlain, M.D.; Wheeler, A.R. Digital Microfluidic Cell Culture. *Annu. Rev. Biomed. Eng.*, **2015**, 17, 91-112.
27. Jones, T.B. On the relationship of dielectrophoresis and electrowetting. *Langmuir*, **2002**, 18, 11, 4437-4443.
28. Lee, J.J.; Karampelas, I.H.; Brakke, K.A.; Theberge, A.B.; Berthier, E.; Berthier, J. Capillary flow in open microgrooves: bifurcations and networks. *Langmuir*. **2019**, 35, 32, 10667-10675.
29. Fidalgo, L.M.; Abell, C.; Huck, W.T.S. Surface-induced droplet fusión in microfluidic devices. *Lab Chip*, **2007**, 7, 984-986.
30. Yang, Y.H.; Song, E.; Lee, B.R.; Kim, E.J.; Park, S.H.; Kim, Y.G.; *et al*. Rapid functional screening of *Streptomyces coelicolor* regulators by use of a pH indicator and application to the MarR-like regulator AbsC. *Appl. Environ. Microbiol.*, **2010**, 76, 11, 3645-3656.
31. Onaka, H.; Mori, Y.; Igarashi, Y.; Furumai, T. Mycolic acid-containing bacteria induce natural-product biosynthesis in *Streptomyces* species. *Appl. Environ. Microbiol.*, **2011**, 77, 2 400-406.
32. Adnani, N.; Vazquez-Rivera, E.; Adibhatla, S.N.; Ellis, G.A.; Braun, D.R.; Bugni, T.S. Investigation of interspecies interactions with marine micromonosporaceae using an improved co-culture approach. *Mar. Drugs*, **2015**, 13, 6082-6098.
33. Mehrabian, H.; Gao, P.; J.J. Feng, J.J. Wicking flow through microchannels. *Physics of Fluids*, **2011**, 23, 122108.
34. Berthier, J; Brakke, K.A.; Gosselin, D.; Navarro, F.; Belgacem, N.; Chaussy, D.; Berthier, E. On the halt of spontaneous capillary flows in diverging open channels. *Med. Eng. Phys.* **2017**, 75-80.

Chapter 3. Open-Microfluidic Patterning of Surfaces for Segregated Coculture of Cells

Reproduced in part with permission from Berry, S.B.*; Zhang, T.*; Day, J.H.; Su, X.; Wilson, I.Z.; Berthier, E.; Theberge, A.B. "Upgrading well plates using open microfluidic patterning". *Lab Chip*, 2017, 17, 4253-4264.

*denotes co-authorship

Abstract:

Cellular communication between multiple cell types is a ubiquitous process that is responsible for vital physiological responses observed *in vivo* (*e.g.*, immune response, organ function). Many *in vitro* coculture strategies have been developed, both in traditional culture and microscale systems, and have shown the potential to recreate some of the physiological behaviors of organs or groups of cells. A fundamental limitation of current systems is the difficulty of reconciling the additional engineering requirements for creating soluble factor signaling systems (*e.g.*, segregated cell culture) with the use of well-characterized materials and platforms that have demonstrated successful results and biocompatibility in assays. We present a new open microfluidic platform, the Monorail Device, that is placed in any existing well plate or Petri dish and enables patterning of segregated coculture regions, thereby allowing the direct upgrade of monoculture experiments into multiculture assays. Our platform patterns biocompatible hydrogel walls *via* microfluidic spontaneous capillary flow (SCF) along a rail insert set inside commercially available cultureware, creating customized pipette-accessible cell culture chambers that require fewer cells than standard macroscale culture. Importantly, the device allows the use of native surfaces without additional modification or treatments, while creating permeable dividers for the diffusion of soluble factors. Additionally, the ease of patterning afforded by our platform makes reconfiguration of the culture region as simple as changing the rail insert. We demonstrate the ability of the device to pattern flows on a variety of cell culture surfaces and create hydrogel walls in complex and precise shapes. We characterize the physical parameters that enable a reproducible SCF-driven flow and highlight specialized

design features that increase the ease of use of the device and control of the open microfluidic flow. Further, we present the performance of our platform according to useful coculture criteria, including permeability and integrity of our hydrogel walls and surface-sensitive cell culture. Lastly, we show the potential of this type of platform to create modular multikingdom culture systems that can be used to study soluble factor signaling between mammalian cells, bacteria, and fungi, as well as the potential for adaptation of this technology by researchers across multiple fields.

3.1 Introduction

Modeling soluble factor signaling between human cell types and across cells, bacteria, and fungi is essential for studying organ function and disease mechanisms. A powerful approach in modeling this type of signaling utilizes systems that physically separate cell types yet permit soluble small molecules and proteins to diffuse and perform their signaling mechanism. This can typically be accomplished using engineered systems such as Transwell inserts or innovative microfluidic platforms. Both approaches have been enabling for soluble factor signaling and coculture studies, but are fundamentally limited in that they require specifically engineered systems, limiting their versatility and transferability – two important aspects we build upon. For established assays to be compatible with engineered microsystems, the assays must be adapted to match technological requirements that differ between established cultureware and engineered microsystems (*e.g.*, accessibility, workflow for changing media, device material, cell culture surface treatments). In contrast, we aimed to create a segregated culture device to study heterotypic cellular communication that can simply be inserted into existing culture systems (*e.g.*, well plates) to enable facile augmentation of an established monoculture assay without significant alterations of experimental protocols. We propose a method to perform segregated multiculture and signaling studies through the creation of a hydrogel-wall network patterned using open microfluidics in a well plate-compatible insert.

Cell cocultures have been used to recapitulate specific aspects of *in vivo* cellular signaling phenomena, providing insight into complex physiological systems (*e.g.*, organs, immune response).[1]

Specifically, segregated coculture, in which cell types are physically separated but are still able to communicate *via* diffusion of signaling molecules, can capture dynamic, reciprocal signaling between cell types[2,3] and isolate the effects of soluble factors from the effects of heterotypic contact that include juxtacrine signaling pathways and cell stimulation.[4,5] Segregated coculture methods are widely available as commercial Transwell inserts which are easy to use and integrate with standard culture plates[6,7], but are limited by fixed culture configurations, the inability to tune the size of the culture regions, the number of cultures in communication, the use of alternative surface materials (*e.g.*, PC, PET, PTFE), poorly defined diffusion gradients that rapidly decay,[8,9] and the inability to culture multiple cell types on a single surface.

Alternatively, researchers have turned to custom engineered microfluidic systems for segregated coculture, as these systems can provide precise control over cell culture environments, require fewer cells, and can be tailored to mimic physiological conditions.[10-20] These engineering approaches have generated effective and creative segregated coculture platforms, using techniques such as hydrogel patterning and laminar flow patterning for precise cell seeding and microchannel systems for the isolation of soluble factor effects in complex cocultures.[5, 21-26] For example, Hui *et al.*[27] created a reconfigurable, interdigitated coculture system that permitted precise temporal and spatial manipulation of coculture. In addition, Lee *et al.*[28] fabricated a micromolded polydimethylsiloxane (PDMS) device that utilized flow along a rail to pattern gels and selectively seed cells and microbes. Similarly, Patel *et al.* and others created hydrogel-based barriers that selectively manipulate the chemical and temporal signaling, as well as movement, of cell types in coculture.[29-32] Further, Carney *et al.*[26] utilized a dual-chambered polystyrene (PS) microfluidic device that allowed transport of signaling molecules through diffusion channels connecting the segregated chambers. These examples represent impressive endeavors to create simple engineering solutions for difficulties associated with segregated coculture, yet they remain limited. Many of these approaches[3,5, 13-17,19,22-24,28-32] use PDMS, which has been shown to absorb small molecules,[33,34] while others use enclosed culture chambers,[24,26,28] which are only accessible from the inlet/outlet ports, and have not demonstrated compatibility of their platforms with unmodified commercially available tissue-culture surfaces.[26,28] These customized microsystems are a valuable alternative to commonly used

methods and provide important insight into physiological interactions that cannot be easily examined in traditional cultureware. However, despite the remarkable push towards simplifying complex cocultures with these engineered systems, integration of custom microsystems with established cultureware remains difficult. Commercially available well plates and tissue culture treated (TCT) surfaces are easy to handle and use, have been validated through decades of experimentation, and are familiar to biological laboratories.[35] Further, production of cell culture-treated surfaces is a technically challenging and labor intensive process that has been optimized by industry through decades of effort. Therefore, there exists a need for an easy-to-use tool that provides investigators with the flexibility to upgrade their model with multiple cell types while maintaining optimized experimental materials and methods.

We developed a segregated coculture technology, called the Monorail Device, that integrates with established cell culture methods and enables the partitioning of cell-culture surfaces in commercially available well plates by flowing biocompatible hydrogel solutions to create hydrogel walls. Importantly, the Monorail Device upgrades simple monoculture assays by adding any number of additional cell-culture wells in controlled configurations on the same plane. Our method builds upon previous work in open microfluidics by incorporating spontaneous capillary flow (SCF) along an open microfluidic channel comprised of a plastic 'rail' insert (channel ceiling), the well plate (channel floor), and two open air interfaces (channel sides).[28,36,37] This type of flow allows the easy patterning of hydrogel solution and its polymerization, thereby creating permeable cell culture regions. Additionally, the incorporation of SCF as the mechanism of flow eliminates the need for external pumping systems during the hydrogel wall fabrication process. Our platforms are insertable into individual wells, similar to Transwells inserts, and easy to use, as gels and cells can be applied in open wells by simple pipetting. The accessibility to cell culture areas is a key design consideration of the platform; the open chambers and channels demarcated by the hydrogel walls do not have a ceiling and as such are pipette accessible from the top. Thus, cell seeding, media changing, reagent addition, and the removal of media for endpoint analysis (*e.g.*, enzyme-linked immunosorbent assay (ELISA), liquid chromatography-mass spectrometry (LC-MS)) can all be achieved by pipetting directly into the culture regions from the top, just as in a traditional well plate.

Additionally, the use of open microfluidics (*i.e.*, simple 'rail' insert) enables straightforward rapid prototyping *via* 3D printing[38,39] for platform design and injection molding (Figure B6) for scale-up and reproducible use in biology research environments. We demonstrate the application of our Monorail Device by patterning hydrogel walls onto multiple different surfaces and characterizing the integrity, permeability, flow, and dimensions of the wall. We detail specific design features that improve function within the device and increase the versatility of our design. Importantly, our device can be easily integrated into biological laboratories to fulfill a range of experimental needs, including multikingdom coculture, small molecule diffusion, and surface-sensitive cell culture.

3.2 Spontaneous capillary flow along a rail

We created a hydrogel-wall patterning platform that easily integrates into existing cultureware and utilizes SCF along a rail as the principal mechanism of function (Figure 3.1). Operation of our Monorail Device is simple and fast, as wall fabrication *via* SCF requires minimal user interaction through a two-step process: placing the device in a well or on a cell culture surface (Figure 3.1a), similar to a Transwell, and pipetting of the hydrogel solution into the loading zone (Figure 3.1b and c). In this work, we optimized our platform for use with Matrigel, and we have also used our platform with fibrin and collagen I. Flow within our platform is described by an open microfluidic rail system, in which liquid flows in a channel with no side-walls. The cross-section of the open channel thus defines a wetted perimeter (P_w), comprising of all the solid surfaces, and a free perimeter (P_f), comprising of all the open interfaces. SCF along a rail has been previously modeled[28,36,37]; additionally, to describe the specific conditions of flow in our device embodiment, we performed a balance-of-pressure analysis between the inlet surface-tension-based Laplace pressure and the Laplace pressure in the advancing fluid under the rail, which led to the development of an analytical model of the conditions for flow based on the aspect ratio of the open channel (Figure B1, Figure 3.2b).

Our model states that flow within our platform is dependent upon the height (h) and width (w) of the rail (Figure 3.1d); these two physical parameters can be utilized as guidelines for customizing our

open microfluidic system, in which the Laplace pressure affects the performance of a system with different aspect ratios or shapes (Figure 3.1e). Using experimentally measured values for the contact angles of Matrigel on the rail surface ($\theta = 22.3° \pm 1.6°$) and a TCT PS surface ($\theta = 38.4° \pm 1.1°$), we derived a relationship between *h* and *w* which determines the limit between "flow" and "no flow" (illustrated by the boundary between the red and green shaded regions in Figure 3.2b). To validate our model, we characterized conditions for flow in our system using devices of different heights and widths on the TCT PS surface. We use a simple single rail device and a qualitative binary system to differentiate between "flow" and "no flow" conditions: "flow" is defined as complete reproducible flow of Matrigel *via* SCF along the entire length of the rail, whereas "no flow" is defined as no initiation of flow along the rail after reservoir filling or incomplete flow along the rail (Figure 3.2a). According to our model, the region below the boundary (shaded green) represents favorable flow conditions, and the region above the boundary (shaded red) represents conditions for which "no flow" was predicted (Figure 3.2b). Indeed, when we plotted the experimental data of the flow and no-flow observations for devices with a range of heights and widths, we found that the model predicted the conditions for flow well (only one experimental point showed a deviation) and presented an experimental trend, as expected, in which larger widths and smaller heights promoted flow within our platform (Figure 3.2b). We expect this trend to hold for dimensions below those presented in this work, as we were limited by the fabrication capabilities of the 3D printing technology used in this paper (see Methods). However, open microfluidics has been demonstrated and the laws governing open fluid flow have been validated at scales smaller than those employed here,[28,36] supporting that our method could be extended to smaller length scales achieved with alternative fabrication procedures.[43]

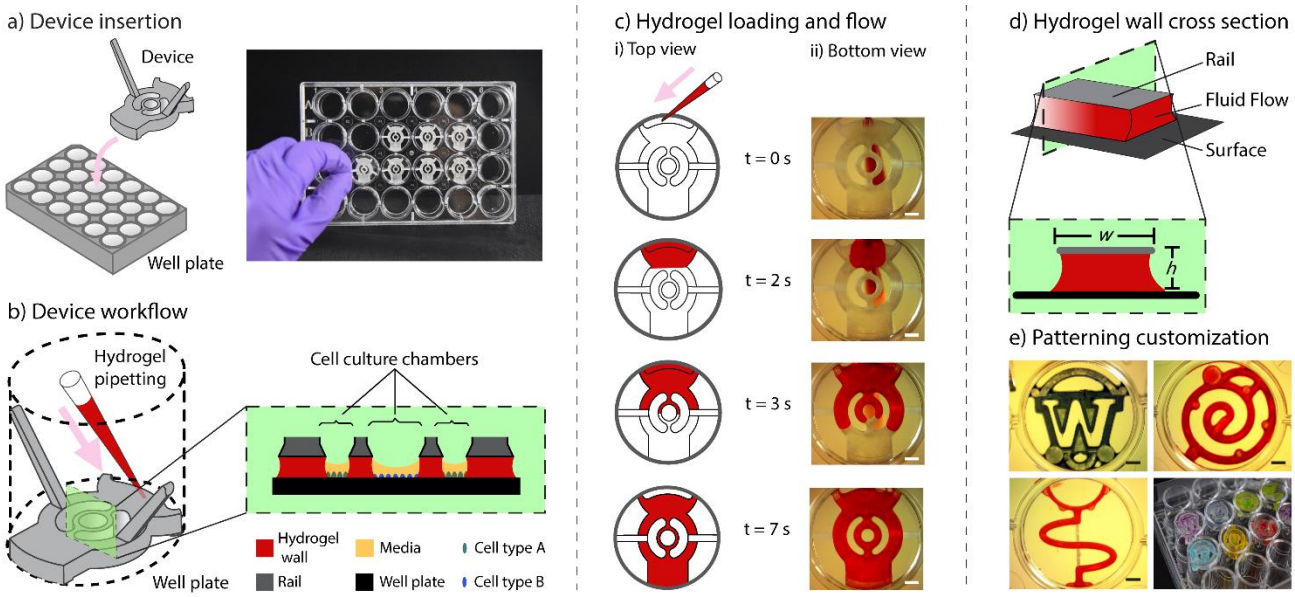

Figure 3.1: Overview of device operation and cross section showing SCF in a rail system. a) Insertion of the Monorail Device into a 24 well plate for hydrogel-wall patterning; image shows the device in a standard 24 well plate. b) Hydrogel solution is loaded into the inlet, filling the device; the cross section demonstrates a hydrogel-filled device with two separate cell types seeded in the inner and outer culture chambers. c) Schematics (i) and images (ii) of selected time points corresponding to device filling, as imaged through the bottom of a 24 well plate. d) Cross section of rail system with SCF. SCF is governed by the physical parameters height (h) and width (w), as well as the contact angles (θ_1 and θ_2, not shown) between the gel and the rail and the gel and the bottom surface. e) The patterning method is versatile and can be used to create chambers of diverse geometries. Scale bars = 2 mm.

Cell-culture platforms are highly tuned towards specific cell types, often matching cell-surface requirements with functionalizing treatments to favorably alter cell adhesion on the culture surface. In order to assess the ability of our platform to adapt to any cultureware surface, we characterized flow on the surface of commonly used cell culture materials (*e.g.*, glass, PS) with different contact angles. We tested the ability of our platform to pattern hydrogel walls on surfaces with a range of contact angles (17.9° – 49.9°) and observed successful hydrogel solution flow on each surface (Figure 3.2c). These results agree with behavior predicted from our model, in which a device with a height of 0.25 mm and a width of 1 mm would be expected to facilitate SCF on the surfaces tested. The ability of our platform to successfully pattern hydrogel walls on a range of common surfaces illustrates the versatility of our platform. The manipulation of the height, width, and contact angles of the platform can allow our method to be used with a wide range of surfaces.

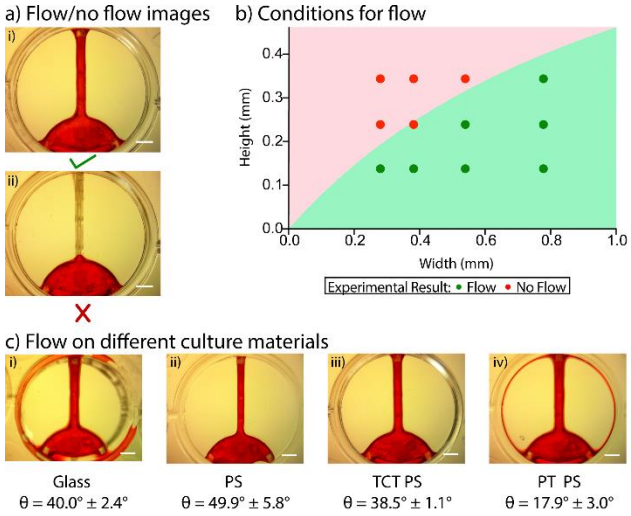

Figure 3.2: Characterization of flow along rails. a) Representative images showing i) "flow" and ii) "no flow" of Matrigel along rail (n = 3 devices). Scale bar = 2 mm. b) Phase diagram of theoretical (shaded region) and experimental observations (plotted points) of "flow" and "no flow." Theoretical predictions were according to our model (see Appendix B), wherein the green region represents the region in which flow is expected to occur, and the red region represents the region in which flow is not expected to occur. Experimental results (plotted as red or green points for "no flow" and "flow," respectively) were obtained by varying the height between the rail and well plate or width of the rail in our device (representative of n = 3 devices). All devices were used on tissue culture treated (TCT) polystyrene well plates. Theoretical values were calculated based on contact angles collected on a TCT Omnitray and the 3D printer resin. c) Successful flow conditions on surfaces with varied contact angles. All trials were conducted with the same device design (w = 1 mm, h = 0.25 mm), and images are representative of n = 3 devices. The results show that SCF along the rail occurs on all surfaces tested, as predicted by our model. In image i), the ring of Matrigel along the periphery of the well is due to a gap created from adhering a glass slide to a PS well plate to create a glass-bottomed well. In image iv), the ring of Matrigel along the periphery of the well is due to Concus-Finn flow (*i.e.*, flow along a wedge).[36,44] Scale bars = 2 mm.

3.3 Design optimization of open microfluidic patterning platform

The ability to precisely control fluid flow in open channels dictates the shape, size, and ease of use of our platform. To achieve greater control over the fluids and more reproducible filling of the device *via* SCF, we added features to control the capillary forces along the pathway of flow. These features ensure that the hydrogel solution flows along the rail and accurately patterns the surface; additionally, these regions increase tolerance to pipetting speed and pipette placement by the user. To ensure reproducible initiation of flow, we incorporated a controlled inlet (Figure 3.3a, (ii)) that confines the hydrogel solution beneath the rail as it flows from the inlet to the end of device; without the controlled inlet, we observed

uncontrolled wetting by the inputted fluid in culture chambers and around the device (Figure 3.3a, (3)). Additionally, the controlled inlet contains a height gradient that directs the hydrogel solution towards the middle of the inlet (Figure B2), thereby enabling the user to load the hydrogel solution by placing a pipette anywhere in the loading zone. In conjunction with the controlled inlet, we incorporated a region of high capillary favorability (*i.e.*, a capillary sink) at the end of the flow path to ensure controlled flow within the device (Figure 3.3b, (ii)); without the capillary sink, we observed flooding into the culture chambers (Figure 3.3b, (3)). The capillary sink promotes controlled flow because of an increased favorability of the hydrogel solution to wet a feature with a larger width (resulting from a lower h:w ratio, as h is kept constant from the rail to the sink); therefore, inputted hydrogel solution preferentially flows to the capillary sink instead of into the culture chambers.

As the channels are open, there is the potential for the fluid to wick vertically up along the sides of the rails, a phenomenon also known as capillary rise (Figure 3.3c, (3)). Indeed, we observed capillary rise within our platform, which led to an increased width at the base of the wall and flooding into the culture chambers while in the process of device filling. At the conclusion of device filling, we observed recession of the hydrogel solution back towards the rail, leaving a faint residue on the surface where the gel had originally flooded into the culture chamber. To halt the capillary rise of the hydrogel solution, we improved the pinning ability of the rail by increasing the acuteness of the angles on the sides of the rail, creating a trapezoidal cross section (Figure 3.3c, (ii)). It is important to note that the width at the base of the wall is greater than the width of the rail even with the trapezoidal cross-section, as the bottom surface is not bound laterally (Figure 3.3c, (3)); however, the width at the base is consistent, with the extent of flooding remaining < 260 μm into the chamber, and therefore can be accounted for when designing platform dimensions (Figure B3, B5). Lastly, another source of error is Concus-Finn filaments (*i.e.*, filaments of fluid in a wedge defined by two surfaces intersecting)[36,44] that may occur when rails change direction, split, or merge. The Concus-Finn filaments can be prevented by rounding all the concave angles of the device. By removing wedge-shaped regions conducive to Concus-Finn flow, flow within our device more closely resembled a solid fluid front (*i.e.*, without additional fluid filaments). When combined with

the controlled inlet and the capillary sink, these flow-controlling features represent necessary design aspects for the successful execution of SCF in our platform and across different designs.

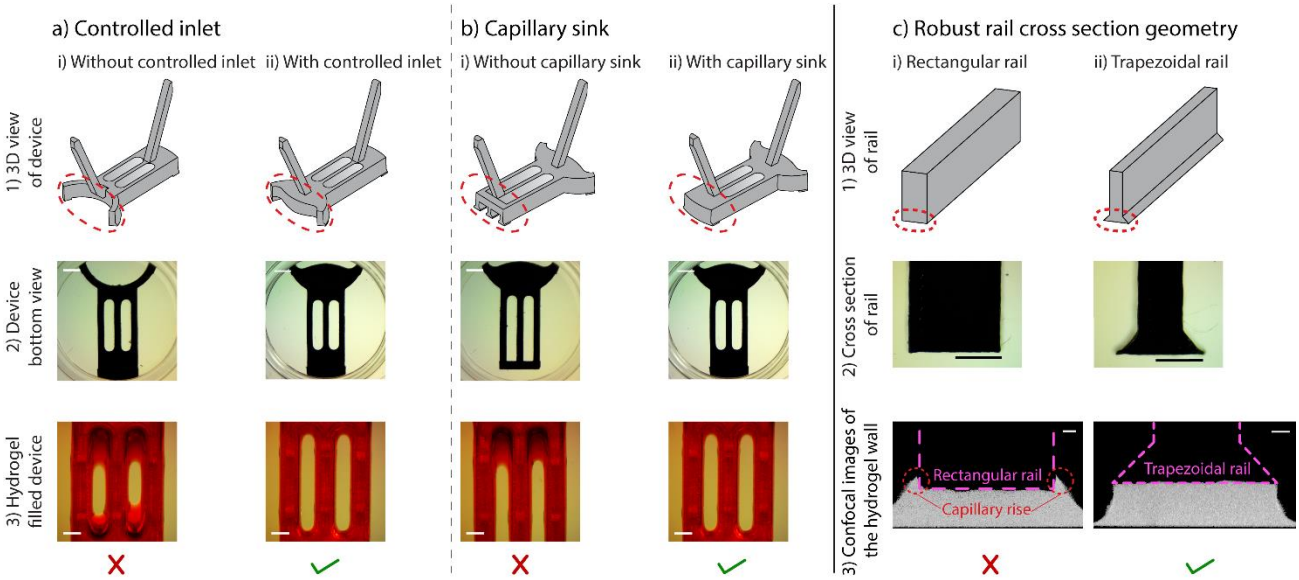

Figure 3.3: Integrated design features for improving control of hydrogel flows. Schematics and images depicting functional design features of our platform include a) a controlled inlet, b) a capillary sink, and c) a trapezoidal rail cross section. For each feature, a 3D schematic (1) and image (2) illustrates the presence or absence of the design feature in the device. For each design, a device containing the design feature and a device without the feature were loaded with hydrogel solution and allowed to flow to completion (3); devices without the functional design feature experienced flooding of the hydrogel solution into the culture chamber (a,b) or capillary rise (c, red circles). Devices for a) and b) were used on TCT PS with Matrigel that was dyed red for visualization. Images are representative of n = 3 devices. Scale bar = 2 mm (2), = 1 mm (3). For c), rails for cross sectional images were printed larger for imaging purposes (Scale bar = 1 mm); actual-sized rail images are in Appendix B (Figure B4). Confocal images of AlexaFluor-488-dyed Matrigel flow were obtained on glass 24 well plates to minimize autofluorescence. Scale bar = 100 μm.

3.4 Application of hydrogel patterning for cell culture systems

The intrinsic characteristics of hydrogels provide several advantages when used for wall fabrication; hydrogels are permeable, thereby enabling diffusion of soluble factors through the wall, yet are able to maintain a defined shape that can act as a physical barrier for objects like cells. These characteristics support the use of hydrogels as a barrier for segregated coculture systems, as they permit soluble factor signaling while prohibiting physical contact between cell types.[32] To demonstrate the segregation and containment of cells by the hydrogel walls, we selectively stained and seeded benign

prostate stromal cells (BHPrS1) and umbilical arterial smooth muscle cells (HUASMC) into separate chambers within a device, separated by the hydrogel wall (Figure 3.4a). After cell incubation and adhesion, we imaged the device and observed no mixing of the cell populations, clearly demonstrating the physical compartmentalization of each cell type. Importantly, this platform can be used with reduced cell numbers (≈2000 cells/chamber), illustrating utility for experiments involving rare or limited cell types (*e.g.*, patient cells).

We then quantified the diffusion of a model small molecule (AlexaFluor-488) through the hydrogel wall to model soluble factor signaling. We generated a diffusion profile by measuring the concentration of AlexaFluor-488 as it diffused through the hydrogel wall from the sourcing chamber to the receiving chamber (Figure 3.4b). The concentration of AlexaFluor-488 followed the model predicted by the quasi-static Fick law indicating a linear diffusion gradient of AlexaFluor-488 across the hydrogel wall. The diffusion profile demonstrates predictable and controllable signaling across the hydrogel wall. Diffusion time is dependent upon the size of the molecule, the thickness and permeability of the wall, and the distance between the source and the receiver. Therefore, for applications where different diffusion rates are required, the dimensions of the wall and culture chambers and the concentration/type of hydrogel can be adjusted. Importantly, these results support the use of this platform as a method to study intercellular communication while maintaining physical separation of cell types.

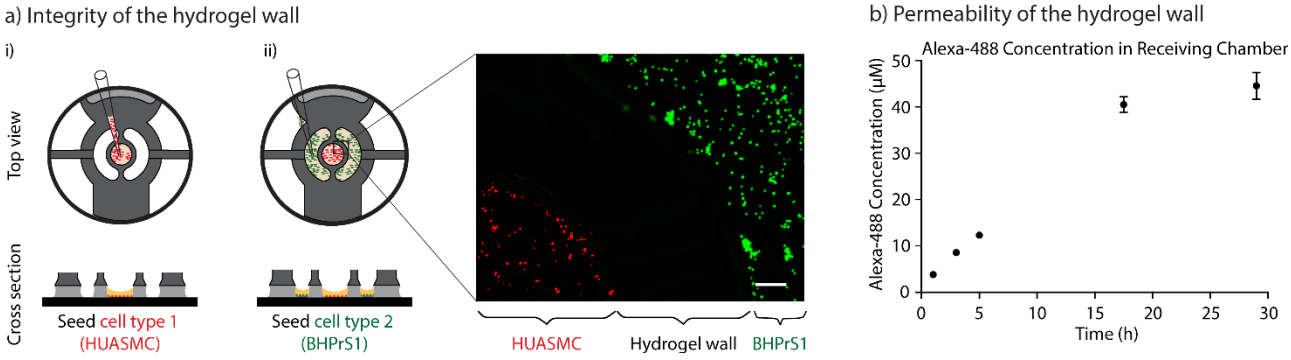

Figure 3.4: Integrity and permeability of patterned hydrogel walls. A) Integrity of the hydrogel walls is demonstrated by the segregation and containment of cells on either side of the patterned hydrogel wall: i) HUASMC cells stained with CellTracker Red were selectively seeded into the inner culture chamber of the device; ii) BHPrS cells stained with CellTracker Green were selectively seeded into the outer culture chambers of the device. After cell adhesion (overnight incubation), the cells were imaged at the border of the two culture chambers demonstrating the integrity of the hydrogel wall (image is representative of n = 3 devices). Scale bar = 200 μm. B) Permeability of the hydrogel wall was demonstrated *via* diffusion through the wall. AlexaFluor-488 solution was loaded into the sourcing chamber, and PBS was loaded into a receiving chamber at time = 0 h. The solution in the receiving chambers was collected at t = 1 h, 3 h, 5 h, 17.5 h, and 29 h, and the fluorescence intensity of each sample was measured. Data are expressed as mean ± standard error of the mean (n = 3 devices).

The versatility of our Monorail Device extends into applications involving specialized cultureware and sensitive cell types; as a tunable insert, our platform can be incorporated into any "off the shelf" well plate, including those with pretreated and coated surfaces. As a proof of concept, we demonstrate the compatibility of our patterning platform with the human prostate cancer cell line, LNCaP, that is sensitive to culture surface chemistry and that grows better on plates with surface chemistry tuned for improved adherence.[45] Prior work has shown that LNCaP cells exhibit better adherence and spreading on Corning's commercially available PureCoat™ Carboxyl PS (C-PS) than traditional TCT PS.[46] First, we tested and observed successful rail-based hydrogel patterning with our platform on Corning's specialized C-PS well plates. After validation of the compatibility of our platform with the C-PS well plates, we thawed LNCaP cells and directly seeded the cells on TCT PS and C-PS in the absence or presence of hydrogel walls patterned by our platform. As expected based on prior studies,[46] we observed morphological differences between LNCaP cells cultured on TCT and C-PS, with LNCaP cells cultured on C-PS displaying more spread out, adherent morphology than the LNCaP cells cultured on TCT PS, which showed predominantly rounded morphologies (Figure 3.5). The effect was independent of the presence of our platform. In these experiments, we used PS rails fabricated using CNC milling rather than the 3D printed rails used in prior figures because we observed that the 3D printer resin affected LNCaP morphology. We believe this is due to leaching of compounds from the 3D printer resin into the cell culture media; previous work has shown that some printer resins are detrimental to certain cell types.[47] A key advantage of our open microfluidic design is that it is injection moldable (Figure B6); in the future, inserts can be

injection molded in established cell culture materials (*e.g.*, PS). In summary, these results support the use of our device as a compatible culture platform for sensitive cell types and illustrate its use on custom commercially available culture surfaces beyond traditional TCT plastics.

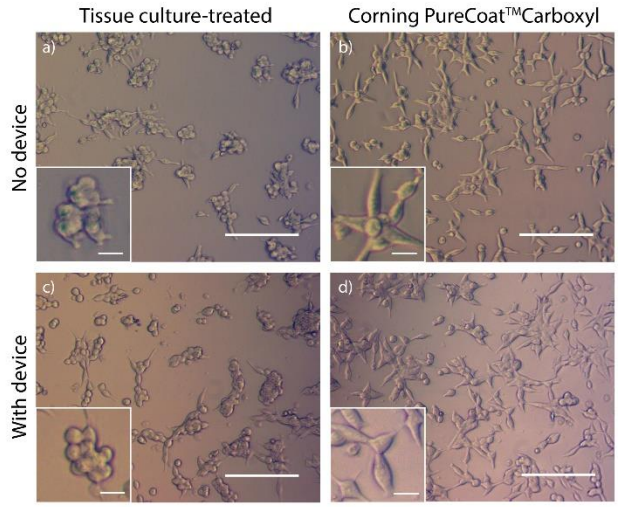

Figure 3.5: Rail-based hydrogel wall patterning technique is compatible with surface-modified commercial well plates designed for sensitive cell types. Consistent with prior studies,[46] LNCaP cells cultured on PureCoat™ Carboxyl well plates exhibited more spread out morphology compared to cells cultured on traditional TCT well plates; this effect was observed when LNCaP cells were cultured in well plates without ((a) and (b)) and with ((c) and (d)) hydrogel wall patterning. Rail devices used in this experiment were micromilled from PS. All images are representative of n = 3 replicates; images were taken between the middle of the culture chamber and the well wall ((c) and (d)) or at a corresponding location off center in the well plate ((a) and (b)). Scale bars = 200 μm, inset scale bars = 20 μm.

To further demonstrate the versatility of our Monorail Device in cell culture applications, we created a modular system that can be used to study multikingdom soluble factor signaling (*e.g.*, signaling between bacteria, fungi, and human cells). Coculture of cell types from different kingdoms can be used to decipher complex physiological microenvironments (*e.g.*, human microbiome) and to better understand transkingdom relationships.[48-52] Key challenges of establishing multikingdom cocultures include differential media and culture conditions for each cell type, and the tendency of microbial cultures to overgrow human cultures. These challenges, along with the complexity of existing engineered multikingdom coculture platforms, have made it difficult for multikingdom coculture to expand into most microbiology and cell biology laboratories, with much of the current work accomplished within

specialized engineered platforms,[53] further illustrating the need for simple and easily-adapted systems that researchers can use to approach these complex environments. Therefore, building upon previously demonstrated reconfigurable systems[27,54,55] and Transwell technology, we present a modular multikingdom coculture platform in which removable coculture "pegs" can be inserted into an existing hydrogel-wall patterned region (Figure 3.6a). Modularity of the individual culture compartments (*i.e.*, peg and hydrogel-patterned well plate) allows users to separately culture each kingdom in its optimized conditions before combining the compartments to initiate soluble factor signaling. Additionally, the ability to load and remove multiple pegs simultaneously allows users to build combinatorial coculture systems (Figure 3.6b). To demonstrate the physical device workflow, we combined a model yeast organism (*S. cerevisiae*) with model adherent and non-adherent human cells (BHPrS1 and Jurkat E6.1 cells, respectively). We cultured the *S. cerevisiae* atop agar-filled pegs while the BHPrS1 and Jurkat E6.1 cells were cultured in their own media in hydrogel-defined culture chambers. After overnight incubation, the three separate cultures were combined by insertion of the *S. cerevisiae*-containing peg into the hydrogel-patterned ring containing human cells (Figure 3.6c.). Further, we recapitulated a separate multikingdom coculture system of two human pathogenic microbes, *A. fumigatus* (fungus) and *P. aeruginosa* (bacterium), demonstrating an additional use of our rail-based hydrogel patterning platform and characterizing the ability of our platform to permit soluble factor signaling in a multikingdom coculture. Prior work has demonstrated that coculture of these two organisms in soluble factor contact results in reduced growth of *A. fumigatus* due to secretion of inhibitory factors by *P. aeruginosa.*[25,56-58] Therefore, we examined *A. fumigatus* growth in our modular Monorail Device while in coculture with *P. aeruginosa*. Briefly, *A. fumigatus* was seeded into the inner chamber of a hydrogel-patterned well plate, in which the outer chambers were filled with media, and *P. aeruginosa* was then seeded into LB-agarose-filled pegs and inserted into a peg-holder directly above the *A. fumigatus.* As expected, we observed growth of *A. fumigatus* over four days in monoculture and decreased *A. fumigatus* growth when *A. fumigatus* was cocultured with *P. aeruginosa* (Figure 3.6d). The inhibition of *A. fumigatus* growth by *P. aeruginosa* demonstrates cellular communication between two different kingdoms, supporting the use of

our modular Monorail Device as a platform to study soluble factor signaling in multikingdom cultures. In future work, to study signaling mechanisms between human cells and microbial pathogens, human cell types such as lung endothelial or epithelial cells could be incorporated into separate culture chambers within the modular Monorail Device. The modularity of our proof of concept platform, in addition to the customizability of our rail-based system, demonstrates the potential of our platform as a simple yet versatile tool for studying multikingdom communication.

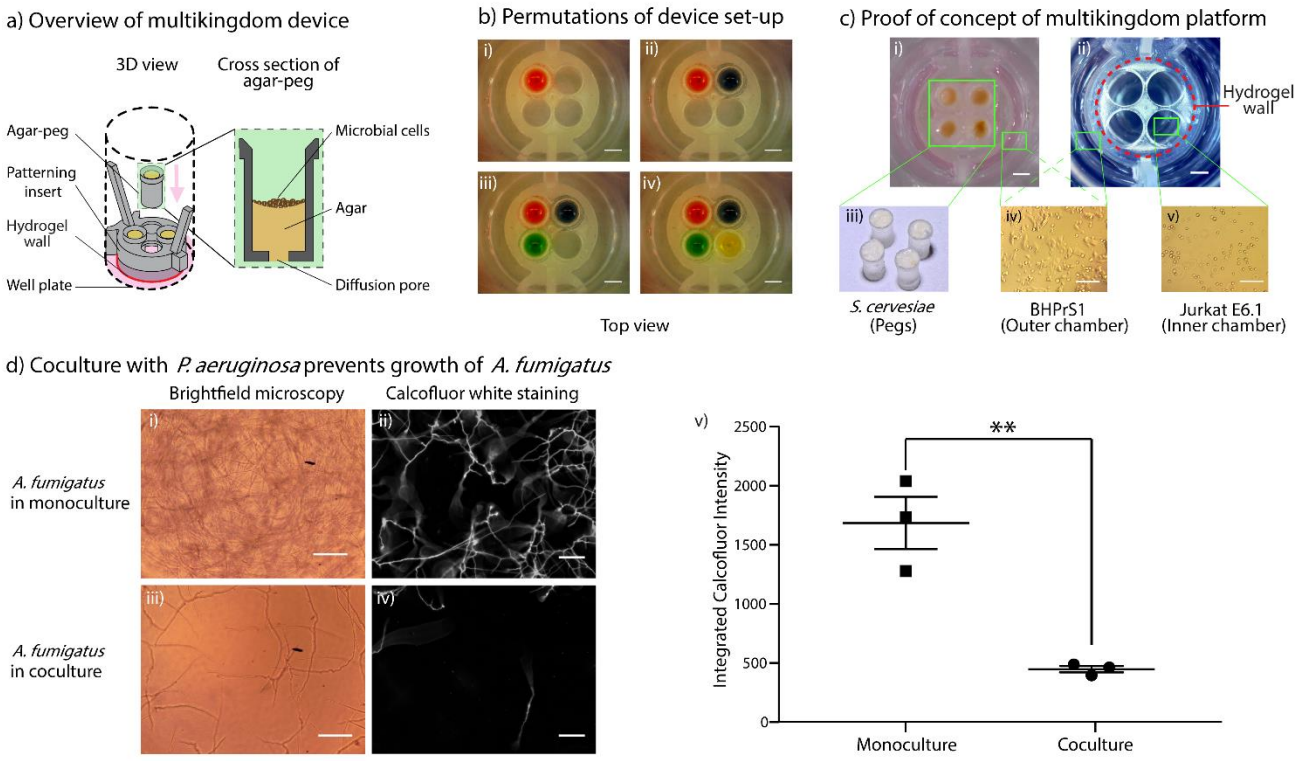

Figure 3.6: Multikingdom coculture in a modular rail-based hydrogel patterning platform. a) An insertable multikingdom coculture platform containing two hydrogel-patterned culture compartments on the well plate surface and four modular "pegs" for temporal or spatial manipulation of multiple cell types. b) Different cell types can be easily added or removed in different permutations to create combinatorial multikingdom cultures; i) Monorail Device with one peg, representing one cell type, while the other ports remain empty; ii-iv) a second, third, and fourth peg can be added as desired. Scale bar = 2 mm. c) A model yeast strain (*S. cerevisiae*) was cultured on agar-filled pegs (iii) and model human adherent and non-adherent cells (BHPrS1 and Jurkat E6.1, respectively) were cultured separately in a hydrogel-patterned 24 well plate ((iv) and (v)). Jurkat E6.1 cells were seeded into the inner culture chamber of the device, and BHPrS1 cells were seeded into the outer culture chamber. The pegs were then inserted into the device, placing the yeast proximal to the BHPrS1 and Jurkat E6.1 cells. Images are representative of n = 3 devices. The device used for this experiment contained 4 yeast-filled pegs. Scale bar = 2 mm ((i-ii)), 200 µm ((iii - v)). d) Coculture of *A. fumigatus* with *P. aeruginosa*

inhibits growth of *A. fumigatus*. Brightfield microscopy images of *A. fumigatus* in monoculture and coculture (with *P. aeruginosa*) on Day 1 ((i) and (iii)). Fluorescent images of Calcofluor white stained *A. fumigatus* in monoculture and coculture on Day 4 ((ii) and (iv)). Quantification of Calcofluor white fluorescent signal from *A. fumigatus* in mono- and coculture conveys decreased *A. fumigatus* growth in coculture (v). Images are representative of n = 3 devices, scale bars = 100 μm. Data is the average of two pegs images per device across three devices plus standard error of the mean (SEM) (error bars). ** indicates significantly different values according to a two-tailed unpaired Student's t-test ($p \leq 0.01$).

3.5 Conclusion

In this work, we present the creation of a new hydrogel-wall patterning platform, the Monorail Device, that utilizes SCF along a rail to pattern hydrogel walls on commercially available cultureware. The pipette-accessible cell culture chambers, compatibility with a range of cultureware materials, and the potential to reconfigure design geometries facilitate easy integration of our technology into biological laboratories and with established detection methods (*e.g.*, microscopy, ELISA, LC-MS). The ease of use of our device is on par with that of Transwells inserts, and the potential scalability of our technology to existing manufacturing techniques such as injection molding (Figure B6) can lower fabrication costs, as our technology relies on SCF instead of specialized fabrication methods to create a cell-segregating membrane. We envision use of this device as a tool to probe underlying mechanisms of cellular communication and multikingdom soluble factor signaling. The platform that we present can further be used for applications that require good control over the cellular micro-environment (*e.g.* cell migration) as well as applications that require a higher level of complexity, such as host-microbe interactions. The patterned regions can sustain 2D and 3D cell culture, in which cell-laden hydrogels could be loaded into the culture chambers or used to pattern walls. The use of customizable hydrogels can also enable the selective filtering of specific biomolecules in order to tailor the communication between the cells in culture.[32] We acknowledge the need for further optimization with regards to specific assay requirements, such as extended culture times, incorporating specific cell types depending on the application, and maintaining gel adherence and integrity (or degradability) over time as desired for a given application. Our optimization in the present paper centered on the physical hydrogel patterning capabilities of our platform to create open coculture chambers and we outline foundational technological features that will

allow personalized optimization and development of our platform. Ultimately, we aim to create a platform that can be easily translated across fields and adapted by researchers for their own research questions.

3.6 Materials and Methods

Devices

Devices were fabricated using a Form 2 SLA 3D printer (Formlabs, Somerville, MA) or a 770 Series 3 PCNC Mill (Tormach, Waunakee, WI). 3D-printed devices were designed with AutoCAD (Autodesk, San Rafael, CA) and converted to .form files with PreForm 2.11.0 (Formlabs) prior to being printed with Clear V2 (Figure 3.1, 3.2, 3.3a, 3.3b, and 3.6a-c), Black V2 (Figure 3.3c, and 3.4), or High Temp (Figure 3.6d) printer resin (Formlabs). After printing, devices were sonicated in isopropanol (IPA) for 15 min, rinsed with IPA, and UV-cured (Quans 20W UV Lamp) for 10-30 min. Milled devices (used in Figure 3.5) were designed with Solidworks 2016 x64 (Solidworks, Waltham, MA) and converted to .TAP files with Sprutcam (Sprutcam, Naberezhnye Chelny, Russia). Devices were milled from 4 mm thick polystyrene (PS) sheets (Goodfellow USA, Coraopolis, PA), rinsed with deionized water, and sonicated for 10 min in 70% ethanol. All devices and surfaces were plasma treated for 5 min at 0.25 mbar and 70 W in a Zepto LC PC Plasma Treater (Diener Electronic GmbH, Ebhausen, Germany) using ambient air.

Characterization of SCF

Devices of different height and width dimensions (Table B1), as well as those with integrated design features, were designed as shown in Figures 3.2 and 3.3 with n = 3 replicate devices. After fabrication, devices were inserted into the bottom of a 24 well plate, and an optimized volume of Matrigel (20-35 μL, exact volumes provided in Table B1) was loaded into the device *via* the loading region. All 24 well plates were purchased from the following: polystyrene well plates (Nest Scientific, #702011, Rahway, NJ), tissue-culture-treated (TCT) well plates (Corning Inc., #353047, Corning, NY), glass-bottomed well plates (MatTek Corp., #P24G -1.0-13-F, Ashland, MA), PureCoat™ Carboxyl well plates (Corning Inc., #354775, Corning, NY). For imaging purposes, Matrigel (8.0 - 9.1 mg/mL, Corning Inc.,

Corning, NY) was mixed 5:1 with red food dye (McCormick, Hunt Valley, MD) to give a final concentration of 6.5 - 6.7 mg/mL Matrigel. We observed no difference in performance between the Matrigel concentrations used. The process of loading, filling, and halting of flow was recorded and imaged using an AmScope MU1403B High Speed Microscope Camera on a SM-3TZ-80S Stereoscope (AmScope, Irvine, CA) set up beneath the well plate for bottom-up imaging. Device width and height dimensions were measured using image measurement tools (ImageJ), and a C112JE Digitmatic Indicator (Mitutoyo, Aurora, IL), respectively. For contact angle measurements, Matrigel was placed on glass (#12-542B, Fisher Scientific, Pittsburgh, PA), PS, plasma-treated PS, or TCT PS and the resulting contact angle was measured using a Kruss DSA25 (Kruss GmbH, Hamburg, Germany). The contact angles were measured and analyzed through ADVANCE Software using an elliptical droplet shape with an automatic baseline and set volume of 2 μL (Kruss GmbH, Hamburg, Germany). All PS contact angle measurements were done on PS Nunc™ OmniTrays™ (Thermofisher, Frederick, MD) since contact angle measurements required imaging from the side, which was not feasible with PS well plates. Flow experiments on glass were conducted on fabricated well plates in which the PS bottom was replaced with glass microscope slides (#16004-422, VWR International LLC, Radnor, PA). Where indicated in Figure 3.2, surfaces were plasma treated according to the same protocol as described in the previous section.

Confocal imaging of patterned hydrogel wall

Fluorescent Matrigel was prepared by mixing 1 μL of 1 μg/mL AlexaFluor-488 solution (Thermo Fisher, Cat# A33077) with 400 μL of 8.0 mg/mL Matrigel. Devices with and without a trapezoidal rail pinning feature were fabricated *via* the 3D printing protocol described above. The devices were inserted into the bottom of glass-bottomed well plates and loaded with 35 μL of the AlexaFluor-488-dyed Matrigel. After conclusion of flow, the Matrigel wall in devices with and without a trapezoidal rail pinning feature was imaged with a Leica TCS SP5 II Laser Scanning Confocal Microscope. All z-stack images were obtained at an emission wavelength range of 505 nm to 550 nm with an Argon 488 nm laser and a section thickness of 6.229 μm. All the .tif files were processed with Fiji (Version 10, ImageJ) using the following operations: “Transform > Stack-Orthogonal Views”.

Cell culture

Benign human prostate stromal cells (BHPrS1)[40] were cultured in RPMI-1640 medium (containing 2 mM L-glutamine) with 5% fetal bovine serum (FBS, Hyclone™), penicillin (100 units/mL), and streptomycin (100 μg/mL). Human umbilical artery smooth muscle cells (HUASMC) (Cell Applications, Cell Applications Inc., San Diego, CA) were cultured in Human Smooth Muscle Cell Growth Medium (#311-500, Cell Applications) and passaged using Subculture Reagent Kit (#090K, Cell Applications). Human prostate adenocarcinoma cells (LNCaP clone FGC, ATCC, Manassas, VA)[41] were cultured in RPMI-1640 medium with 10% FBS, penicillin (100 units/mL), and streptomycin (100 μg/mL). Human T lymphocyte cells (Jurkat E6.1) (Sigma-Aldrich, St. Louis, MO) were cultured in RPMI-1640 medium with 10% FBS. All mammalian cells were maintained in a 37°C incubator with 5% carbon dioxide. *S. cervesiae* (gift from Dr. Jesse Zalatan and Dr. Alshakim Nelson, University of Washington) were grown on YPD Agar (Sigma-Aldrich) stored at 4°C. *A. fumigatus* (AF293) and *P. aeruginosa* (PA14) (gifts from Dr. Nancy Keller, University of Wisconsin) were grown on glucose minimal media (GMM)[42] with low-gelling temperature agarose (Sigma-Aldrich) and Luria broth (LB) (BD Biosciences, Franklin Lakes, NJ) with low-gelling temperature agarose, respectively, and stored at 4°C. Cells were used at the following passage number: BHPrS1 P8-9, HUASMC P14, LNCaP P59, Jurkat E6.1 P12.

For the initiation and maintenance of cultures in our devices, specialized protocols were developed as described in each section below. To prevent evaporation of media in all of our device cultures, the spaces between wells were filled with 1:1 deionized water/phosphate buffered saline (PBS), and the well plates were stored within a humidified bioassay dish (#240835, Thermo Fisher) with saturated (1:1 water/PBS) Kimwipes. All optimized hydrogel loading volumes are in Table B1 in Appendix B.

Determination of the permeability of the hydrogel wall

The devices (Figure 3.4b) were inserted into the bottom of a TCT PS 24 well plate. Each device was loaded with 85 μL of 9.1 mg/mL Matrigel, and the plate was incubated for at least 3 min at 37°C after conclusion of flow. Fluorescent dye solution was prepared by mixing AlexaFluor-488 with PBS (final concentration of 237.2 μM). 120 μL of the dye solution was loaded into the sourcing chamber, 120 μL of

PBS was loaded into the receiving chamber (t = 0 h), and the plate was incubated at 37°C. 100 µL of solution in the receiving chamber was collected separately at t = 1 h, 3 h, 5 h, 17.5 h, and 29 h. Samples were diluted by a factor of 50 (t = 1 h, 3 h, 5 h) or 100 (t = 17.5 h, 29 h) with PBS prior to analysis. The fluorescence of each sample was measured using a Multiskan Spectrum UV/Visible Microplate Reader (Thermo Labsystems, Waltham, MA) (n=3 devices per time point).

Validation of the hydrogel wall integrity for compartmentalized cell culture

The coculture device (Figure 3.4a) was inserted into the bottom of a TCT PS 24 well plate, loaded with 35 µL of 8.0 mg/mL Matrigel, and incubated for at least 3 min at 37°C after conclusion of flow. BHPrS1 cells and HUASMC were stained with green and red CellTracker Dye at a concentration of 4.55 µg/mL and 6.25 µg/mL for 45 min (ThermoFischer), respectively, and selectively seeded into the outer and inner chambers of the device, respectively. Cells were suspended in culture media at a concentration of $2.3x10^5$ cells/mL. 14 µL (outer chamber) or 7 µL (inner chamber) of the cell suspension were seeded into each culture chamber to achieve a seeding density of 400 cells/mm^2. After overnight adhesion, fluorescent images of the cells along the wall were obtained using a Zeiss Axiovert 200 with a 4x objective and Axiocam 503 mono camera (Carl Zeiss AG, Oberkochen, Germany) (n=3 devices). All the images were processed with Fiji using the following operations: "Subtract Background > Adjust-Brightness/Contrast > Color-Merge Channels > Adjusted-Color Balance".

Comparison of LNCaP morphology on different well plate surfaces

The device (Figure 3.5) was placed into the bottom of a TCT PS or a Corning PureCoat™ Carboxyl PS (C-PS) 24 well plate. 40 µL of 9.1 mg/mL Matrigel was loaded into the device and incubated for at least 3 min at 37°C after conclusion of flow. LNCaP cells were thawed from liquid nitrogen storage and seeded directly onto a pre-wetted TCT PS 24 well plate or a C-PS 24 well plate in the presence or absence of the device. Cells were suspended in culture media at a concentration of $2.4x10^5$ cells/mL. In the absence of the device, 320 µL of the cell suspension were seeded into a well containing 200 µL of media to achieve a seeding density of 400 cells/mm^2 and a final volume of 520 µL. In the presence of the device, 120 µL of cell suspension were seeded into a well containing 75 µL of media to achieve a seeding density

of 400 cells/mm^2 and a final volume of 195 μL. The cells were incubated overnight at 37°C and 5% CO_2, and then imaged with phase contrast using a Zeiss Primovert Microscope ((Carl Zeiss AG, Oberkochen, Germany) and an AmScope MU1403B High Speed Microscope Camera (AmScope, Irvine, CA) (n=3 devices).

Validation of the modular rail-based hydrogel patterning platform

The device (Figure 3.6) was inserted into the bottom of a TCT PS 24 well plate, loaded with 50 μL of 8.0 mg/mL Matrigel, and incubated for at least 3 min at 37°C after conclusion of flow. For Figure 3.6c, BHPrS1 cells were suspended in culture media at a concentration of 2.3x10^5 cells/mL, and 240 μL of the cell suspension were seeded into each outer culture chamber to achieve a seeding density of 400 cells/mm^2. Jurkat E6.1 cells were suspended in culture media at a concentration of 4.0x10^5 cells/mL and 100 μL of the suspension was seeded into the inner culture chamber. The insertable pegs were loaded with 2% BD Bacto™ Agar solution (Fisher Scientific) and allowed to gel at room temperature. A *S. cervesiae* colony was scraped (≈ 1 mm) with a sterile toothpick from Petri dish culture and streaked onto the center of an agar-filled peg. After overnight incubation at 30 °C, the yeast-containing peg was loaded into the top of the hydrogel-patterning device, which contained BHPrS1 and Jurkat E6.1 cells. The assembled platform, containing all three cell types, was imaged. The human cells were imaged with phase contrast using a Zeiss Primovert Microscope with a 20x objective and an AmScope MU1403B High Speed Microscope Camera (n=3 devices). The yeast was imaged with an Ultra-High-Resolution SLR camera (Nikon-D5300).

For Figure 3.6d, 100 μL of *A. fumigatus* in liquid GMM were seeded into the bottom of the central chamber of the modular Monorail Device at a concentration of 1x10^5 spores/mL and 250 μL media added to the outer chambers. 3 μL of *P. aeruginosa* were seeded onto LB-agarose (5 μL) in a peg at a concentration of 1x10^8 bacteria/mL and the peg was inserted on top of the *A. fumigatus* culture and maintained at 37°C. Phase contrast images were taken after 24 hours using a Zeiss Primovert Microscope with a 10x objective and an AmScope MU1403B High Speed Microscope Camera (AmScope, Irvine, CA) (n=3 devices). Fluorescence images of *A. fumigatus* stained with Calcofluor white (1 mg/mL, 10 μL

+ 10 μL 10% KOH, Sigma-Aldrich) were taken after 4 days in coculture; for staining, a peg was removed, the Calcofluor white solution was added directly to the media in the *A. fumigatus* culture in the bottom of the well plate, incubated for 1 minute, and then imaged with a Zeiss Axiovert 200 with a 10x objective and Axiocam 503 mono camera. All fluorescence images were obtained in a single focal plane; as the *A. fumigatus* was not confined to a single plane by Day 4, the focal plane with the highest intensity of Calcofluor white staining was captured in each well. Two fluorescence images were captured for each well at different fields of view; when quantifying the Calcofluor white signal (Figure 3.6d, v), the integrated intensity of both replicate images was averaged. The plotted points represent the average of two images (collected for each of the three replicate wells), and the plotted standard error of the mean (SEM) is the SEM of the three replicate wells. Fluorescence images were quantified with Fiji following the protocol: "Subtract Background > Adjust Brightness/Contrast > Analyze > Measure > IntDen". Prism (GraphPad Software) was used to conduct a two-tailed unpaired Student's t-test (Figure 3.6d, v).

3.7 References

1. L. Goers, P. Freemont, K.M. Polizzi, "Co-culture systems and technologies: taking synthetic biology to the next level." *J. R. Soc. Interface,* 2014, **11**, 0065.
2. D.R. Bogdanowicz and H.H. Lu. "Studying cell-cell communication in co-culture." *Biotechnol. J*. 2013, April, 8(**4**), 395-396.
3. V.V. Abhyankar, D.J. Beebe, "Spatiotemporal micropatterning of cells on arbitrary substrates". *Anal. Chem*., 2007, **79**, 4066-4073.
4. S.N. Bhatia, U.J. Balis, M.L. Yarmush, M. Toner, "Microfabrication of hepatocyte/fibroblast co-cultures: Role of homotypic cell interactions." *Biotechnol. Prog*., 1998, May-Jun, **14** (3), 378-387.
5. H.J. Kim, J.Q. Boedicker, J.W. Choi, R.F. Ismagilov, "Defined spatial structure stabilizes a synthetic multispecies bacterial community." *PNAS*, 2008, Nov., **105**, 18188-18193.
6. Y. Miki, K. Ono, S. Hata, T. Suzuki, H. Kumamoto, H. Sasano, "The advantages of co-culture over mono cell culture in simulating *in vivo* environment". *Journal of Steroid Biochemistry and Molecular Biology*, 2012, **131**, 68-75.
7. K. Hatherell, P.O. Couraud, I.A. Romero, B. Weksler, G.J. Pilkington, "Development of a three-dimensional, all-human *in vitro* model of the blood-brain barrier using mono-, co-, and tri-cultivation Transwell models". *Journal of Neuroscience Methods*, 2011, **199**, 223-229.
8. D.A. Lauffenburger, S.H. Zigmond. "Chemotactic factor concentration gradients in chemotaxis assay systems", *Journal of Immunological Methods,* **40**, (1981), 45-60.
9. T.M. Keenan, A. Folch. "Biomolecular gradients in cell culture systems", *Lab Chip*, 2008, **8**, 34-57.
10. A.D. Gracz, I.A. Williamson, K.C. Roche, M.J. Johnston, F. Wang, Y. Wang, P.J. Attayek, J. Balowski, X.F. Liu, R.J. Laurenza, L.T. Gaynor, C.E. Sims, J.A. Galanko, L. Li, N.L. Allbritton, S.T. Magness, "A high-throughput platform for stem cell niche co-cultures and downstream gene expression analysis", *Nature Cell Biology*, 2015, **17**, 340-349.
11. L.M. Borland, S. Kottegoda, K.S. Phillips, N.L. Allbritton, "Chemical analysis of single cells", *Annu. Rev. Anal. Chem.*, 2008, **1**, 191-227.
12. S.N. Bhatia, D.E. Ingber. *Nature Biotechnology,* 2014, **32**, 760–772.

13. S. March, V. Ramanan, K. Trehan, S. Ng, A. Galstain, N. Gural. et al, "Micropatterned coculture of primary human hepatocytes and supportive cells for the study of hepatotropic pathogens". *Nature Protocols*, 2015, **10**, 2027-2053.
14. S. Takayama, J.C. McDonald, E. Ostuni, M.N. Liang, P.J. Kenis, R.F. Ismagilov, G.M. Whitesides, "Patterning Cells and Their Environments Using Multiple Laminar Fluid Flows in Capillary Networks." *PNAS*, 1999, May, **96**, 5545-5548
15. T. Kojima, C. Moraes, S.P. Cavnar, G.D. Luker, S. Takayama, "Surface templated hydrogel patterns prompt matrix-dependent migration of breast cancer cells towards chemokine-secreting cells." *Acta Biomaterialia*, 2015, **13**, 68-77.
16. A.P. Wong, R. Perez-Castillejos, J.C. Love, G.M. Whitesides, "Partitioning microfluidic channels with hydrogel to construct tunable 3-D cellular microenvironments." *Biomaterials*, 2008, **29**, 1853-1861.
17. C.Y. Li, K.R. Stevens, R.E. Schwartz, B.S. Alejandro, J.H. Huang, S.N. Bhatia, "Micropatterned cell-cell interactions enable functional encapsulation of primary hepatocytes in hydrogel microtissues". *Tissue Eng. Part A*, 2014, Aug, **20** (15-16), 2200-2212.
18. E.W.K. Young, C. Pak, B.S. Kahl, D.T. Yang, N.S. Callander, S. Miyamoto, D.J. Beebe, "Microscale functional cytomics for studying hematologic cancers" *Blood*, 2012, **119**, e76-e85.
19. Y. Torisawa, B. Mosadegh, G.D. Luker, M. Morell, K.S. O'Shea, S. Takayama "Microfluidics hydrodynamic cellular patterning for systematic formation of co-culture spheroids." *Integr. Bio.*, 2009, **1**, 649-654.
20. P. Gheibi, K.J. Son, G. Stybayeva, A. Revzin. "Harnessing endogenous signals from hepatocytes using a low-volume multi-well plate", *Integr. Biol.*, 2017, 9, 427.
21. C.J. Flaim, S. Chien, S.N. Bhatia, "An extracellular matrix microarray for probing cellular differentiation." *Nature Methods*, 2005, Feb., **2**, 119-125. Feb. 2005.
22. C.P. Huang, J. Li, H. Seon, A.P. Lee, L.A. Flanagan, H.Y. Kim, A.J. Putnam, N.L. Jeon, "Engineering microscale cellular niches for three-dimensional multicellular co-cultures". *Lab Chip*, 2009, **9**, 1740-1748.
23. Y.S. Torisawa, B Mosadegh, S.P. Cavnar, M. Ho, S. Takayama, "Transwells with microstamped membranes produce micropatterned two-dimensional and three-dimensional cocultures." *Tissue Eng Part C Methods*, 2011, Jan, 17 (**1**), 61-67.
24. M. Domenech, H. Yu, J. Warick, N.M. Badders, I. Meyvantsson, C.M. Alexander, D.J. Beebe, "Cellular observations enabled by microculture: paracrine signaling and population demographics." *Integr. Biol.*, 2009, **1**, 267-274.
25. L.J. Barkal, A.B. Theberge, C.J. Guo, J. Spraker, L. Rappert, J. Berthier, *et al.*, "Microbial metabolomics in open microscale platforms." *Nature Com.* 2016, Feb, **7**, 10610.
26. C.M. Carney, J.L Muszynski, L.N. Strotman, S.R. Lewis, R.L. O'Connell, D.J. Beebe, A.B. Theberge, J.S. Jorgenson, "Cellular microenvironment dictates androgen production by murine fetal Leydig cells in primary culture", Biol Reprod, 2014, Oct., 91 (4), 85.
27. E.E. Hui, S.N. Bhatia, "Micromechanical control of cell-cell interactions". *PNAS*, 2007, April, **104**, 5722-5726.
28. S.H. Lee, A.J. Heinz, S. Shin, Y.G. Jung, S.E. Choi, W. Park, J.H. Roe, S. Kwon. "Capillary based patterning of cellular communities in laterally open channels", *Anal. Chem.*, 2010, **82**, 2900-2906.
29. S. Bersini, J.S. Jeon, G. Dubini, C. Arrigoni, S. Chung, J.L. Charest *et al.* "A microfluidic 3D *in vitro* model for specificity of breast cancer metastasis to bone", *Biomaterials*, **35**, (2014), 2454-2461.
30. Y. Gao, D. Majumdar, B. Jovanovic, C. Shaifer, P.C. Lin, A. Zijlstra *et al.* "A versatile valve-enabled microfluidic cell co-culture platform and demonstration of its applications to neurobiology and cancer biology", *Biomed Microdevices*, (2011), **13**:539-548.
31. K.J. Son, P. Gheibi, G. Stybayeva, A. Revzin. "Detecting cell-secreted growth factors in microfluidic devices using bead-based biosensors", *Microsystems and Nanoengineering* (2017), **3**, 17025.
32. D. Patel, Y. Gao, K. Son, C. Siltanen, R.M. Neve, K. Ferrara, A. Revzin. "Microfluidic co-cultures with hydrogel-based ligand trap to study paracrine signals giving rise to cancer drug resistance", *Lab Chip*, 2015, **15**, 4614.
33. K.J. Regehr, M. Domenech, J.T. Koepsel, K.C. Carver, S.J. Ellison-Zelski, W.L. Murphy, L.A. Schuler, E.T. Alarid, D.J. Beebe, "Biological implications of polydimethylsiloxane-based microfluidic cell culture", *Lab Chip*, 2009, Aug., 9 (**15**), 2132-2139.
34. J.N. Lee, C. Park, G.M. Whitesides, "Solvent compatibility of poly(dimethylsiloxane)-based microfluidic devices", *Anal. Chem*, 2003, 75 (**23**), pp 6544-6554.

35. E. Berthier, E.W. Young, D.J. Beebe, "Engineers are from PDMS-land, biologists are from polystyrenia." *Lab Chip*, 2012, 12(**7**), 1224-37.
36. B.P. Casavant, E. Berthier, A.B. Theberge, J. Berthier, S.I. Montanez-Sauri, L.L. Bischel, *et al.* "Suspended Microfluidics." *PNAS*, 2016, April, **110**, 10111-10116.
37. J. Berthier, K.A. Brakke, E. Berthier, "Open Microfluidics". Wiley; 2016
38. A.K. Au, W. Lee, A. Folch, "Mail-order microfluidics: evaluation of stereolithography for the producton of microfluidic devics." *Lab Chip*, 2014, **14**, 1294.
39. A.K. Au, W. Huynh, L.F. Horowitz, A. Folch; "3D-Printed Microfluidics". *Angew. Chem. Int. Ed.* 2016, **55**, 3862 – 3881.
40. O.E. Franco, M. Jiang, D. W. Strand, J. Peacock, S. Fernandez, R.S. Jackson II, *et al.* "Altered TGF-β Signaling in a Subpopulation of Human Stromal Cells Promotes Prostatic Carcinogenesis". *Cancer Res.*, 2011, Feb., 71 (**4**), 1272-1281.
41. D.R. Church, E. Lee, T.A. Thompson, H.S. Basu, M.O. Ripple, E.A. Ariazi, G. Wilding. "Induction of AP-1 Activity by Androgen Activation of the Androgen Receptor in LNCaP Human Prostate Carinoma Cells". *The Prostate*, 2005, **63**,155-168.
42. K. Shimizu, N.P. Keller. "Genetic involvement of a cAMP-dependent protein kinase in a G protein signaling pathway regulating morphological and chemical transitions in Aspergillus nidulans". Genetics, 2001, 157, 591–600.
43. M. Verhulsel, M. Vignes, S. Descroix, L. Malaquin, D.M. Vignjevic, J.L. Viovy. "A review of microfabrication and hydrogel engineering for micro-organs on chips", *Biomaterials*, **35**, (2014), 1816-1832.
44. P. Concus, R. Finn; "On the behavior of a capillary surface in a wedge". *PNAS*, 1969, June, 2 (**63**), 292-299.
45. M.S. Liberio, M.C. Sadowski, C. Soekmadji, R.A. Davis, C.C. Nelson; "Differential effects of tissue culture coating substrates on prostate cancer cell adherence, morphology, and behavior". *PLoS ONE*, 2014, 9(**11**): e112122.
46. Corning® PureCoat™ Cultureware, Corning Data Sheet CLS-DL-CC-046 REV1, 2013. Web. https://www.corning.com/media/worldwide/cls/documents/CLS-DL-CC-046_REV1.pdf. Accessed 8/12/17.
47. N. Bhattacharjee, A. Urrios, S. King, A. Folch. "The upcoming 3D-printing revolution in microfluidics", *Lab Chip*, 2016, **16**, 1720.
48. S. Saegusa, M. Totsuka, S. Kaminogawa, T. Hosoi; "*Saccharomyces cerevisiae* and *Candida albicans* stimulate cytokine secretion from human neutrophil-like HL-60 cells differentiated with retinoic acid or dimethylsulfoxide". *Biosci. Biotechnol. Biochem.*, 2009, 73, (**12**), 2600-2608.
49. R. Hatoum, S. Labrie, I. Fliss. "Antimicrobial and probiotic properties of yeasts: from fundamental to novel applications". *Front. Microbiol.*, 2012, **3**, 421.
50. G.B. Huffnagle, M.C. Noverr. "The emerging world of the fungal microbiome". *Trends Microbiol*, 2013, July, 7 (**21**), 334-341.
51. The Human Microbiome Project Consortium. "Structure, function, and diversity of the healthy human microbiome". *Nature*, 2012, June, **486**, 207-214.
52. L.J. Barkal, C.L. Procknow, Y.R. Alvarez-Garcia, M. Niu, J.A. Jimenez-Torres, R.A. Brockman-Schneider, *et al.* "Microbial volatile communication in human organotypic lung models", *Nat. Comm.*, Accepted.
53. L.J. Barkal, E. Berthier, A.B. Theberge, N.P. Keller, D.J. Beebe. "Multikingdom microscale models", *PLoS Pathog*, 2017, **13**, 8: e1006424.
54. K.H. Spencer, M.Y. Kim, C.C.W. Hughes, E.E. Hui, "A screen for short-range paracrine interactions", *Integr. Biol.*, 2014, **6**, 382.
55. N. Rao, G.N. Grover, L.G. Vincent, S.C. Evans, Y.S. Choi, K.H. Spencer, E.E. Hui, A.J. Engler, K.L. Christman, "A co-culture device with a tunable stiffness to understand combinatorial cell-cell and cell-matrix interactions", *Integr. Biol.*, 2013, **5**¸1344.
56. K. Smith, R. Rajendran, S. Kerr, D. Lappin, W.G. Mackay, C. Williams, G. Ramage. "*Aspergillus fumigatus* enhances elastase production in *Pseudomonas aeruginosa* co-cultures", *Medical Mycology*, 2015, **53**¸645-655.
57. E. Mowat, R. Rajendran, C. Williams, E. McCulloch, B. Jones, S. Lang, G. Ramage. "*Pseudomonas aeruginosa* and their small diffusible extracellular molecules inhibit *Aspergillus fumigatus* biofilm formation", *FEMS Microbiol Lett*, 2010, **313**, 96-102.
58. H. Zheng, J. Kim, M. Liew, J.K. Yan, O. Herrera, J.W. Bok, N.L. Kelleher, N.P. Keller, Y. Wang. "Redox metabolites signal polymicrobial biofilm development *via* the NapA oxidative stress cascade in *Aspergillus*", *Current Biology*, 2015, **25**, 29-37.

Chapter 4. Mechanisms and Models of Host-Pathogen Communication in Respiratory Microenvironments

Reproduced in part with permission from Berry, S.B.; Haack, A.; Theberge, A.B.; Brighenti, S.; Svensson, M.; "Host and pathogen communication in the respiratory tract: mechanisms and models of a complex signaling microenvironment". *Front. Med.* Submitted.

The content in this chapter is a discussion of cell signaling mechanisms in the lung microenvironment in the context of chronic lung infections, as well as an overview of *in vitro* model platforms that have been used to study this complex biological system. Additionally, this chapter serves as an introduction into Chapters 5 and 6, which focus more on cellular communication and the development of tools to enable study of cellular signaling phenomena.

Abstract:

Chronic lung diseases are a leading cause of morbidity and mortality across the globe, encompassing a diverse range of conditions from infections with pathogenic microorganisms (*e.g. Mycobacterium tuberculosis, Aspergillus fumigatus*) to underlying genetic disorders (*e.g.* cystic fibrosis (CF), chronic granulomatous disease (CGD)). The respiratory tract represents an active interface with the external environment having the primary function of resisting pathogen intrusion and maintaining homeostasis in response to the myriad of stimuli encountered within its microenvironment. To perform these vital functions and prevent lung disorders, a chemical and biological cross-talk occurs in the complex milieu of the lung that mediates and regulates the numerous cellular processes contributing to lung health. In this review, we will focus on the role of pathogen-host and host-host cross-talk in chronic lung infections, and discuss how different cell types and signaling pathways contribute to chronicity of infection(s) and prevent effective immune clearance of pathogens. In the lung microenvironment, pathogens have developed the capacity to evade mucosal immunity using different mechanisms or virulence factors, leading to colonization and infection of the host; such mechanisms include the release of soluble and volatile factors, as well as contact dependent (juxtracrine) interactions. We explore the diverse modes of communication between the host and

pathogen in the lung tissue milieu in the context of chronic lung infections, as well as tissue-level signaling mechanisms. Lastly, we review current methods and approaches used to model and study these host-pathogen interactions *in vitro*, and the role of these technological platforms in advancing our knowledge about chronic lung diseases.

4.1 Introduction

Disruption of pulmonary function and development of chronic lung disease (CLD) contributes to a substantial global burden of disease, as CLDs are ranked among the top causes of mortality and morbidity in the world, with over 400 million people estimated to be afflicted [1]. CLDs can result from numerous factors either in isolation or in combination, including exposure to environmental pollutants and toxins, infection by pathogenic microbes, and genetic predisposition, leading to various manifestations of lung disease. [1] While there are often multiple factors influencing the development of a CLD, infection by pathogenic microbes can drive the development of some of the most serious and lethal conditions ranging from acute lower respiratory tract infections (LRTI) to chronic pulmonary infections (CPI) (*e.g.*, cystic fibrosis (CF) exacerbations, tuberculosis (TB)). The severity and progression of lung infections are frequently determined by factors such as the pathogen-specific mechanism of infection, patient physiology (*e.g.*, immune and vaccination status, age, transplants, *etc.*), and microenvironment composition [2–6]; however, there is still uncertainty as to how these factors drive infections toward an acute or chronic state.

Chronic pulmonary infections can manifest in a myriad of forms, resulting from persistence of a microbial population after initial medical treatment, external exacerbations of underlying medical conditions or latent infections, or even from shifts in internal microenvironmental cues [6,7]. Despite these varying causes, CPIs are commonly characterized by pathogen persistence and immune evasion as the pathogen adapts to, or manipulates, its microenvironmental niche in the lung [6]. This initial survival is complemented by persistence through initial medical treatments, leading to repeated symptomatic episodes or long-term (months to years) illness. While there is no single causative factor that leads to

chronicity over an acute response, current research has focused on identifying components of the lung microenvironment that can contribute to the development of a CPI, such as the composition of the lung microbiome and host-pathogen interactions [2,8]. Indeed, a new view of how communication in the lung microenvironment drives infection and homeostasis reveals how previously overlooked or unknown interactions drive immunity, pathogen evasion, and host health. Our understanding of host-microbiome interactions in the lung, a region long thought to be sterile and devoid of commensal organisms, is only starting to develop and reveal potentially important ramifications for human health. This subject, while briefly covered in this review, is more deeply discussed elsewhere [2,9–11].

Host-host, host-pathogen, and pathogen-pathogen communication in the lung play a vital role in mediating homeostasis, coordinating immune response and tissue repair, and propagating infection. The ability to translate the chemical and biological communication in the lung microenvironment enables us to better comprehend the vital conversations that drive the disease state in chronic infections; however, translating these conversations from intrinsic signals to actionable disease mechanisms by the host is complex, as pathogens have evolved numerous mechanisms to evade host defense systems and confound host communication. Further, this communication, which includes the release of signaling factors (*e.g.*, soluble factor or volatile signaling) and physical interactions (*e.g.*, juxtacrine signaling), acts in a cumulative manner to simultaneously promote many different aspects of the infection ranging from epithelial adhesion and invasion by *Burkholderia pseudomallei* to secretion of *Aspergillus fumigatus* growth-promoting volatiles by *Pseudomonas aeruginosa* [12,13]. Understanding how the complex signaling pathways in the lung microenvironment are shifted and manipulated in response to specific stimuli can elucidate key insight into the pathogenic mechanisms of numerous pathogens, and provide information that can lead to novel diagnostics and treatments.

In this review, we focus on the microenvironment of lung infections and how chemical and biological signaling events unfold during chronic lung infections, including recurrent, persistent, and latent infections with *Mycobacterium tuberculosis, Aspergillus fumigatus, Pseudomonas aeruginosa, Streptococcus pneumoniae, Staphylococcus aureus, Cryptococcus neoformans,* and *Burkholderia*

pseudomallei. These host-pathogen interactions use similar modes of cellular signaling and communication in the lung that involves soluble factor paracrine signaling (*e.g.*, cytokines), juxtacrine signaling (*e.g.*, pattern recognition receptors (PRR)), and volatile signaling (*e.g.*, volatile organic compounds (VOC)). Additionally, we will discuss host and pathogen signaling within the tissue to create a more comprehensive view of the signaling network that contributes to disease progression. To support future studies of these systems, we describe recent innovative technologies and platforms that are used to probe these signaling events and model the lung environment *in vitro*. For information regarding the role of viruses and signaling in pulmonary viral infections, we refer readers to these detailed reviews [14–16].

4.2 Infections and molecular cross-talk

The lung microenvironment is a heterogenous interface consisting of innate immune cells (*e.g.*, alveolar macrophages, neutrophils, monocytes, dendritic cells, *etc.*), mucous-producing and ciliated epithelial cells, rare immune populations (*e.g.*, mucosal-associated invariant T cells (MAIT cells)[17,18], innate lymphoid cells (ILCs)[19–21]), commensal and pathogenic microbes, and underlying tissue and vascular networks that are all in constant reciprocal communication (Figure 4.1). This tissue organization, which supports multiple cell populations with vastly different environmental requirements, must parse through the signaling milieu of soluble, volatile, and physical cues to identify the biological and chemical stimuli needed for proper respiratory function and effective immune defense. However, upon pathogen challenge, the lung microenvironment faces new obstacles in converting these stimuli into a coherent immune response, as oftentimes pulmonary pathogens use multiple modes of communication (*e.g.*, physical, soluble) simultaneously to evade immunity and propagate infection; for example, *S. pneumoniae*-derived neuraminidase (NanA) cleaves mucins on the epithelial surface to enable pathogen attachment on host glycoconjugates, while subsequently secreting pore-forming toxin pneumolysin to disrupt the epithelium [3,22,23]. Inability of the host to respond to these pathogen challenges leads to an impaired microenvironment where slight deviations from signaling equilibria can promote a chronic condition [24,25], highlighting the importance of understanding the signaling landscape in CPIs.

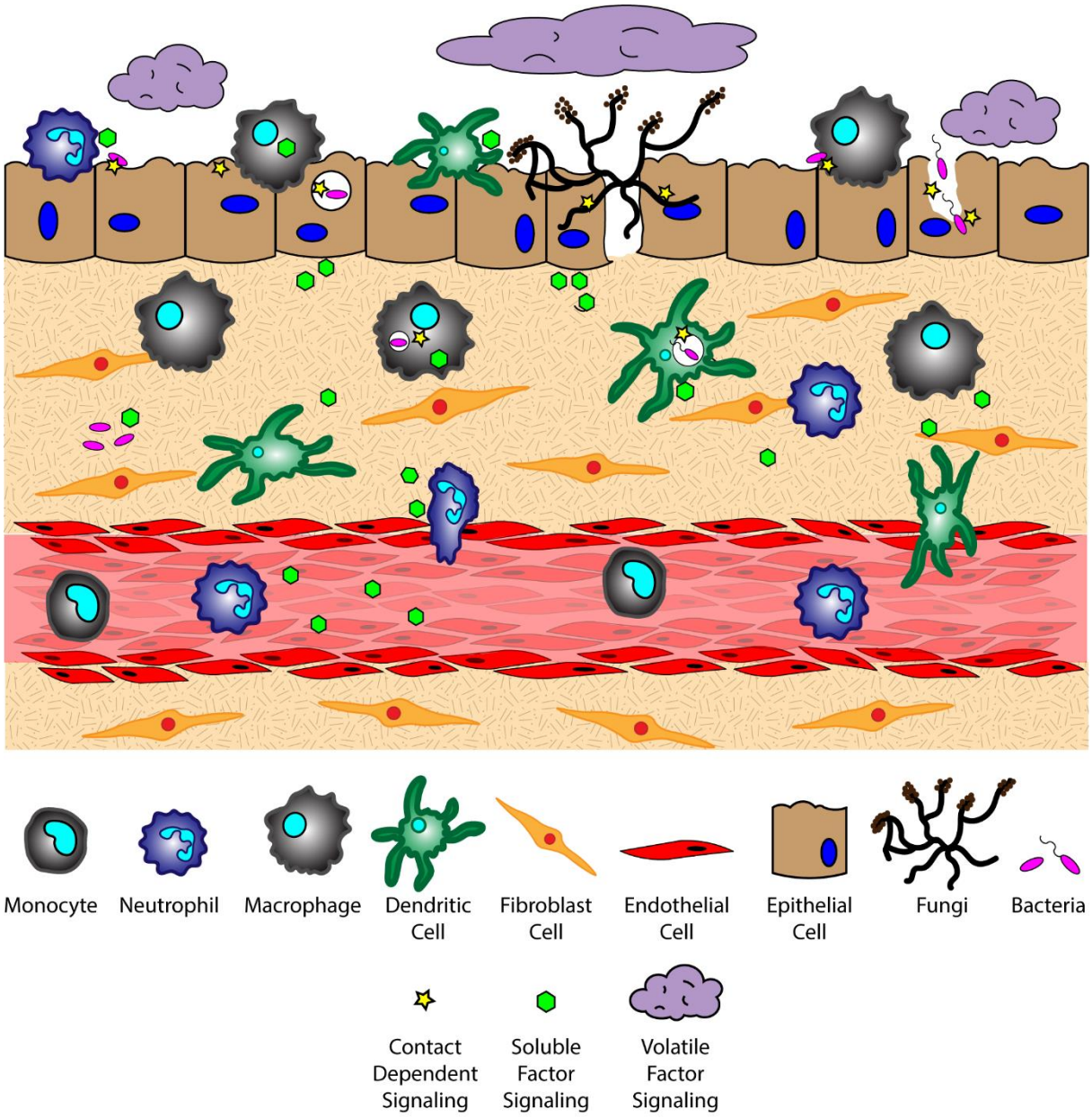

Figure 4.1: The lung microenvironment is home to a complex signaling network that interprets factors from various sources simultaneously. Signaling phenomena includes the exchange of soluble, volatile, and physical signals between cells of the host immune system, microbes, and host tissue components at varying spatiotemporal concentrations. Translating this complex quagmire of signals requires a broad perspective to see the role of each type of communication in the context of host-pathogen, pathogen-pathogen, and host-host signaling.

4.2.1 Soluble factor paracrine signaling

Virulence Factors - Toxins

Pathogenic microbes employ a wide range of soluble virulence factor signaling mechanisms to combat the host immune response and persist *in vivo*, the most notable of which includes the use of host-targeting toxins. These toxins function in the early stages of infection to directly cause damage to the host microenvironment and create a favorable niche for the pathogen to survive. For example, *S. pneumoniae* makes use of a potent pore-forming toxin, pneumolysin (PLY), that binds to membrane-bound cholesterol and perforates the host cell, causing cell death through multiple mechanisms including destruction of DNA and cell cycle arrest [26]. Pneumolysin acts to induce the complement pathway, as well as to induce a proinflammatory cytokine response, which can lead to widespread tissue damage; this highly inflammatory environment, coupled with the cytolytic effect of pneumolysin, can degrade the barrier function of the host epithelium and lead to pathogen uptake through platelet-activating factor receptor (PAFr)-mediated endocytosis, which traffics the pathogen across the epithelium into the underlying tissue, allowing *S. pneumonia* dissemination [3,27–29]. Another prominent pathogen-derived toxin is the pore-forming compound α-hemolysin (α-toxin) utilized by *S. aureus* during the course of pulmonary infection. A-toxin acts *via* binding to its specific cell receptor, ADAM10, wherein it oligomerizes to form the cytolytic pore and induce host cell lysis [30]. The degradation of epithelial barrier integrity enables *S. aureus*, in a manner similar to *S. pneumoniae*, to invade into the underlying tissue, or to reside within the epithelial layer itself, where internalized bacteria can survive within a quasi-protective niche [31,32]. This intracellular residence permits the pathogen to enter into a dormant state protected from the host immune response and antibiotic therapy, contributing to its chronicity and enabling recurrent *S. aureus* infection [32].

The effect of *S. aureus*-derived α-toxin can be amplified during coinfection as well. Polymicrobial infections with fungal pathogen *C. albicans* activates the *agr* quorum sensing system in *S. aureus*, which leads to enhanced α-toxin secretion and decreased host survival, demonstrating how coinfection not only adds complexity to the lung microenvironment, but also promotes increased virulence [33]. Further, invasive

fungal species, such as *A. fumigatus* and *C. neoformans*, are armed with a variety of toxins that impede or interfere with intracellular functions required to mount an effective immune response. *A. fumigatus,* one of the most successful opportunistic fungal pathogens, has a wide array of immunosuppressive secondary metabolites and toxins at its disposal including trypacidin, endocrocin, and gliotoxin [34–38]. These toxins confer protection to *A. fumigatus* against numerous components of the host immune system. Trypacidin, found to localize to fungal conidia, induces high levels of nitric oxide (NO) and hydrogen peroxide (H_2O_2) production in bronchial epithelial cells, leading to severe oxidative stress and cell necrosis [34]. Similarly, endocrocin, another spore-derived fungal toxin, inhibits neutrophil migration and displays significant virulence in a *Drosophila* model of infection [35]. The most widely characterized *A. fumigatus* toxin, gliotoxin, has been found to inhibit multiple antimicrobial functions (*e.g.*, superoxide defense) in a wide range of leukocytes, in addition to inducing apoptosis and inhibiting NFκB signaling, providing *A. fumigatus* with a broad repertoire to defend itself against a range of host immune responses [39–42]; for a detailed review of gliotoxin's extensive immunomodulatory effects, refer to [43]. The culmination of the effects from this library of toxins enables *A. fumigatus* to survive continual immune assault and create an environment favorable for colonization and proliferation. Although mostly associated with the initiation of an acute infection, pathogen-derived toxins promote the establishment of a chronic infection by disturbing host immunity and initiating pathogen-protective functions.

Virulence Factors – Immune Modulators

In addition to toxins, there are other virulence factors used to evade host immune responses and confound the cross-talk required for effective pathogen clearance; these factors are a series of distinct compounds ranging from surface-expressed cell wall components to quorum sensing (QS) molecules used for intermicrobial communication. *In vivo*, these virulence factors play many roles, including inducing the innate immune response while also offering protection for the pathogen. During infection with *M. tuberculosis*, the pathogen utilizes alternative strategies to manipulate immune cells in the local tissue environment, such as expression of the type VII secretion system, ESX-1 [44]. This secretion system transports potent early secreted antigen target 6 kDa (ESAT-6) and culture filtrate protein (CFP-10) that

are essential for phagolysosomal escape into the cytosol and induction of host cell necrosis [44–47]. This will trigger a pro-inflammatory reaction and secretion of MMP9 by epithelial cells and *M. tuberculosis*-infected macrophages, leading to the recruitment of uninfected macrophages and other immune cells to contain the infection in a granuloma [48,49]. While a granuloma containing T cells is considered protective, early granuloma formation may be exploited by pathogenic mycobacteria to seed the infection into uninfected cells and thus disseminate the infection [50–52]. The extent of virulence, and the capability of the mycobacteria to evade the host immune response, has been directly linked to the presence and function of ESAT-6 and other RD1/ESX-1 derived virulence factors, as avirulent strains lack this secretion system [53–55]. The exact mechanism of action of ESAT-6 is still somewhat unclear, yet it has been recently found that the ESX-1 secretion system does not completely depend on ESAT-6 for membrane lysis and that its function is contact dependent, despite ESAT-6 being able to disrupt lysosome membranes at an acidic pH [45,56]. Another important virulence factor of *M. tuberculosis* is the cell wall component, mannosylated lipoarabinomannan (Man-Lam), that has a central role in inhibition of phagosomal maturation inside infected macrophages [57–59]. Secreted Man-Lam can bind to different receptors expressed by human macrophages including mannose receptor, complement receptors, and DC-SIGN, and can manipulate the induction of proinflammatory responses to reduce local activation of immune cell subsets in lung tissue.

Recently, QS molecules have been identified as another group of potential virulence factors capable of programming pathogen populations to evade immune responses, as well as to inhibit or manipulate the host immune response directly [60]. This is widely observed in the case of *P. aeruginosa*, where quorum sensing molecule N-3-oxo-dodecanoyl-L-homoeserine lactone (3O-C_{12}-HSL), which regulates the LasR QS circuit and numerous virulence factors, acts as a virulence factor itself that inhibits the production of proinflammatory cytokines (*e.g.*, TNF, IL-12) and the proliferation and differentiation of T cells [60,61]. Additionally, 3O-C_{12}-HSL does not only target human cells, in which 3O-C_{12}-HSL often interacts with the intracellular activation protein IQGAP1 [60], but also commensal organisms. In a mixed coculture with opportunistic fungal pathogen *C. albicans*, 3O-C_{12}-HSL was found to inhibit filamentation of the fungi, indicating that *P. aeruginosa* can use its QS molecules to influence the host as well as other microbes in

its surrounding microenvironment [62]. This dual functionality of QS molecules is observed with other *P. aeruginosa*-derived factors, such as *Pseudomonas* quinolone signal (PQS), which dysregulates host immunity through manipulation of cytokine production and reduction of antibacterial activity of host immune cells [63,64]. The ability of a pulmonary pathogen to utilize QS molecules for more than one function (*i.e.*, to self-regulate and evade immunity) supports their persistence against constant immune challenge while maintaining the ability to proliferate and survive. Other virulence factors take on a more traditional or singular role in establishing a pathway for infection. *C. neoformans*, a fungal species often associated with meningitis in immunocompromised patients, is capable of establishing a chronic lung infection in immunocompetent patients through the secretion of host-targeting enzymes (*e.g.*, phospholipases, proteases) that degrade host immune components (*e.g.*, phagocytic compartment membranes, lung surfactant)[65–69]. These secreted virulence factors drive the ability of *C. neoformans* to survive and protect itself from initial immune responses until it adapts to the host environment and takes on phenotypic forms to support its persistence in a dormant state [67,70,71]. The secretion or release of virulence factors across a wide range of pathogens mediates various anti-immune behaviors which ultimately enable the pathogen to persist in the microenvironment and develop into a CPI. Further, the presence of QS molecules adds to the complex milieu already present in the lung microenvironment, and demonstrates that understanding the signaling phenomena in this location requires a broad perspective encompassing not only host-pathogen communication, but also signaling amongst bacterial and/or fungal kingdoms as well.

Cytokines

Pathogen-derived soluble factors contribute partially to the cross-talk events in the lung microenvironment, as host-derived signals are also present, often in response to or to defend from pathogen-derived factors. Host-derived signals vary extensively in function and form, ranging from eicosanoids to interleukins. Specifically, cytokines are a principle form of secreted soluble factor used to trigger the immune system and induce diverse effector functions upon pathogen challenge. However, it is necessary that the secretion and local concentrations of these factors are carefully regulated, as impaired

cytokine signaling leads to pathogen survival, persistence, and the development of chronicity, while excess cytokine-mediated inflammation can promote pathological tissue destruction in the lung. *M. tuberculosis*-infected macrophages secrete multiple inflammatory cytokines, including TNF, IL-1β, and IL-6, which induce an early proinflammatory response that promotes immune cell activation and migration and results in generation of a granuloma. Activated T cells producing IFNγ initiate antimicrobial responses, such as the induction of NO, to promote mycobacterial clearance. However, disruption of IFNγ signaling due to a shortage of activated effector T cells or an increase in regulatory T cells can lead to pathogen persistence within infected macrophages and increased bacterial burden in the lung [72–75]. Indeed, the immune activating factors IFNγ and TNF are crucial for inducing intracellular antimicrobial functions such as autophagy and phagolysosomal fusion [76], making inhibition of these factors an attractive immune evasion target for pathogens.

Contrary to the role of IFNγ in *M. tuberculosis* infection, there is evidence suggesting that the immune activating effects of IFNγ can in fact lead to an increase in virulence by *P. aeruginosa*, wherein IFNγ binds to *P. aeruginosa* surface receptor OprF to induce downstream PA-I expression *via* its QS signaling network [77]. This unintended response to a host cytokine illustrates that cytokine signaling can have dual, context-dependent outcomes. In addition to intercepting host signaling molecules, pathogens can also manipulate the expression and secretion of host factors to alter the signaling environment in their favor. The *C. neoformans*-derived virulence factor glucuronoxylomannan (GXM) increases secretion of immunomodulatory factors IL-10 and IL-4 while downregulating pro-inflammatory compounds TNF and IFNγ in stimulated CD4+ T cells, driving a permissive immune response that supports increased yeast cell growth [78]. Overall, IL-4 and IFNγ play opposite roles in macrophage polarization and function, as varying ratios of IL-4 and IFNγ induce a range of macrophage phenotypes – ranging from classically activated to alternatively activated and intermediate – that simultaneously contribute to antimicrobial and acquiescent outcomes [79]. Similarly, macrophages infected with *M. tuberculosis* secrete increased levels of VEGF while granuloma-associated macrophages have an increased expression ANG-2; the increased levels of VEGF and ANG-2 correlate with increased vascularization and vessel permeability around the site of

infection, respectively, which is subsequently used for pathogen dissemination and host manipulation [80,81]. Chronic pulmonary pathogens can not only usurp the balance of pro- and anti-inflammatory cytokines found in the signaling microenvironment to alter the type of immune response, but also influence the surrounding tissue infrastructure to its own benefit [82].

Chemokines

The manipulation of host signaling by pulmonary pathogens also extends to chemokine signaling, which is a vital process for the recruitment of immune cells to the site of infection. Early in the course of pulmonary infections, neutrophils play a vital role in counteracting invading pathogens by inducing a proinflammatory response. Their pro-inflammatory role, which can also have negative host effects, is an attractive target for pathogen manipulation and evasion. *S. aureus* utilizes multiple mechanisms to impede the recruitment of neutrophils to the site of infection by using secreted staphopain (*i.e.*, cysteine proteases) that inactivates CXCR2 on neutrophils and blocks the attractant effects of infection-associated chemoattractants [83]; additionally, *S. aureus* utilizes exoprotein SSL5 to scavenge chemokines and bind to chemokine surface receptors, effectively blocking the ability of neutrophils to respond to receptor-bound chemokines [84]. Further, SSL5 is found to act on neutrophils through its capacity as a MMP-inhibitor, blocking potentiation of neutrophil chemokine IL-8 (CXCL8) and preventing neutrophil migration through collagen [85]. The modulation of neutrophil recruitment is not limited to *S. aureus*-derived soluble factors, as *S. pneumoniae*-derived virulence factor PepO is found to contrastingly increase secretion of chemoattractants CXCL8 and IP-10 (CXCL10) from bronchial cell line BEAS-2B, suggesting that this factor may increase recruitment of neutrophils to the site of infection [86]. T cell chemokine CXCL10 has also been associated with *Cryptococcus* infections; during murine infection with *C. gattii*, a close pathogenic relative to *C. neoformans*, an impaired T_H1 migration in the lung is correlated with decreased *Ip10* expression and poor DC maturation when compared to *C. neoformans* infection, leading to an attenuated effector T cell response and increased pulmonary infection [87]. Maintenance of intact cytokine and chemokine signaling during an active infection is integral to defeat invading pulmonary pathogens, as

disturbed cytokine signaling leads to improper immune cell function and delayed antimicrobial response resulting in increased bacterial expansion and persistence [74].

Antimicrobial Molecules

Beyond paracrine cytokine and chemokine signaling, which is often seen as occurring between host cells, the role of host-secreted factors directed towards pathogens is also an essential functionality in clearing pathogens and preventing chronicity. Host cells utilize an array of armaments to directly kill pathogens, such as reactive oxygen and nitrogen species (ROS, RNS respectively), cytotoxic molecules (*e.g.*, granzymes, lysozymes, perforins) or antimicrobial peptides (*e.g.*, human cathelicidin, LL-37, defensins, granulysin), and antimicrobial small molecules (*e.g.*, extracellular vesicles (EVs), miRNA). ROS play a vital role in the clearance of pathogenic microbes, but must also be tightly controlled to minimize the risk of host-tissue damage *via* extensive oxidation. High local concentrations of ROS or RNS can also suppress immune cell functions at the site of infection. The tight regulation of this defense is evident in the ability of neutrophils to induce different types of ROS signaling based on the size of the microbe it encounters, triggering intracellular ROS against ingested small yeast cells, while secreting extracellular ROS against the larger hyphal form of fungi [88]. In contrast, pathogens can activate this defense in their favor through toxin secretion, such as *P. aeruginosa*-derived pyocyanin, which triggers neutrophil apoptosis through inducing ROS and disrupting mitochondrial membrane potential [89]. However, ROS-mediated pathogen clearance is not limited to neutrophils, as plasmacytoid DCs are also found to utilize ROS to inhibit the growth of *C. neoformans in vitro*, although they remain less effective at fungal killing than conventional DCs [90].

In *B. pseudomallei* infection, bacteremic patients were found to have increased levels of pro-apoptotic compounds granzyme A and B [91]; further, stimulating patient-derived monocyte-derived DCs with *B. pseudomallei* antigens LolC and Hsp60 led to downstream activation of CD8+ T cells and increased granzyme B secretion [92]. The increased secretion of granzyme B likely plays a role in patient survival, as NK-cells from deceased patients are characterized by significantly lower levels of granzyme B expression [93]. Similarly, control of intracellular *M. tuberculosis* has been shown to involve CD8+

cytotoxic T cells using the pore-forming protein perforin to enable the entrance of granulysin into infected cells and the subsequent killing of mycobacterium through osmotic lysis [94]. Accordingly, a reduced expression of perforin and granulysin in *M. tuberculosis* infected tissues have been show to correlate with disease progression [95,96].

More recently, work has focused on identifying the antimicrobial effects of other components found in the extracellular communication milieu, such as extracellular vesicles (EVs). For example, in interactions between *A. fumigatus* and host immunity, both host and pathogen secrete bioactive EVs that target its respective counterpart and generate proinflammatory and antimicrobial responses [97,98]. Important components of these EVs, such as miRNA, are also involved in mediating intra- and intercellular immune mechanisms and responses [99,100], and are implicated as potential biomarkers of infections such as tuberculosis [101]. These mechanisms represent some of the most important methods of antimicrobial defense by host immune cells, yet pathogens are still capable of usurping this defensive signaling and surviving the acute immune response, enabling development of CPIs.

An additional mode of communication that is starting to come to light as an important factor in multiple infection models is the metabolic cross-talk that occurs between pathogens, commensal organisms, and the hosts. Indeed, many pulmonary pathogens such as *A. fumigatus* and *P. aeruginosa* are known to secrete siderophores that chelate iron from the host for their own use [60,102,103]. Additionally, nitrogen and sulfur availability is thought to significantly contribute to pathogen survival, where availability of nutrients such as tryptophan and asparagine can modulate pathogen behavior and metabolism, as well as influence host immunity. We refer readers to these excellent recent reviews on the role of metabolic cross-talk in infections [104,105].

4.2.2 Physical contact juxtacrine signaling

Contact dependent signaling, or juxtacrine signaling, complements soluble factor signaling and is a crucial component of the intercellular signaling microenvironment, as one of the first modes of communication used to detect pathogens in the lung. Innate immune cells, such as macrophages and

dendritic cells, rely on the expression of germline-encoded receptors (*e.g.*, pathogen recognition receptor (PRR)) to sample and detect pathogen-specific molecules (*e.g.*, pathogen associated molecular patterns (PAMPs)). Surface bound receptors toll-like receptor (TLR) and c-type lectin receptor (CLR) detect conserved pathogenic molecules such as lipopolysaccharide (LPS) on the surface of gram-negative bacteria *P. aeruginosa* and *B. pseudomallei*, and β-glucans on fungi such as *A. fumigatus*, respectively [106–108].

Pathogen Recognition Receptors and Associated Molecular Patterns

The TLR-signaling axis is present in a wide range of infections, including TB, where innate immune cells expressing TLR2 are able to detect multiple *M. tuberculosis* surface components [109], such as LpqH [110], LprG [111], and LprA [112], which impede intracellular signaling pathways and interfere with MHC II antigen processing and presentation. TLR4 detection of intracellular *M. tuberculosis* modulates intracellular signaling pathways governing the immune response in an antigen-dependent manner. Detection of cell wall components PIM and Man-LAM result in robust anti-inflammatory responses characterized by decreased secretion of TNF and IL-12p40 and increased secretion of IL-37, respectively [113,114], while HSP70-cofactor GrpE activates DCs and leads to their subsequent preferential induction of proinflammatory Th1 cells *via* TLR4 recognition [115]. In conjunction with TLR pathogen sampling, CLR detection mechanisms also complement the innate immune system's ability to detect a wide range of pathogens. CLRs, such as Dectin-1 and DC-SIGN, are crucial to the detection of fungal cell surface markers. Both Dectin-1 and DC-SIGN have been implicated in the recognition, binding, and phagocytosis of *A. fumigatus* [116,117], as single nucleotide polymorphisms in genes coding for Dectin-1 and DC-SIGN were associated with a greater risk of invasive pulmonary aspergillosis [118]. Further, the absence of dectin-1 ligand β-1,3-glucan on the surface of *A. fumigatus* leads to a more efficient complement-mediated antifungal immune response driven by DCs; this is found to be due to improved complement binding in the absence of β-1,3-glucan, and that galactomannan binding *via* DC-SIGN drives a proinflammatory cytokine response [119]. However, *A. fumigatus* leverages other cell wall components to drive virulence, such as DHN melanin, which is able to block LC3-associated phagocytosis and subsequent fungal killing

through impediment of NADPH oxidase from entering the phagosome [120]. Host immunity is able to combat the virulence factor DHN melanin through binding *via* the melanin-sensing C-type lectin receptor (MelLec) found on endothelial cells and myeloid cells, the mutation of which is found to increase susceptibility of stem-cell transplant patients to aspergillosis and to decrease proinflammatory cytokine secretion in macrophages [121]. The interactions between these PRRs and PAMPs strongly activate immune cells and initiate intra- and intercellular signaling to recruit other immune cells and clear the pathogen; however, this interaction is also vulnerable to manipulation by pathogens through suppression of PRRs or masking of PAMPs to avoid detection [102]. Similar to *A. fumigatus*, *C. neoformans* utilizes L-DOPA melanin as a defense against oxidative stress from phagocytic immune cells [122–124], yet it relies mostly on its complex capsule to evade detection by host PRRs. *C. neoformans* contains a heterogenous multi-layered polysaccharide capsule that can block immune detection of fungal PAMPs, such as β-1,3-glucan, while preventing the adherence of complement proteins or antibodies to the surface [125]. To further protect itself, *C. neoformans* can alter the physical characteristics of the capsule to adapt to environmental cues [126,127], and capsule component glucuronoxylomannan (GXM) can induce L-selectin shedding and decreased TNFR expression on neutrophils, likely impeding their ability to bind to cell surfaces at the site of infection [128]. The diverse functions performed by the *C. neoformans* capsule ultimately contributes to its ability to survive the innate immune response and persist towards a chronic latent infection that can later reactivate or disseminate. Interactions between host-PRRs and their pathogen counterparts provides a strong line of defense against active and chronic infections, yet is not exempt from the effects of pathogen virulence factors, nor the creative immune evasion mechanisms employed by these pathogens to ensure persistence.

Epithelial-Pathogen Interactions

Pulmonary epithelial cells play multiple roles in maintaining lung immunity, ranging from a mucous-coated ciliated physical barrier between the body and the external world to expressing TLRs and initiating immune responses *via* proinflammatory cytokine secretion [129,130]. For a pathogen, epithelial cells often represent the first challenge that must be overcome in order to successfully establish an infection,

thereby requiring passage through or destruction of epithelial cells. After entrance into the airway, pathogens must surmount the outer layer of the epithelium – containing mucous, surfactant, and scavenging immune cells – as this region is a hostile environment for the establishment of colonies or infections. Therefore, microbes have developed an array of physical methods to pass through the mucous layers and bind to the surface epithelium to prevent their clearance. The pathogen *B. pseudomallei* express genes *boaA* and *boaB*, which code for proteins comparable to the *Y. enterocolitis* adhesin YadA; these adhesin proteins have been found to significantly increase the adhesion of *E. coli* expressing *boaA* and *boaB* to alveolar and bronchial cell lines, and have been implicated in intracellular survival of the pathogen [131]. Further, this adhesive capability of *B. pseudomallei* can be complemented by the adaptation of a biofilm phenotype, which was found to promote greater adhesion and subsequent invasion and infection by the bacteria [132]. Indeed, the ability of *B. pseudomallei* to adhere to the airway epithelium is directly correlated with its virulence and ability to induce cellular damage [133], as well as to the expression of genes regulating QS and virulence pathways [134,135], underscoring the importance of pathogen adhesion for initiating a successful infection. Similarly, *C. neoformans* utilizes secreted phospholipase B to improve its ability to adhere to pulmonary epithelial cells, likely through interactions between surfactant protein D (SP-D) and polysaccharides on the surface of the *C. neoformans* capsule [66]; additionally, capsule components GXM and MP84 are known to facilitate the binding of different *C. neoformans* strains to airway epithelial cells [136], enabling *C. neoformans* to initiate infection at this primary immune barrier [137]. SP-D binding is also found to play a role in the immune response against *A. fumigatus*, wherein SP-D binds specifically to melanin on the fungal conidia and associates with galactomannan and galactosaminogalactan on the fungal cell wall; further, SP-D bound conidia were phagocytosed more readily than un-opsonized conidia, and induced a greater transcription of proinflammatory cytokines [138]. While the lung epithelium can deploy some defense mechanisms against adherent pulmonary pathogens, once adhered, these pulmonary pathogens can invade into or through the epithelium to establish a protective niche for growth and persistence. Discovery of mechanisms or treatments to decrease this

adherence and enable clearance from the lung epithelium prior to pathogen entry can have a significant impact on disease outcome.

Intracellular Cross-talk

However, for many pathogens, passage through the epithelial barrier is unknowingly assisted by phagocytic immune cells. Physical detection of pathogens by PRRs can initiate an endocytic process wherein a membrane receptor (and the pathogen attached to it) is internalized into a self-contained vacuole within the cell. This vacuole typically acts in a host-protective manner, as the host uses numerous mechanisms to clear the vacuole contents such as vacuole acidification or fusion with vacuoles containing antimicrobial peptides (*e.g.*, human cathelicidin, LL-37), antimicrobial molecules (*e.g.*, RNS, ROS), or lytic proteins (*e.g.*, cathepsins, phospholipases)[139]. For example, during the course of infection with *M. tuberculosis*, activated macrophages release a collection of reactive nitrogen and oxygen species generated *via* NOX2 into the phagosome to induce oxidative stress and destruction of microbial membranes and intracellular components [139]. Induction of autophagy and xenophagy pathways in *M. tuberculosis*-infected macrophages provides an alternative mechanism of defense against the intracellular pathogen, and modulation of these pathways has been the target of host-directed-therapies [140]. This intracellular communication between the host cell and pathogen enables a strong form of self-defense for the cell, as well as a method to clear an acute infection and potentially avoid chronicity. Yet, for many pathogens, including *M. tuberculosis*, the ability to escape the phagocytic vacuole is the key to survival and persistence and an important mechanism for immune evasion [141–144].

Though not commonly perceived as an intracellular pathogen, *S. aureus* utilizes several methods to persist within a protective intracellular niche, ranging from secreting factors to block the acidification of the phagosome in leukocytes to disrupting phagosomal membranes for escape into the cytosol in epithelial cells [145,146]. Indeed, *S. aureus* utilizes its presence inside PMNs to usurp PMN expression of "danger" signals and to manipulate the phenotype of innate immune cells when in coculture, ultimately altering the ability of macrophages to clear *S. aureus* – infected PMNs and enabling intracellular persistence of the bacteria [147,148]. *S. aureus* can evade and manipulate PMN cell (*i.e.*, neutrophil) function

and antimicrobial effects in different ways, which is reviewed in depth here [147]. *S. aureus* also utilizes the intracellular space of nonprofessional phagocytes, such as epithelial cells, as a protective niche to hide from host immune cells and to diverge into a heterogenous population of replicating invasive or non-replicating persistent phenotypes depending on its intracellular environment, host cell metabolism, and bacterial colony variance [32,149].

Once an intracellular pathogen manages to escape from the phagosome, they must rely on additional mechanisms for movement through the cell itself. An important component of this intracellular mobility is actin-based motility, which is utilized by a wide range of pathogens including *B. pseudomallei* and *C. neoformans* to manipulate the host cell cytoskeleton for their own movement and eventual dissemination through cell-cell spreading [150,151]. Intracellular *B. pseudomallei* that have escaped the phagosome utilize bacterial proteins BimA and BimC to polymerize and remodel actin at its poles, enabling the pathogen to move through the cell to the outer membrane, from which it can protrude out of the cell and infect proximal cells [150–152]. *C. neoformans* similarly uses cell to cell spreading to infect neighboring cells while evading immune surveillance mechanisms, relying on an actin-dependent method for phagosomal escape and extrusion; however, the host cell utilizes actin flashes, or rapid repolymerizations, to temporarily prevent *C. neoformans* escape from the phagosome [153,154]. The importance of actin in the pathogenesis of *C. neoformans* is also demonstrated by the dependence of macrophages on actin for the uptake and internalization of the extracellular yeast cells, which is significantly decreased in the presence of actin depolymerizing agents [155]. Further understanding of how both host cells and pathogens utilize intracellular communication to their own advantage can provide important insight into disrupting the establishment of chronic infections.

4.2.3 Volatile signaling

Whereas there exists a substantial amount of information regarding soluble factor signaling and juxtacrine signaling mechanisms, much less is known regarding volatile signaling. Principally regarded as a potential diagnostic for identifying bacterial species *in vivo* [156–158], volatile chemicals secreted by

microbial species perform multiple functions as both symbiotic and antagonistic factors in complex signaling environments [159–162]; indeed, microbial volatile organic compounds (mVOCs) have been described to play an important role in both intra- and inter-kingdom interactions [162]. Additionally, these factors can originate from various microbes and kingdoms, and vary based on the microbial makeup of colonies, as well as the morphological form of microbe (*i.e.*, spore vs. filamentous). Secreted mVOCs have been correlated with pathogen identity and even disease severity [163,164], yet how these mVOCs influence pathogen behavior and host response is still widely unknown. We review mVOCs that target other commensal microbes and VOCs that target host cells, as well as any downstream effects that result from this volatile cross-talk. However, volatile signaling between pathogens and the host lung is a vastly understudied area that represents a potentially significant wealth of information regarding host-pathogen interactions and as such requires further studies.

Pathogen-Targeted Volatile Signaling

Commensal microbes secrete volatile factors to promote synergetic interactions within an environment, wherein one microbe may secrete a VOC that is then sequestered and metabolized by another or promote the growth of a neighboring microbe [159,162]. In the widely studied coculture system of *P. aeruginosa* and *A. fumigatus,* it has been found that volatile signaling between these two organisms results in stimulation of *A. fumigatus* growth from *P. aeruginosa*-derived dimethyl sulfide [12]; this result is contrary to what is observed when these two pathogens are in physical contact, where *P. aeruginosa* secretes toxins that inhibit the growth of *A. fumigatus* [165,166]. These interactions illustrate that the chemical communication between two organisms cannot be solely examined in one context, and that growth conditions and the spatial distribution of microbes can yield different pathogen outcomes. This is further evident from the impact of oxygen availability on the *A. fumigatus* "volatilome", which generates discernable volatile metabolite profiles dependent on the hypoxic state in the surrounding environment [167]. The secretion of specific volatiles can also promote the survival and antibiotic resistance of pathogens, often to the benefit of the rest of the infectious colony. H_2S is released by a wide range of pulmonary pathogens, such as *Bacillus anthracis, P. aeruginosa,* and *S. aureus,* and inhibition of H_2S was found to

increase the susceptibility of the bacteria to antibiotics [168]. The cytoprotective role of H_2S is believed to result from its ability to control oxidative stress around the bacteria and prevent oxidation and DNA damage [168]; this protection not only helps the bacteria resist antibiotic treatment, but also host-based oxidative stress (*i.e.*, ROS). Antibiotic resistance can also be modulated by biogenic ammonia, which has been shown to improve resistance to tetracycline in *S. aureus* and *P. aeruginosa*, illustrating the impact of the volatile signaling landscape in the ability of a lung pathogen to survive and persist in a chronic infection [169]. This beneficial effect on growth and resistance is important for infections where there are multiple distal sites of pathogen colonies, as communication between these locations is not limited by the soluble diffusion- or contact-based signaling required for paracrine and juxtacrine signaling, making it more difficult for the host to intercept or impede these signals. However, much is still unknown regarding the detrimental and antagonistic effects of pathogen-derived volatiles on other pathogens in the lungs, as much of the research has focused on either the positive effects of microbial volatile signaling for pathogen survival, or the use of these volatile signals as diagnostics for bacterial colonization and infection [156,157,169].

Host-Targeted Volatile Signaling

The effects of volatile communication between microbes and their host counterparts is even less studied due to difficulties associated with subjecting host cells to volatile chemicals in a biomimetic manner; complex *in vitro* models can partially solve this difficulty, as cells are not cultured in a traditional submerged manner [170,171]. Pathogen-derived volatile signals received by host cells can vary extensively from QS molecules to mVOCs; these factors can then in turn manipulate the behavior of host barriers to infection. One well characterized volatile compound that performs a range of pathogen functions is 2-amino acetophenone (2-AA), a QS-regulated compound secreted by *P. aeruginosa* and *B. thailandensis* (a close nonpathogenic relative of *B. pseudomallei*) that has been linked to a persistent chronic phenotype in *P. aeruginosa* [172]. Pretreatment with 2-AA in a murine burn infection model and in *ex vivo* murine macrophages led to a decrease in proinflammatory cytokine secretion while modulating innate immune signaling pathways, ultimately leading to an increase in subject survival without efficiently clearing *P.*

aeruginosa in vivo [173]. Additionally, 2-AA impacts mitochondrial function in muscles through disruption of oxidative homeostasis, leading to induction of ROS-mediated oxidative stress and apoptosis signaling, which is believed to further aid in the establishment of an environment conducive to chronic infection [174,175]. While diffusion of these factors into the host tissue has detrimental effects, the influence of pathogen-derived volatiles on the host epithelial and immune cells is much lesser known. Some cytotoxicity studies have been conducted demonstrating the harmful effects of volatiles such as 1-decanol and 1-octen-3-ol, but these studies used submerged cell cultures exposed to media containing the VOC and lacking an air-exposure component, or subjected bacterial cells to the compounds for *umu* and Ames testing [176,177]. Overall, there is a substantial and immediate need for research in this field that relates the effect of pulmonary pathogen-derived volatiles to human host immunology and disease outcome, as much of the fundamental characterization of this space is still missing [178].

4.3 Tissue-level communication in the context of pulmonary infection

It is important to look at the development of chronic infection from a tissue level perspective — considering how cross-talk between the pathogen, immune system, and surrounding microenvironment can contribute to the process of lung injury, remodeling, and the transition from acute infection to chronic pulmonary infection. Similar to immune interactions, tissue level reorganization in response to a pathogen includes a complex milieu of signaling and communication between the multiple components of the tissue; understanding this accompanying signaling environment requires consideration of all the cell types involved (*i.e.*, epithelial, mesenchymal, vascular, *etc.*) and changes in the complex tissue architecture (*i.e.*, ECM, vascularization, airway constriction, *etc.*).

While pathogens can modify the tissue microenvironment to create a favorable niche, underlying diseases or conditions can also disrupt tissue architecture or function; these specific tissue level changes create a favorable environment for colonization by specific pathogens and predispose individuals to chronic pulmonary infections. These conditions can include genetic causes, such as cystic fibrosis (CF), or pathologic reasons, such as chronic obstructive pulmonary disease (COPD). In addition to physical

tissue disruption that disposes individuals to chronic infections, such as impaired mucociliary clearance, cellular signaling mechanisms including host-host and host-pathogen signaling are often disrupted in these cases which can further exacerbate the host defenses at the tissue level.

4.3.1 Signaling in tissue components

There are many cell types in the tissue microenvironment that participate in cellular communication in the context of infection; this milieu of cellular conversations amongst many cell types and tissue components are in concert with immune cell-pathogen signaling and/or evasion of immune cells by a pathogen. The epithelial layer, for example, is of particular importance as it serves as an immune barrier to pathogen invasion into the tissue [130,179–181], leading pathogens to evolve various strategies to disrupt this barrier [3,29,31,32]. However, recent research has revealed that the airway epithelium has an expanded and active role in the tissue microenvironment with respect to its contribution during infections [29,130,179–182]. For example, epithelial cells exhibit innate immune functions, including the secretion of antimicrobial peptides (AMPs) [183–186], and cytokines [182,187,188] to induce the appropriate immune response, as well as chemokine and growth factor secretion to assist in tissue remodeling and repair during an infection. Epithelial secreted antimicrobial peptides (AMPs) include classes such as defensins [183,185,186], cathelicidins [184,186], lysozymes [189,190], lactoferrins [189–191], and secretory leukocyte proteinase inhibitor [192,193]. For example, the primary defensin secreted by epithelial cells, human β-defensin-1 (hBD-1), is constitutively secreted, but other β-family defensins are secreted by epithelial cells in response to signaling events; these events include direct contact signaling of the epithelium with pathogen components that activate the TLRs or NF-κB signaling pathways or soluble factors signaling such as the presence of pro-inflammatory cytokines [130,179,183].

The epithelium is also in communication with other cell types in the tissue, such as mesenchymal cells in the underlying airway connective tissue, which are subsequently communicating with the epithelium and tissue-resident immune cells. This signaling pathway is critical for tissue repair and the remodeling processes that occur in response to the pathogenic assault to tissue integrity. Lung fibroblasts,

for example, which are classically thought to have the primary function of maintaining the ECM, also are involved in coordination of inflammation and tissue repair response [194–196] through the secretion of a variety of cytokines [195–197], chemokines [196], and other signaling molecules [194,196]. For example, it has been found that bacterial components such as LPS can induce fibroblasts to produce chemokines (*e.g.* CXCL2, CCL2) to attract other immune cells to the site of infection in the connective tissue [196]. Further, fibroblasts have also been shown to secrete the cytokine IL-8, the overexpression of which has been implicated in cystic fibrosis [196–198]. These secretions, along with physical cross-talk interactions between fibroblasts and leukocytes (*e.g.*, CD40–CD40 ligand binding) and stimulatory molecules (*e.g.*, CD80/CD86 mediated binding) can contribute to chronic inflammation in the tissue [194,199,200].

4.3.2 Tissue disruption by underlying disease

Chronic infections in patients with underlying diseases represents a significant burden of disease and mortality and understanding how normal communication and defense is disrupted in these cases can help lead to a better understanding of the mechanisms involved, as well as improved treatment and prevention. Here we discuss two examples, CF and COPD, where disruptions in cellular signaling contribute to the propensity for chronic infections.

Cystic Fibrosis

The cause of death in the majority of patients with cystic fibrosis (CF) is respiratory failure, often accompanied by chronic bacterial infection and associated airway inflammation [201,202]. Cystic fibrosis is characterized by a mutation in the cystic fibrosis transmembrane conductance regulator (*CTFR*) gene [201,203]. This mutation disrupts the function of a key ion transport protein, which functionally leads to disrupted mucous production and movement. This mucous stasis can lead to impaired mucosal immunity [179,198,201]. Ultimately, this increase in mucous impedes microbial clearance and allows the creation of favorable microenvironments for the proliferation and dissemination of microbial colonies[179,198,201].

There is a great interest in the bacterial microbiome of cystic fibrosis patients, as it has been found to differ significantly from non-CF individuals [201,204]. As cellular communication in the microbiome is

thought to be important in host response and the prevention of infections, it is hypothesized that this difference in the commensal microbiome of CF patients can contribute to different infection profiles (*i.e.*, specific populations or identities of pathogens). However, the CF microbiome and its effect on immunity is still not completely understood [179,201,204]. The identity of the bacterial infections that are typically found in CF are better characterized. In early childhood, individuals with CF are often infected with *S. aureus* and *Hemophilis influenzae;* this differs from the infections seen most commonly in adulthood, which are typically caused by *P. aeruginosa* [201,204]. In addition to the distinct microbiome and infection profiles, perturbations in intracellular and extracellular signaling in the cells of cystic fibrosis individuals has been elucidated [187,188,198]. These perturbations, which include several intracellular signaling pathways, such as NF-κB, and low molecular weight GTPases, lead to abnormal production of secretory cytokines, particularly those dependent on NF-κB (*e.g.* IL-1, TNF, IL-6, and IL-8), coupled with decreased response to certain extracellular such as IFNγ and TGFβ [198]. A more detailed description of the signaling abnormalities in cystic fibrosis individuals can be found here [198].

COPD

Patients suffering from COPD have pathologically compromised tissue architecture, which can lead to or be exacerbated by a chronic infection. COPD is described as airflow obstruction caused by emphysema and chronic bronchitis [205]. Chronic bacterial infection is associated with COPD. In many cases, infections are a principal cause of an exacerbation of COPD, or acute worsening of symptoms [206,207]. Exposure to cigarette smoke is a major risk factor for the development of COPD, and the mechanism by which infection can occur is largely driven by cellular damage from chronic smoke exposure in the lower airways [208,209]. This cellular damage, particularly of the airway epithelial cells, leads to dysregulated mucociliary clearance and impaired secretion of antimicrobial peptides, amongst other critical functions of host defense [179,210]. Moreover, the pathogen driven disruption of cellular signaling, in addition to detrimental microbial toxins and virulence factors, can further damage the burdened lung architecture, feeding into the cycle of tissue damage and impaired immune responses [179,206,209,210]. Like CF, there is a unique pathogen signature commonly associated with pulmonary infection in COPD.

Patients with underlying COPD tend to have chronic infections where the colonizing bacteria is *H. influenzae*, *S. pneumoniae*, or *Moraxella catarrhalis* [206,208–210].

4.4 Modeling pulmonary infections and cellular cross-talk

The role of cross-talk in pulmonary infections is beginning to be more understood as new analytical methods enable the examination of the cellular secretome [211–213] and novel *in vitro* lung tissue models facilitate scrutiny of the role of complex microenvironment conditions on lung pathology [160,171,214–216]. Recapitulating lung tissue *in vitro* is challenging due to the complexity of the organ. Notable important features include an air liquid interface at the epithelium, an extracellular matrix that facilitates both mechanical stretch of breathing while providing support, a complex system of vasculature throughout allowing for gas exchange, and the presence of a myriad of immune components (Figure 4.1). The airway itself varies in shape and size as the respiratory tree progresses from the bronchi to bronchioles to the alveoli, reflecting a change in function from a conducting region to a gas exchange region [214,216,217]. Owing to these regional differences in functionality, the cell phenotypes and histology also change depending on the location on the respiratory tree. For example, the small airways are lined with pseudostratified columnar ciliated epithelium with interspersed mucin secreting goblet cells; these features are functionally equipped to generate and move mucus, an important immune defense against extracellular microbes [179,218,219]. The small airway histology looks very different from the simple squamous epithelium found in the alveoli, which are functionally equipped for diffusion of gases between the alveoli and the surrounding capillary network [217,220]. Immune cells are also interspersed at all levels of the respiratory tree [221]. Importantly, the lung is not a sterile environment, containing its own unique microbiome that contributes to the complexity and extensive exchange of cellular signals within the lung microenvironment and surrounding tissue structure [2,204,222].

A significant challenge in the development of *in vitro* lung models is finding a balance between a simple and robust system suited for high throughput examination and a system that more closely recapitulates the full complexity of the human lung microenvironment. Perhaps the greatest power of *in*

vitro systems is that they can be engineered along this spectrum, tailored to a particular level of complexity to answer a specific biological question. This configurability of an *in vitro* system, including choice of cell types (*e.g.*, epithelial, endothelial, stromal, immune cells, *etc.*), cell source (*e.g.*, immortalized human cells or primary human cells), ECM components (*e.g.*, collagen, matrigel, laminin *etc.*), and two- or three-dimensional placement of these components relative to each other, grants the researcher unprecedented control over the microenvironment and the ability to manipulate the *in vitro* system more easily than within an animal model [15,214,223].

In addition to the increased biological engineering control over the microenvironment offered by *in vitro* models, the ability to use human-derived cells is another beneficial feature. Studies utilizing animal models have helped to develop much of our understanding of lung pathologies. However, there are well known limitations to animal models in fully elucidating the complex microenvironment and cross-talk between pathogens and the human tissue microenvironment. Physiological differences between the animal immune system and human immune system, as well as differences in susceptibility to and development of disease present a problem for studying cross-talk in chronic infections. For example, mice do not become infected with *M. tuberculosis* in the same way as humans, as they form structurally different granulomas and do not commonly develop necrotizing lesions [224]. While other animal models offer closer homology to humans for the study of CPIs, such as non-human primates or humanized mice [225–230], these are more expensive and logistically demanding to use.

Innovative organotypic and tissue engineered models have incorporated key biological functions (*e.g.*, cell differentiation [231,232], tight junction formation [231], physical components (*e.g.*, extracellular matrix (ECM), air and liquid flow [170,233,234], mechanical stimuli [170,210,233–236], and placement of pathogens with respect to lung tissue components to mimic *in vivo* interactions, (*i.e.*, diffusion based signaling [170,233] and volatile signaling [160])), all of which allow researchers to hone in on specific aspects of the lung physiology and manipulate conditions to better understand the underlying signaling mechanisms governing the pathology of infection. Here we describe the current landscape of *in vitro* lung models, with a focus on utilizing these models as a tool for studying the microenvironmental cross-talk in CPIs. Many

of these models have already elucidated key insights into CPIs, such as the dependence of early *M. tuberculosis* granuloma formation on ESAT-6 and the disruption of this granuloma formation with inhibition of tissue matrix metalloproteinases (MMPs)[49,237]. However, there are many models that were not explicitly designed for modeling infection that have the potential to be adapted for studying cross-talk in infection. Further, many of these models can be kept in culture for extended periods of time (±4-8 weeks)[232–234,238,239], which may enable some investigation into long term host-pathogen interactions similar to that found in chronic infections. While we do not discuss *in vitro* organoid models here, we refer readers to these sources for lung organoid models [240–243].

4.4.1 Conventional macroscale platforms

Transwell inserts: a simple, robust coculture model

Advances in culturing techniques have led to an expansion beyond a submerged simple monolayer culture of lung epithelial cells, which fails to replicate lung tissue-level biological functionality [244–246]. For example, there is much interest and limited successes in developing culturing conditions for inducing differentiation of easy to obtain cell lines into various other cellular phenotypes that are found in the airway, such as ciliated pseudostratified epithelial cells and mucin producing goblet cells [231,232]. Establishment of an air liquid interface (ALI) can differentiate a small-airway epithelial cell from a cobblestone monolayer culture into a mucociliary phenotype complete with ciliated pseudostratified columnar epithelium [231,232] and mucin-producing goblet cells [232,238,247]. Using other epithelial cell lines, an ALI can help create alveolar epithelial models, characterized by a simple squamous epithelium. The ALI of these cell types can recapitulate alveolar function as measured by the increased surfactant secretion from type II - like alveolar epithelia [170,248]. Notably, ALI models better mimic the native environment of the lung epithelium and promote the recapitulation of the physical complexity of the lung. Widespread use of cell culture insert technologies, such as Transwell inserts, have allowed for multiple monoculture and coculture experiments utilizing an ALI to differentiate epithelial cells into a biomimetic small airway model [231,232,249]. The Transwell insert, produced by Corning Life Sciences, utilizes a simple and robust

design that integrates into standard laboratory equipment. The insert consists of a permeable membrane that sits above the bottom of a standard tissue culture well. The membrane pore size can be chosen from 0.4 μm to 8.0 μm, with the larger pore sizes often used for cell migration assays, and the smaller pore sizes (typically 0.4 μm) used for coculture, soluble factor signaling, and creating ALI cultures. The inserts can also be used to establish an ALI in lung epithelial models [231,232,249] by culturing epithelial cells on the permeable membrane and removing the appropriate amount of media such that the cells are exposed to air on the apical (top) side, while still receiving nutrients through the permeable membrane on the basolateral (bottom) side. For coculture, cells can be cultured on top of the permeable membrane, and a different cell type can be cultured in the well plate floor or even on the underside of the membrane, allowing the two cell types to communicate *via* soluble factor signaling through the porous membrane [250,251]. This functionality is particularly useful for studying cross-talk in infections. Finally, neutrophil extravasation can be modelled using a Transwell system due to the porosity of the membrane [250].

Due to the ease of use and efficacy of the Transwell cell inserts for establishing an ALI and a mucocilliary differentiated population, Transwell insert models have been utilized in a number of studies specifically for studying signaling involved in lung infections, with varying levels of complexity in the model. The simplest of which is utilizing a single cell type (*e.g.*, epithelial cells) cultured on the Transwell insert membrane to first establish an ALI and a differentiated airway epithelium. The cells are then exposed to a pathogen of interest either by incorporating pathogen conditioned media into the bottom chamber [249] or by placing a pathogen (*e.g.*, bacterium or fungus) on the apical side of the airway epithelium [252,253]. An example of both these approaches can be seen in a study done by Halldorsson *et al* in 2010. This study took advantage of the ability to induce tight junction formation using an ALI produced by a Transwell insert to study the effect of azithromycin treatment for maintaining tight junction integrity during a challenge with live *P. aeruginosa* and bacterial culture conditioned media. Tight junction integrity was measured by trans-epithelial electrical resistance (TEER), a widely-utilized metric of tight junction formation. Increasing in complexity, the two-chamber system provided by the Transwell insert also lends itself to coculture with an additional cell type in the bottom chamber, such as endothelial

or PMC cells in a simple setup [250,251]. This feature enables investigations into the soluble factor signaling between different cell types.

Building upon these relatively simplistic Transwell insert systems, advanced models have also been developed that incorporate a three-dimensional culture into a Transwell insert-based platform. These models often include other tissue features such as an ECM/stromal component [171,254] and/or immune components [171]. For example, Bhowmick *et al.* created a 3D chitosan-collagen scaffold polymerized on top of a Transwell insert membrane before culturing human small airway epithelial cells on top of this scaffold and airlifting (exposing to air) the model. When compared to a non-3D scaffold control, they found differences in protein expression in uninfected and H1N1 and H3N3 flu virus-infected epithelial cells [254]. These results suggest that the addition of ECM components makes a difference in cellular functions. Additionally, Nguyen Hoang *et al.* developed a Transwell insert model that incorporates both a stromal component and an immune component within the model [171]. In this model, fibroblasts were suspended in type 1 collagen forming a 3D stromal layer on top of the Transwell insert membrane. Dendritic cells are then cultured on top of this stromal layer prior to epithelial cell culture and airlifting [171]. It was found that the capacity of DC to produce chemokines is regulated by the 3D organotypic model, and that soluble components secreted in their lung tissue model induced CCL18 in DC, a function absent in other culture conditions, including conditioned media, suggesting that control over the 3D microenvironment is critical for immune system function – an important consideration when designing models for studying host-pathogen interactions.

Transwell insert models are versatile and easily integrated into standard cell culture equipment, supporting their widespread use and adaptation. However, on the spectrum of complexity for *in vitro* models, they are relatively limited in recapitulating the lung tissue microenvironment and function. For example, the membrane separating the compartments is made of a polymeric material and does not fully recapitulate the extracellular matrix environment seen in the lamina propria of lung tissue [238]. Therefore, any desired control over 2D or 3D placement of ECM hydrogels or cell types is challenging in Transwell inserts, which are designed for a monolayer or single layer of 3D gel in each compartment. Further, while

96 well Transwell inserts are available, cell insert models tend to require relatively numerous amounts of cells and reagents. This can limit these models to easy-to-obtain cell types, which may not be as biologically relevant as valuable cells, such as primary cells from patients with lung disease. Therefore, meso- or microscale models may be better suited than traditional well plate scale culture for applications requiring the use of rare or valuable cell types. Lastly, the diffusion profile of factors between the apical chamber and the basal chamber is poorly characterized, making it difficult to use Transwells for studies where diffusion of signaling factors needs to be tightly controlled [255,256].

4.4.2 Microfluidic and microfabricated *in vitro* models

Microfluidic and microfabrication techniques have become a useful tool for adding additional control and complexity to *in vitro* models. Microfluidic systems, which typically contain a channel or network of channels with at least one dimension on the micrometer scale, permit more complex control of fluid and airflow, allowing for dynamic culturing conditions [170,233,238,257]. Other systems create dynamic culture conditions by adding modular functionalities and components (*i.e.*, different cell types, microorganisms, *etc.*) at different experimental timepoints [160,258]. Moreover, the ability to shape hydrogels or create microscale compartments offers spatial control of different cell types that have varying levels of communication with each other from diffusion-based signaling to volatile signaling [160,170,233,238]. Finally, microfabrication techniques enable microscale culture dimensions and volumes, thus requiring the use of fewer cells than a traditional macroscale (*e.g.*, well plate) approach [216,223,259,260].

The microfabricated *in vitro* lung model (the "lung-on-a-chip") developed by Huh *et al.* in 2010 has been an influential model over the past decade. A schematic of a "lung-on-a-chip" type model and other models discussed can be found in Table C1. The model features a thin microfabricated porous membrane separating a top and bottom chamber. Alveolar-like epithelial cells are seeded on top of the porous membrane in the top chamber, where an air-liquid interface is created. Endothelial cells are seeded on the basal side of the membrane on the basal side of the membrane in the bottom channel where blood or media is flowed. Because it is a closed system, airflow can be controlled both on the apical ALI and flow

rate of blood or media can be controlled in the bottom chamber. To add an additional functionality to the model, the design includes two side chambers on either side of the central channels, which can be put under cyclic vacuum or pressure, thus stretching the membrane that contains the cells in the inner channel. By modulating the pressure on the side chambers, the researchers can induce cyclical mechanical strain, similar to the mechanical stretching that alveolar tissue undergoes during breathing [170]. This model is versatile and has found widespread use for studying different pathologies such COPD [233], pulmonary edema [261], and cigarette-induced lung damage [234], and has also been adapted to model the small airway where pseudostratified epithelium and mucin producing cells are observed after ALI exposure [233,234]. The alveolar model has notably been used as an infection model similarly to how the Transwell insert models are used, where bacteria (or potentially other pathogens) are introduced to the apical compartment and the effect of this direct contact is measured in the epithelium and endothelium below [170]. Conditioned media or other relevant factors can also be introduced into the bottom compartment as method for soluble factor signaling.

Other models have also been developed with the goal of modeling cyclical mechanical stretching to mimic breathing *in vitro*, such as Stucki *et al.*, who developed a lung model that has actuation functionality. Much like Huh *et al.*, this model cultures alveolar epithelial cells on a thin porous membrane where the bottom side of the membrane is lined with endothelial cells. The actuation is brought by another flexible membrane at the bottom of the media chamber on top of a void channel. When negative pressure is applied in the void channel, the flexible membrane at the bottom of the media channel pulls down, thus pulling down on the flexible membrane containing the epithelial cells. This is similar to how the diaphragm decreases the pressure in the air cavity as breathing occurs *in vivo*. While the concept and materials (*i.e.*, a porous membrane) are similar to the Huh *et al* "lung-on-a-chip", this model differs slightly in geometry of where the actuation occurs, pulling down on the membrane rather than from the side. Further, the upper chamber is open, as it does not have a ceiling, removing the ability to control the apical airflow, but providing pipette access to the culture by users. In fact, human primary pulmonary alveolar cells collected from patients who underwent partial lung resection were utilized in

this model, illustrating its applicability for valuable cell populations [210]. This model has also been used for applications such as wound healing [235] and has been modified to include microelectronics for impedance measurements [236]. Similar to the Huh *et al.* model, this model can be used for study of cross-talk such as direct or soluble factor signaling, as pathogens can be directly introduced on the apical side or conditioned media can be introduced to the bottom compartment.

These alveolar models focus on the interaction between epithelial and endothelial cells, as these are the most dominant cell type in that region of the lung. Other small airway microfluidic models, including the 'small-airway on a chip' pioneered by Benam *et al.* in 2016, also looks at the interaction between endothelial and epithelial cells [233]. However, at the level of the small airway, such as the bronchioles, smooth muscle cells are also a relevant component, as the bronchioles will constrict or relax to increase the diameter of the airway, thus regulating airflow to different parts of the lung. Humayun *et al.* developed a microfabricated small airway model that incorporates smooth muscle cells and epithelial cells. The model looks similar to the small-airway on a chip from Benem *et al.* in that it contains a top chamber where the epithelial cells are grown, separated by a thin membrane with a bottom chamber that contains a second cell type (in this case smooth muscle cells). However, this model differs in several key ways. For one, the cell type in the bottom chamber is smooth muscle cells and not endothelial, which enables the researcher to model diseases such as asthma or pulmonary hypertension where SMC are important in disease pathogenesis. Secondly the 'membrane' separating the two chambers is a suspended ECM hydrogel, more specifically a mixture of matrigel and collagen. This more closely represents the ECM environment than Transwell inserts or the other *in vitro* models previously discussed that rely on a bioinert polymer such as polydimethylsiloxane (PDMS). Further, this model does not include the mechanical functionality of the other *in vitro* models, as it is not a closed microfluidic system. Notably, the open microfluidic system is beneficial in other ways, as it offers simple fabrication and pipette accessibility. Since this model represents the functionality of the small airway for bronchoconstriction, it is perhaps better suited for studies of diseases where bronchoconstriction is relevant, such as asthma and

COPD. However, it can be used as an interesting model to investigate the cross-talk involvement of smooth muscle cells in infections.

Apart from models that incorporate mechanical components to stimulate breathing *in vitro,* Barkal *et al.* developed a platform specifically designed for probing multikingdom cell signaling in the lung microenvironment [160]; this model not only allows for investigating direct and soluble factor cross-talk *via* placing pathogens in direct contact with the host lung tissue model, but also incorporates functionality for investigating volatile signaling. Moreover, this model incorporates a wide range of cellular components, including a three-dimensional collagen-based ECM with suspended fibroblast cells, where channels for the epithelium and endothelium are cast through, with one larger epithelium channel in the middle and two smaller endothelium channels on either side parallel to the epithelial channel. Similar to the Humayun *et al.* model, the compartments are not separated by an inert plastic or polymer, such as PDMS, but rather a more biologically relevant hydrogel with the addition of suspended fibroblasts. Further, the air liquid interface is uniquely created in a three-dimensional tubular channel, more similar to *in vivo* bronchial structure [160]. Additionally, the endothelium lined channels are cast cylindrically in the same manner as the epithelial lined channels. The authors are able to uniquely model a microenvironmental infection by introducing *A. fumigatus* (causative agent of invasive pulmonary aspergillosis) directly into the apical lung endothelial channel and allowing it to grow out into the surrounding ECM. They measure cytokine concentrations in the media in the side endothelial channels in response to this "infection". The authors further took advantage of the side endothelial channels and ECM by introducing blood immune components to the endothelial channels. Specifically, neutrophils were introduced *via* capillary flow into the side channels of the *A. fumigatus* infected model and migration into the ECM as a result of infection was measured. Finally, the authors designed an insert that clicks into the lung *in vitro* model chip that can culture two separate fungi or bacteria next to the model, enabling examination of multikingdom volatile signaling by culturing *A. fumigatus* and *P. aeruginosa* in this side insert. Cytokine levels again were measured from the endothelial side channels and shown to differ based on what combination of pathogens were included in the multi-kingdom culture. Notably this model offers multiple functionalities for

studying pathogens that can contribute to chronic infections and cross-talk amongst these different cell types and kingdoms within a co-infection scenario. Ultimately, this platform, in addition to those described above, can enable researchers to probe very specific aspects of the lung microenvironment for a wide range of conditions and infections in a controlled and versatile manner.

4.5 Conclusion

Deciphering the complex signaling phenomena of the lung microenvironment, in the context of CPIs, remains a significant challenge due to the myriad of factors contributing to this signaling milieu. The communication amongst host and pathogen cells through secreted factors, physical contact, and even volatile factors, can drive acute and chronic infections as pathogens evade immunity, but it can also control and impede progression of disease through coordinated immune defenses. Further, accounting for the tissue-level signaling in the lung responsible for maintaining pulmonary function and mediating damage from infection, the exchange of signals in this microenvironment becomes extremely convoluted, requiring innovative and creative studies to develop an understanding of this space. The recent advances in *in vitro* modeling can help facilitate these studies, as these platforms are continually increasing in complexity and adaptability, enabling researchers to utilize these models in conjunction with *in vivo* studies and answer specific research queries. Further, the large gap in our understanding surrounding volatile signaling in the lung represents a significant opportunity for fundamental and applied research studies, which can be further facilitated through the use of these novel *in vitro* platforms. Ultimately, we aimed to highlight similar signaling mechanisms in diverse pulmonary infections to elucidate novel connections and similarities between diseases, as well as to paint a picture of the complexity of this signaling environment during infection.

4.6 References

1. European Respiratory Society. *The Global Impact of Respiratory Disease- Second Edition*.; 2017.
2. O'Dwyer DN, Dickson RP, Moore BB. The Lung Microbiome, Immunity, and the Pathogenesis of Chronic Lung Disease. *J Immunol*. 2016;196(12):4839-4847. doi:10.4049/jimmunol.1600279

3. Henriques-Normark B, Tuomanen EI. The pneumococcus: Epidemiology, microbiology, and pathogenesis. *Cold Spring Harb Perspect Med*. 2013;3(7):1-16. doi:10.1101/cshperspect.a010215
4. Belperio J, Palmer SM, Weigt SS. Host–pathogen interactions and chronic lung allograft dysfunction. *Ann Am Thorac Soc*. 2017;14(September):S242-S246. doi:10.1513/AnnalsATS.201606-464MG
5. Vila-Córcoles A, Ochoa-Gondar O, Llor C, Hospital I, Rodríguez T, Gómez A. Protective effect of pneumococcal vaccine against death by pneumonia in elderly subjects. *Eur Respir J*. 2005;26(6):1086-1091. doi:10.1183/09031936.05.00030205
6. Malhotra S, Hayes D, Wozniak DJ. Cystic Fibrosis and Pseudomonas aeruginosa: the Host-Microbe Interface. *Clin Microbiol Rev*. 2019;32(3):00138-18.
7. Harris J, Keane J. How tumour necrosis factor blockers interfere with tuberculosis immunity. *Clin Exp Immunol*. 2010;161(1):1-9. doi:10.1111/j.1365-2249.2010.04146.x
8. Faure E, Kwong K, Nguyen D. Pseudomonas aeruginosa in Chronic Lung Infections: How to Adapt Within the Host? *Front Immunol*. 2018;9(OCT):1-10. doi:10.3389/fimmu.2018.02416
9. Budden KF, Shukla SD, Rehman SF, *et al.* Functional effects of the microbiota in chronic respiratory disease. *Lancet Respir Med*. 2019;7(10):907-920. doi:10.1016/S2213-2600(18)30510-1
10. Huffnagle GB, Dickson RP, Lukacs NW. The respiratory tract microbiome and lung inflammation: A two-way street. *Mucosal Immunol*. 2017;10(2):299-306. doi:10.1038/mi.2016.108
11. Ubags NDJ, Marsland BJ. Mechanistic insight into the function of the microbiome in lung diseases. *Eur Respir J*. 2017;50(3). doi:10.1183/13993003.02467-2016
12. Briard B, Heddergott C, Latgé JP. Volatile compounds emitted by pseudomonas aeruginosa stimulate growth of the fungal pathogen aspergillus fumigatus. *MBio*. 2016;7(2):1-5. doi:10.1128/mBio.00219-16
13. David J, Bell RE, Clark GC. Mechanisms of disease: Host-pathogen interactions between burkholderia species and lung epithelial cells. *Front Cell Infect Microbiol*. 2015;5(NOV):1-13. doi:10.3389/fcimb.2015.00080
14. Britto CJ, Brady V, Lee S, Dela Cruz CS. Respiratory Viral Infections in Chronic Lung Diseases. *Clin Chest Med*. 2017;38(1):87-96. doi:10.1016/j.ccm.2016.11.014
15. Kimura H, Yoshizumi M, Ishii H, Oishi K, Ryo A. Cytokine production and signaling pathways in respiratory virus infection. *Front Microbiol*. 2013;4(SEP):1-9. doi:10.3389/fmicb.2013.00276
16. Troy NM, Bosco A. Respiratory viral infections and host responses; insights from genomics. *Respir Res*. 2016;17(1):1-12. doi:10.1186/s12931-016-0474-9
17. Hartmann N, Harriff MJ, McMurtrey CP, Hildebrand WH, Lewinsohn DM, Kronenberg M. Role of MAIT cells in pulmonary bacterial infection. *Mol Immunol*. 2018;101(May):155-159. doi:10.1016/j.molimm.2018.06.270
18. Meierovics A, Yankelevich WJC, Cowley SC. MAIT cells are critical for optimal mucosal immune responses during in vivo pulmonary bacterial infection. *Proc Natl Acad Sci U S A*. 2013;110(33):3119-3128. doi:10.1073/pnas.1302799110
19. Barlow JL, McKenzie ANJ. Innate Lymphoid Cells of the Lung. *Annu Rev Physiol*. 2019;81(1):429-452. doi:10.1146/annurev-physiol-020518-114630
20. Lai DM, Shu Q, Fan J. The origin and role of innate lymphoid cells in the lung. *Mil Med Res*. 2016;3(1):1-10. doi:10.1186/s40779-016-0093-2
21. Ardain A, Porterfield JZ, Kløverpris HN, Leslie A. Type 3 ILCs in lung disease. *Front Immunol*. 2019;10(JAN). doi:10.3389/fimmu.2019.00092
22. Berry AM, Paton JC. Additive attenuation of virulence of Streptococcus pneumoniae by mutation of the genes encoding pneumolysin and other putative pneumococcal virulence proteins. *Infect Immun*. 2000;68(1):133-140. doi:10.1128/IAI.68.1.133-140.2000
23. Canvin JR, Marvin AP, Sivakumaran M, *et al.* The Role of Pneumolysin and Autolysin in the Pathology of Pneumonia and Septicemia in Mice Infected with a Type 2 Pneumococcus. *J Infect Dis*. 1995;172(1):119-123. doi:10.1093/infdis/172.1.119
24. Cavalcanti YVN, Brelaz MCA, Neves JKDAL, Ferraz JC, Pereira VRA. Role of TNF-alpha, IFN-gamma, and IL-10 in the development of pulmonary tuberculosis. *Pulm Med*. 2012;2012. doi:10.1155/2012/745483
25. Flynn JL, Chan J. Tuberculosis : Latency and Reactivation MINIREVIEW Tuberculosis : Latency and Reactivation. *Infect Immun*. 2001;69(7):4195-4201. doi:10.1128/IAI.69.7.4195
26. Rai P, He F, Kwang J, Engelward BP, Chow VTK. Pneumococcal Pneumolysin Induces DNA Damage and Cell Cycle Arrest. *Sci Rep*. 2016;6(November 2015):1-12. doi:10.1038/srep22972
27. van Pee K, Neuhaus A, D'Imprima E, Mills DJ, Kühlbrandt W, Yildiz Ö. CryoEM structures of membrane pore and prepore complex reveal cytolytic mechanism of Pneumolysin. *Elife*. 2017;6:1-22.

doi:10.7554/eLife.23644
28. Tweten RK. Cholesterol-dependent cytolysins, a family of versatile pore-forming toxins. *Infect Immun*. 2005;73(10):6199-6209. doi:10.1128/IAI.73.10.6199-6209.2005
29. Thornton JA, Durick-Eder K, Tuomanen EI. Pneumococcal pathogenesis: innate invasion yet organ-specific damage. *J Mol Med*. 2011;88(2):103-107. doi:10.1007/s00109-009-0578-5.Pneumococcal
30. Berube BJ, Wardenburg JB. Staphylococcus aureus α-toxin: Nearly a century of intrigue. *Toxins (Basel)*. 2013;5(6):1140-1166. doi:10.3390/toxins5061140
31. Soong G, Martin FJ, Chun J, Cohen TS, Ahn DS, Prince A. Staphylococcus aureus protein A mediates invasion across airway epithelial cells through activation of RhoA GTPase signaling and proteolytic activity. *J Biol Chem*. 2011;286(41):35891-35898. doi:10.1074/jbc.M111.295386
32. Palma Medina LM, Becker AK, Michalik S, *et al.* Metabolic Cross-talk between Human Bronchial Epithelial Cells and Internalized Staphylococcus aureus as a Driver for Infection. *Mol Cell Proteomics*. 2019;18(5):892-908. doi:10.1074/mcp.RA118.001138
33. Todd OA, Fidel PL, Harro JM, *et al.* Candida albicans augments staphylococcus aureus virulence by engaging the staphylococcal agr quorum sensing system. *MBio*. 2019;10(3):1-16. doi:10.1128/mBio.00910-19
34. Gauthier T, Wang X, Dos Santos J, *et al.* Trypacidin, a spore-borne toxin from Aspergillus fumigatus, is cytotoxic to lung cells. *PLoS One*. 2012;7(2). doi:10.1371/journal.pone.0029906
35. Berthier E, Lim FY, Deng Q, *et al.* Low-Volume Toolbox for the Discovery of Immunosuppressive Fungal Secondary Metabolites. *PLoS Pathog*. 2013. doi:10.1371/journal.ppat.1003289
36. Malekinejad H, Fani F, Hassani-Dizaji S, Shafie-Irannejad V, Fink-Gremmel F. Aspergillus fumigatus toxins cause cytotoxic and apoptotic effects on human T lymphocytes (Jurkat cells). *World Mycotoxin J*. 2013;6(1):65-71. doi:10.3920/WMJ2012.1481
37. Kamei K, Watanabe A. Aspergillus mycotoxins and their effect on the host. *Med Mycol*. 2005;43(SUPPL.1):95-99. doi:10.1080/13693780500051547
38. Suen YK, Fung KP, Lee CY, Kong SK. Gliotoxin induces apoptosis in cultured macrophages *via* production of reactive oxygen species and cytochrome c release without mitochondrial depolarization. *Free Radic Res*. 2001;35(1):1-10. doi:10.1080/10715760100300541
39. Schlam D, Canton J, Carreño M, Kopinski H, Freeman SA, Grinstein S. Gliotoxin Suppresses Macrophage Immune Function by Subverting. *MBio*. 2016;7(2):1-15. doi:10.1128/mBio.02242-15.Editor
40. Niide O, Suzuki Y, Yoshimaru T, Inoue T, Takayama T, Ra C. Fungal metabolite gliotoxin blocks mast cell activation by a calcium- and superoxide-dependent mechanism: Implications for immunosuppressive activities. *Clin Immunol*. 2006;118(1):108-116. doi:10.1016/j.clim.2005.08.012
41. Kupfahl C, Geginat G, Hof H. Gliotoxin-mediated suppression of innate and adaptive immune functions directed against Listeria monocytogenes. *Med Mycol*. 2006;44(7):591-599. doi:10.1080/13693780600815411
42. Pahl HL., Krauss B., Schulze-Osthoff K., *et al.* The immunosuppressive fungal metabolite gliotoxin specifically inhibits transcription factor NF-kappaB. *J Exp Med*. 1996;183(4):1829-1840.
43. Arias M, Santiago L, Vidal-García M, *et al.* Preparations for invasion: Modulation of host lung immunity during pulmonary aspergillosis by gliotoxin and other fungal secondary metabolites. *Front Immunol*. 2018;9(NOV):1-12. doi:10.3389/fimmu.2018.02549
44. van der Wel N, Hava D, Houben D, *et al.* M. tuberculosis and M. leprae Translocate from the Phagolysosome to the Cytosol in Myeloid Cells. *Cell*. 2007;129(7):1287-1298. doi:10.1016/j.cell.2007.05.059
45. Conrad WH, Osman MM, Shanahan JK, *et al.* Mycobacterial ESX-1 secretion system mediates host cell lysis through bacterium contact-dependent gross membrane disruptions. *Proc Natl Acad Sci U S A*. 2017;114(6):1371-1376. doi:10.1073/pnas.1620133114
46. Houben D, Demangel C, van Ingen J, *et al.* ESX-1-mediated translocation to the cytosol controls virulence of mycobacteria. *Cell Microbiol*. 2012;14(8):1287-1298. doi:10.1111/j.1462-5822.2012.01799.x
47. Simeone R, Bobard A, Lippmann J, *et al.* Phagosomal rupture by Mycobacterium tuberculosis results in toxicity and host cell death. *PLoS Pathog*. 2012;8(2). doi:10.1371/journal.ppat.1002507
48. Volkman HE, Pozos TC, Zheng J, Davis JM, Rawls JF, Ramakrishnan L. Tuberculous granuloma induction *via* interaction of a bacterial secreted protein with host epithelium. *Science (80-)*. 2010;327(5964):466-469. doi:10.1126/science.1179663
49. Parasa VR, Muvva JR, Rose JF, Braian C, Brighenti S, Lerm M. Inhibition of tissue matrix metalloproteinases interferes with Mycobacterium tuberculosis-induced granuloma formation and reduces

bacterial load in a human lung tissue model. *Front Microbiol*. 2017;8(DEC):1-14. doi:10.3389/fmicb.2017.02370
50. Ehlers S, Schaible UE. The granuloma in tuberculosis: Dynamics of a host-pathogen collusion. *Front Immunol*. 2012;3(JAN):1-9. doi:10.3389/fimmu.2012.00411
51. Silva Miranda M, Breiman A, Allain S, Deknuydt F, Altare F. The tuberculous granuloma: An unsuccessful host defence mechanism providing a safety shelter for the bacteria? *Clin Dev Immunol*. 2012;2012. doi:10.1155/2012/139127
52. Ramakrishnan L. Revisiting the role of the granuloma in tuberculosis. *Nat Rev Immunol*. 2012;12(5):352-366. doi:10.1038/nri3211
53. Pym AS, Brodin P, Brosch R, Huerre M, Cole ST. Loss of RD1 contributed to the attenuation of the live tuberculosis vaccines Mycobacterium bovis BCG and Mycobacterium microti. *Mol Microbiol*. 2002;46(3):709-717. doi:10.1046/j.1365-2958.2002.03237.x
54. Lewis KN, Liao R, Guinn KM, *et al.* Deletion of RD1 from Mycobacterium tuberculosis Mimics Bacille Calmette-Guérin Attenuation . *J Infect Dis*. 2003;187(1):117-123. doi:10.1086/345862
55. Brodin P, Rosenkrands I, Andersen P, Cole ST, Brosch R. ESAT-6 proteins: Protective antigens and virulence factors? *Trends Microbiol*. 2004;12(11):500-508. doi:10.1016/j.tim.2004.09.007
56. De Leon J, Jiang G, Ma Y, Rubin E, Fortune S, Sun J. Mycobacterium tuberculosis ESAT-6 exhibits a unique membrane-interacting activity that is not found in its ortholog from non-pathogenic Mycobacterium smegmatis. *J Biol Chem*. 2012;287(53):44184-44191. doi:10.1074/jbc.M112.420869
57. Fratti RA, Chua J, Vergne I, Deretic V. Mycobacterium tuberculosis glycosylated phosphatidylinositol causes phagosome maturation arrest. *Proc Natl Acad Sci U S A*. 2003;100(9):5437-5442. doi:10.1073/pnas.0737613100
58. Hmama Z, Sendide K, Talal A, Garcia R, Dobos K, Reiner NE. Quantitative analysis of phagolysosome fusion in intact cells: Inhibition by mycobacterial lipoarabinomannan and rescue by an 1α,25-dihydroxyvitamin D3-phosphoinositide 3-kinase pathway. *J Cell Sci*. 2004;117(10):2131-2139. doi:10.1242/jcs.01072
59. Kang PB, Azad AK, Torrelles JB, *et al.* The human macrophage mannose receptor directs Mycobacterium tuberculosis lipoarabinomannan-mediated phagosome biogenesis. *J Exp Med*. 2005;202(7):987-999. doi:10.1084/jem.20051239
60. Turkina M V., Vikström E. Bacteria-Host Crosstalk: Sensing of the Quorum in the Context of Pseudomonas aeruginosa Infections. *J Innate Immun*. 2019;11(3):263-279. doi:10.1159/000494069
61. Hooi DSW, Bycroft BW, Chhabra SR, Williams P, Pritchard DI. Differential Immune Modulatory Activity of. *Society*. 2004;72(11):6463-6470. doi:10.1128/IAI.72.11.6463
62. Hogan DA, Vik Å, Kolter R. A Pseudomonas aeruginosa quorum-sensing molecule influences Candida albicans morphology. *Mol Microbiol*. 2004;54(5):1212-1223. doi:10.1111/j.1365-2958.2004.04349.x
63. Lin J, Cheng J, Wang Y, Shen X. The Pseudomonas quinolone signal (PQS): Not just for quorum sensing anymore. *Front Cell Infect Microbiol*. 2018;8(JUL):1-9. doi:10.3389/fcimb.2018.00230
64. Skindersoe ME, Zeuthen LH, Brix S, *et al.* Pseudomonas aeruginosa quorum-sensing signal molecules interfere with dendritic cell-induced T-cell proliferation. *FEMS Immunol Med Microbiol*. 2009;55(3):335-345. doi:10.1111/j.1574-695X.2008.00533.x
65. Feldmesser M, Kress Y, Novikoff P, Casadevall A. Cryptococcus neoformans is a facultative intracellular pathogen in murine pulmonary infection. *Infect Immun*. 2000;68(7):4225-4237. doi:10.1128/IAI.68.7.4225-4237.2000
66. Ganendren R, Carter E, Sorrell T, Widmer F, Wright L. Phospholipase B activity enhances adhesion of Cryptococcus neoformans to a human lung epithelial cell line. *Microbes Infect*. 2006;8(4):1006-1015. doi:10.1016/j.micinf.2005.10.018
67. Djordjevic JT. Role of phospholipases in fungal fitness, pathogenicity, and drug development - lessons from Cryptococcus neoformans. *Front Microbiol*. 2010;1(NOV):1-13. doi:10.3389/fmicb.2010.00125
68. Santangelo RT, Nouri-Sorkhabi MH, Sorrell TC, *et al.* Biochemical and functional characterisation of secreted phospholipase activities from Cryptococcus neoformans in their naturally occurring state. *J Med Microbiol*. 1999;48(8):731-740. doi:10.1099/00222615-48-8-731
69. Garcia-Hermoso D, Janbon G, Dromer F. Epidemiological evidence for dormant Cryptococcus neoformans infection. *J Clin Microbiol*. 1999;37(10):3204-3209.
70. Hommel B, Mukaremera L, Cordero RJB, *et al. Titan Cells Formation in Cryptococcus Neoformans Is Finely Tuned by Environmental Conditions and Modulated by Positive and Negative Genetic Regulators*. Vol 14.; 2018. doi:10.1371/journal.ppat.1006982

71. Casadevall A, Coelho C, Alanio A. Mechanisms of Cryptococcus neoformans-mediated host damage. *Front Immunol*. 2018;9(APR):1-8. doi:10.3389/fimmu.2018.00855
72. Green AM, DiFazio R, Flynn JL. IFN-γ from CD4 T Cells Is Essential for Host Survival and Enhances CD8 T Cell Function during Mycobacterium tuberculosis Infection . *J Immunol*. 2013;190(1):270-277. doi:10.4049/jimmunol.1200061
73. Cowley SC, Elkins KL. CD4 + T Cells Mediate IFN-γ-Independent Control of Mycobacterium tuberculosis Infection Both In Vitro and In Vivo . *J Immunol*. 2003;171(9):4689-4699. doi:10.4049/jimmunol.171.9.4689
74. Shafiani S, Tucker-Heard G, Kariyone A, Takatsu K, Urdahl KB. Pathogen-specific regulatory T cells delay the arrival of effector T cells in the lung during early tuberculosis. *J Exp Med*. 2010;207(7):1409-1420. doi:10.1084/jem.20091885
75. Scott-Browne JP, Shafiani S, Tucker-Heard G, *et al.* Expansion and function of Foxp3-expressing T regulatory cells during tuberculosis. *J Exp Med*. 2007;204(9):2159-2169. doi:10.1084/jem.20062105
76. Cadwell K. Crosstalk between autophagy and inflammatory signalling pathways: Balancing defence and homeostasis. *Nat Rev Immunol*. 2016;16(11):661-675. doi:10.1038/nri.2016.100
77. Wu L, Estrada O, Zaborina O, *et al.* Microbiology: Recognition of host immune activation by Pseudomonas aeruginosa. *Science (80-)*. 2005;309(5735):774-777. doi:10.1126/science.1112422
78. Andrade RM, Almeida GM, DosReis GA, Bento CAM. Glucuronoxylomannan of Cryptococcus neoformans exacerbates in vitro yeast cell growth by interleukin 10-dependent inhibition of CD4+ T lymphocyte responses. *Cell Immunol*. 2003;222(2):116-125. doi:10.1016/S0008-8749(03)00116-3
79. Arora S, Olszewski MA, Tsang TM, McDonald RA, Toews GB, Huffnagle GB. Effect of cytokine interplay on macrophage polarization during chronic pulmonary infection with Cryptococcus neoformans. *Infect Immun*. 2011;79(5):1915-1926. doi:10.1128/IAI.01270-10
80. Oehlers SH, Cronan MR, Beerman RW, *et al.* Infection-induced vascular permeability aids mycobacterial growth. *J Infect Dis*. 2017;215(5):813-817. doi:10.1093/infdis/jiw355
81. Polena H, Boudou F, Tilleul S, *et al.* Mycobacterium tuberculosis exploits the formation of new blood vessels for its dissemination. *Sci Rep*. 2016;6(August):1-11. doi:10.1038/srep33162
82. Osherov N, Ben-Ami R. Modulation of Host Angiogenesis as a Microbial Survival Strategy and Therapeutic Target. *PLoS Pathog*. 2016. doi:10.1371/journal.ppat.1005479
83. Laarman AJ, Mijnheer G, Mootz JM, *et al.* Staphylococcus aureus Staphopain A inhibits CXCR2-dependent neutrophil activation and chemotaxis. *EMBO J*. 2012;31(17):3607-3619. doi:10.1038/emboj.2012.212
84. Bestebroer J, Van Kessel KPM, Azouagh H, *et al.* Staphylococcal SSL5 inhibits leukocyte activation by chemokines and anaphylatoxins. *Blood*. 2009;113(2):328-337. doi:10.1182/blood-2008-04-153882
85. Koymans KJ, Bisschop A, Vughs MM, van Kessel KPM, de Haas CJC, van Strijp JAG. Staphylococcal superantigen-like protein 1 and 5 (SSL1 & SSL5) limit neutrophil chemotaxis and migration through MMP-inhibition. *Int J Mol Sci*. 2016;17(7):1-16. doi:10.3390/ijms17071072
86. Zou J, Zhou L, Hu C, *et al.* IL-8 and IP-10 expression from human bronchial epithelial cells BEAS-2B are promoted by Streptococcus pneumoniae endopeptidase O (PepO). *BMC Microbiol*. 2017;17(1):1-7. doi:10.1186/s12866-017-1081-8
87. Angkasekwinai P, Sringkarin N, Supasorn O, *et al.* Cryptococcus gattii infection dampens Th1 and Th17 responses by attenuating dendritic cell function and pulmonary chemokine expression in the immunocompetent hosts. *Infect Immun*. 2014;82(9):3880-3890. doi:10.1128/IAI.01773-14
88. Warnatsch A, Tsourouktsoglou TD, Branzk N, *et al.* Reactive Oxygen Species Localization Programs Inflammation to Clear Microbes of Different Size. *Immunity*. 2017;46(3):421-432. doi:10.1016/j.immuni.2017.02.013
89. Managò A, Becker KA, Carpinteiro A, *et al.* Pseudomonas aeruginosa Pyocyanin Induces Neutrophil Death *via* Mitochondrial Reactive Oxygen Species and Mitochondrial Acid Sphingomyelinase. *Antioxidants Redox Signal*. 2015;22(13):1097-1110. doi:10.1089/ars.2014.5979
90. Hole CR, Leopold Wager CM, Mendiola AS, *et al.* Antifungal activity of plasmacytoid dendritic cells against Cryptococcus neoformans In Vitro requires expression of dectin-3 (CLEC4D) and reactive oxygen species. *Infect Immun*. 2016;84(9):2493-2504. doi:10.1128/IAI.00103-16
91. Lauw FN, Simpson AJH, Hack CE, *et al.* Soluble Granzymes Are Released during Human Endotoxemia and in Patients with Severe Infection Due to Gram-Negative Bacteria. *J Infect Dis*. 2000;182(1):206-213. doi:10.1086/315642
92. Tippayawat P, Pinsiri M, Rinchai D, *et al.* Burkholderia pseudomallei proteins presented by monocyte-derived dendritic cells stimulate human memory T cells in vitro. *Infect Immun*. 2011;79(1):305-313. doi:10.1128/IAI.00803-10

93. Kronsteiner B, Chaichana P, Sumonwiriya M, *et al.* Diabetes alters immune response patterns to acute melioidosis in humans. *Eur J Immunol*. 2019;49(7):1092-1106. doi:10.1002/eji.201848037
94. Stenger S, Hanson DA, Teitelbaum R, *et al.* An antimicrobial activity of cytolytic T cells mediated by granulysin. *Science (80-).* 1998;282(5386):121-125. doi:10.1126/science.282.5386.121
95. Andersson J, Samarina A, Fink J, Rahman S, Grundström S. Impaired expression of perforin and granulysin in CD8+ T cells at the site of infection in human chronic pulmonary tuberculosis. *Infect Immun.* 2007;75(11):5210-5222. doi:10.1128/IAI.00624-07
96. Rahman S, Gudetta B, Fink J, *et al.* Compartmentalization of immune responses in human tuberculosis: Few CD8+ effector T cells but elevated levels of FoxP3+ regulatory T cells in the granulomatous lesions. *Am J Pathol*. 2009;174(6):2211-2224. doi:10.2353/ajpath.2009.080941
97. Souza JAM, Baltazar L de M, Carregal VM, *et al.* Characterization of Aspergillus fumigatus Extracellular Vesicles and Their Effects on Macrophages and Neutrophils Functions. *Front Microbiol*. 2019;10(September):1-13. doi:10.3389/fmicb.2019.02008
98. Shopova IA., Belyaev I., Dasari P., *et al.* Human neutrophils produce antifungal extracellular vesicles against Aspergillus fumigatus. *bioRxiv*. 2019;620294.
99. Aguilar C, Mano M, Eulalio A. MicroRNAs at the Host–Bacteria Interface: Host Defense or Bacterial Offense. *Trends Microbiol*. 2019;27(3):206-218. doi:10.1016/j.tim.2018.10.011
100. Alexander M, Hu R, Runtsch MC, *et al.* Exosome-delivered microRNAs modulate the inflammatory response to endotoxin. *Nat Commun.* 2015;6. doi:10.1038/ncomms8321
101. Correia CN, Nalpas NC, McLoughlin KE, *et al.* Circulating microRNAs as potential biomarkers of infectious disease. *Front Immunol*. 2017;8(FEB):1-17. doi:10.3389/fimmu.2017.00118
102. Hernández-Chávez MJ, Pérez-García LA, Niño-Vega GA, Mora-Montes HM. Fungal strategies to evade the host immune recognition. *J Fungi*. 2017;3(4):1-28. doi:10.3390/jof3040051
103. Haas H. Fungal siderophore metabolism with a focus on Aspergillus fumigatus. *Nat Prod Rep*. 2014;31(10):1266-1276. doi:10.1039/c4np00071d
104. Olive AJ, Sassetti CM. Metabolic crosstalk between host and pathogen: Sensing, adapting and competing. *Nat Rev Microbiol*. 2016;14(4):221-234. doi:10.1038/nrmicro.2016.12
105. Ren W, Rajendran R, Zhao Y, *et al.* Amino acids as mediators of metabolic cross talk between host and pathogen. *Front Immunol*. 2018;9(FEB). doi:10.3389/fimmu.2018.00319
106. Amarsaikhan N, Templeton SP. Co-recognition of β-glucan and chitin and programming of adaptive immunity to Aspergillus fumigatus. *Front Microbiol*. 2015;6(APR):1-7. doi:10.3389/fmicb.2015.00344
107. Norris MH, Schweizer HP, Tuanyok A. Structural diversity of Burkholderia pseudomallei lipopolysaccharides affects innate immune signaling. *PLoS Negl Trop Dis*. 2017;11(4):1-27. doi:10.1371/journal.pntd.0005571
108. Pier GB. Pseudomonas aeruginosa lipopolysaccharide: A major virulence factor, initiator of inflammation and target for effective immunity. *Int J Med Microbiol*. 2007;297(5):277-295. doi:10.1016/j.ijmm.2007.03.012
109. Shukla S., Richardson ET., Drage MG., Boom WH., Harding CV. Mycobacterium tuberculosis lipoprotein and lipoglycan binding to toll-like receptor 2 correlates with agonist activity and functional outcomes. *Infect Immun*. 2018;86(10):00450-18.
110. Sánchez A, Espinosa P, García T, Mancilla R. The 19 kDa mycobacterium tuberculosis lipoprotein (lpqh) induces macrophage apoptosis through extrinsic and intrinsic pathways: A role for the mitochondrial apoptosis-inducing factor. *Clin Dev Immunol*. 2012;2012. doi:10.1155/2012/950503
111. Gehring AJ, Dobos KM, Belisle JT, Harding C V., Boom WH. Mycobacterium tuberculosis LprG (Rv1411c): A Novel TLR-2 Ligand That Inhibits Human Macrophage Class II MHC Antigen Processing . *J Immunol*. 2004;173(4):2660-2668. doi:10.4049/jimmunol.173.4.2660
112. Pecora ND, Gehring AJ, Canaday DH, Boom WH, Harding C V. Mycobacterium tuberculosis LprA Is a Lipoprotein Agonist of TLR2 That Regulates Innate Immunity and APC Function . *J Immunol*. 2006;177(1):422-429. doi:10.4049/jimmunol.177.1.422
113. Doz E, Rose S, Court N, *et al.* Mycobacterial phosphatidylinositol mannosides negatively regulate host toll-like receptor 4, MyD88-dependent proinflammatory cytokines, and TRIF-dependent co-stimulatory molecule expression. *J Biol Chem.* 2009;284(35):23187-23196. doi:10.1074/jbc.M109.037846
114. Huang Z, Zhao GW, Gao CH, *et al.* Mannose-capped lipoarabinomannan from mycobacterium tuberculosis induces IL-37 production *via* upregulating ERK1/2 and p38 in human type ii alveolar epithelial cells. *Int J Clin Exp Med*. 2015;8(5):7279-7287.
115. Kim WS, Jung ID, Kim JS, *et al.* Mycobacterium tuberculosis GrpE, A heat-shock stress responsive

chaperone, promotes Th1-biased T cell immune response *via* TLR4-mediated activation of dendritic cells. *Front Cell Infect Microbiol*. 2018;8(MAR):1-15. doi:10.3389/fcimb.2018.00095
116. Serrano-Gómez D, Domínguez-Soto A, Ancochea J, Jimenez-Heffernan JA, Leal JA, Corbí AL. Dendritic Cell-Specific Intercellular Adhesion Molecule 3-Grabbing Nonintegrin Mediates Binding and Internalization of Aspergillus fumigatus Conidia by Dendritic Cells and Macrophages . *J Immunol*. 2004;173(9):5635-5643. doi:10.4049/jimmunol.173.9.5635
117. Taylor PR, Tsoni SV, Willment JA, *et al.* Dectin-1 is required for β-glucan recognition and control of fungal infection. *Nat Immunol*. 2007;8(1):31-38. doi:10.1038/ni1408
118. Sainz J, Lupiáñez CB, Segura-Catena J, *et al.* Dectin-1 and DC-SIGN polymorphisms associated with invasive pulmonary aspergillosis infection. *PLoS One*. 2012;7(2):1-10. doi:10.1371/journal.pone.0032273
119. Steger M, Bermejo-Jambrina M, Yordanov T, *et al.* β-1,3-glucan-lacking Aspergillus fumigatus mediates an efficient antifungal immune response by activating complement and dendritic cells. *Virulence*. 2019;10(1):957-969. doi:10.1080/21505594.2018.1528843
120. Akoumianaki T, Kyrmizi I, Valsecchi I, *et al.* Aspergillus Cell Wall Melanin Blocks LC3-Associated Phagocytosis to Promote Pathogenicity. *Cell Host Microbe*. 2016;19(1):79-90. doi:10.1016/j.chom.2015.12.002
121. Stappers MHT, Clark AE, Aimanianda V, *et al.* Recognition of DHN-melanin by a C-type lectin receptor is required for immunity to Aspergillus. *Nature*. 2018;555(7696):382-386. doi:10.1038/nature25974
122. Missall TA, Moran JM, Corbett JA, Lodge JK. Distinct Stress Responses of Two Functional Laccases in Cryptococcus neoformans Are Revealed in the Absence of the. *Society*. 2005;4(1):202-208. doi:10.1128/EC.4.1.202
123. Emery HS, Shelburne CP, Bowman JP, Fallon PG, Schulz CA, Jacobson ES. Genetic study of oxygen resistance and melanization in Cryptococcus neoformans. *Infect Immun*. 1994;62(12):5694-5697.
124. Wang Y, Casadevall A. Susceptibility of melanized and nonmelanized Cryptococcus neoformans to nitrogen- and oxygen-derived oxidants. *Infect Immun*. 1994;62(7):3004-3007.
125. Campuzano A, Wormley FL. Innate immunity against cryptococcus, from recognition to elimination. *J Fungi*. 2018;4(1). doi:10.3390/jof4010033
126. O'Meara TR, Andrew Alspaugh J. The Cryptococcus neoformans capsule: A sword and a shield. *Clin Microbiol Rev*. 2012;25(3):387-408. doi:10.1128/CMR.00001-12
127. Yoneda A, Doering TL. Regulation of Cryptococcus neoformans capsule size is mediated at the polymer level. *Eukaryot Cell*. 2008;7(3):546-549. doi:10.1128/EC.00437-07
128. Dong ZM, Murphy JW. Cryptococcal polysaccharides induce L-selectin shedding and tumor necrosis factor receptor loss from the surface of human neutrophils. *J Clin Invest*. 1996;97(3):689-698. doi:10.1172/JCI118466
129. Dudek M, Puttur F, Arnold-Schrauf C, *et al.* Lung epithelium and myeloid cells cooperate to clear acute pneumococcal infection. *Mucosal Immunol*. 2016;9(5):1288-1302. doi:10.1038/mi.2015.128
130. McClure R, Massari P. TLR-dependent human mucosal epithelial cell responses to microbial pathogens. *Front Immunol*. 2014;5(AUG):1-13. doi:10.3389/fimmu.2014.00386
131. Balder R, Lipski S, Lazarus JJ, *et al.* Identification of Burkholderia mallei and Burkholderia pseudomallei adhesins for human respiratory epithelial cells. *BMC Microbiol*. 2010;10:20-25. doi:10.1186/1471-2180-10-250
132. Kunyanee C, Kamjumphol W, Taweechaisupapong S, *et al.* Burkholderia pseudomallei biofilm promotes adhesion, internalization and stimulates proinflammatory cytokines in human epithelial A549 cells. *PLoS One*. 2016;11(8):1-17. doi:10.1371/journal.pone.0160741
133. Kespichayawattana W, Intachote P, Utaisincharoen P, Sirisinha S. Virulent Burkholderia pseudomallei is more efficient than avirulent Burkholderia thailandensis in invasion of and adherence to cultured human epithelial cells. *Microb Pathog*. 2004;36(5):287-292. doi:10.1016/j.micpath.2004.01.001
134. Essex-Lopresti AE, Boddey JA, Thomas R, *et al.* A type IV pilin, PilA, contributes to adherence of B. pseudomallei and virulence in vivo. *Infect Immun*. 2005;73(2):1260-1264. doi:10.1128/IAI.73.2.1260
135. Srisanga K, Suthapot P, Permsirivisarn P, Govitrapong P, Tungpradabkul S, Wongtrakoongate P. Polyphosphate kinase 1 of Burkholderia pseudomallei controls quorum sensing, RpoS and host cell invasion. *J Proteomics*. 2019;194(December 2018):14-24. doi:10.1016/j.jprot.2018.12.024
136. Teixeira PAC, Penha LL, Mendonça-Previato L, Previato JO. Mannoprotein MP84 mediates the adhesion of cryptococcus neoformans to epithelial lung cells. *Front Cell Infect Microbiol*. 2014;4(AUG):1-9. doi:10.3389/fcimb.2014.00106
137. Taylor-Smith LM. Cryptococcus–epithelial interactions. *J Fungi*. 2017;3(4). doi:10.3390/jof3040053

138. Wah Wong SS, Rani M, Dodagatta-Marri E, *et al.* Fungal melanin stimulates surfactant protein D-mediated opsonization of and host immune response to Aspergillus fumigatus spores. *J Biol Chem*. 2018;293(13):4901-4912. doi:10.1074/jbc.M117.815852
139. Weiss G, Schaible UE. Macrophage defense mechanisms against intracellular bacteria. *Immunol Rev*. 2015;264(1):182-203. doi:10.1111/imr.12266
140. Sultana Rekha R, Rao Muvva SJ, Wan M, *et al.* Phenylbutyrate induces LL-37-dependent autophagy and intracellular killing of mycobacterium tuberculosis in human macrophages. *Autophagy*. 2015;11(9):1688-1699. doi:10.1080/15548627.2015.1075110
141. Mehta M, Rajmani RS, Singh A. Mycobacterium tuberculosis WhiB3 Responds to vacuolar pH-induced changes in mycothiol redox potential to modulate phagosomal maturation and virulence. *J Biol Chem.* 2016;291(6):2888-2903. doi:10.1074/jbc.M115.684597
142. Ehrt S, Schnappinger D. Mycobacterial survival strategies in the phagosome: Defence against host stresses. *Cell Microbiol*. 2009;11(8):1170-1178. doi:10.1111/j.1462-5822.2009.01335.x
143. Vandal OH, Nathan CF, Ehrt S. Acid resistance in Mycobacterium tuberculosis. *J Bacteriol*. 2009;191(15):4714-4721. doi:10.1128/JB.00305-09
144. Zhai W, Wu F, Zhang Y, Fu Y, Liu Z. The immune escape mechanisms of Mycobacterium Tuberculosis. *Int J Mol Sci*. 2019;20(2). doi:10.3390/ijms20020340
145. Grosz M, Kolter J, Paprotka K, *et al.* Cytoplasmic replication of Staphylococcus aureus upon phagosomal escape triggered by phenol-soluble modulin α. *Cell Microbiol*. 2014;16(4):451-465. doi:10.1111/cmi.12233
146. Moldovan A, Fraunholz MJ. In or out: Phagosomal escape of Staphylococcus aureus. *Cell Microbiol*. 2019;21(3):1-9. doi:10.1111/cmi.12997
147. Guerra FE, Borgogna TR, Patel DM, Sward EW, Voyich JM. Epic immune battles of history: Neutrophils vs. Staphylococcus aureus. *Front Cell Infect Microbiol*. 2017;7(JUN):1-19. doi:10.3389/fcimb.2017.00286
148. Greenlee-Wacker MC, Rigby KM, Kobayashi SD, Porter AR, DeLeo FR, Nauseef WM. Phagocytosis of Staphylococcus aureus by Human Neutrophils Prevents Macrophage Efferocytosis and Induces Programmed Necrosis . *J Immunol*. 2014;192(10):4709-4717. doi:10.4049/jimmunol.1302692
149. Rollin G, Tan X, Tros F, *et al.* Intracellular survival of Staphylococcus aureus in endothelial cells: A matter of growth or persistence. *Front Microbiol*. 2017;8(JUL):1-10. doi:10.3389/fmicb.2017.01354
150. Allwood EM, Devenish RJ, Prescott M, Adler B, Boyce JD. Strategies for intracellular survival of Burkholderia pseudomallei. *Front Microbiol*. 2011;2(AUG):1-19. doi:10.3389/fmicb.2011.00170
151. Srinon V, Chaiwattanarungruengpaisan S, Korbsrisate S, Stevens JM. Burkholderia pseudomalleiBimC Is required for actin-based motility, intracellular survival, and virulence. *Front Cell Infect Microbiol*. 2019;9(MAR):1-9. doi:10.3389/fcimb.2019.00063
152. Stevens MP., Stevens JM., Jeng RL., *et al.* Identification of a bacterial factor required for actin-based motility of Burkholderia pseudomallei. *Mol Microbiol*. 2005;56:40-53.
153. Alvarez M, Casadevall A. Cell-to-cell spread and massive vacuole formation after Cryptococcus neoformans infection of murine macrophages. *BMC Immunol*. 2007;8:1-7. doi:10.1186/1471-2172-8-16
154. Johnston SA, May RC. The human fungal pathogen Cryptococcus neoformans escapes macrophages by a phagosome emptying mechanism that is inhibited by arp2/3 complex- mediated actin polymerisation. *PLoS Pathog*. 2010;6(8):27-28. doi:10.1371/journal.ppat.1001041
155. Guerra CR, Seabra SH, De Souza W, Rozental S. Cryptococcus neoformans is internalized by receptor-mediated or "triggered" phagocytosis, dependent on actin recruitment. *PLoS One*. 2014;9(2):1-10. doi:10.1371/journal.pone.0089250
156. Sethi S, Nanda R, Chakraborty T. Clinical application of volatile organic compound analysis for detecting infectious diseases. *Clin Microbiol Rev*. 2013;26(3):462-475. doi:10.1128/CMR.00020-13
157. Rees CA, Burklund A, Stefanuto PH, Schwartzman JD, Hill JE. Comprehensive volatile metabolic fingerprinting of bacterial and fungal pathogen groups. *J Breath Res.* 2018;12(2). doi:10.1088/1752-7163/aa8f7f
158. Lewis JM, Savage RS, Beeching NJ, Beadsworth MBJ, Feasey N, Covington JA. Identifying volatile metabolite signatures for the diagnosis of bacterial respiratory tract infection using electronic nose technology: A pilot study. *PLoS One*. 2017;12(12):1-10. doi:10.1371/journal.pone.0188879
159. Rodriguez PA, Rothballer M, Chowdhury SP, Nussbaumer T, Gutjahr C, Falter-Braun P. Systems Biology of Plant-Microbiome Interactions. *Mol Plant*. 2019;12(6):804-821. doi:10.1016/j.molp.2019.05.006
160. Barkal LJ, Procknow CL, Álvarez-Garciá YR, *et al.* Microbial volatile communication in human organotypic lung models. *Nat Commun*. 2017;8(1). doi:10.1038/s41467-017-01985-4
161. Schmidt R, Cordovez V, De Boer W, Raaijmakers J, Garbeva P. Volatile affairs in microbial interactions.

ISME J. 2015;9(11):2329-2335. doi:10.1038/ismej.2015.42
162. Schulz-Bohm K, Martín-Sánchez L, Garbeva P. Microbial volatiles: Small molecules with an important role in intra- and inter-kingdom interactions. *Front Microbiol*. 2017;8(DEC):1-10. doi:10.3389/fmicb.2017.02484
163. Bos LDJ, Sterk PJ, Schultz MJ. Volatile Metabolites of Pathogens: A Systematic Review. *PLoS Pathog*. 2013;9(5):1-8. doi:10.1371/journal.ppat.1003311
164. Zhu J, Jiménez-Díaz J, Bean HD, *et al.* Robust detection of P. aeruginosa and S. aureus acute lung infections by secondary electrospray ionization-mass spectrometry (SESI-MS) breathprinting: From initial infection to clearance. *J Breath Res*. 2013;7(3). doi:10.1088/1752-7155/7/3/037106
165. Briard B, Bomme P, Lechner BE, *et al.* Pseudomonas aeruginosa manipulates redox and iron homeostasis of its microbiota partner Aspergillus fumigatus *via* phenazines. *Sci Rep*. 2015;5:1-13. doi:10.1038/srep08220
166. Mowat E, Rajendran R, Williams C, *et al.* Pseudomonas aeruginosa and their small diffusible extracellular molecules inhibit Aspergillus fumigatus biofilm formation. *FEMS Microbiol Lett*. 2010;313(2):96-102. doi:10.1111/j.1574-6968.2010.02130.x
167. Rees CA, Stefanuto PH, Beattie SR, Bultman KM, Cramer RA, Hill JE. Sniffing out the hypoxia volatile metabolic signature of Aspergillus fumigatus. *J Breath Res*. 2017;11(3). doi:10.1088/1752-7163/aa7b3e
168. Shatalin K., Shatalina E., Mironov A., Nudler E. H2S: a universal defense against antibiotics in bacteria. *Science (80-)*. 2011;334(6058):986-990.
169. Bernier SP, Létoffé S, Delepierre M, Ghigo JM. Biogenic ammonia modifies antibiotic resistance at a distance in physically separated bacteria. *Mol Microbiol*. 2011;81(3):705-716. doi:10.1111/j.1365-2958.2011.07724.x
170. Huh D, Matthews BD, Mammoto A, Montoya-Zavala M, Yuan Hsin H, Ingber DE. Reconstituting Organ-Level Lung. *Science (80-)*. 2010;(June):1662-1668. doi:10.1126/science.1188302
171. Hoang ATN, Chen P, Juarez J, *et al.* Dendritic cell functional properties in a three-dimensional tissue model of human lung mucosa. *Am J Physiol - Lung Cell Mol Physiol*. 2012;302(2):226-237. doi:10.1152/ajplung.00059.2011
172. Kesarwani M, Hazan R, He J, *et al.* A quorum sensing regulated small volatile molecule reduces acute virulence and promotes chronic infection phenotypes. *PLoS Pathog*. 2011;7(8). doi:10.1371/journal.ppat.1002192
173. Bandyopadhaya A, Kesarwani M, Que YA, *et al.* The Quorum Sensing Volatile Molecule 2-Amino Acetophenon Modulates Host Immune Responses in a Manner that Promotes Life with Unwanted Guests. *PLoS Pathog*. 2012;8(11). doi:10.1371/journal.ppat.1003024
174. Tzika AA, Constantinou C, Bandyopadhaya A, *et al.* A Small Volatile Bacterial Molecule Triggers Mitochondrial Dysfunction in Murine Skeletal Muscle. *PLoS One*. 2013;8(9). doi:10.1371/journal.pone.0074528
175. Bandyopadhaya A, Constantinou C, Psychogios N, *et al.* Bacterial-excreted small volatile molecule 2-aminoacetophenone induces oxidative stress and apoptosis in murine skeletal muscle. *Int J Mol Med*. 2016;37(4):867-878. doi:10.3892/ijmm.2016.2487
176. Kreja L, Seidel HJ. On the cytotoxicity of some microbial volatile organic compounds as studied in the human lung cell line A549. *Chemosphere*. 2002;49(1):105-110. doi:10.1016/S0045-6535(02)00159-5
177. Nakajima D, Ishii R, Kageyama S, *et al.* Genotoxicity of microbial volatile organic compounds. *J Heal Sci*. 2006;52(2):148-153. doi:10.1248/jhs.52.148
178. Bennett JW, Inamdar AA. Are some fungal volatile organic compounds (VOCs) mycotoxins? *Toxins (Basel)*. 2015;7(9):3785-3804. doi:10.3390/toxins7093785
179. Hiemstra PS, McCray PB, Bals R. The innate immune function of airway epithelial cells in inflammatory lung disease. *Eur Respir J*. 2015;45(4):1150-1162. doi:10.1183/09031936.00141514
180. Whitsett JA, Alenghat T. Respiratory epithelial cells orchestrate pulmonary innate immunity. *Nat Immunol*. 2015;16(1):27-35. doi:10.1038/ni.3045
181. Tam A, Wadsworth S, Dorscheid D, Man S f. P, Sin DD. The airway epithelium: More than just a structural barrier. *Ther Adv Respir Dis*. 2011;5(4):255-273. doi:10.1177/1753465810396539
182. Ohkuni T, Kojima T, Ogasawara N, *et al.* Poly(I:C) reduces expression of JAM-A and induces secretion of IL-8 and TNF-α *via* distinct NF-κB pathways in human nasal epithelial cells. *Toxicol Appl Pharmacol*. 2011;250(1):29-38. doi:10.1016/j.taap.2010.09.023
183. Alekseeva L, Huet D, Féménia F, *et al.* Inducible expression of beta defensins by human respiratory epithelial cells exposed to Aspergillus fumigatus organisms. *BMC Microbiol*. 2009;9. doi:10.1186/1471-2180-9-33

184. Bals R, Wang X, Zasloff M, Wilson JM. The peptide antibiotic LL-37/hCAP-18 is expressed in epithelia of the human lung where it has broad antimicrobial activity at the airway surface. *Proc Natl Acad Sci U S A*. 1998;95(16):9541-9546. doi:10.1073/pnas.95.16.9541
185. Doss M, White MR, Tecle T, Hartshorn KL. Human defensins and LL-37 in mucosal immunity. *J Leukoc Biol*. 2010;87(1):79-92. doi:10.1189/jlb.0609382
186. Hielpos MS, Ferrero MC, Fernández AG, *et al.* CCL20 and beta-defensin 2 production by human lung epithelial cells and macrophages in response to Brucella abortus infection. *PLoS One*. 2015;10(10):1-23. doi:10.1371/journal.pone.0140408
187. Bonfield, Konstan, Berger. BECs and cell lines Statistical analysis. *J Allergy Clin Immunol*. 1999;104(1):72-78.
188. Becker MN, Sauer MS, Muhlebach MS, *et al.* Cytokine Secretion by Cystic Fibrosis Airway Epithelial Cells. *Am J Respir Crit Care Med*. 2004;169(5):645-653. doi:10.1164/rccm.200207-765oc
189. Dubin RF, Robinson SK, Widdicombe JH. Secretion of lactoferrin and lysozyme by cultures of human airway epithelium. *Am J Physiol - Lung Cell Mol Physiol*. 2004;286(4 30-4):750-755. doi:10.1152/ajplung.00326.2003
190. Ganz T. Antimicrobial polypeptides in host defense of the respiratory tract. *J Clin Invest*. 2002;109(6):693-697. doi:10.1172/JCI0215218
191. Vargas Buonfiglio LG, Borcherding JA, Frommelt M, *et al.* Airway surface liquid from smokers promotes bacterial growth and biofilm formation *via* iron-lactoferrin imbalance. *Respir Res*. 2018;19(1):1-11. doi:10.1186/s12931-018-0743-x
192. Doumas S, Kolokotronis A, Stefanopoulos P. Anti-inflammatory and antimicrobial roles of secretory leukocyte protease inhibitor. *Infect Immunity2*. 2005;73(3):1271-1274.
193. Sallenave JM. The role of secretory leukocyte proteinase inhibitor and elafin (elastase-specific inhibitor/skin-derived antileukoprotease) as alarm antiproteinases in inflammatory lung disease. *Respir Res*. 2000;1(2):87-92. doi:10.1186/rr18
194. Buckley CD, Pilling D, Lord JM, Akbar AN, Scheel-Toellner D, Salmon M. Fibroblasts regulate the switch from acute resolving to chronic persistent inflammation. *Trends Immunol*. 2001;22(4):199-204. doi:10.1016/S1471-4906(01)01863-4
195. Vancheri C, Mastruzzo C, Tomaselli V, *et al.* Normal human lung fibroblasts differently modulate interleukin-10 and interleukin-12 production by monocytes: Implications for an altered immune response in pulmonary chronic inflammation. *Am J Respir Cell Mol Biol*. 2001;25(5):592-599. doi:10.1165/ajrcmb.25.5.4609
196. Smith RS, Smith TJ, Blieden TM, Phipps RP. Fibroblasts as sentinel cells. Synthesis of chemokines and regulation of inflammation. *Am J Pathol*. 1997;151(2):317-322.
197. Smith RS, Fedyk ER, Springer TA, Mukaida N, Iglewski BH, Phipps RP. IL-8 Production in Human Lung Fibroblasts and Epithelial Cells Activated by the Pseudomonas Autoinducer N -3-Oxododecanoyl Homoserine Lactone Is Transcriptionally Regulated by NF-κB and Activator Protein-2 . *J Immunol*. 2001;167(1):366-374. doi:10.4049/jimmunol.167.1.366
198. Nichols D, Chmiel J, Berger M. Chronic inflammation in the cystic fibrosis lung: Alterations in inter- and intracellular signaling. *Clin Rev Allergy Immunol*. 2008;34(2):146-162. doi:10.1007/s12016-007-8039-9
199. Sempowski GD, Chess PR, Phipps RP. CD40 is a functional activation antigen and B7-independent T cell costimulatory molecule on normal human lung fibroblasts. *J Immunol*. 1997;158(10):4670-4677. http://www.ncbi.nlm.nih.gov/pubmed/9144479.
200. Kaufman J, Sime PJ, Phipps RP. Expression of CD154 (CD40 Ligand) by Human Lung Fibroblasts: Differential Regulation by IFN-γ and IL-13, and Implications for Fibrosis. *J Immunol*. 2004;172(3):1862-1871. doi:10.4049/jimmunol.172.3.1862
201. Lyczak JB, Cannon CL, Pier GB. Lung Infections Associated Cystic Firosis. *Clin Microbiol Rev*. 2002;15(2):194-222. doi:10.1128/CMR.15.2.194
202. Courtney JM, Bradley J, Mccaughan J, *et al.* Predictors of mortality in adults with cystic fibrosis. *Pediatr Pulmonol*. 2007;42(6):525-532. doi:10.1002/ppul.20619
203. Tsui LC. The cystic fibrosis transmembrane conductance regulator gene. *Am J Respir Crit Care Med*. 1995;151(3 II SUPPL.):547-553. doi:10.1164/ajrccm/151.3_pt_2.s47
204. Vandeplassche E, Tavernier S, Coenye T, Crabbé A. Influence of the lung microbiome on antibiotic susceptibility of cystic fibrosis pathogens. *Eur Respir Rev*. 2019;28(152). doi:10.1183/16000617.0041-2019
205. Mannino DM. COPD. *Chest*. 2002;121(5):121S-126S. doi:10.1378/chest.121.5_suppl.121S
206. Sethi S. Infection as a comorbidity of COPD. *Eur Respir J*. 2010;35(6):1209-1215.

doi:10.1183/09031936.00081409
207. Pauwels R, Calverly P, Buist AS, *et al.* COPD exacerbations: The importance of a standard definition. *Respir Med*. 2004;98(2):99-107. doi:10.1016/j.rmed.2003.09.001
208. Sethi S, Sethi R, Eschberger K, *et al.* Airway bacterial concentrations and exacerbations of chronic obstructive pulmonary disease. *Am J Respir Crit Care Med*. 2007;176(4):356-361. doi:10.1164/rccm.200703-417OC
209. Sethi S, Evans N, Grant BJB, Murphy TF. New strains of bacteria and exacerbations of chronic obstructive pulmonary disease. *N Engl J Med*. 2002;347(7):465-471. doi:10.1056/NEJMoa012561
210. Stucki AO, Stucki JD, Hall SRR, *et al.* A lung-on-a-chip array with an integrated bio-inspired respiration mechanism. *Lab Chip*. 2015;15(5):1302-1310. doi:10.1039/c4lc01252f
211. Mariappan V, Vellasamy KM, Thimma JS, Hashim OH, Vadivelu J. Identification of immunogenic proteins from Burkholderia cepacia secretome using proteomic analysis. *Vaccine*. 2010;28(5):1318-1324. doi:10.1016/j.vaccine.2009.11.027
212. Zheng J, Ren X, Wei C, *et al.* Analysis of the secretome and identification of novel constituents from culture filtrate of bacillus calmette-guérin using high-resolution mass spectrometry. *Mol Cell Proteomics*. 2013;12(8):2081-2095. doi:10.1074/mcp.M113.027318
213. Zhao Y, Jamaluddin M, Zhang Y, *et al.* Systematic Analysis of Cell-Type Differences in the Epithelial Secretome Reveals Insights into the Pathogenesis of Respiratory Syncytial Virus–Induced Lower Respiratory Tract Infections. *J Immunol*. 2017;198(8):3345-3364. doi:10.4049/jimmunol.1601291
214. Miller AJ, Spence JR. In vitro models to study human lung development, disease and homeostasis. *Physiology*. 2017;32(3):246-260. doi:10.1152/physiol.00041.2016
215. Shambat SM, Chen P, Hoang ATN, *et al.* Modelling staphylococcal pneumonia in a human 3D lung tissue model system delineates toxin-mediated pathology. *DMM Dis Model Mech*. 2015;8(11):1413-1425. doi:10.1242/dmm.021923
216. Barkal LJ, Berthier E, Theberge AB, Keller NP, Beebe DJ. Multikingdom microscale models. *PLoS Pathog*. 2017;13(8):6-11. doi:10.1371/journal.ppat.1006424
217. Hsia CCW, Hyde DM, Weibel EE. Lung structure and the intrinsic challenges of gas exchange. *Compr Physiol*. 2016;6(2).
218. Voynow JA, Mengr BKR. Mucins, mucus, and sputum. *Chest*. 2009;135(2):505-512. doi:10.1378/chest.08-0412
219. Ma J, Rubin BK, Voynow JA. Mucins, Mucus, and Goblet Cells. *Chest*. 2018;154(1):169-176. doi:10.1016/j.chest.2017.11.008
220. Shi W, Bellusci S, Warburton D. Lung development and adult lung diseases. *Chest*. 2007;132(2):651-656. doi:10.1378/chest.06-2663
221. Torrelles JB, Schlesinger LS. Integrating Lung Physiology, Immunology, and Tuberculosis. *Trends Microbiol*. 2017;25(8):688-697. doi:10.1016/j.tim.2017.03.007
222. Garg N, Wang M, Hyde E, *et al.* Three-Dimensional Microbiome and Metabolome Cartography of a Diseased Human Lung. *Cell Host Microbe*. 2017;22(5):705-716.e4. doi:10.1016/j.chom.2017.10.001
223. Bhatia SN, Ingber DE. Microfluidic organs-on-chips. *Nat Biotechnol*. 2014;32(8):760-772. doi:10.1038/nbt.2989
224. Zhan L, Tang J, Sun M, Qin C. Animal models for tuberculosis in translational and precision medicine. *Front Microbiol*. 2017;8(MAY). doi:10.3389/fmicb.2017.00717
225. Perlman RL. Mouse Models of Human Disease: An Evolutionary Perspective. *Evol Med Public Heal*. 2016:eow014. doi:10.1093/emph/eow014
226. Masopust D, Sivula CP, Jameson SC. Of Mice, Dirty Mice, and Men: Using Mice To Understand Human Immunology. *J Immunol*. 2017;199(2):383-388. doi:10.4049/jimmunol.1700453
227. Foreman TW, Mehra S, Lackner AA, Kaushal D. Translational research in the nonhuman primate model of tuberculosis. *ILAR J*. 2017;58(2):151-159. doi:10.1093/ilar/ilx015
228. Kaushal D, Mehra S, Didier PJ, Lackner AA. The non-human primate model of tuberculosis. *J Med Primatol*. 2012;41(3):191-201. doi:10.1111/j.1600-0684.2012.00536.x
229. Scanga CA, Flynn JL. Modeling tuberculosis in nonhuman primates. *Cold Spring Harb Perspect Med*. 2014;4(12). doi:10.1101/cshperspect.a018564
230. Yong KSM, Her Z, Chen Q. Humanized Mice as Unique Tools for Human-Specific Studies. *Arch Immunol Ther Exp (Warsz)*. 2018;66(4):245-266. doi:10.1007/s00005-018-0506-x
231. Halldorsson S, Asgrimsson V, Axelsson I, *et al.* Differentiation potential of a basal epithelial cell line established from human bronchial explant. *Vitr Cell Dev Biol - Anim*. 2007;43(8-9):283-289.

doi:10.1007/s11626-007-9050-4
232. Rayner RE, Makena P, Prasad GL, Cormet-Boyaka E. Optimization of Normal Human Bronchial Epithelial (NHBE) Cell 3D Cultures for in vitro Lung Model Studies. *Sci Rep*. 2019;9(1):2-11. doi:10.1038/s41598-018-36735-z
233. Benam KH, Villenave R, Lucchesi C, *et al.* Small airway-on-a-chip enables analysis of human lung inflammation and drug responses in vitro. *Nat Methods*. 2016;13(2):151-157. doi:10.1038/nmeth.3697
234. Benam KH, Novak R, Nawroth J, *et al.* Matched-Comparative Modeling of Normal and Diseased Human Airway Responses Using a Microengineered Breathing Lung Chip. *Cell Syst*. 2016;3(5):456-466.e4. doi:10.1016/j.cels.2016.10.003
235. Felder M, Trueeb B, Stucki AO, *et al.* Impaired wound healing of alveolar lung epithelial cells in a breathing lung-on-a-chip. *Front Bioeng Biotechnol*. 2019;7(JAN):1-5. doi:10.3389/fbioe.2019.00003
236. Mermoud Y, Felder M, Stucki JD, Stucki AO, Guenat OT. Microimpedance tomography system to monitor cell activity and membrane movements in a breathing lung-on-chip. *Sensors Actuators, B Chem*. 2018;255:3647-3653. doi:10.1016/j.snb.2017.09.192
237. Parasa VR, Rahman MJ, Hoang ATN, Svensson M, Brighenti S, Lerm M. Modeling Mycobacterium tuberculosis early granuloma formation in experimental human lung tissue. *DMM Dis Model Mech*. 2014;7(2):281-288. doi:10.1242/dmm.013854
238. Humayun M, Chow CW, Young EWK. Microfluidic lung airway-on-a-chip with arrayable suspended gels for studying epithelial and smooth muscle cell interactions. *Lab Chip*. 2018;18(9):1298-1309. doi:10.1039/c7lc01357d
239. Wiszniewski L, Jornot L, Dudez T, *et al.* Long-term cultures of polarized airway epithelial cells from patients with cystic fibrosis. *Am J Respir Cell Mol Biol*. 2006;34(1):39-48. doi:10.1165/rcmb.2005-0161OC
240. Paolicelli G, Luca A De, Jose SS, *et al.* Using lung organoids to investigation epithelial barrier complexity and IL-7 signaling during repiratory infection. *Front Immunol*. 2019;10(FEB):1-6. doi:10.3389/fimmu.2019.00323
241. Barkauskas CE, Chung MI, Fioret B, Gao X, Katsura H, Hogan BLM. Lung organoids: Current uses and future promise. *Dev*. 2017;144(6):986-997. doi:10.1242/dev.140103
242. Gkatzis K, Taghizadeh S, Huh D, Stainier DYR, Bellusci S. Use of three-dimensional organoids and lung-on-a-chip methods to study lung development, regeneration and disease. *Eur Respir J*. 2018;52(5). doi:10.1183/13993003.00876-2018
243. Sachs N, Papaspyropoulos A, Zomer-van Ommen DD, *et al.* Long-term expanding human airway organoids for disease modeling. *EMBO J*. 2019;38(4):1-20. doi:10.15252/embj.2018100300
244. Pampaloni F, Reynaud EG, Stelzer EHK. The third dimension bridges the gap between cell culture and live tissue. *Nat Rev Mol Cell Biol*. 2007;8(10):839-845. doi:10.1038/nrm2236
245. Ravi M, Paramesh V, Kaviya SR, Anuradha E, Paul Solomon FD. 3D cell culture systems: Advantages and applications. *J Cell Physiol*. 2015;230(1):16-26. doi:10.1002/jcp.24683
246. Barrila J, Radtke AL, Crabbé A, *et al.* Organotypic 3D cell culture models: Using the rotating wall vessel to study hostâ€"pathogen interactions. *Nat Rev Microbiol*. 2010;8(11):791-801. doi:10.1038/nrmicro2423
247. Faber SC, McCullough SD. Through the Looking Glass: In Vitro Models for Inhalation Toxicology and Interindividual Variability in the Airway. *Appl Vitr Toxicol*. 2018;4(2):115-128. doi:10.1089/aivt.2018.0002
248. Ren H, Birch NP, Suresh V. An optimised human cell culture model for alveolar epithelial transport. *PLoS One*. 2016;11(10):1-22. doi:10.1371/journal.pone.0165225
249. Halldorsson S, Gudjonsson T, Gottfredsson M, Singh PK, Gudmundsson GH, Baldursson O. Azithromycin maintains airway epithelial integrity during Pseudomonas aeruginosa infection. *Am J Respir Cell Mol Biol*. 2010;42(1):62-68. doi:10.1165/rcmb.2008-0357OC
250. Yonker LM, Mou H, Chu KK, *et al.* Development of a Primary Human Co-Culture Model of Inflamed Airway Mucosa. *Sci Rep*. 2017;7(1):1-12. doi:10.1038/s41598-017-08567-w
251. Hermanns MI, Unger RE, Kehe K, Peters K, Kirkpatrick CJ. Lung epithelial cell lines in coculture with human pulmonary microvascular endothelial cells: Development of an alveolo-capillary barrier in vitro. *Lab Investig*. 2004;84(6):736-752. doi:10.1038/labinvest.3700081
252. Imundo L, Barasch J, Prince A, Al-awqatit Q. Cystic fibrosis epithelial cells have. *Spring*. 1995;92(March):3019-3023.
253. Duff C, Murphy PG, Callaghan M, McClean S. Differences in invasion and translocation of Burkholderia cepacia complex species in polarised lung epithelial cells in vitro. *Microb Pathog*. 2006;41(4-5):183-192. doi:10.1016/j.micpath.2006.07.005
254. Bhowmick R, Derakhshan T, Liang Y, Ritchey J, Liu L, Gappa-Fahlenkamp H. A Three-Dimensional

Human Tissue-Engineered Lung Model to Study Influenza A Infection. *Tissue Eng - Part A*. 2018;24(19-20):1468-1480. doi:10.1089/ten.tea.2017.0449
255. Keenan TM, Folch A. Biomolecular gradients in cell culture systems. *Lab Chip*. 2007;8(1):34-57. doi:10.1039/b711887b
256. Lauffenburger DA, Zigmond SH. Chemotactic factor concentration gradients in chemotaxis assay systems. *J Immunol Methods*. 1981;40(1):45-60. doi:10.1016/0022-1759(81)90079-X
257. Huh D, Fujioka H, Tung YC, *et al.* Acoustically detectable cellular-level lung injury induced by fluid mechanical stresses in microfluidic airway systems. *Proc Natl Acad Sci U S A*. 2007;104(48):18886-18891. doi:10.1073/pnas.0610868104
258. Yu J, Berthier E, Craig A, *et al*. Reconfigurable open microfluidics for studying the spatiotemporal dynamics of paracrine signalling. *Nat Biomed Eng*. 2019;3(10):830-841. doi:10.1038/s41551-019-0421-4
259. Sackmann EK, Fulton AL, Beebe DJ. The present and future role of microfluidics in biomedical research. *Nature*. 2014;507(7491):181-189. doi:10.1038/nature13118
260. Kimura H, Sakai Y, Fujii T. Organ/body-on-a-chip based on microfluidic technology for drug discovery. *Drug Metab Pharmacokinet*. 2018;33(1):43-48. doi:10.1016/j.dmpk.2017.11.003
261. Huh D, Leslie DC, Matthews BD, *et al.* A human disease model of drug toxicity-induced pulmonary edema in a lung-on-a-chip microdevice. *Sci Transl Med*. 2012;4(159):159ra147.

Chapter 5. Cell-Targeting Beads to Probe the Cellular Signaling Microenvironment

Reproduced in part with permission from van Neel, T.L.*; Berry, S.B.*; Berthier, E.; Theberge, A.B. "Localized cell-surface sampling of secreted factors using cell-targeting beads". In preparation.

*denotes co-authorship

Abstract:

Intercellular communication through the secretion of soluble factors plays a vital role in a wide range of biological processes (*e.g.*, homeostasis, immune response), yet identification and quantification of many of these factors can be challenging due to their degradation or sequestration in cell culture media prior to analysis. Here, we present a customizable bead-based system capable of simultaneously binding to live cells (through antibody-mediated cell-tethering) and capturing cell-secreted molecules. Our functionalized beads capture secreted molecules (*e.g.*, hepatocyte growth factor secreted by fibroblasts) that are diminished when sampled *via* traditional supernatant analysis techniques ($p < 0.05$), effectively rescuing reduced signal in the presence of neutralizing components in the cell culture media. Our system enables capture and analysis of molecules integral to chemical communication that would otherwise be markedly decreased prior to analysis.

5.1 Introduction

Chemical signaling events involving cell-secreted soluble factors (*e.g.*, growth factors, cytokines) play a vital role in the induction of cellular functions and larger systematic biological processes including immune response, maintenance of homeostasis, and cellular differentiation.[1] However, detecting these molecules to decipher this complex signaling landscape is often hindered through the degradation, sequestration, or neutralization of important signaling molecules by extracellular factors such as enzymes or receptors.[2,3] The elimination of these short-lived soluble factors from a cellular microenvironment is an important component of chemical signaling processes, yet their absence leads to an incomplete snapshot of the signaling microenvironment, as these transient factors cannot be easily analyzed. Identification and quantification of these key short-lived factors in the context of their localized signaling milieu can

provide important insight into the signaling mechanisms that mediate biological processes within complex *in vivo* and *in vitro* systems.[4,5]

Various analytical and quantification methods, such as mass spectrometry and enzyme-linked immunosorbent assays (ELISA), have been developed that examine cell culture supernatants (*i.e.*, conditioned media) or biological fluids (*e.g.*, serum, urine) to provide important information on the makeup of cellular secretion profiles.[6] However, these methods often rely on sampling processes wherein important effector molecules may be degraded, sequestered, or converted on time scales faster than those required for sample preparation and analysis, resulting in diminished signal; further, these readouts are typically used as end-point analyses that lack the temporal resolution provided by *in situ* methods and analyses.[7] More targeted approaches that integrate sample collection and readout, such as compartmentalized microfluidic cell culture platforms for *in situ* bead-based assays[8,9], small-volume cell-encapsulation and -sensor systems[10-13], and enzyme-linked immunosorbent spot (ELISpot) assays[14,15], address the limitations posed by traditional techniques and enable precise *in situ* analysis of culture systems at flexible timepoints throughout the experiment. These integrated culture and analysis platforms allow users to probe specific phenomena using systems with excellent spatial and temporal detection resolution, and we sought to add to these analytical capabilities through the creation of a transferable and easily-deployed system compatible with virtually all culture systems, removing the need for specialized platforms or devices.

Bead-based technologies have been widely used for both the analysis of soluble factors within biological samples (*e.g.*, bead-based ELISA) and to selectively capture and analyze cells from a mixed culture (*e.g.*, magnetic bead-based cell isolation)[16-18]; however, to our knowledge, these two functionalities have yet to be combined to examine the production of transient soluble factors and the origin of those factors (Figure 5.1). Here, we introduce a customized bead-based approach to enable capture of short lived or unavailable compounds from within existing cell culture systems that can then be coupled with downstream analytical methods such as immunoassays (Figure 5.1). Our platform consists of a dual-functionalized (DF) magnetic bead with two distinct antibodies, enabling simultaneous cell-

binding and signal capture (Figure 5.1 Bii). Through cell tethering, our DF beads can target a specific cell type *via* cell-specific surface markers, as well as capture cell-secreted signals before they enter the bulk solution, where they may be sequestered or degraded. Here, we demonstrate that our DF beads capture a cell-secreted signal (hepatocyte growth factor, HGF) localized near the cell surface from live fibroblast cultures in the presence of a neutralization factor; in contrast HGF levels are markedly diminished when collected through traditional supernatant analysis. We envision these dual-functionalized beads being employed in a wide range of mono- and multi-cultures, enabling researchers to easily "listen" to cellular communication between different cell populations *in situ* without needing to modify their culture protocols or setup.

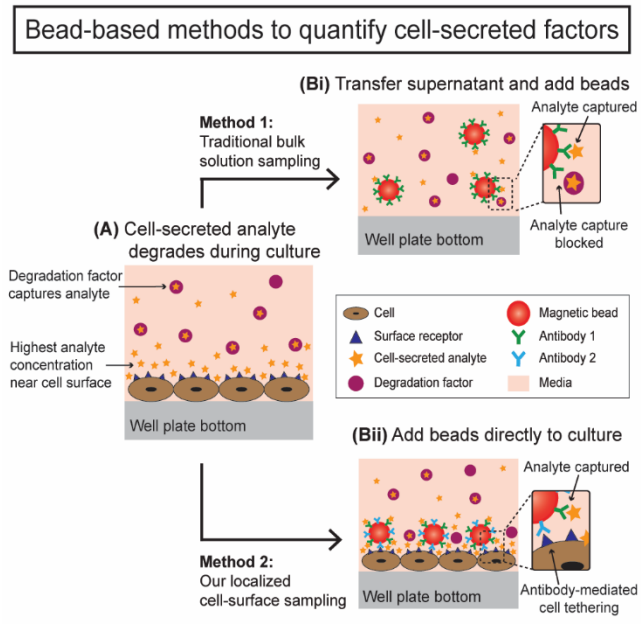

Figure 5.1: Bead-based approaches to quantifying cell-secreted factors. (A) Cells secrete soluble factors for communication, with the highest concentration immediately after secretion being near the cell surface. (Bi) Traditional methods transfer the cell culture supernatant to another well plate and use beads for bulk solution analyte sampling while (Bii) our new approach utilizes cell-targeting beads *in situ* for analyte sampling.

5.2 Development and validation of *in situ* sampling bead system

To probe the myriad of diverse environments where intercellular signaling occurs, an adaptable platform capable of being deployed across a wide range of signaling landscapes is required. Herein, we present a dual-functionalized (DF) bead system that binds to cells within a live *in vitro* cell culture system to analyze a secreted factor of interest in the presence and absence of a factor that may degrade or neutralize, or sequester the factor of interest. As a proof-of-concept model, we selected neonatal normal human dermal fibroblasts (NHDFn) expressing surface marker CD90 (Figure D1) and secreting hepatocyte growth factor (HGF) as our cellular and molecular target,

respectively. HGF is a vital factor in multiple biological processes, including organ development, liver repair, and cancer progression, underscoring the importance of fibroblast-driven chemical communication in a range of biological settings.[19] We designed and created dual-functionalized MagPlex beads covalently bound with antibodies against CD90 (anti-CD90) and HGF (anti-HGF) to target the cell surface marker and secreted factor, respectively (Figure D2).[20] To validate that the DF beads can successfully capture HGF at biologically relevant concentrations while simultaneously binding to the cell surface, we conducted two independent cell-binding and analyte capture assays (Figure 5.2, D3-5).

First, we performed a standard sandwich immunoassay using our DF beads (anti-CD90 and anti-HGF) and commercially available mono-functionalized (MF, anti-HGF only) beads with spiked HGF to compare HGF detection capabilities using the DF beads and MF beads when used according to traditional protocols (*i.e.*, supernatant analysis). Both DF and MF beads successfully captured spiked HGF at a range of concentrations, enabling fitting to a five-parameter logistic (5PL) calibration curve as recommended by the manufacturer[20] and supporting the use of the DF beads as a tool for capturing and measuring secreted factors from cells (Figure S5). We observed different limits of detection (LODs) between the two beads consistent with the different bead functionalization: DF beads, 104.25 pg/mL; MF beads, 34.87 pg/mL (Figure D5). We also observed that DF beads had a 17-36% lower total fluorescent signal than the MF beads (Figure D5). This is expected, as the number of available binding sites on the surface of the DF beads is less than on the MF beads due to the presence of anti-CD90 antibodies, thereby decreasing the total number of fluorescent detection antibodies that will bind to HGF on the surface of the DF bead.

Second, we performed a cell-binding assay wherein we incubated DF beads with CD90-expressing NHDFn cells (Figure 5.2) and quantified their ability to remain bound to the cell surface after multiple wash steps (Figure D3). Beads were added directly to a 96-well plate culture of NHDFn cells and incubated for 2 hours; after incubation, the culture was rinsed three times to remove unbound or nonspecifically-bound beads. The remaining beads were then imaged and counted to quantify the ability of the DF beads to bind $CD90^+$ cells (*i.e.*, NHDFn) (Figure 5.2, D3-D4). After washing, 74% of the beads were retained, suggesting successful CD90-mediated cell binding (Figure 5.2 and D3). Further

optimization of the bead functionalities (*i.e.*, analyte capture and cell binding) can be accomplished by adjusting the ratio of antibodies on the surface, as well as through modulation of the specific biological system of interest to increase expression of cell-binding markers or secretion of soluble factors.

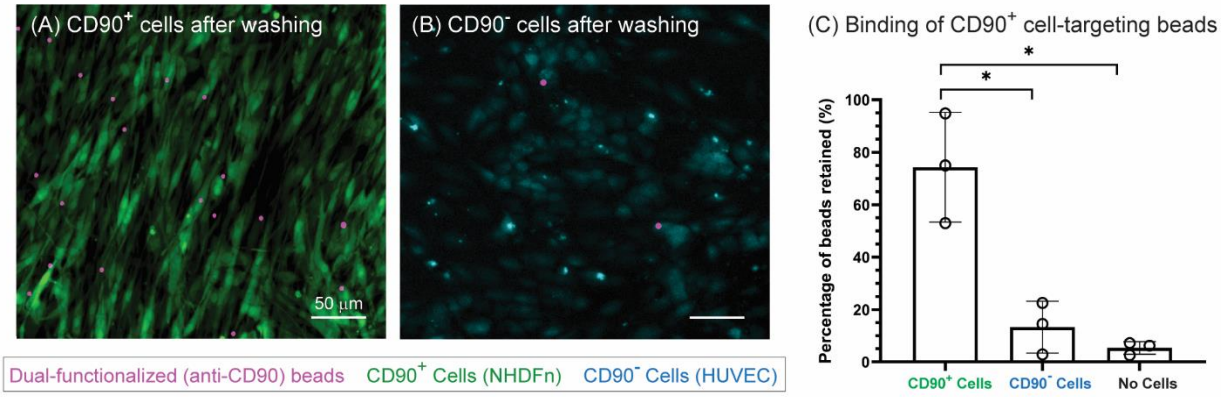

Figure 5.2: Dual-functionalized (DF) beads (functionalized with anti-CD90 and anti-HGF) target $CD90^+$ cells (NHDFn). (A and B) Representative images of $CD90^+$ cells stained with CellTracker Green (green) and $CD90^-$ cells stained with CellTracker Blue (blue); cells were seeded at a density of $2.6x10^4$ cells/mL, cultured for 3 days, and incubated with DF beads (pink) for 2 h. Images of wells were taken after washing to determine successful bead-binding to the cell surface receptor CD90. (A) $CD90^+$ cells show an increased bead retention compared to (B) $CD90^-$ cells. (C) An average of 74% of DF beads were retained when incubated with $CD90^+$ cells, significantly higher bead retention than for $CD90^-$ cells or no cells (empty well). Some nonspecific binding was observed for beads placed in an empty well (5% of beads retained). Bar graphs represent mean ± SD of n=3 independent experiments. Brown-Forsynthe and Welch ANOVA tests were used followed by Dunnett's T3 test. * $p < 0.05$.

5.3 Application of dual-functionalized beads for resuscitation of sequestered signals

To demonstrate one utility of our DF bead system, we created a model NHDFn culture system where we test the ability of the beads to capture HGF signal before the signal is diminished in the bulk solution through neutralization with free anti-HGF antibodies; we hypothesized that this resuscitation of HGF signal would be achieved through binding of the DF beads to the cell surface so that the beads can capture HGF as it is being secreted from the cell. To test this hypothesis, we cultured NHDFn cells with our DF beads and free anti-HGF antibodies so that secreted HGF could bind to either the beads (and be detected) or the free anti-HGF (and be neutralized); after a 2-hour incubation, the supernatant was collected and the culture was washed to remove any unbound beads or remaining free anti-HGF (Figure 5.3). The cells were then lysed to release the beads, which were subsequently washed and analyzed using

standard Luminex assay protocols.[20] In parallel, we analyzed the HGF signal captured by MF beads according to the manufacturer's protocol (*i.e.*, traditional cell culture supernatant sampling) (Figure 5.3). Following traditional cell culture supernatant sampling protocols, we observed a significant decrease ($p < 0.05$) in HGF quantification as a result of the presence of free anti-HGF in the cell culture media in comparison to controls without free anti-HGF (Figure 5.3 Bi), suggesting that a sequestering factor (such as free anti-HGF) is able to reduce the secreted HGF available for quantification in bulk media. In contrast, under identical culture conditions, our dual-functionalized beads deployed on the cell surface restored HGF signal to levels comparable to those found in the absence of free anti-HGF (Figure 5.3 Bii), suggesting that the DF beads are able to capture signal prior to its reduction in the bulk supernatant.

As a control, to verify that the proximity of the DF to the cell promotes improved HGF capture, and to eliminate any artifacts associated with cell-bead-binding and the lysis step employed in our localized cell-surface method, we cultured NHDFn cells in close proximity to (10 μm) and at a distance (1.3 mm) from the beads in the presence and absence of free anti-HGF using a Transwell insert setup (Figure D6 A and B). We found that the beads captured increased levels of HGF (both in the presence and absence of free anti-HGF) when in close proximity to the cells when compared to at a distance. This finding supports that the increased signal capture capabilities of our localized cell-surface sampling method are due to the proximal location of the DF beads on the cell surface (Figure 5.3, D6 C). While it is likely that MF beads would provide a similar signal if allowed to settle nonspecifically on the cell surface, the ability of the dual-functionalized beads to specifically bind to cell types of interest enables beads to target the desired cell and ensure the cellular origin of the secreted signal (Figure D4). Further, to validate that the observed HGF signal in our localized cell-surface sampling method (Figure 5.3 Bii) was not simply intracellular HGF released during the lysis steps and that the lysis buffer did not interfere with or disrupt HGF-bead binding, we sought to separately quantify HGF concentrations in samples containing lysis buffer. Utilizing the DF beads, we quantified the concentration of HGF present in the cell lysate (cells had been rinsed to remove extracellular HGF prior to lysis) and observed significantly less HGF signal in cell lysate when compared to the signals captured from localized cell-surface sampling (Figure D7), indicating

that the majority of the HGF captured using our localized cell-surface sampling method is secreted from the cell. Further, in future work, we will develop gentler methods to remove the bead from the cell surface without lysing the cell. In summary, our DF beads can selectively bind to the surface of a cell and capture signal directly secreted from the cell before the secreted factor is sequestered and lost in bulk solution.

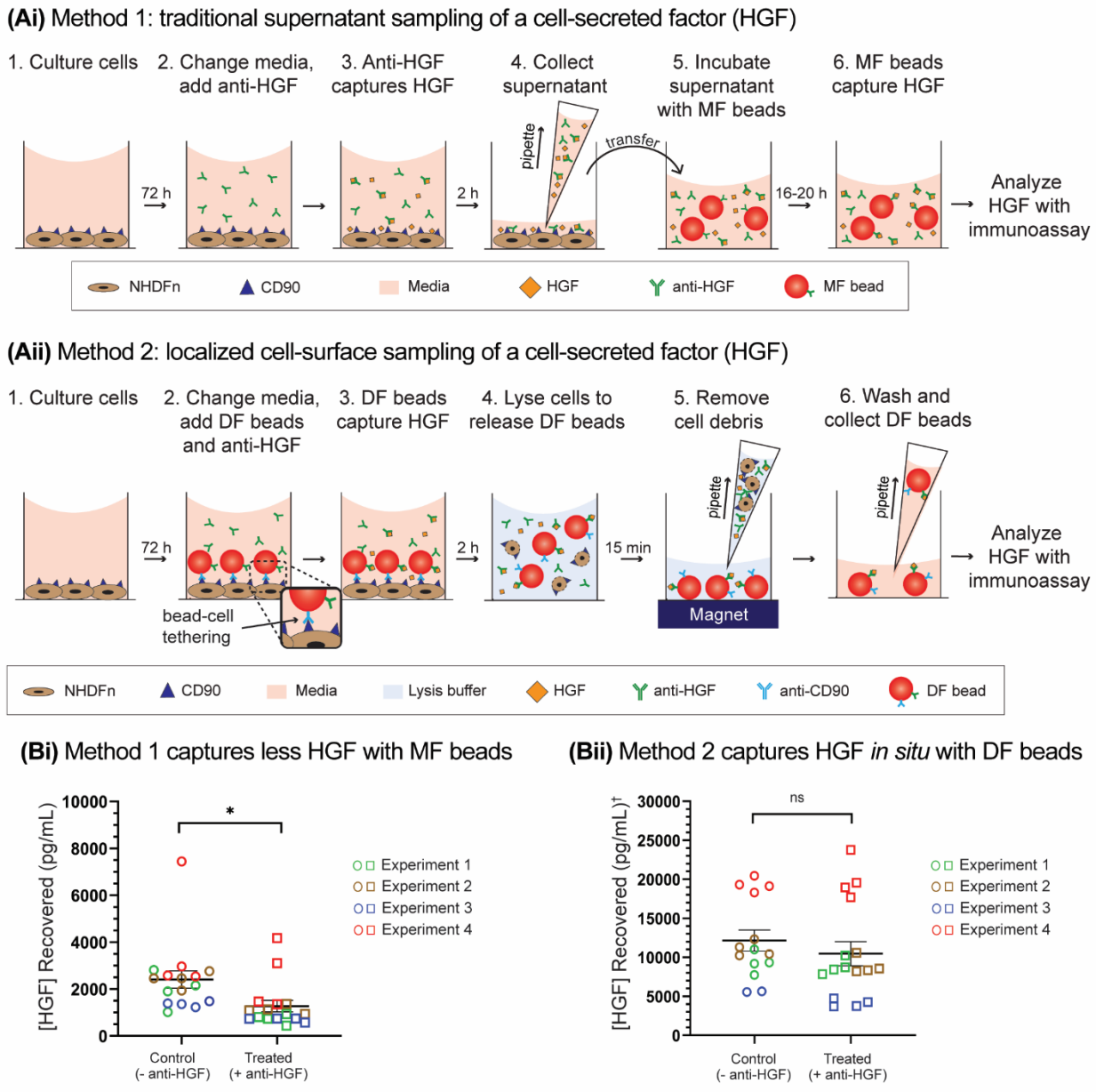

Figure 5.3: Localized cell-surface sampling recovers HGF signal in the presence of a neutralizing factor. Schematics showing workflow of (Ai) traditional supernatant sampling and (Aii) localized cell-surface sampling of a cell-secreted factor. Mono-functionalized (MF) beads (functionalized with anti-HGF) were used for supernatant sampling while dual-functionalized (DF) beads (functionalized with anti-HGF and anti-CD90) were used for *in situ* sampling. (Ai) MF beads are added to supernatant samples collected from cell cultures after 2 h incubation. (Aii) DF beads are added to directly to cultures for a 2 h sampling period.

(Bi) Supernatant analysis shows a decrease in recovered HGF when cells are incubated with free anti-HGF whereas (Bii) localized cell-surface sampling with DF beads shows no change in recovered HGF since beads capture HGF before neutralization by free anti-HGF. Experiments were performed in the absence (-) or presence (+) of free anti-HGF and are represented as circles or squares, respectively; each point represents an averaged technical replicate (supernatant) or culture replicate (*in situ*). († HGF recovered using DF beads is captured at the surface of the cell, rather than the bulk, leading to increased overall HGF capture. Traditional immunoassay calculations use bulk solution sampling; here, we are sampling a smaller volume on the cell surface. Thus, the absolute values in (Bii) should not be directly compared to the absolute values in (Bi), but rather the trend between the two conditions.) Unpaired Student's t-test. * $p = 0.016$; ns $p = 0.428$.

5.4 Conclusion

In this work, we present a new bead-based system that enables *in situ* capture of a secreted molecule (HGF) in the presence of a known neutralization factor (anti-HGF); through targeted cell-tethering of DF beads, we can capture secreted HGF as it is released from the cell, rescuing signal that is lost in traditional supernatant analysis due to HGF binding to free anti-HGF in the bulk solution (Figure 5.3). MagPlex beads were chosen to enable future development and multiplexing of different analytes and cell types, as they are commercially available and compatible with a wide range of antibodies, allowing easy adaptation of this technology without the need for specialized fabrication or experimental protocols.[20] Further development of this platform will focus on selective bead detachment methods and optimizing antibody ratios to improve binding capabilities and permit continuation of cultures after bead detachment. Future application of this technology includes deploying this method in complex biological system containing multiple cell types (*e.g.*, mixed cocultures of mammalian cells, multikingdom culture containing microbial and mammalian cells, and *ex vivo* tissue slices) to demonstrate our method's potential to selectively target a specific cell type in a complex environment containing multiple cell types.

5.5 Materials and Methods

Reagents and materials

Luminex kits (Product # HAGP1MAP-12K) containing wash buffer, assay buffer, secondary detection antibody, mono-functionalized beads, recombinant human hepatocyte growth factor (HGF), and streptavidin-R-phycoerythrin conjugate (SAPE) were purchased from EMD Millipore (Burlington, MA)

and used for anti-HGF/HGF Assay experiments (details below). Clear tissue culture treated (TCT) 96-, 24-, and 12-well plates (Corning #3596, #3526, and #3515, respectively) and black TCT 96-well plates (Corning #3603) were purchased from Corning (Corning, NY). Falcon Transwell 24-well plate inserts (Corning #353104) were purchased from Fisher Scientific (Hampton, NH). Antibody coupling kits (Product #40-50016) were purchased from Luminex Corporation (Austin, TX).

Cell Culture

Normal Human Dermal Fibroblast neo-natal cells (NHDFn) (ATCC, Manassas, VA) were cultured, passaged, and seeded in fibroblast basal medium supplemented with a low-serum growth kit (ATCC, #PCS-201-030 and #PCS-201-041) (fibroblast media). 24 hours after seeding cells in well plates or Transwell inserts, media was replaced with Endothelial Cell Growth Medium-2 BulletKit (EGM-2) (Lonza, Basel, Switzerland) supplemented with 10% heat-inactivated (HI) fetal bovine serum (FBS); media was changed daily. NHDFn passage numbers ranged from 6-8 for experiments. Human Umbilical Vein Endothelial cells (HUVEC) (Lonza, Basel, Switzerland, #C2517A) were cultured, passaged, and seeded in EGM-2 media. HUVEC passage numbers ranged from 3-5 for experiments.

CD90 Expression by Normal Human Dermal Fibroblast neo-natal Cells (NHDFn)

Expression of CD90 by NHDFn cells was validated through standard immunocytochemistry techniques. NHDFn cells were fixed for 10 minutes with 4% paraformaldehyde, permeabilized with 0.2% Triton X-100, and then blocked with 3% bovine serum albumin (BSA). After blocking, primary anti-CD90 monoclonal antibody (clone AF-9, Abcam, #ab23894) (1:50 dilution) was added and incubated overnight at 4°C; goat anti-mouse secondary polyclonal antibody conjugated with Alexa-488 (1:200 dilution) (Jackson ImmunoResearch Laboratories Inc., #115-545-166) was then allowed to incubate for 1 hour at room temperature. After washing, DAPI (ThermoFisher, #D1306) (1:200 dilution) was incubated for 5 minutes at RT before washing and imaging (Figure D1). HUVECs were simultaneously cultured as described above to serve as a negative control. HUVECs were stained with CellTracker Blue (ThermoFisher, #C2110) for 1 hour before seeding according to the manufacturer's protocols. Fixing and staining protocols outlined above were followed before imaging (Figure D1).

Bead Functionalization

MagPlex microspheres (region 34) were purchased from Luminex Corp. and functionalized with anti-human hepatocyte growth factor (anti-HGF) monoclonal antibody [(clone 24516) (R&D Systems, Inc., Minneapolis, MN)] and anti-human cluster of differentiation 90 (anti-CD90) monoclonal antibody (clone AF-9) (Abcam, Cambridge, MA) according to the manufacturer's instructions (Luminex antibody coupling kit, #40-50016).[20] Briefly, carboxylated microspheres were first activated with 1-ethyl-3-[3-dimethylaminopropyl] carbodiimide hydrochloride (EDC) and sulfo-N-hydroxysulfosuccinimide (Sulfo-NHS). Once activated, anti-CD90 and anti-HGF antibodies were added at a 1:1 concentration-based ratio to covalently bind to the surface of the activated microspheres. Once coupled, microspheres were rinsed and stored in phosphate buffered saline (PBS) containing 1% bovine serum albumin (BSA) at 4°C until use. Care was taken to protect the microspheres from light to prevent photobleaching during coupling. Microspheres were used as per the manufacturer's instructions and within 6 months of coupling. To validate successful coupling of the antibodies with the microspheres, we performed a secondary antibody labeling and subsequent analysis.[20] Briefly, phycoerythrin-conjugated rat anti-mouse IgG (clone M1-14D12) (ThermoFisher Scientific) was added to the microspheres at a range of concentrations (0.0625 μg/mL to 4 μg/mL), incubated, and analyzed to generate a calibration curve as per the manufacturer's instructions (Figure D2).

Bead-Cell Binding Validation

To validate the bead-cell binding, NHDFn cells were seeded in a well plate at a density of $2.6x10^4$ cells/mL and cultured for 3 days in fibroblast media. As a negative control, HUVECs were passaged, incubated with CellTracker Blue for 1 hour at RT, washed with 1X PBS, and seeded at a density of $2.6x10^4$ cells/mL; cells were cultured for 3 days in EGM-2 media. Dual-functionalized (DF) beads (coupled with both anti-CD90 and anti-HGF antibodies) at a concentration of 50 beads/μL were added to the cultures on Day 3, post-seeding. An additional negative control was used in which different dual-functionalized beads [(coupled with both anti-CD64 (cluster of differentiation 64) and anti-MMP12 (matrix metallopeptidase 12) antibodies) (Abcam, #ab119843 and #ab52897, respectively)] were added to

separate wells containing NHDFn cultured in the same manner as stated above. Plates were shaken at 100 rpm for 1 minute then placed on a plate magnet (Stemcell Technologies, #18102) for 1 minute; this was repeated twice more for a total of three rounds followed by a 2-hour incubation. After incubation, wells were washed with media 3 times. Wells were imaged before adding beads, before washing wells, and after washing wells (Figure D3). To demonstrate cell-targeting ability, a device (Monorail2) was used to pattern NHDFn and HUVECs in separate regions of the well plate.[21] Full device operation and protocol is provided in Day *et al.*[21] Briefly, a Monorail2 device was placed into a 24-well plate and a 1.5 wt% low gelling temperature agarose pre-gel solution (Sigma-Aldrich, #39346-81-1) was flowed to create a hydrogel wall; gel was cooled at RT until solidified. 1X PBS was loaded into wells for 24 hours before use in experiments. Prior to seeding, NHDFn were incubated with CellTracker green dye for 1 hour at RT and HUVECs were incubated with CellTracker blue dye for 1 hour at RT (following dilution instructions provided) and washed with 1X PBS. Both cell types were seeded at a density of $2.6x10^4$ cells/mL and cultured for 3 days in EGM-2 media. On Day 3 post-seeding, Monorail2 devices were removed and dual-functionalized beads (coupled with both anti-CD90 and anti-HGF antibodies) at a concentration of 50 beads/μL were added to the cultures. Experimental workflow outlined above (shaking, washing, incubation, and imaging steps) were followed (Figure D4).

Bead-Analyte Binding Validation

A model capture sandwich immunoassay was performed using both dual-functionalized beads (anti-CD90 and anti-HGF antibodies) and commercial mono-functionalized kit beads (Product # HAGP1MAP-12K) (anti-HGF antibody only) according to manufacturer's instruction. Briefly, diluted beads (50 beads/μL) were incubated with recombinant human HGF protein [(clone #24516) (R&D Systems, Minneapolis, MN)] at concentrations ranging from 0 to 20,000 pg/mL (standard curve range according to each commercial kit). After incubation, beads were washed and detection antibody (biotinylated anti-human HGF polyclonal antibody, #BAF294, R&D Systems) was added to label the captured HGF. After binding of the detection antibody, streptavidin-R-phycoerythrin conjugate (SAPE) (ThermoFisher,

#S866) was added and the corresponding fluorescence of the beads was analyzed. A five-parameter logistic fit (5PL) was used to fit calibration curves based on kit protocols. Calibration curves from each experiment, for both mono- and dual-functionalized beads, are shown in Figure S5. Curves were used to determine HGF concentration for each independent experiment. Limit of detection (LOD) was calculated using the standard definition of three times the background signal for each curve.

Anti-HGF/HGF Assay

Media preparation: Two different media were used, one control and one treated. The control media consisted of EGM-2 supplemented with 10% HI-FBS and 1X PBS in place of antibody (control media). The treated media consisted of EGM-2 supplemented with 10% HI-FBS and anti-HGF [(clone 24516) (R&D Systems, Inc., Minneapolis, MN)] in 1X PBS for a final concentration of 10 ng/mL anti-HGF (treated media). Media were made fresh on the day of the experiment.

96 well plate assay: (Localized cell-surface sampling) NHDFn cells were cultured as described above; experiments were performed +/- anti-HGF. On Day 3 post seeding, cells were washed once with media; 75 μL control or treated media and 50 μL of diluted dual-functionalized (anti-HGF and anti-CD90) beads (100 beads/μL) were added and incubated with cells for 2 hours. To distribute added beads within a well, the plate was shaken at 100 rpm for 1 minute, then placed on a plate magnet for 1 minute; this was done for a total of 3 rounds in the beginning of the incubation period. After 2 hours, well contents were washed twice with 125 μL control media to remove any beads not bound to the cell surfaces; 50 μL of lysis buffer (10 mM Tris-HCl, 1 mM EDTA, 1% Triton X-100, 0.1% SDS, 140 mM NaCl) was then added and incubated for 15 minutes to detach beads from the cell surface. A mini cell scraper (ABI Scientific Inc., catalog #MCS-200) was used 5 minutes into the 15-minute lysis step to break up cellular debris during the lysing period. The plate was then placed on a magnet, and beads were washed with control media 3 times before being resuspended in 50 μL control media, collected, and added to assay plate; this resuspension was used as sample with no additional beads added. *(Traditional bulk supernatant sampling)* Supernatant samples, +/- anti-HGF, were also collected in parallel from

separate wells to be analyzed with mono-functionalized beads. The assay was continued using the Luminex kit and procedure.[20] Briefly, mono-functionalized (anti-HGF only) beads are added to supernatant samples and controls to incubate for 16-20 hours on an orbital shaker at 4˚C for HGF analyte capture; while dual-functionalized beads (anti-HGF and anti-CD90) undergo the same process, it is important to note that analyte capture is completed prior to addition onto the assay plate for the dual-functionalized beads. Beads are washed with wash buffer and secondary detection antibodies are added for a 1-hour room temperature incubation. SAPE is then added for an additional 30 minutes. Additional wash steps remove any unbound antibodies and SAPE before beads are resuspended in 1% BSA for analysis.

24 well plate Transwell assays: Inverted Transwell inserts were placed into a 12-well plate after which a 50 μL fibroblast cell suspension ($2.6x10^4$ cells/mL) was placed on top of the Transwell inverted insert (in the pore membrane area); cells were incubated for 2 hours to allow cell adherence before Transwell inserts were flipped and placed correctly into a 24-well plate with 500 μL control media in the basal side (Figure D6A). Additionally, in other wells, cells were also cultured on the bottom of a 24-well plate at the same density (Figure D6B). Cells were cultured as described above for the remainder of the experiment. On Day 3 post seeding, 50 μL diluted beads (100 beads/μL) and 50 μL +/- anti-HGF media were added to the apical side of the Transwell inserts while 500 μL +/- anti-HGF media was added to the basal side for a 2-hour incubation. Beads were collected from the apical side of the Transwell inserts and washed twice before being resuspended in 100 μL control media and added to assay plate; this resuspension was used as sample with no additional beads added. The assay was continued as previously described above using the Luminex kit and procedure. The data are presented in Figure D6.

Instrumentation

Analysis for all bead-based assays (MF and DF beads) were performed on a FLEXMAP 3D System (Luminex Corp.) in the Immune Monitoring Lab (Fred Hutchinson Cancer Research Center, Seattle, WA). The microspheres were analyzed with the following settings: 50 beads, 50 events/bead, 75 μL, bead

region 45 (commercial kit mono-functionalized beads) or 34 (dual-functionalized beads), 5000 – 30000 gate, 60 second time out. Fluorescent images of the cells and beads were obtained using a Zeiss Axiovert 200 and an Axiocam 503 mono camera (Carl Zeiss AG, Oberkochen, Germany). Data and statistical analyses were completed using Prism (Graphpad, San Diego, CA) software and FIJI image software (ImageJ, NIH).

5.6 References

1. Cooper, G. M. The Cell: A Molecular Approach, Signaling Molecules and Their Receptors. **2000**, 2nd Ed, Sunderland (MA), Sinauer Associates.
2. Zhao, W.; Oskeritzian, C.A.; Pozez, A.L.; Schwartz, L.B. Cytokine Production by Skin-Derived Mast Cells: Endogenous Proteases are Responsible for Degradation of Cytokines. *J. Immunol*. **2005**, 175, 2635-2642.
3. Niwa, Y.; Akamatsu, H.; Sumi, H.; Ozaki, Y.; Abe, A. Evidence for degradation of cytokines in the serum of patients with atopic dermatitis by calcium-dependent protease. *Arch. Dermatol. Res.*, **2000**, 292, 391-396.
4. Inal, J.M.; Kosgodage, U.; Azam, S.; Stratton, D.; Antwi-Baffour, S.; Lange, S. Blood/plasma secretome and microvesicles. *Biochim. Biophys. Acta*. **2013**, 1834, 11, 2317–2325.
5. Haslene-Hox, H.; Tenstad, O.; Wiig, H. Interstitial fluid-A reflection of the tumor microenvironment and secretome. *Biochim. Biophys. Acta.* **2013**, 1834, 11, 2336–2346.
6. Mukherjee, P.; Mani, S. Methodologies to Decipher the Cell Secretome. *Biochim. Biophys. Acta.* **2013**, 1834, 11, 2226–2232.
7. Müller P, Schier A.F. Extracellular movement of signaling molecules. *Dev. Cell.* **2011**, 21, 1, 145-158.
8. Son, K.J.; Gheibi, P.; Stybayeva, G.; Rahimian, A.; Revzin, A. Detecting cell-secreted growth factors in microfluidic devices using bead-based biosensors. *Microsystems & Nanoengineering*. **2017**, 3, 17025.
9. Son, K.J.; Rahimian, A.; Shin, D.S.; Siltanen, C.; Patel, T. Revzin, A. Microfluidic compartments with sensing microbeads for dynamic monitoring of cytokine and exosome release from single cells. ***Analyst*** **2016**, **141**, 679-688.
10. Hsu, M.N.; Wei, S.C.; Guo, S.; Phan, D.T.; Zhang, Y.; Chen, C.H.; Smart hydrogel microfluidics for single-cell multiplexed secretomic analysis with high sensitivity. *Small* **2018**, 1802918.
11. Barbulovic-Nad, I.; Yang, H.; Park, P.S.; Wheeler, A.R. Digital microfluidics for cell-based assays. ***Lab Chip***, **2008**, **8**, 519-526.
12. Gerard, A.; Woolfe, A.; Mottet, G. *et al.* High-throughput single-cell activity-based screening and sequencing of antibodies using droplet microfluidics. *Nat. Biotechnol.*, **2020**, 38, 715-721.
13. Eyer, K.; Doineau, R.; Castrillon, C. *et al.* Single-cell deep phenotyping of IgG-secreting cells for high-resolution immune monitoring. *Nat. Biotechnol.*, **2017**, 35, 977-982.
14. Cox J.H., Ferrari G., Janetzki S. Measurement of cytokine release at the single cell level using the Elispot assay. *Methods* **2006**, 38, 274–282.
15. Janetzki, S.; Rueger, M.; Dillenbeck, T. Stepping up ELISpot: multi-level analysis in fluorospot assays. *Cells* **2014**, 3, 4, 1102–1115.
16. Reslova, N.; Michna, V.; Kasny, M.; Mikel, P.; Kralik, P. xMAP technology: applications in detection of pathogens. *Front. Microbiol.*, **2017**, 8, 55.
17. Plouffe, B.D.; Murthy, S.K.; Lewis, L.H. Fundamentals and Application of Magnetic Particles in Cell Isolation and Enrichment. *Rep. Prog. Phys.* 2015, 78, 1, 016601.
18. Miltenyi Biotec, 2018. Cytokine Capture System (IFN-gamma) Product Sheet. 200-070-217. Accessed 2020/06/09.
19. Nakamura T, Mizuno S. The discovery of hepatocyte growth factor (HGF) and its significance for cell biology, life sciences and clinical medicine. *Proc. Jpn. Acad. Ser. B. Phys. Biol. Sci*. **2010**, 86, 6, 588–610.
20. Angeloni, S.; Das, S.; Dunbar, S.; Stone, V.; Swift, S. XMAP Cookbook: A Collection of Methods and Protocols for Developing Multiplex Assays with XMAP Technology. **2018**, 4th Ed, Austin (TX), Luminex.
21. Day, J. H.*; Nicholson, T. M.*; Su, X.; van Neel, T. L.; Clinton, I.; Kothandapani, A.; Lee, J.; Greenberg, M. H.; Amory, J. K.; Walsh, T. J.; Muller, C. H.; Franco, O. E.; Jefcoate, C. R.; Crawford, S. E.; Jorgensen,

J. S.; Theberge, A. B. “Injection molded open microfluidic well plate inserts for user-friendly coculture and microscropy.” *Lab Chip*, **2020**. *20*, 107.

Chapter 6. An Open-Microfluidic Platform for Immune-Microenvironment Signaling During Infection

Reproduced in part with permission from Berry, S.B.; Gower, M.S.; Su, X.; Seshadri, C.; Theberge, A.B. "A modular microscale granuloma model for immune-microenvironment signaling studies *in vitro*". *Front. Bioeng. Biotech.* Submitted.

Abstract:

Tuberculosis (TB) is one of the most potent infectious diseases in the world, causing more deaths than any other single infectious agent. TB infection is caused by inhalation of *Mycobacterium tuberculosis* (Mtb) and subsequent phagocytosis and migration into the lung tissue by innate immune cells (*e.g.*, alveolar macrophages, neutrophils, dendritic cells), resulting in the formation of a fused mass of immune cells known as the granuloma. Considered the pathological hallmark of TB, the granuloma is a complex microenvironment that is crucial for pathogen containment as well as pathogen survival. Disruption of the delicate granuloma microenvironment *via* numerous stimuli, such as variations in cytokine secretions, nutrient availability, and the makeup of immune cell population, can lead to an active infection. Herein, we present a novel *in vitro* model to examine the soluble factor signaling between a mycobacterial infection and its surrounding environment. Adapting a newly developed suspended microfluidic platform, known as Stacks, we established a modular microscale infection model containing human immune cells and a model mycobacterial strain that can easily integrate with different microenvironmental cues through simple spatial and temporal "stacking" of each module of the platform. We validate the establishment of suspended microscale (4 μL) infection cultures that secrete increased levels of proinflammatory factors IL-6, VEGF, and TNFα upon infection and form 3D aggregates (granuloma model) encapsulating the mycobacteria. As a proof of concept to demonstrate the capability of our platform to examine soluble factor signaling, we cocultured an *in vitro* angiogenesis model with the granuloma model and quantified morphology changes in endothelial structures as a result of culture conditions ($P < 0.05$ when comparing infected vs. uninfected coculture systems). We envision our

modular *in vitro* granuloma model can be further expanded and adapted for studies focusing on the complex interplay between granulomatous structures and their surrounding microenvironment, as well as a complementary tool to augment *in vivo* signaling and mechanistic studies.

6.1 Introduction

Tuberculosis (TB) is one of the most potent infectious diseases in the world, causing more deaths than any other single infectious agent.[1] TB infection is caused by inhalation of *Mycobacterium tuberculosis* (Mtb) and subsequent phagocytosis and migration into underlying lung tissue and the lymph system by responding immune cells (*e.g.*, alveolar macrophages, dendritic cells).[2,3] Due to the inability of these innate immune cells to clear Mtb, persistent Mtb induce an adaptive immune response, leading to the formulation of a fused mass of immune cells around Mtb known as a granuloma.[2] Within the granuloma, Mtb typically enter a latent phase characterized by a non-proliferative phenotype and lipid uptake[4–6], leading to a latent infection that is effectively contained.[1] However, disruption of the delicate equilibrium between proinflammatory factors (*e.g.*, tumor necrosis factor-α (TNFα), interferon-γ (IFNγ)), microenvironment conditions (*e.g.*, hypoxia, pH), and immune cell populations (*e.g.*, macrophages, T cells) can lead to reactivation of latent Mtb and deterioration of the granuloma, initiating an active TB infection and dissemination of infectious mycobacteria.[4,7]

Deciphering the impact of microenvironment variations around the granuloma remains a significant challenge, and researchers often rely on *in vivo* animal models or biological samples (*e.g.*, blood, tissue biopsy), considered the gold standard for studying TB, to reconstruct this complex environment. These methods have laid the foundation for understanding the pathogenesis and immunology behind TB, yet many existing *in vivo* models do not accurately recapitulate Mtb infection as seen in humans (although recent advances in mouse models and the established zebrafish/*M. marinum* model are closing this gap)[8–13]. Additionally, despite recreating the complexity of an *in vivo* environment, spatial manipulation and probing of the granuloma microenvironment through introduction or removal of immune and tissue components is difficult in most animal models.[12,14,15] Further, human-derived biological samples provide

detailed cellular information regarding the granuloma, the immune response, and disease status [16–19], but are inherently limited as they only reflect a singular point in time, rather than the dynamic interactions that occur during the early stages of infection or disease progression.

Alternatively, researchers have utilized *in vitro* models to examine specific processes and immune phenomena associated with TB infection and granuloma formation, augmenting the valuable information elucidated from *in vivo* models.[5,6,20–22] These models, which often rely on infection of patient-derived peripheral blood mononuclear cells (PBMCs) with mycobacterial strains, have successfully mimicked granuloma formation and behavior through soluble factor signaling between immune cells [20,23,24], Mtb reactivation[21], and PBMC differentiation.[5] However, many of these *in vitro* models consist of granulomas grown inside of well plates[5,20,21,23,24], limiting the ability of the researchers to easily manipulate the microenvironment of the granulomas and increase the complexity of their granuloma models through multiculture and introduction of key components of the microenvironment on demand. Recently, more complex, biomimetic models have been developed that have successfully recapitulated important biological phenomena[25,26] and examined novel therapeutic approaches to combat TB infection [27,28], while simultaneously demonstrating innovative and tractable platforms. However, these models face limitations in studies where users wish to subject granulomas to various microenvironmental cues over time, or in enabling the addition of tissue components after the model is established.

Building upon the foundation created by previous *in vitro* models, we present the creation of a novel microscale *in vitro* granuloma model that can be adapted to study the soluble factor signaling between granulomas and their surrounding microenvironment immediately following infection. Using a recently developed modular microfluidic coculture platform, known as "Stacks"[29], we demonstrate a multi-layered coculture that can be spatially and temporally manipulated to mimic different microenvironments and timepoints. The Stacks platform utilizes suspended cultures, wherein a droplet is contained in a well consisting of walls but lacking a ceiling or floor [30–32], thereby enabling users to vertically stack layers containing different cell types and place them in signaling contact.[29] The modular component of the Stacks, as well as of other microfluidic platforms, offers a notable advantage as users

can optimize model conditions individually and connect each component to create different complex systems.[29,33] As a proof of concept, we use a model mycobacterial strain known to induce granuloma formation *in vitro*[23,34], *Mycobacterium bovis* Bacillus Calmette-Guerin (BCG), with human blood-derived immune cells and validate its ability to form an *in vitro* granuloma model on the microscale (4 µL culture volume) in a layer of the Stacks platform. Further, to demonstrate the ability of our stackable microscale infection model to signal with its surrounding microenvironment, we miniaturize an existing *in vitro* angiogenesis model (containing primary human endothelial cells) within a separate stackable layer.[29,35,36] Here, we validate the development of our microscale *in vitro* granuloma model and demonstrate the capability of the system to support soluble factor signaling between the granuloma model and a separate stackable endothelial culture. We envision our modular *in vitro* granuloma model can be further developed to include additional layers of immune cells, tissue models, and pathogens for studies examining the complex interplay between granulomatous structures and their surrounding environment, as well as a complementary tool to augment *in vivo* signaling and mechanistic studies.

6.2 Design and establishment of microscale granuloma model

Microscale Granuloma Model Design and Overview

We present a modular *in vitro* platform that we adapted to enable the ability to add, modify, and manipulate the granuloma microenvironment for studying the effects of cellular signaling on granuloma formation and development. To create this *in vitro* model, we adapted a previously described open microfluidic platform ("Stacks"[29]) (Figure 6.1) that relies on key fluidic principles, namely capillary pinning, to enable vertical stacking and removal of discrete cell culture wells without leakage or horizontal flow between stacked layers. The pinning of fluids within this platform is vital to contain cultures within the open wells and allows for the connection and separation of the wells without bonding or disruption of the cultures, respectively. Additionally, the Stacks platform provides numerous advantages such as pipette accessibility (due to its open culture wells), bio- and imaging compatibility (due to its fabrication from polystyrene or polypropylene), and microscale culture wells. Further, the

Stacks device relies on surface tension and capillary forces for functionality, removing the need for external pumps commonly associated with microfluidic chips (*i.e.*, syringe pumps) and allowing it to fit within common cell culture materials (*e.g.*, OmniTray™, petri dish) and incubators. For our *in vitro* model, we created two independent layers that can be clicked together to initiate paracrine signaling or separated for independent analysis, thereby allowing us to temporally introduce different signaling microenvironments to our *in vitro* granuloma model (Figure 6.1).[29] The first layer, herein called the granuloma layer, consists of an infection model of monocyte-derived macrophages (MDMs) and a model mycobacterium strain, *Mycobacterium bovis* Bacillus Calmette-Guérin (BCG), suspended in a 3D extracellular matrix (ECM) plug to mimic some aspects of *in vivo* granuloma behavior (*e.g.*, pathogen encapsulation, soluble factor secretion, aggregate formation) previously observed in other *in vitro* granuloma models.[20,21,24] The second layer, herein called the endothelial layer, consists of an *in vitro* angiogenesis model in which endothelial cells are cultured on a hydrogel plug. By placing the primary human endothelial cells on a separate Stacks layer, our model can be used to examine the induction of angiogenic processes around the granuloma layer and how those angiogenic processes are affected by the soluble factor signaling profile of the granuloma layer. It is important to note that in our platform, the granuloma layer is not vascularized directly, as is observed *in vivo*[37], and that in our system, our endothelial layer is more akin to modeling the surrounding vasculature that is manipulated during early TB infection (Figure 6.1).[38]

Previous *in vitro* granuloma models successfully recapitulated important components of granulomatous infections including leukocyte recruitment and signaling, establishment of dormancy and resuscitation, and genetic diversity at scales ranging from 12 well plates to 96 well plates.[20,21,24] Our model adds to these existing techniques through miniaturization and introduction of modularity to enable examination of the signaling phenomena between a mycobacterial infection and its surrounding microenvironment. We reduce the volume of our cultures (4 μL/well) more than 10-fold from previous examples (50-500 μL/well) to decrease cell and reagent usage in our model; further, we mix BCG and MDMs together in a 3D extracellular matrix (ECM), without pre-infecting the MDMs, to establish the

infection in our granuloma layer after a minimum of 24 hours (Figure 6.1). However, due to the scale of the model (4 μL/well), the media buffering capacity, nutrient availability, waste accumulation, and multiplicity of infection (MOI) all needed to be optimized to permit successful formation of the granuloma layer (Appendix E2). This is consistent with prior investigations on the effects of miniaturization on mammalian cultures.[39] Similarly, we adapted and miniaturized the established *in vitro* angiogenesis assay[35,36] that is seeded into a separate Stacks layer and subsequently clicked together with the granuloma layer to initiate soluble factor signaling between the two layers (Figure 6.1, 6.4, Appendix E3).

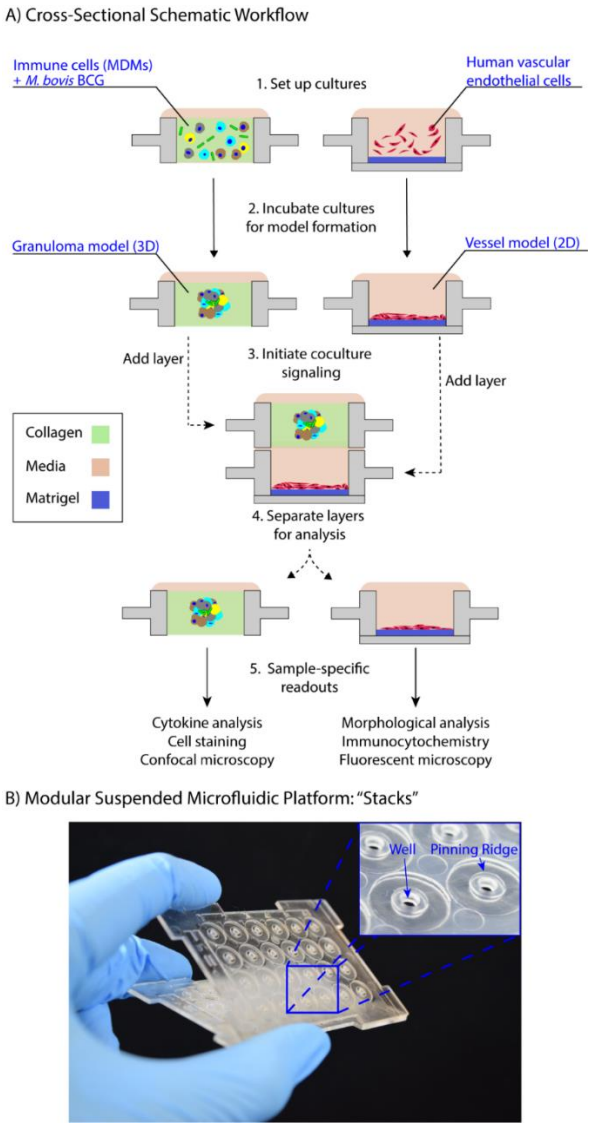

Figure 6.1: Suspended open microfluidic platform enables creation of a modular *in vitro* granuloma model. A) Schematic workflow showing cross sections of establishing the granuloma and endothelial layers and stacking of layers to initiate coculture paracrine signaling. B) The "Stacks" platform[29] contains an array of 24 individual suspended wells to facilitate the exchange of signals through the top and bottom of the well to neighboring layers and can be easily combined and removed. The inset illustrates the open suspended wells (2 mm diameter) and pinning ridges required to prevent leakage within the platform.

6.3 Validation of model within an open microfluidic platform

To validate the successful establishment of a microscale *in vitro* granuloma model within our platform, we used three separate previously reported readouts: 1) aggregate formation, 2) encapsulation of the mycobacterium within host immune cells, and 3) soluble factor analysis.[20,21,24,27] After initiating

infection by mixing MDMs and BCG into the ECM (collagen I) and seeding it into the wells, we consistently observed aggregate formation in the granuloma layer containing BCG when wells were fixed and imaged on Day 4 post infection (p.i.) (Figure 6.2). Using mCherry-expressing BCG, we were able to observe aggregation of CellTracker Green-stained MDMs around the BCG in infection wells, whereas little to no aggregate formation was observed in the uninfected control wells (Figure 6.2); the 3D structure of the aggregates containing MDMs and BCG was confirmed through confocal imaging of the granuloma layers on Day 4 p.i. (Figure 6.2). We observed complete encapsulation of BCG within the multi-cellular aggregate, oftentimes noting the presence of multiple spatially distinct BCG within one aggregate and little to no extracellular BCG (Figure 6.2). An advantage of mixing the BCG and MDMs without direct pre-infection of the MDMs is that MDMs must sample and migrate through the 3D collagen matrix in order to initiate the infection and respond to other infected MDMs, a process which is further supported by the microscale culture wells and an optimized MOI of 0.05.

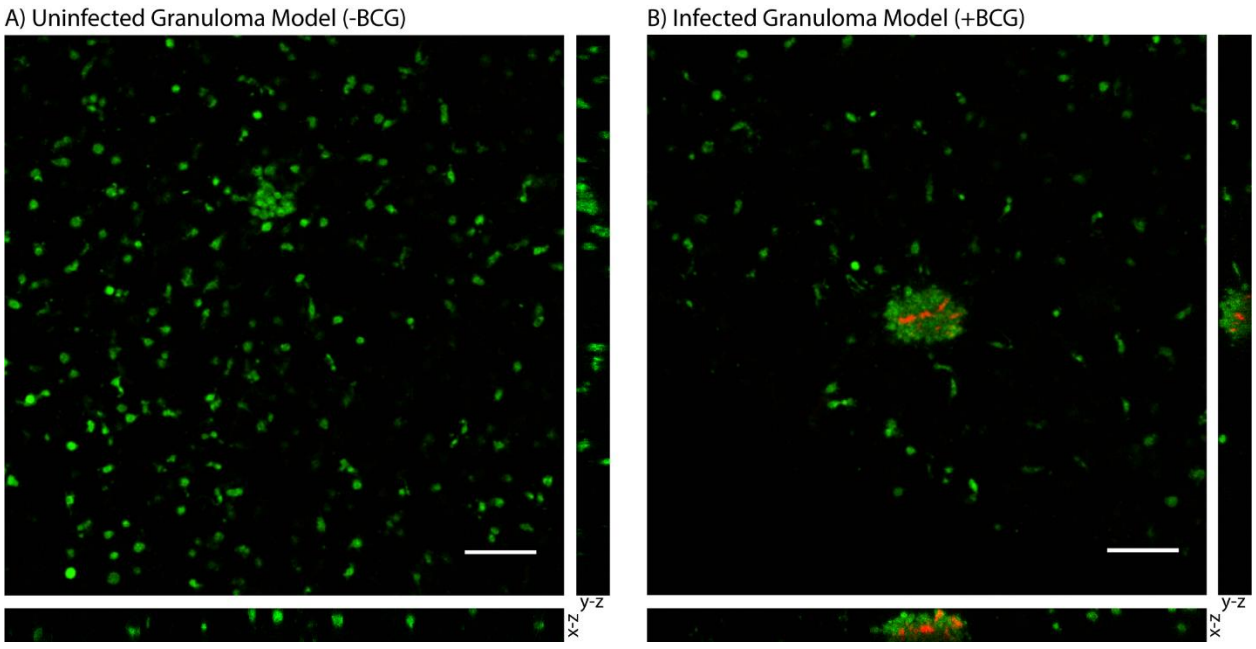

Figure 6.2: Aggregation of *M. bovis* BCG and MDMs in 3D collagen plugs within a layer of the Stacks microscale culture system. A) CellTracker Green-stained MDMs remain dispersed in a 3D collagen plug in the absence of coincubation with BCG. B) MDMs encapsulate mCherry-expressing BCG in the granuloma layer and form large multicellular aggregates that surround the BCG-infected MDMs and contain the mycobacterium within the aggregate. Confocal microscopy shows the structure of the aggregated MDMs with BCG and illustrates containment of the BCG within the

aggregate of MDMs in the suspended 3D collagen plug. Representative images obtained on Day 4 p.i. MOI: 0.05. Scale bar: 100 μm. Bottom image depicts x-z plane (66.5 μm thickness) and right image depicts y-z plane (66.5 μm thickness).

To illustrate the capability of our model to be used for soluble factor signaling studies, we analyzed the secretion profile of three granuloma-associated proinflammatory factors: interleukin-6 (IL-6), tumor necrosis factor α (TNFα), and vascular endothelial growth factor (VEGF) (Figure 6.3).[38,40–42] In accordance with previous models and studies[20,38,40–42] we observed significantly greater secretion of IL-6 ($P = 0.005$) and VEGF ($P = 0.039$) in our infected granuloma layers (+BCG) when compared to our control layers containing uninfected MDMs in monoculture (-BCG); further, we observed a 5-17-fold increase in TNFα secretion in 3 out of 4 independent experiments under the same conditions and a strong overall trend towards greater TNFα secretion (Figure 6.3). We also observed decreasing secretion of IL-6, TNFα, and VEGF over 5 days, with the greatest concentrations observed for IL-6 and TNFα on Day 1 and for VEGF on Day 2 (Figure 6.3). These results indicate that there is a large burst of proinflammatory factors immediately following infection, that then decreases and stabilizes over time as we begin to observe aggregate formation in the granuloma layers. Additionally, while we observe the anticipated increases in the secretion of these factors, we would expect a more robust response if more virulent strains than BCG were used, as increased secretion of factors has been observed with infection by more virulent mycobacterial strains.[38,43] Thus, these results support the use of our microscale granuloma model for studies of soluble factor signaling involving the granuloma layer, and its broader use for mycobacterial infection cytokine studies.[44]

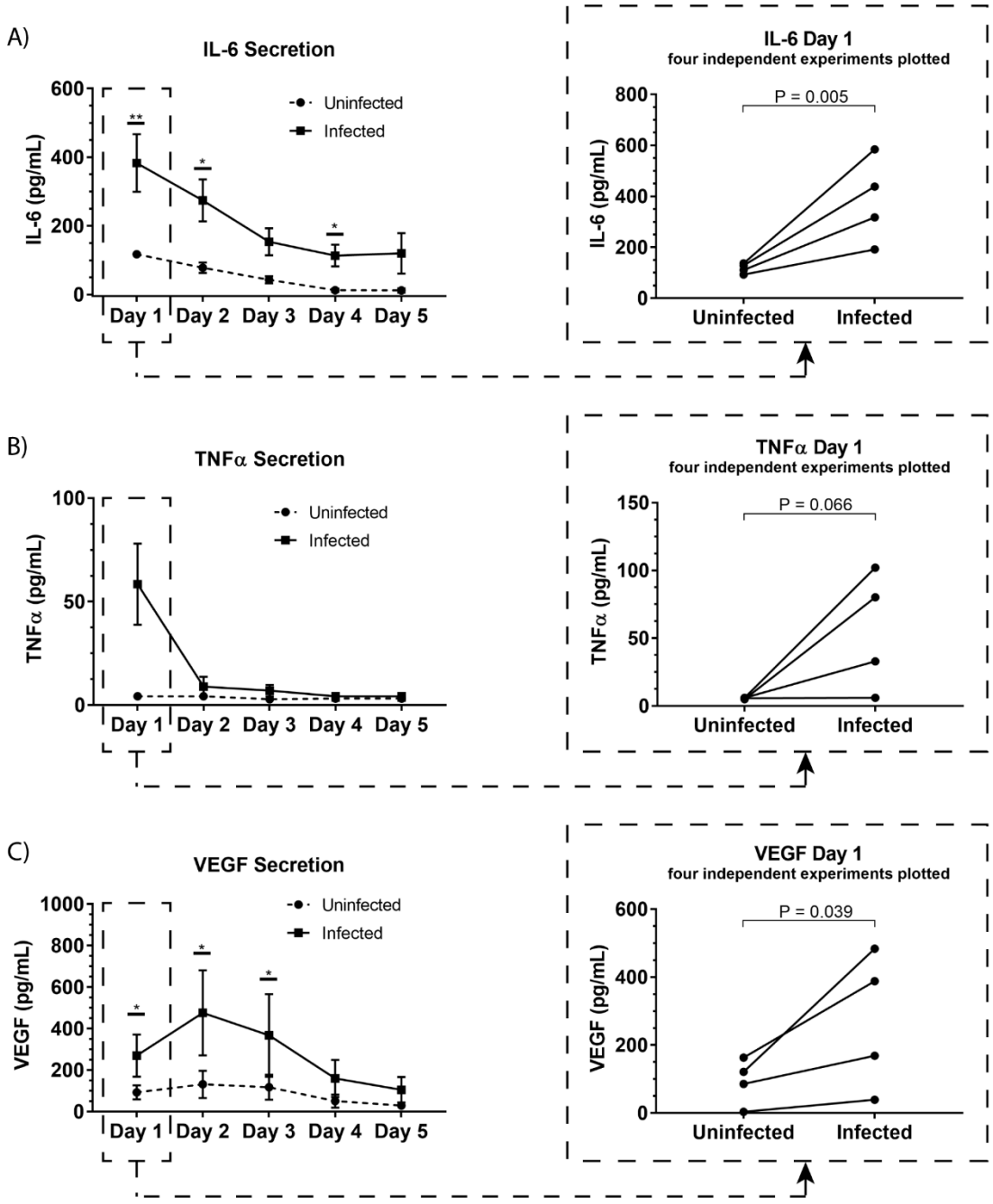

Figure 6.3: Soluble factor analysis of granuloma layer supernatants illustrates proinflammatory profile of infection model. Infection with BCG causes significant increases in secretion of (A) IL-6 and (C) VEGF in the Stacks platform, and shows an increasing trend in (B) TNFα secretion Day 1 p.i. Secretion of IL-6, TNFα, and VEGF decreases over time in infected granuloma layers following infection, corresponding with the formation of aggregates starting around Day 3 p.i. For Day 1-5 p.i., media was replaced daily and supernatant collected from each day was analyzed. Each point represents pooled supernatant samples from 24 technical replicates from n=4 independent experiments (each of the four independent experiments is plotted as a separate point in the plots on the right for the Day 1 data). Error bars on left plot: SEM. *P < 0.05; **P < 0.01; Ratio paired *t*-test.

6.4 Modulation of cellular morphology through coculture signaling

As a proof of concept to demonstrate the use of our microscale granuloma model in the Stacks platform, we developed a coculture system containing an established angiogenesis model[29,35,36,45,46] that can be used to probe granuloma-associated angiogenesis.[37,38,47,48] Mycobacterium-mediated angiogenic processes and granuloma vascularization result from the secretion of proangiogenic factors by the infected immune cells that compose the granuloma and play a complex and evolving role during the course of infection.[38,48–50] Extensive work has been conducted on understanding the role of angiogenesis in granuloma outcome, finding that inhibition of VEGF and other signaling pathways reduces pathogenicity and dissemination of infectious mycobacteria[38,48,51] while normalizing surrounding vasculature, improving small molecule delivery, and decreasing hypoxia within the granuloma.[37] Similarly, we observed increased secretion of VEGF from infected cells within our microscale granuloma model (Figure 6.3C), and therefore sought to illustrate one potential use of our platform as a complimentary tool for studies examining this infection-mediated process.

To establish this granuloma-vasculature model coculture system, we created a second Stacks layer containing a floor, enabling culture of human endothelial cells on a hydrogel plug (Matrigel) while retaining the ability to be placed in soluble factor signaling contact with the granuloma layer. We selected an *in vitro* model of angiogenesis that has been extensively used to screen angiogenic stimulants and inhibitors, wherein human endothelial cells cultured in well plates self-assemble into tubule-like networks and demonstrate cell sprouting and branching, and adapted it for our endothelial layer.[35,36,46,52] In order to examine the influence of the soluble factor profile from the granuloma layer on the endothelial layer, we independently established the granuloma layer and the endothelial layer under their optimized culture conditions; the modularity of the Stacks platform enables both layers to be cultured in their optimal conditions (and in separate incubators) without risk of cross contamination prior to joining the layers. The granuloma layers were infected and incubated 24 hours prior to clicking with the endothelial layer, and the endothelial layers were seeded 2 hours prior to allow the cells to self-assemble into a tubule-like

network.[36,46] Separate layers were then stacked together and connected by a bridge of shared media to allow passage of factors between the two layers. After 16 hours of signaling, we separated the layers and fixed, stained, and imaged the vasculature to analyze its morphology as a result of coculture with the granuloma layer (Figure 6.4). We found that after 16 hours of coculture, endothelial cells in contact with infected granuloma layers (+BCG) formed thinner, centralized structures with diffuse cell sprouts extending from the center, whereas endothelial cells in contact with uninfected control layers (-BCG) formed wider and larger structures that retained some interconnected networks (Figure 6.4). We quantified these morphological differences through measurement of their tubule index, a metric that measures the ratio of the endothelial structure perimeter to the endothelial structure area and can be used to discern between endothelial structure morphologies (*e.g.*, tubule network, single tubule, islands/clusters)[53], and found significant morphological differences between endothelial layers cocultured with infected granuloma layers (+BCG) when compared uninfected granuloma layers (-BCG) (Figure 6.4). The morphological change is likely the result of the increased secretion of factors from BCG-infected MDMs, such as VEGF (Figure 6.3C); however, it is possible that additional factors we did not quantify are also contributing to the differences in endothelial morphology. Ultimately, the induction of morphology changes in the endothelial layer as a result of coculture with different model granuloma layers illustrates the ability of the granuloma layer to signal with a neighboring layer representing microenvironmental components.

As we chose to connect the layers at Day 1 p.i. to correlate with increased levels of VEGF and cytokine secretion (Figure 6.3), we expect our model and results would mimic an earlier time point in infection, when the mycobacteria-infected cells are still secreting proinflammatory factors to recruit other immune cells and the vasculature. Depending on user queries, these layers can also be stacked at more advanced time points to study the effect of a later soluble factor profile on the surrounding vasculature, illustrating a key advantage of the modularity of the Stacks system and the flexibility in timing to combine the layers. Further, the ability of the model granuloma layer to communicate with the vasculature and modulate the endothelial morphology demonstrates the usage of this platform for

signaling studies between our infected granuloma layers and microenvironment components. The ability to create two independent layers that are in soluble factor signaling contact enables users to isolate the effects of the soluble factors from the granuloma layer on its surrounding microenvironment without interference from juxtacrine signaling or physical interactions.

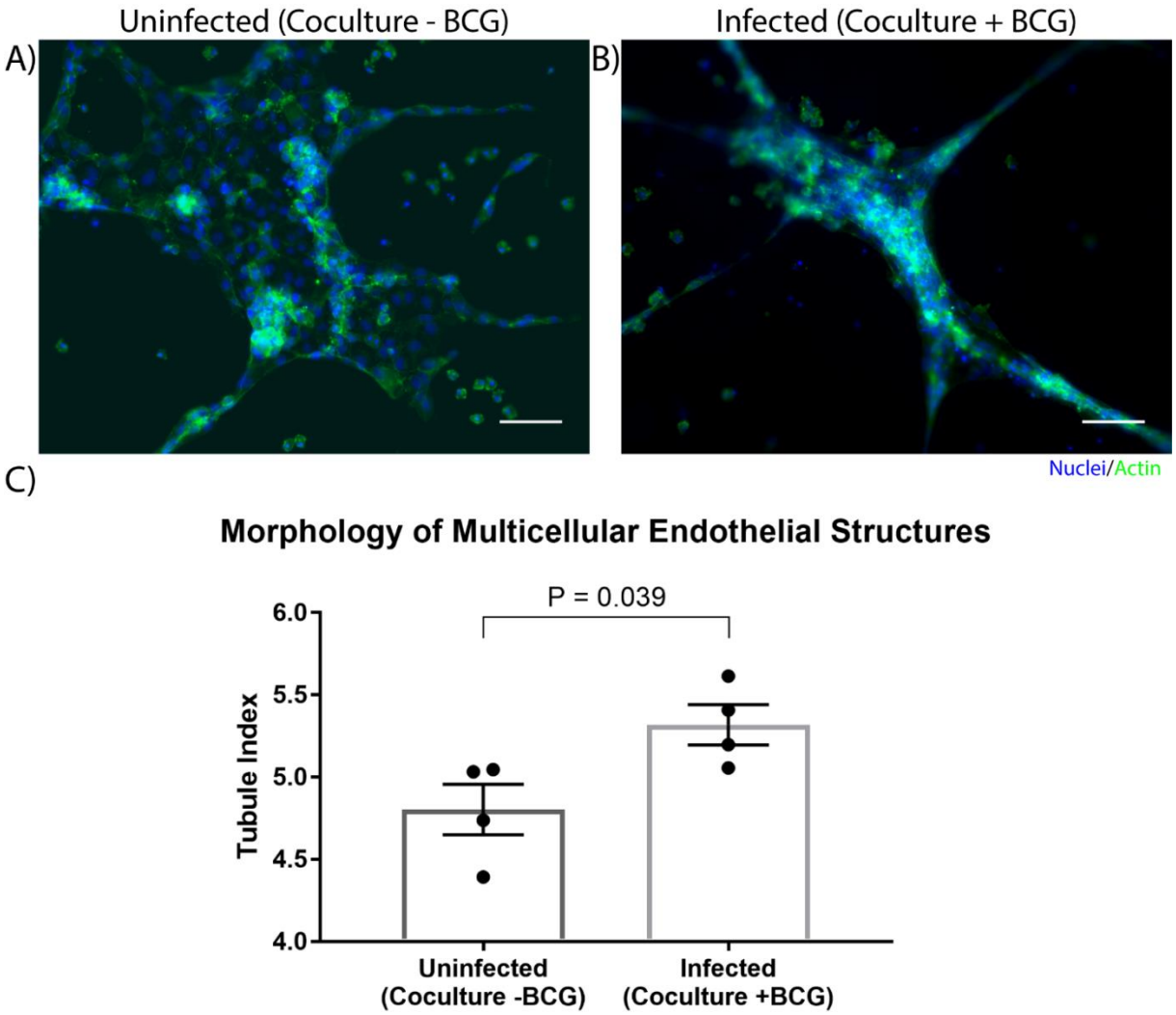

Figure 6.4: Coculture of endothelial layer with granuloma layer impacts morphology of multicellular endothelial structures. Representative images of an endothelial layer cocultured with an uninfected (-BCG) layer (A) or infected (+BCG) layer (B) for 16 hours, illustrating the difference in endothelial morphology as a result of coculture. C) The tubule index (perimeter/area ratio) was used to quantify the morphology of endothelial structures and shows a significant difference between coculture conditions, demonstrating the ability of the model granuloma layer to signal with the endothelial layer. Scale bar: 100 μm. Error bars: SEM. $P < 0.05$, unpaired *t*-test. Each point represents the average ratio of an independent experiment (n=4 independent experiments are plotted).

6.5 Conclusion

Microenvironmental effects, such as soluble factor signaling, play a vital role in granuloma outcome, as the immune system attempts to contain and impede pathogenic mycobacterium from manipulating its environment in favor of its survival.[7] For example, induction of angiogenic processes by Mtb in the microenvironment surrounding a granuloma have been linked to pro-pathogen outcomes[47,48], while treatment with anti-angiogenic factors can be a potential treatment option to improve the effects of existing drug regiments.[37] To further understand the signaling environment and timeline of these phenomena, we created a novel *in vitro* granuloma model that can be used to study soluble factor signaling between the granuloma and its surrounding microenvironment. As a proof of concept model, we created a two-layered modular microfluidic system containing a mycobacterial infection and an endothelial vasculature model that can be used to compliment *in vivo* granuloma and angiogenesis models.[37,38,48,50] We demonstrate creation of a viable mycobacterial infection using human blood-derived immune cells and BCG within a 4 μL suspended collagen plug, and validate the secretion of proinflammatory cytokines associated with mycobacterial infection. Further, we provide a model coculture system that can be used to probe granuloma-associated angiogenic processes *in vitro*. The modularity and microscale size of our model enables users to add or remove additional cell types at various time points, and to utilize limited cell populations, such as patient cells or rare immune cells, and valuable reagents, such as antibodies or expensive drugs. Additionally, the design of the platform and fabrication method supports the creation of arrays to test various culture conditions/treatments and customizability to introduce additional functionality (*e.g.*, flow), as well as easy integration with BSL3 laboratory workflows as the device is disposable and fits inside common cell culture materials (*e.g.*, petri dish, OmniTray™, *etc.*). Further development of our system includes the addition of adaptive immune cells (*e.g.*, T cells) and introduction of parenchymal and stromal cells (*e.g.*, epithelial cells, fibroblasts) to model signaling interactions in the pulmonary environment, as well as the use of virulent *M. tuberculosis* to induce more *in vivo*-like responses. Ultimately, we created a tractable and customizable mycobacterial

infection model that can be utilized by other researchers to examine the various signaling components of a complex tuberculosis infection.

6.6 Materials and Methods

Stacks Device Fabrication:

Stacks devices[29] were fabricated from either polypropylene (PP) (granuloma layer) or polystyrene (PS)(endothelial layer)(Figure E1). PP devices were injection molded (ProtoLabs, Maple Plain, MN, USA) and were flattened using a bench top manual heated press (#4386, Carver Inc., Wabash, IN) for 1 h at 110°C (protocol in Appendix E1). After flattening, devices were cleaned with isopropanol (IPA) sonication for 1 h to remove any fabrication residue or contaminants, and then rinsed twice with fresh IPA before drying with compressed air. Prior to use, devices were UV-sterilized for 30 min in a biosafety cabinet. PS devices containing a floor were designed using Fusion360 CAD software (Autodesk, San Rafael, CA, USA) and milled using a Datron Neo CNC mill (Datron Dynamics Inc., Livermore, CA, USA). PS devices and bottoms (floors, 53 mm x 53 mm) were milled from 1.2 mm thick PS sheets (Goodfellow Corp, Coraopolis, PA, USA). To attach the floor to the PS Stacks layer, floors were solvent bonded to the bottom of the Stacks layer using acetonitrile at 75°C for 10 min, followed by 15 min at 75°C to allow excess acetonitrile to evaporate. Solvent-bonded devices were then sonicated in IPA for 80 min and 70% ethanol for 15 min. Devices were then soaked in sterile deionized water for a minimum of 3 hours, dried with compressed air, and UV-sterilized for 30 min prior to use. Device holders were designed on Solidworks CAD software (Solidworks Corp., Waltham, MA, USA), converted into G-code using SprutCAM CAM software (SprutCAM, Naberezhnye Chelny, Russia), and milled using a Tormach PCNC Micromill (Tormach Inc., Waunakee, WI). Device holders were fabricated from 4 mm thick PS and were sonicated in IPA for 1 h and UV-sterilized for 30 min prior to use.

To prevent evaporation of microliter volumes of samples, culture platforms were placed in a Nunc Omnitray™ (ThermoFisher) which was then placed in a bioassay dish (#240835, ThermoFisher) for secondary containment; both the Omnitray and bioassay dish were filled with sacrificial water droplets (1

mL and 5 mL, respectively) to create a humidified environment around the platform, and all cultures were then placed into a water-jacketed incubator.

Cell Culture:

Human peripheral blood mononuclear cells (PBMCs) were isolated from patient whole blood samples (Bloodworks NW, Seattle, WA, USA) using the Ficoll-Paque PLUS media density separation protocol (ThermoFisher, Waltham, MA, USA). Briefly, blood samples were diluted with PBS (Fisher Scientific) and layered atop the Ficoll-Paque. Tubes were then centrifuged for 20 min at 1900 RPM without brakes, and afterwards white blood cells at the plasma-Ficoll-Paque interface were collected and resuspended in PBS + 2% fetal bovine serum (FBS, ThermoFisher) + 1 mM ethylenediaminetetraacetic acid (EDTA, Gibco, ThermoFisher). Cells were then rinsed with subsequent centrifugation (10 min, 500g) and resuspension until the supernatant was clear. Isolated PBMCs were then cryopreserved in solution containing 90% heat-inactivated FBS (HI-FBS) (ThermoFisher) and 10% dimethyl sulfoxide (DMSO) (Sigma-Aldrich, St. Louis, MO) and stored in liquid nitrogen until use. To differentiate the PBMCs into monocyte-derived macrophages (MDMs), PBMCs were thawed and resuspended in serum free RPMI 1640 media (Gibco, ThermoFisher); following resuspension, PBMCs were seeded into a 6 well plate (#3516, Corning Inc., Corning, NY, USA) and allowed to incubate for 3 h at 37°C and 5% CO_2 for monocyte adhesion. After 3 h, suspended cells were removed, adherent cells were washed once with 1X phosphate-buffered saline (PBS, Fisher Scientific), and then RPMI 1640 containing 10% HI-FBS, 2 mM L-glutamine, 25 mM HEPES, and 50 ng/mL macrophage colony-stimulating factor (M-CSF) (R&D Systems, Minneapolis, MN, USA) was added to each well. Media was changed on Day 3 and Day 6 post-seeding, and MDMs were used after Day 6.

mCherry-expressing *M. bovis* Bacillus Calmette-Guérin (BCG) (graciously provided by the Urdahl Lab, Seattle Children's Research Institute, WA, USA) was cultured in Middlebrook 7H9 broth (ThermoFisher) containing 10% Middlebrook ADC enrichment supplement (ThermoFisher), 0.003% Tween-80 (Fisher Scientific), and 50 μg/mL hygromycin B (Sigma-Aldrich). A lower Tween-80 concentration had to be used to ensure that the surfactant did not interfere with the microfluidic media

pinning in the Stacks device (Appendix E2). BCG was cultured at 37°C and 170 RPM to an OD of 0.7-1.0 for use, passed through a 27G needle to break up aggregates, and diluted to a working concentration for the experiment. BCG was used for all experiments as it can be used within a BSL2 facility, and we did not have access to virulent mycobacterium strains nor a BSL3 facility to perform these experiments.

Human umbilical vein endothelial cells (HUVECs) (Lonza, Basel, Switzerland) were cultured in completed EGM-2 media and maintained at 37°C and 5% CO_2 until 80-90% confluence. Passage 5-7 cells were used.

3D Granuloma Assay:

MDMs were differentiated for a minimum of 6 days prior to use, and BCG was grown to an OD of 0.7-1.0 for use. MDMs were rinsed once with 1X PBS and detached with enzyme-free Cell Dissociation Buffer (#13151014, Life Technologies, ThermoFisher) at 37°C for 5 min and vigorous pipetting. Detached cells were neutralized with complete RPMI 1640 media, counted, and resuspended at a density of $4x10^7$ cell/mL. BCG was vortexed for 30 seconds, vigorously mixed *via* pipetting, and then diluted into 4 mL of complete RPMI 1640 media for a final concentration of $2x10^6$ BCG/mL. An extracellular matrix (ECM) mix containing 80 µL 3 mg/mL type I bovine collagen (Advanced Biomatrix Inc., Carlsbad, CA, USA), 10 µL 10X HEPES buffer, 7 µL deionized H_2O, 3 µL 0.5N NaOH, and 2.25 µL 1 mg/mL human fibronectin (Sigma-Aldrich) was mixed and stored on ice until use. To prepare the suspended cell-laden collagen plugs, 25 µL of MDMs (at $4x10^7$ cells/mL) and 25 µL of BCG (at $2x10^6$ BCG/mL) or 25 µL of complete RPMI 1640 was added to the ECM mix for a final volume of 152.25 µL and an MOI of 0.05. After mixing, 4 µL of the cell-laden ECM mix was added to each well in a PP device and allowed to gel at 37°C and 5% CO_2 for 2 h. After gelation, 8 µL of RPMI 1640 containing 15% HI-FBS and 25 mM HEPES was added atop each well and returned to the incubator. Media was changed daily for the entirety of the experiments. For all monoculture infection experiments (Figures 6.2 and 6.3), MDMs were stained with CellTracker Green CMFDA dye (ThermoFisher) according to manufacturer's protocols. Briefly, MDMs were rinsed with 1X PBS, and 10 µM CellTracker Green in serum-free media was added for 30

min at 37°C, washed once with 1X PBS, and then incubated with complete media for 10 min prior to further processing or use.

2D Angiogenesis Assay:

Prior to seeding, PS Stacks devices containing a floor were chilled for 5 min at -80°C and then kept on ice for Matrigel seeding. 3µL of Matrigel (8.6 mg/mL) was added to each well and devices rested on ice 30 min. The Matrigel was then polymerized for 30 min at 37°C. After polymerization, 3 µL of HUVECs were added atop the Matrigel for a final concentration of 1,650 cells per well ($5.5x10^5$ cells/mL). Cells were allowed to adhere and self-assemble for 2 h at 37°C and 5% CO_2. Media was then aspirated and replaced with 2 µL of EGM-2 + 10% FBS coculture media.

To stack the layers, media was first removed from the model granuloma layers. Model granuloma layers were then placed atop the endothelial layers (containing 3 µL of media) and 7 µL of coculture media was placed atop each well of the stacked granuloma layers, to allow for feeding of both layers. Layers were separated by a thin layer of tape along the sides of the devices to ensure reproducible separation. Stacked devices were then placed in the incubator at 37°C and 5% CO_2. After 16 h, devices were inverted and separated, fixed with 4% paraformaldehyde for 30 min at 25 °C, and stained as specified under Imaging.

Imaging:

To validate granuloma layer formation within our platform, MDMs were prestained with CellTracker Green CMFDA dye prior to infection and seeding into the Stacks. For imaging, the Stacks platform was placed on a 50 mm x 75 mm glass coverslip (#260462, Ted Pella Inc., Redding, CA, USA) and placed into an OmniTray™ with a 45 mm x 70 mm rectangle cut out of the bottom. Fluorescent images were obtained on a Zeiss Axiovert 200 coupled with an Axiocam 503 mono camera (Carl Zeiss AG, Oberkochen, Germany). For confocal imaging, all wells were fixed with 4% paraformaldehyde for 1 h at 25°C and then covered with PBS; the same imaging protocol was then followed as above. Fluorescent confocal images were obtained on a Leica TCS SP5 II Laser Scanning Confocal Microscope (Leica Camera AG, Wetzlar, Germany), with a z-depth of 66.47 µm and step size of 1.01 µm. Images

obtained with the Zeiss Axiovert 200 were analyzed with Fiji (ImageJ), and images obtained with the Leica TCS SP5 II were analyzed with Leica LAS X software (Leica).

For vasculature layer imaging, cells were permeabilized with 0.5% Triton-X 100 for 30 min and then stained with Phalloidin 488 (1:50) (Molecular Probe A12379) and Hoechst nuclear stain (1:1000) (Molecular Probe H1399) overnight. After overnight incubation, cells were rinsed thrice with 0.2% Triton-X 100 for 10 min each and then covered with PBS for imaging. Devices were placed on a 75 mm x 50 mm glass coverslip (#260462, Ted Pella Inc., Redding, CA, USA) and placed in an Omnitray™ with a 45 mm x 70 mm rectangle cut out of the bottom. Fluorescent images were obtained on a Zeiss Axiovert 200 coupled with an Axiocam 503 mono camera (Carl Zeiss AG, Oberkochen, Germany). Images obtained were analyzed with Fiji (ImageJ).

Angiogenesis Morphological Analysis:

To analyze differences in morphology in the endothelial layer we used default functions of Image J (Fiji) to quantify the tubule index (perimeter/area ratio)[53]. The image analysis procedure is described in the methods and SI of Theberge *et al.*[53], a summary is included here. For quantification, the 8-bit image containing the phalloidin channel (488) was selected and a threshold (Huang Dark) was applied to get the outline of the endothelial culture and saved (Image 1). The "Fill Holes" function was applied and saved (Image 2), and then Image 2 was subtracted from Image 1 to generate an image containing the holes/gaps in the endothelial morphology (Image 3). The total area of the phalloidin stain was then calculated by subtracting the area of Image 3 (holes) from Image 2 (fill holes), and the perimeter of the stain was calculated by adding the perimeter of Image 2 and Image 3. The area and perimeter were measured using the function "Analyze Particles", with the following parameters: size: 25-infinity (include pixel units), circularity: 0.00-1.00. The ImageJ macro for this process is included in the supplementary materials and is based off the macro used in Yu *et al.*[29]

Exclusion criteria for experimental artifacts that interfered with the imaging technique was developed to exclude wells unable to be analyzed with this technique. For example, if a collagen plug from the model granuloma layer detached and fell into an endothelial layer well during separation of the

layers, the endothelial morphology was obscured by signal from the MDMs in the collagen plug and therefore unable to be accurately measured. All images were assigned a randomized code and individuals not involved in the project determined which images to exclude base on established criteria. Images were then analyzed according to the measurement protocol above.

Cytokine Analysis:

Cytokine analyses were performed with a custom Luminex ProcartaPlex multiplex assay for IL-6, TNFα, and VEGF (ThermoFisher). Supernatant samples were collected and pooled from a single device (n=24 wells, 8 μL/well) during daily media changes and stored at -80°C until use. Samples were collected from the same device over a five-day period, such that each sample contains cytokines secreted within 24 h of collection (*i.e.*, Day 2 p.i. cytokine levels indicate what was secreted between Day 1 and Day 2 p.i., *etc.*). For analysis, samples were thawed on ice and analyzed according to the manufacturer's protocols for Luminex multiplex assays. Samples were analyzed on a Luminex 100/200 System instrument with xPONENT software (Fred Hutchinson Cancer Center Core Facility). All results were analyzed and visualized using Prism 7 software (GraphPad Software, San Diego, CA, USA).

6.7 References

1. World Health Organization. *Global Tuberculosis Report 2019*.; 2019.
2. Saunders BM, Britton WJ. Life and death in the granuloma: Immunopathology of tuberculosis. *Immunol Cell Biol*. 2007;85(2):103-111. doi:10.1038/sj.icb.7100027
3. Kaufmann SHE. New issues in tuberculosis. *Ann Rheum Dis*. 2004;63(SUPPL. 2):50-56. doi:10.1136/ard.2004.028258
4. Russell DG, Cardona PJ, Kim MJ, Allain S, Altare F. Foamy macrophages and the progression of the human tuberculosis granuloma. *Nat Immunol*. 2009;10(9):943-948. doi:10.1038/ni.1781
5. Peyron P, Vaubourgeix J, Poquet Y, *et al.* Foamy macrophages from tuberculous patients' granulomas constitute a nutrient-rich reservoir for M. tuberculosis persistence. *PLoS Pathog*. 2008;4(11):1-14. doi:10.1371/journal.ppat.1000204
6. Deb C, Lee CM, Dubey VS, *et al.* A novel in vitro multiple-stress dormancy model for mycobacterium tuberculosis generates a lipid-loaded, drug-tolerant, dormant pathogen. *PLoS One*. 2009;4(6). doi:10.1371/journal.pone.0006077
7. Ramakrishnan L. Revisiting the role of the granuloma in tuberculosis. *Nat Rev Immunol*. 2012;12(5):352-366. doi:10.1038/nri3211
8. Cronan MR, Matty MA, Rosenberg AF, *et al.* An explant technique for high-resolution imaging and manipulation of mycobacterial granulomas. *Nat Methods*. 2018;15(12):1098-1107. doi:10.1038/s41592-018-0215-8
9. Myllymäki H, Bäuerlein CA, Rämet M. The zebrafish breathes new life into the study of tuberculosis. *Front Immunol*. 2016;7(MAY). doi:10.3389/fimmu.2016.00196

10. Gern B, Plumlee C, Gerner M, Urdahl K. Investigating immune correlates of protection to tuberculosis using an ultra-low dose infection in a mouse model. *OFID*. 2017;4(Suppl 1):47-48.
11. Cronan MR, Tobin DM. Fit for consumption: Zebrafish as a model for tuberculosis. *DMM Dis Model Mech*. 2014;7(7):777-784. doi:10.1242/dmm.016089
12. Zhan L, Tang J, Sun M, Qin C. Animal models for tuberculosis in translational and precision medicine. *Front Microbiol*. 2017;8(MAY). doi:10.3389/fmicb.2017.00717
13. Yong KSM, Her Z, Chen Q. Humanized Mice as Unique Tools for Human-Specific Studies. *Arch Immunol Ther Exp (Warsz)*. 2018;66(4):245-266. doi:10.1007/s00005-018-0506-x
14. Scanga CA, Flynn JL. Modeling tuberculosis in nonhuman primates. *Cold Spring Harb Perspect Med*. 2014;4(12). doi:10.1101/cshperspect.a018564
15. Foreman TW, Mehra S, Lackner AA, Kaushal D. Translational research in the nonhuman primate model of tuberculosis. *ILAR J*. 2017;58(2):151-159. doi:10.1093/ilar/ilx015
16. Darboe F, Mbandi SK, Naidoo K, *et al.* Detection of tuberculosis recurrence, diagnosis and treatment response by a blood transcriptomic risk signature in HIV-infected persons on antiretroviral therapy. *Front Microbiol*. 2019;10(JUN):1-16. doi:10.3389/fmicb.2019.01441
17. Guyot-Revol V, Innes JA, Hackforth S, Hinks T, Lalvani A. Regulatory T cells are expanded in blood and disease sites in patients with tuberculosis. *Am J Respir Crit Care Med*. 2006;173(7):803-810. doi:10.1164/rccm.200508-1294OC
18. Ogongo P, Steyn AJC, Karim F, *et al.* Differential skewing of donor-unrestricted and γδ T cell repertoires in tuberculosis-infected human lungs. *J Clin Invest*. 2020;130(1):214-230. doi:10.1172/JCI130711
19. Berry MPR, Graham CM, McNab FW, *et al.* An interferon-inducible neutrophil-driven blood transcriptional signature in human tuberculosis. *Nature*. 2010;466(7309):973-977. doi:10.1038/nature09247
20. Birkness KA, Guarner J, Sable SB, *et al.* An in vitro model of the leukocyte interactions associated with granuloma formation in Mycobacterium tuberculosis infection. *Immunol Cell Biol*. 2007;85(2):160-168. doi:10.1038/sj.icb.7100019
21. Kapoor N, Pawar S, Sirakova TD, Deb C, Warren WL, Kolattukudy PE. Human Granuloma In Vitro Model, for TB Dormancy and Resuscitation. *PLoS One*. 2013;8(1). doi:10.1371/journal.pone.0053657
22. Elkington P, Lerm M, Kapoor N, *et al.* In vitro granuloma models of tuberculosis: Potential and challenges. *J Infect Dis*. 2019;219(12):1858-1866. doi:10.1093/infdis/jiz020
23. Puissegur MP, Botanch C, Duteyrat JL, Delsol G, Caratero C, Altare F. An in vitro dual model of mycobacterial granulomas to investigate the molecular interactions between mycobacteria and human host cells. *Cell Microbiol*. 2004;6(5):423-433. doi:10.1111/j.1462-5822.2004.00371.x
24. Crouser ED, White P, Caceres EG, *et al.* A novel in vitro human granuloma model of sarcoidosis and latent tuberculosis infection. *Am J Respir Cell Mol Biol*. 2017;57(4):487-498. doi:10.1165/rcmb.2016-0321OC
25. Parasa VR, Rahman MJ, Hoang ATN, Svensson M, Brighenti S, Lerm M. Modeling Mycobacterium tuberculosis early granuloma formation in experimental human lung tissue. *DMM Dis Model Mech*. 2014;7(2):281-288. doi:10.1242/dmm.013854
26. Parasa VR, Muvva JR, Rose JF, Braian C, Brighenti S, Lerm M. Inhibition of tissue matrix metalloproteinases interferes with Mycobacterium tuberculosis-induced granuloma formation and reduces bacterial load in a human lung tissue model. *Front Microbiol*. 2017;8(DEC):1-14. doi:10.3389/fmicb.2017.02370
27. Tezera LB, Bielecka MK, Chancellor A, *et al.* Dissection of the host-pathogen interaction in human tuberculosis using a bioengineered 3-dimensional model. *Elife*. 2017;6:1-19. doi:10.7554/eLife.21283
28. Bielecka MK, Tezera LB, Zmijan R, *et al.* A bioengineered three-dimensional cell culture platform integrated with microfluidics to address antimicrobial resistance in tuberculosis. *MBio*. 2017;8(1). doi:10.1128/mBio.02073-16
29. Yu J, Berthier E, Craig A, *et al.* Reconfigurable open microfluidics for studying the spatiotemporal dynamics of paracrine signalling. *Nat Biomed Eng*. 2019;3(10):830-841. doi:10.1038/s41551-019-0421-4
30. Casavant BP, Berthier E, Theberge AB, *et al.* Suspended microfluidics. *PNAS*. 2013;110(25):10111-10116. doi:10.1073/pnas.1302566110
31. Humayun M, Chow CW, Young EWK. Microfluidic lung airway-on-a-chip with arrayable suspended gels for studying epithelial and smooth muscle cell interactions. *Lab Chip*. 2018;18(9):1298-1309. doi:10.1039/c7lc01357d
32. Berthier E, Dostie AM, Lee UN, Berthier J, Theberge AB. Open Microfluidic Capillary Systems. *Anal Chem*. 2019;91(14):8739-8750. doi:10.1021/acs.analchem.9b01429
33. Ong LJY, Ching T, Chong LH, *et al.* Self-aligning Tetris-Like (TILE) modular microfluidic platform for

mimicking multi-organ interactions. *Lab Chip*. 2019;19(13):2178-2191. doi:10.1039/c9lc00160c
34. Seitzer U, Gerdes J. Generation and characterization of multicellular heterospheroids formed by human peripheral blood mononuclear cells. *Cells Tissues Organs*. 2003;174(3):110-116. doi:10.1159/000071151
35. Koh W, Stratman AN, Sacharidou A, Davis GE. Chapter 5 In Vitro Three Dimensional Collagen Matrix Models of Endothelial Lumen Formation During Vasculogenesis and Angiogenesis. *Methods Enzymol*. 2008;443(08):83-101. doi:10.1016/S0076-6879(08)02005-3
36. Lonza. Clonetics Endothelial Cell System Technical Information & Instructions. 2018:1-15. https://bioscience.lonza.com/lonza_bs/US/en/download/product/asset/29423.
37. Datta M, *Via* LE, Kamoun WS, *et al.* Anti-vascular endothelial growth factor treatment normalizes tuberculosis granuloma vasculature and improves small molecule delivery. *Proc Natl Acad Sci U S A*. 2015;112(6):1827-1832. doi:10.1073/pnas.1424563112
38. Polena H, Boudou F, Tilleul S, *et al.* Mycobacterium tuberculosis exploits the formation of new blood vessels for its dissemination. *Sci Rep*. 2016;6(August):1-11. doi:10.1038/srep33162
39. Su X, Theberge AB, January CT, Beebe DJ. Effect of microculture on cell metabolism and biochemistry: Do cells get stressed in microchannels? *Anal Chem*. 2013;85(3):1562-1570. doi:10.1021/ac3027228
40. Martinez AN, Mehra S, Kaushal D. Role of interleukin 6 in innate immunity to mycobacterium tuberculosis infection. *J Infect Dis*. 2013;207(8):1253-1261. doi:10.1093/infdis/jit037
41. Lin PL, Plessner HL, Voitenok NN, Flynn JAL. Tumor necrosis factor and tuberculosis. *J Investig Dermatology Symp Proc*. 2007;12(1):22-25. doi:10.1038/sj.jidsymp.5650027
42. Singh PP, Goyal A. Interleukin-6: A potent biomarker of mycobacterial infection. *Springerplus*. 2013;2(1):2-9. doi:10.1186/2193-1801-2-686
43. Engele M, Stöβel E, Castiglione K, *et al.* Induction of TNF in Human Alveolar Macrophages As a Potential Evasion Mechanism of Virulent Mycobacterium tuberculosis . *J Immunol*. 2002;168(3):1328-1337. doi:10.4049/jimmunol.168.3.1328
44. Domingo-Gonzalez R, Prince O, Cooper A, Khader SA. Cytokines and Chemokines in Mycobacterium tuberculosis Infection. *Microbiol Spectr*. 2016;4(5):1-37. doi:10.1128/microbiolspec.tbtb2-0018-2016
45. Theberge AB, Yu J, Young EWK, Ricke WA, Bushman W, Beebe DJ. Microfluidic Multiculture Assay to Analyze Biomolecular Signaling in Angiogenesis. *Anal Chem*. 2015. doi:10.1021/ac503700f
46. Sarkanen JR, Mannerström M, Vuorenpää H, Uotila J, Ylikomi T, Heinonen T. Intra-laboratory pre-validation of a human cell based in vitro angiogenesis assay for testing angiogenesis modulators. *Front Pharmacol*. 2011;JAN(January):1-13. doi:10.3389/fphar.2010.00147
47. Osherov N, Ben-Ami R. Modulation of Host Angiogenesis as a Microbial Survival Strategy and Therapeutic Target. *PLoS Pathog*. 2016. doi:10.1371/journal.ppat.1005479
48. Oehlers SH, Cronan MR, Scott NR, *et al.* Interception of host angiogenic signalling limits mycobacterial growth. *Nature*. 2015;517(7536):612-615. doi:10.1038/nature13967
49. Torraca V, Tulotta C, Ewa Snaar-Jagalska B, Meijer AH. The chemokine receptor CXCR4 promotes granuloma formation by sustaining a mycobacteria-induced angiogenesis programme. *Sci Rep*. 2017;7(February):18-20. doi:10.1038/srep45061
50. Oehlers SH, Cronan MR, Beerman RW, *et al.* Infection-induced vascular permeability aids mycobacterial growth. *J Infect Dis*. 2017;215(5):813-817. doi:10.1093/infdis/jiw355
51. Harding JS, Herbath M, Chen Y, *et al.* VEGF-A from Granuloma Macrophages Regulates Granulomatous Inflammation by a Non-angiogenic Pathway during Mycobacterial Infection. *Cell Rep*. 2019;27(7):2119-2131.e6. doi:10.1016/j.celrep.2019.04.072
52. Bishop ET, Bell GT, Bloor S, Broom IJ, Hendry NFK, Wheatley DN. An in vitro model of angiogenesis: Basic features. *Angiogenesis*. 1999;3(4):335-344. doi:10.1023/A:1026546219962
53. Theberge AB, Yu J, Young EWK, Ricke WA, Bushman W, Beebe DJ. Microfluidic Multiculture Assay to Analyze Biomolecular Signaling in Angiogenesis. *Anal Chem*. 2015;87(6):3239-3246. doi:10.1021/ac503700f

Chapter 7. Conclusions and Outlook

Open microfluidics is a rapidly evolving field, as advances in the theory, fabrication methods, and applications are all supporting innovation in this field.[1] The material presented in this dissertation contributes to the advancement of this field, and links open microfluidics with cell signaling, infectious disease, and biological and chemical analysis. This dissertation is broadly separated into two sections: the first, discussing the creation of platforms that leverage existing and new understanding of the fundamentals of open microfluidics to create novel systems; and the second, demonstrating the development and validation of analytical systems and models that can be used to probe cell-cell signaling phenomena with important biological implications. Overall, the work presented here lays a foundation for future studies that innovate on the described technologies and find novel applications in human physiology and disease.

Translation of important techniques from traditional closed channel microfluidics towards open platforms increases the accessibility, adaptability, customization, and ease of fabrication associated with those techniques. We begin to assemble a toolbox for open-channel droplet-based microfluidics, demonstrating the ability to incubate, translate, mix, split, and analyze droplets within a simple open channel. Additionally, through the derivation of a generalized model describing the fluid flow within our open channel, we provide a basis for further application of our droplet-based system that includes cell culture and on-chip chemical reactions. Further, we add to this open microfluidic toolbox through the development of a hydrogel patterning insert that can be used to create segregated cell culture chambers on commercially available cell culture substrates, allowing straightforward adaptation and integration with existing biological workflows. Importantly, the development of this technology has laid the foundation for new avenues of research within our research group and has been further developed and validated for various biological applications.[2,3] These technologies contribute to the field of microfluidics and the subset of open microfluidics, demonstrating not only the creation of these new technologies, but also the

implementation, use, and transfer of these systems, which are important stages of development that are often not reached with new innovations.

Cell signaling drives physiological functionality across a wide range of biological environments and systems, underlying key processes such as immune response, tissue repair, regulation of homeostasis, and organ development. However, the microenvironments that encompass these complex signaling milieus are difficult to study and prevent researchers from connecting signals (or sets of signals) with their associated role in these processes. Introduction of new analytical methods and models offers new capabilities to probe these environments. We describe the creation of a novel bead-based system that facilitates localization of cell-secreted signals through the ability of the bead to tether to the cell surface and capture soluble factors as they are secreted. This analytical approach enables the resuscitation of signals that are lost in bulk analysis due to the presence neutralizing factors, and future work on this technology is focused on increasing its customizability and compatibility with different biological systems. In addition to the analytical bead-based technique, we adapted an open microfluidic platform to create a modular microscale infection model to study immune-microenvironment signaling during a mycobacterial infection. The creation of this *in vitro* model demonstrates an important contribution towards advancing microfluidic infection models due to its transferability and simplicity, while also illustrating the successful transfer of a previously described platform.[4] Additionally, through the creation of an adaptable *in vitro* granuloma model, this work provides infectious disease researchers with a new tool for the study of mycobacterial infections and infection-induced signaling in general. Lastly, the techniques and technologies described here represent foundational analytical and modeling approaches and warrant further development to increase their potential impact. Therefore, the work described in this dissertation should serve as encouragement to not only develop new strategies that progress the field of open microfluidics and cell-cell signaling, but also to advance existing approaches to increase their relevance and applicability across a wide range of fields and uses.

References:

1. Berthier E, Dostie AM, Lee UN, Berthier J, Theberge AB. Open Microfluidic Capillary Systems. *Anal*

Chem. 2019;91(14):8739-8750. doi:10.1021/acs.analchem.9b01429
2. Lee UN, Day JH, Haack AJ, *et al.* Layer-by-layer fabrication of 3D hydrogel structures using open microfluidics. *Lab Chip*. 2020;20(3):525-536. doi:10.1039/c9lc00621d
3. Day JH, Nicholson TM, Su X, *et al.* Injection molded open microfluidic well plate inserts for user-friendly coculture and microscopy. *Lab Chip*. 2019;20(1):107-119. doi:10.1039/c9lc00706g
4. Yu J, Berthier E, Craig A, *et al.* Reconfigurable open microfluidics for studying the spatiotemporal dynamics of paracrine signalling. *Nat Biomed Eng*. 2019;3(10):830-841. doi:10.1038/s41551-019-0421-4

Appendix A

Reproduced in part with permission from Berry, S.B.*; Lee, J.J.*; Berthier, J.; Berthier, E.; Theberge, A.B. "Droplet incubation and splitting in open microfluidic channels". *Anal. Methods*, 2019, 11, 4528-4536.

*denotes co-authorship

A1: Droplet Behavior Modes in Open Channel Platform

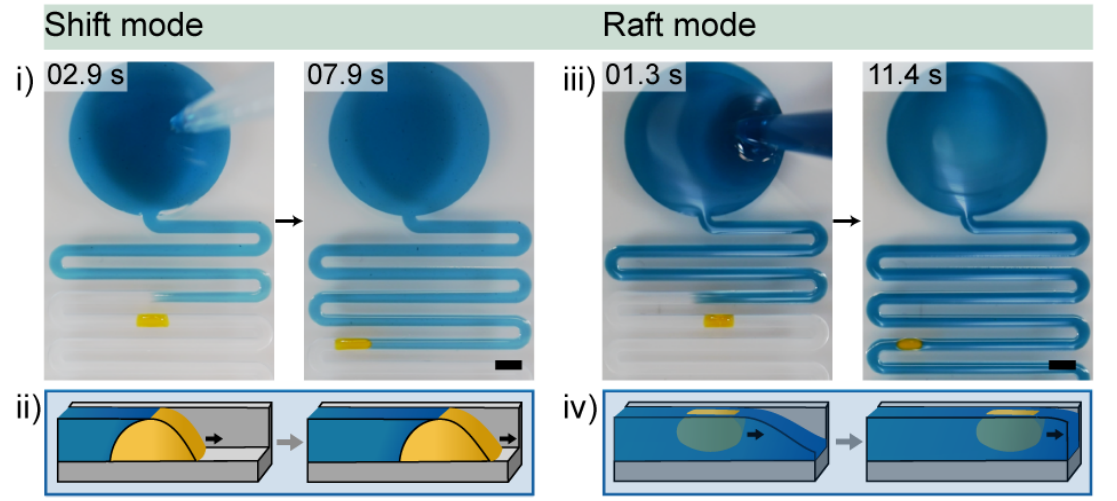

Figure A1: A single static aqueous droplet (yellow) is pipetted into the channel and can display either shift mode ((i) and (ii)) or raft mode ((iii) and (iv)) as carrier fluid (blue) moves the aqueous droplet down channel.[1] For shift mode, the carrier phase is 1-pentanol; for raft mode, the carrier phase is toluene. Scale bar: 2 mm. Schematics in (ii) and (iv) are reproduced from Lee *et al.*[1]

Reference:

1. Lee, J.J.; Berthier, J.; Brakke, K.A.; Dostie, A.M.; Theberge, A.B.; Berthier, E. Droplet behavior in Open Biphasic Microfluidics. *Langmuir*, **2018**, 34, 18, 5358-5366.

A2: Detailed Device Schematics and Dimensions

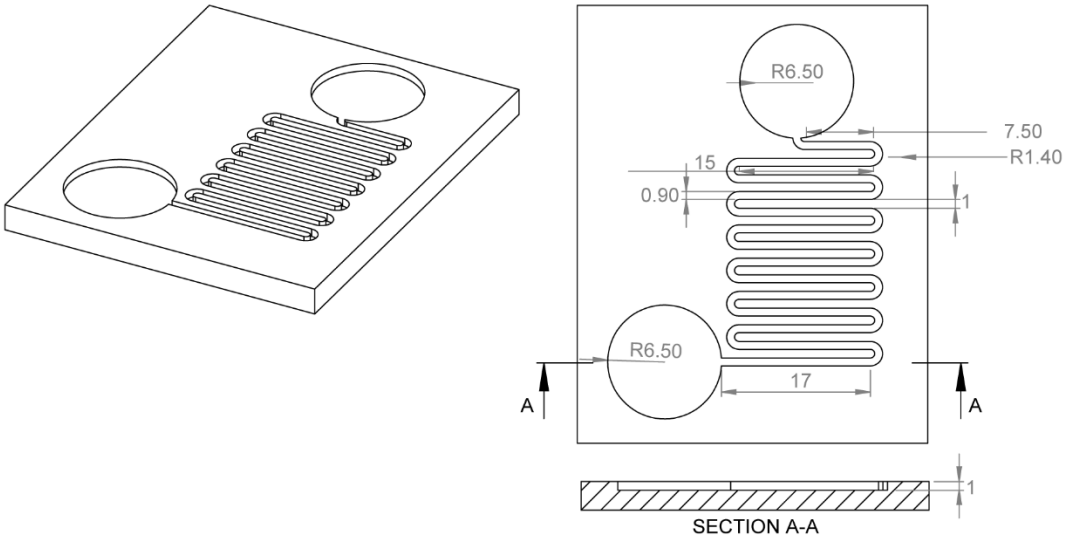

Figure A2i: Detailed device schematics illustrating device dimensions for the Coalescence Device (Figure 2.2A). Units in mm.

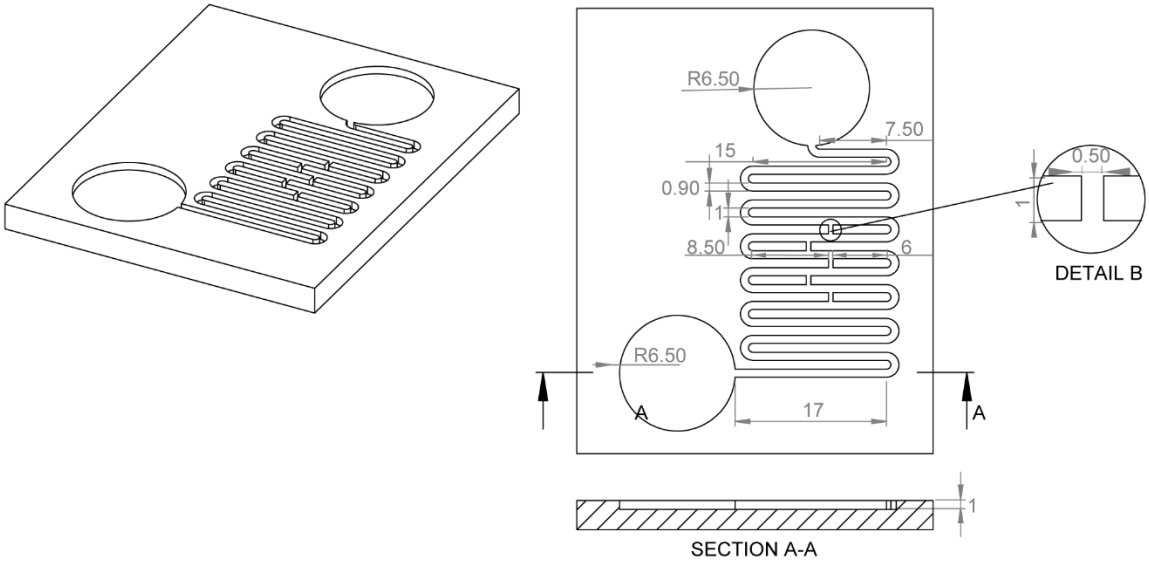

Figure A2ii: Detailed device schematics illustrating device dimensions for the Bypass Device without a step (Figure 2.2B). Units in mm.

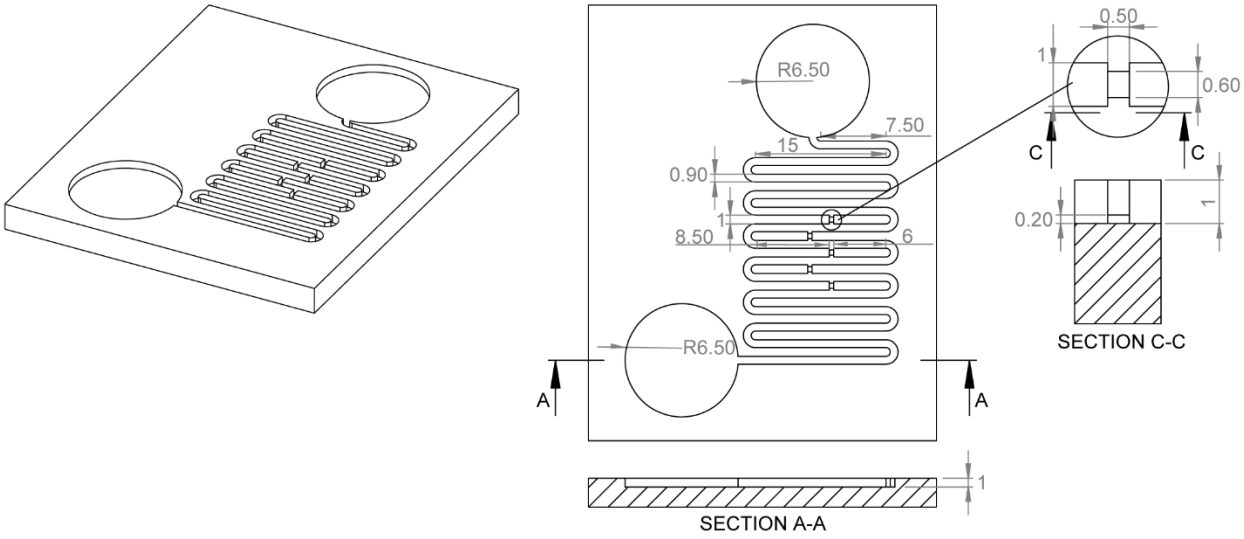

Figure A2iii: Detailed device schematics illustrating device dimensions for the Bypass Device with a step (Figure 2.2C). Units in mm.

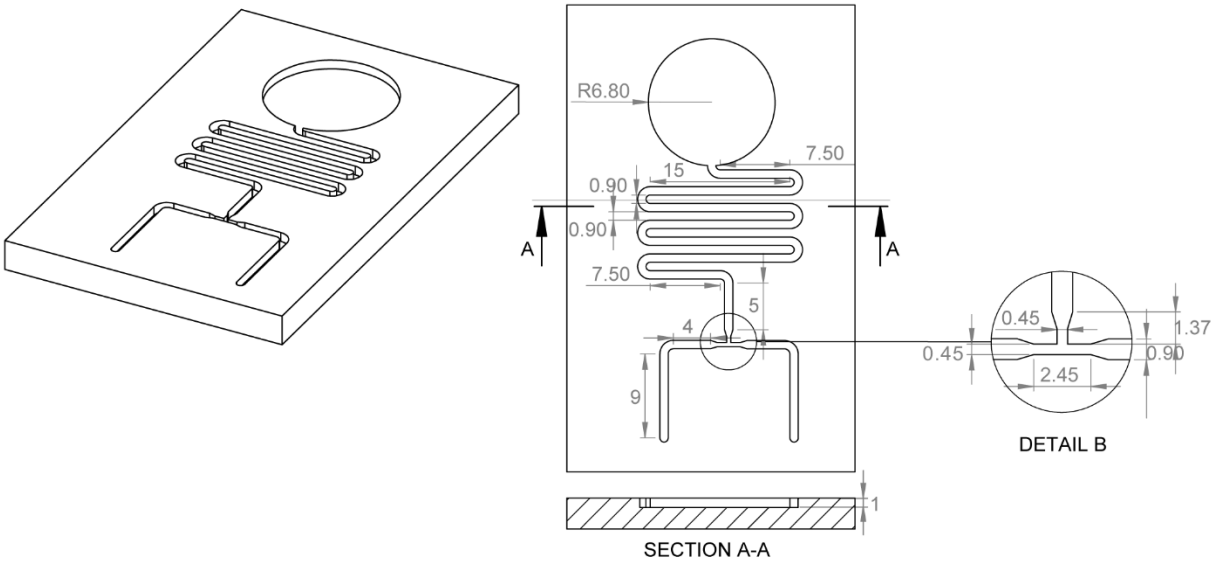

Figure A2iv: Detailed device schematics illustrating device dimensions for the symmetric splitting T junction device (Figure 2.4B). Units in mm.

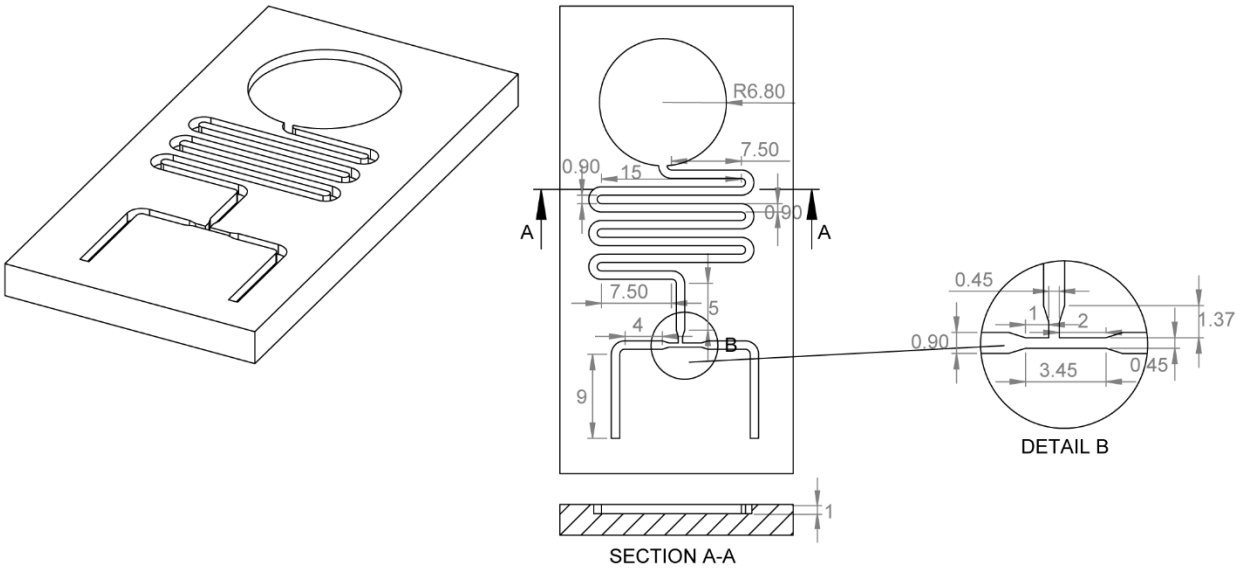

Figure A2v: Detailed device schematics illustrating device dimensions for the asymmetric splitting T junction device (Figure 2.4C). Units in mm.

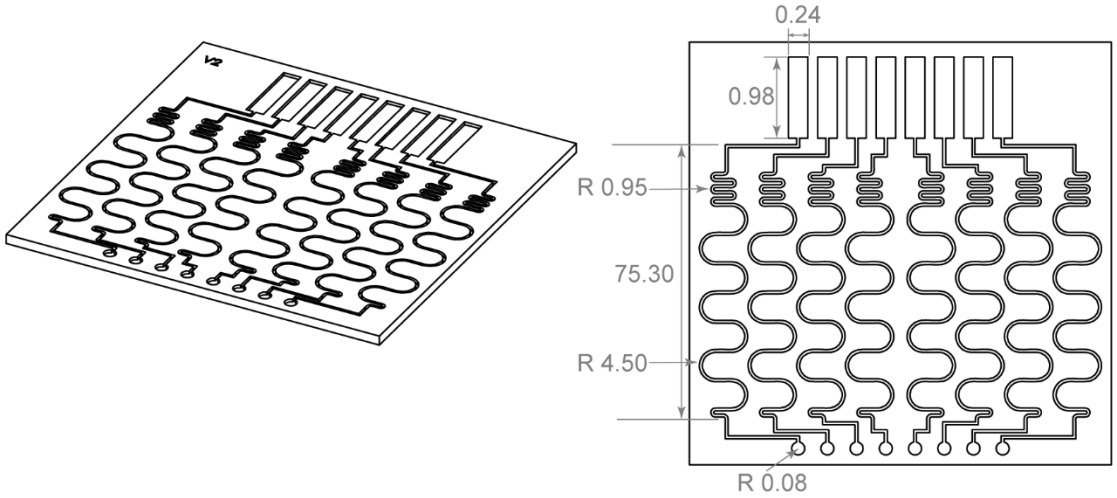

Figure A2vi: Detailed device schematics illustrating device dimensions for the multichannel coalescence device (Figure 2.3). Units in mm.

A3: Derivation of Analytical Model for Resistance and Flux

In this model, we considered an open channel system with a bifurcation and two nodes, where the flows partition at the first node (green dot) and join at the second (red dot). Between the two nodes are two different branches (blue and yellow outlines); Branch 1 is an extension of the main channel, and Branch 2 is the bypass channel with a step in the middle (Figure A3i).

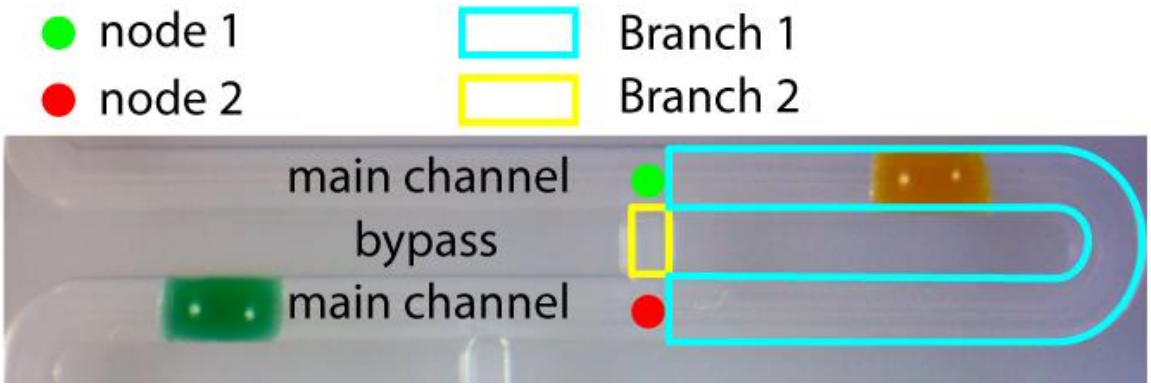

Figure A3i: Labeled top view image of open channel system.

Based on previous work[1] on the creation of a generalized Lucas-Washburn law for varying shapes driven by capillary flow and application of the analogy of an electric circuit, we can write:

$$\Delta P = P_1 - P_2 \approx \tilde{R}_1 Q_1 \approx \tilde{R}_2 Q_2 \quad (1)$$

$$\mu \frac{p}{\lambda S^2} L = R \quad (2)$$

Where P_1 and P_2 are the pressures at node 1 and node 2, respectively, R is the resistance, L is the length, Q is the flux, S is the channel cross sectional area, μ is the liquid viscosity, p is the total perimeter, and λ is the friction length.[2]

Solving equation 1 for Q:

$$\left(\frac{\tilde{R}_1}{\tilde{R}_2}\right) = \left(\frac{Q_2}{Q_1}\right) \quad (3)$$

From Equation 3, we have a relation that describes the flow rate in terms of the resistance and can be used to calculate the specific resistance for each channel with physical parameters from the system. However, Branch 2 has a heterogenous cross section due to the step; therefore, the resistances of each section of the bypass channel must be considered to find the total resistance through Branch 2:

$$\left(\frac{\tilde{R}_1}{\tilde{R}_2}\right) = \left(\frac{\widetilde{R_1}}{\widetilde{R_i}+\widetilde{R_{ii}}+\widetilde{R_{iii}}}\right) = \left(\frac{Q_2}{Q_1}\right) \quad (4a)$$

And plugging in Equation 2:

$$\left(\frac{\mu\frac{p_1}{\lambda_1 S_1^2}L_1}{\mu\frac{p_i}{\lambda_i S_i^2}L_i+\mu\frac{p_{ii}}{\lambda_{ii} S_{ii}^2}L_{ii}+\mu\frac{p_{iii}}{\lambda_{iii} S_{iii}^2}L_{iii}}\right) = \left(\frac{Q_2}{Q_1}\right) \quad (4b)$$

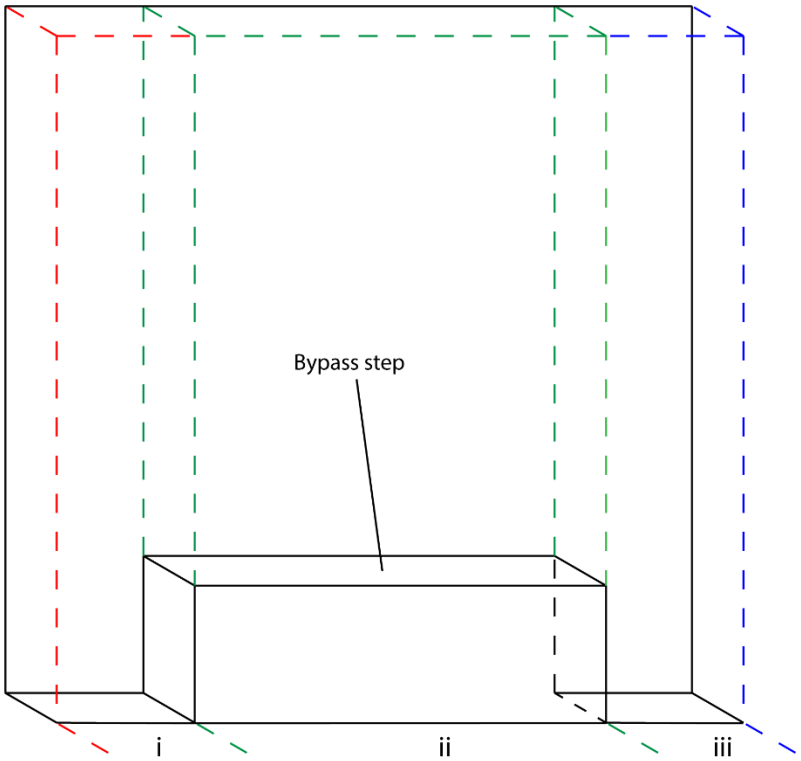

Figure A3ii: Isometric view of cross section of Branch 2 (Bypass)

Where i, ii, and iii represent the separate sections within the bypass channel (Figure A3ii). Plugging in the physical parameters into Equation 4b provides the ratio of the fluxes between the bypass channel and the main channel. For our specific stepped bypass platform:

$$\frac{Q_2}{Q_1} = 2.68 \tag{5a}$$

And without a step in the bypass channel:

$$\frac{Q_2}{Q_1} = 3.18 \tag{5b}$$

These calculations demonstrate that incorporation of the step into the bypass decreases the flux through the bypass by increasing the resistance through the bypass channel. The decreased flux through the bypass (Branch 2) corresponds to an increased flux through the main channel (Branch 1), which drives the droplets completely through the curves in the channels and allows them to flow to the outlet.

References:

2. Berthier, J.; Gosselin, D.; Berthier, E. A generalization of the Lucas-Washburn Rideal law to composite microchannels of arbitrary cross section. Microfluid. Nanofluid., 2015, 19, 3, 497-507.
3. Lee, J.J.; Karampelas, I.H.; Brakke, K.A.; Theberge, A.B.; Berthier, E.; Berthier, J. Capillary flow in open microgrooves: bifurcations and networks. Langmuir. 2019, 35, 32, 10667-10675.

A4: Workflow for Droplet Length Measurements

To measure the length of the aqueous droplets in our channels, we designed and fabricated T junction platforms without outlet reservoirs. As with the devices with the outlet reservoir, we pipetted a 3 µL droplet upstream of the T junction and the added carrier fluid to the inlet reservoir. After initiation of spontaneous capillary flow (SCF) and splitting of the droplet, daughter droplets flowed to the end of the channel, where they stopped and were compressed as the device filled with carrier fluid. Once the device was completely filled and flow had completely ceased, the daughter droplets at the end of the channel were imaged. Images of droplets were then analyzed with ImageJ. Specifically, A-B) images were opened (symmetric droplet image) and scaled (Analyze, set scale); C) the "Segmented Line" tool was then selected and a vertical line was drawn from the top of each droplet to the bottom. D) The segmented line was measured (Analyze, measure) and droplet lengths were recorded.

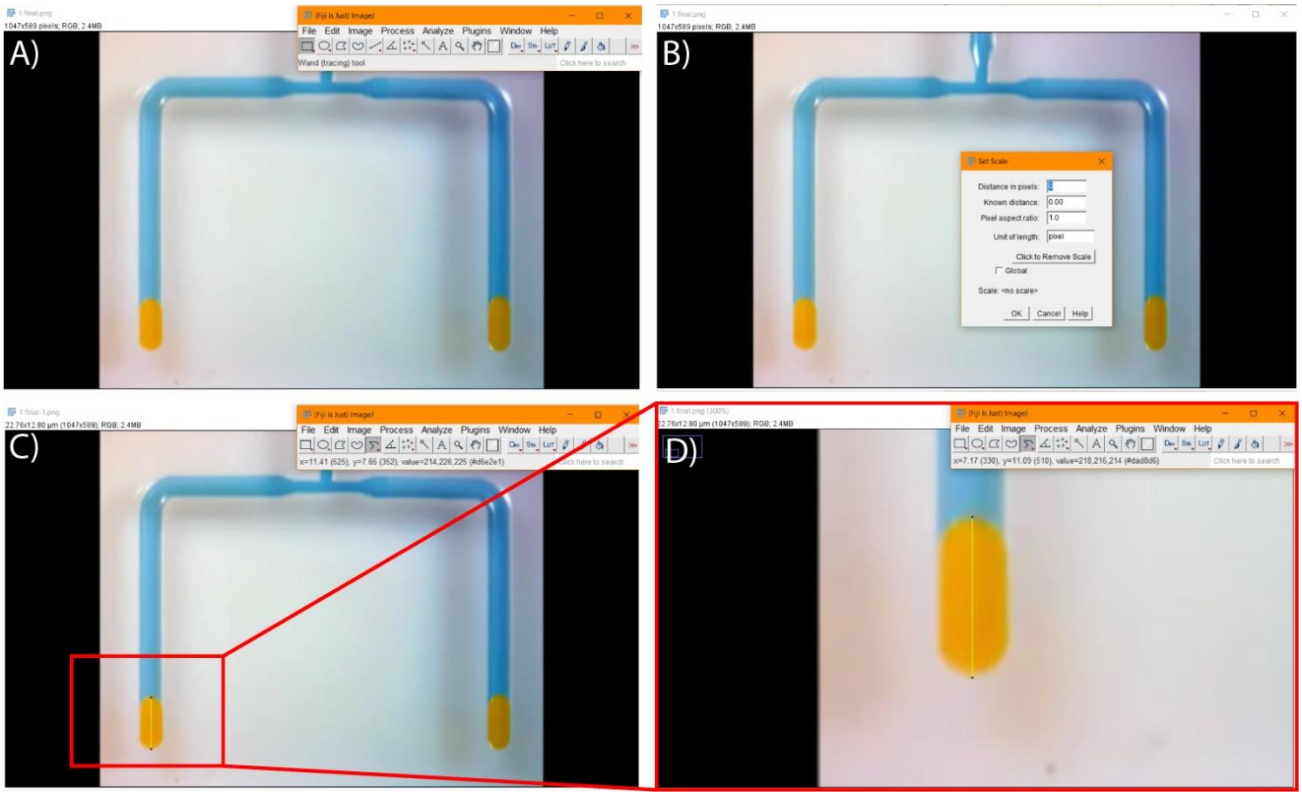

Figure A4: Workflow for droplet length measurement. A) The image to be measured is opened using ImageJ; B) to set the scale, we selected "Analyze, set scale" and changed the scale from pixels to µm; C) the Segmented Line tool is selected, and a line is draw from one end of the droplet to the other (interface of droplet and carrier phase and boundary of droplet and end of channel); D) zoomed-in image illustrating the line drawn on the droplet.

A5: Droplet splitting reproducibility within a single device

To demonstrate the reproducibility of droplet splitting within a single device, we measured the droplet area and perimeter after splitting in one device. After flowing the droplet through the 1:1 T-junction (Fig. 2.4B) and measuring droplet area and perimeter once it reached the outlet reservoir, the device was washed with 70% ethanol, rinsed with water, dried with compressed air, and then reused. Images were analyzed using ImageJ and the "circle" drawing tool to encapsulate the droplet prior to measurement and recording.

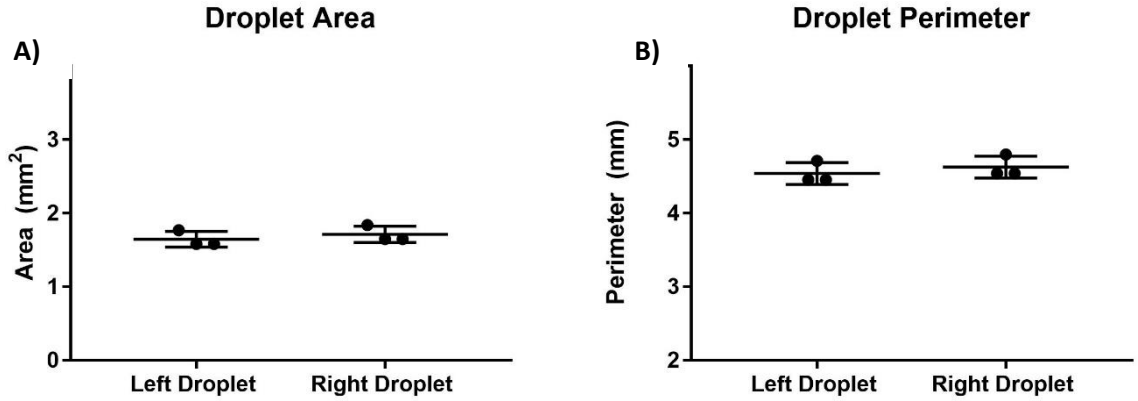

Figure A5: Reproducibility of droplet splitting within one device. Daughter droplet area (A) and perimeter (B) were measured using ImageJ for one droplet split using the 1:1 T-junction device in n=3 independent experiments. After splitting and droplet quantification, the same device was cleaned, dried, and used for the subsequent independent experiment. Mean and standard deviation are indicated for n=3 droplets across n=3 independent experiments.

Appendix B

Reproduced in part with permission from Berry, S.B.*; Zhang, T.*; Day, J.H.; Su, X.; Wilson, I.Z.; Berthier, E.; Theberge, A.B. "Upgrading well plates using open microfluidic patterning". *Lab Chip*, 2017, 17, 4253-4264.

*denotes co-authorship

Derivation of theoretical model for conditions for flow in our platform

The pressure in the aqueous phase is generated by surface tension and can be evaluated using the Young-Laplace equation, where ΔP is the pressure difference across a curved air-liquid interface, γ is the interfacial tension, and R_1 and R_2 are the radii of curvature of the interface at a point on the interface in two orthogonal directions (*e.g.*, horizontal and vertical).

The Laplace pressure difference (ΔP) at every interface is zero when the interface is flat ($R_1 = R_2 = \infty$). When the curvature of an interface is concave due to favorable wetting (*i.e.*, contact angle < 90°), the Laplace pressure difference becomes negative. Inversely, when the curvature is convex, the Laplace pressure difference becomes positive. Laplace pressure is a well-defined phenomenon that can be controlled experimentally and used to predict conditions for flow in our system.

Conditions for flow in an open channel have been derived in a general way by Berthier *et al.*[1] and are known as the spontaneous capillary flow (SCF) equation (in the case of a channel that has the same contact angle on all faces) or as the generalized Cassie angle equation (for the more general case when there are any number of contact angles along the surface of the channel). The current analytical models, however, assume that the pressure at the inlet of the open channel is negligible. The models allow prediction of the theoretical ability for SCF to occur. In order to refine the conditions for flow in our system, we added a pressure balance analysis between the surface tension-based pressures at the inlet and at the advancing fluid front (assuming the front exists).

The inlet of our system is a rectangular cross-section defined by the insert and the walls of the well plate. The liquid meniscus at the inlet is concave due to the wettability of the insert and well (contact angle < 90°) and the interface will take the shape of a cylinder (as the channel cross-section is long (8.6 mm) and narrow (1 mm)). The radius of curvature along the long edge of the channel inlet is thus infinitely large, while the radius of curvature R_3 along the smaller edge of the inlet is uniquely characterized by two different contact angles with the device insert and the well plate, respectively (Figure B1). The pressure of the fluid at the inlet is written as:

$$\Delta P_{\text{inlet}} = \gamma \left(\frac{1}{R_3}\right) \quad \text{(Eq. 1)}$$

The fluid front advancing under the plastic rail has a more complex geometry. The fluid front is described by a saddle point as the liquid is wetting the rail ceiling and well floor plastics (creating a concave fluid interface in the x-z plane) and is rounded from the top view as the channel does not have any side walls (the interface is convex in the x-y plane) (Figure B1). The pressure at the fluid front is described by Eq. 2, where R_1 is chosen to be the radius of curvature in the x-z plane, and R_2 is chosen as the radius of curvature in the x-y plane:

$$\Delta P_{\text{front}} = \gamma \left(\frac{1}{R_1} + \frac{1}{R_2}\right) \quad \text{(Eq. 2)}$$

The condition for flow in our system requires the Laplace pressure of the inlet to be greater than the Laplace pressure at the fluid front in order to drive the fluid towards the area of lowest pressure:

$$\gamma\left(\frac{1}{R_3}\right) > \gamma\left(\frac{1}{R_1}+\frac{1}{R_2}\right) \quad \text{(Eq. 3)}$$

Therefore, the limit of flow will occur when the two pressures are equal:

$$\gamma\left(\frac{1}{R_3}\right) = \gamma\left(\frac{1}{R_1}+\frac{1}{R_2}\right) \quad \text{(Eq. 4)}$$

Or:

$$\frac{1}{R_1}+\frac{1}{R_2}-\frac{1}{R_3}=0 \quad \text{(Eq. 5)}$$

The radii of curvature in our system are governed by the physical aspect ratio of the channel, which includes the width w of the rail and the gap g_{front} between the rail and the well plate ($g_{front} = h$), the gap g_{inlet} between the insert and the well wall, and the contact angles of the fluid on the rail and the well plate surfaces.

We derived an equation for the radius of curvature of the fluid in the advancing filament in the x-z plane in function of the contact angles of the fluid on the well plate (θ_2), the contact angle of the fluid on the rail (θ_1), and the height of the rail (h). Using the geometric relations illustrated in Figure B1, we obtain:

$$R_1 = -\left(\frac{h}{\cos\theta_1+\cos\theta_2}\right) \quad \text{(Eq. 6)}$$

To assess the curvature of radius R_2, we assume that the fluid is minimizing the surface energy, and thus assume that the interface is taking the shape of a large semi-circle of the same radius as the half-width of the rail.

We apply the same reasoning utilized to determine R_1 in Eq. 6 in order to derive R_3, as a function of g_{inlet}, θ_2, and θ_1. Substitution of R_1, R_2, and R_3 into Equation 5 yields:

$$\frac{1}{-\left(\frac{h}{\cos\theta_1+\cos\theta_2}\right)}+\frac{1}{\frac{w}{2}}-\frac{1}{-\left(\frac{g_{\text{inlet}}}{\cos\theta_1+\cos\theta_2}\right)}=0 \quad \text{(Eq. 7)}$$

Where w is the width of the rail, h is the height of the rail, and g_{inlet} is the space between the well and the device at the inlet in mm. Solving for h yields:

$$h = \frac{\cos\theta_1+\cos\theta_2}{\frac{2}{w}+\frac{\cos\theta_1+\cos\theta_2}{g_{\text{inlet}}}} \quad \text{(Eq. 8)}$$

Equation 8 is graphed to give the boundary between the red and green shaded regions in Figure 3.2b, providing a model to predict when flow will occur in our system for devices based on the device dimensions.

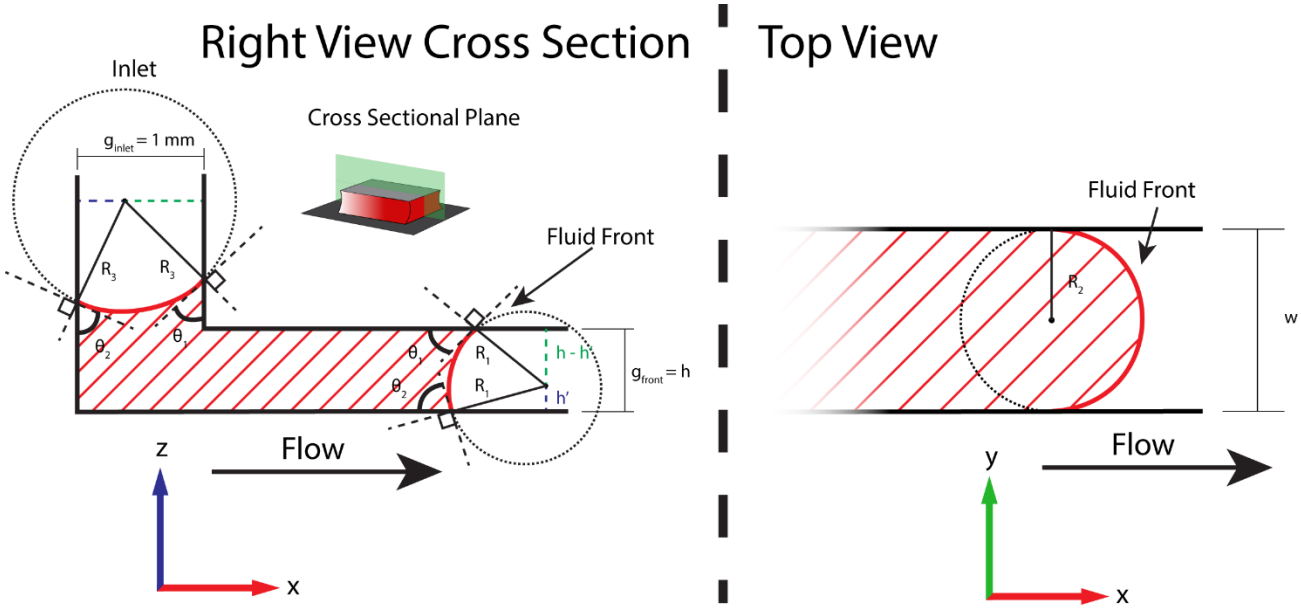

Figure B1. Illustrations of radii of curvature for the calculation of Laplace pressure differences in our system. Perspectives demonstrate the radii of curvature (R), the contact angle between the liquid and the surface (θ), the height of the channel (h), the width of the channel (w), and the gap between the insert and the patterned surface (g).

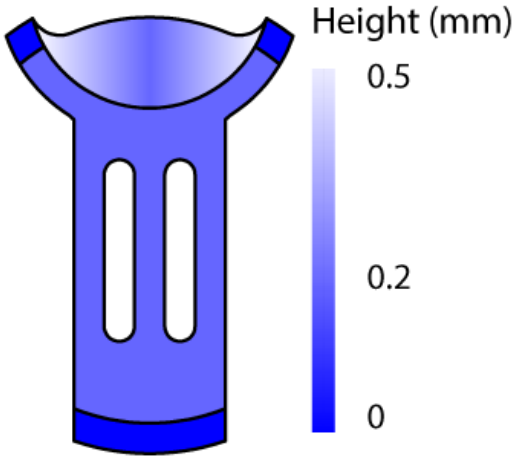

Figure B2. Heat map illustrating the height of the rail above the well plate surface. Regions of the device with a lower height to width ratio are more favorable for spontaneous capillary flow (SCF), and tuning the height as shown enables controlled and reproducible hydrogel flow. The height gradient along the loading zone directs flow towards the middle of the flow path while feet (shown in dark blue, h = 0 mm) keep the patterning region off the surface.

a)

Device aspect ratio (designed width vs height)	Measured width of 3D printed rail (mm)	Measured hydrogel wall width (mm)	Difference between measured hydrogel wall width and rail width (mm)
1 mm x .15 mm	0.778 ± .010	1.220 ± 0.028	0.442
.75 mm x .15 mm	0.540 ± .012	0.968 ± 0.035	0.428
.75 mm x .25 mm	0.540 ± .012	1.044 ± 0.014	0.504

b)

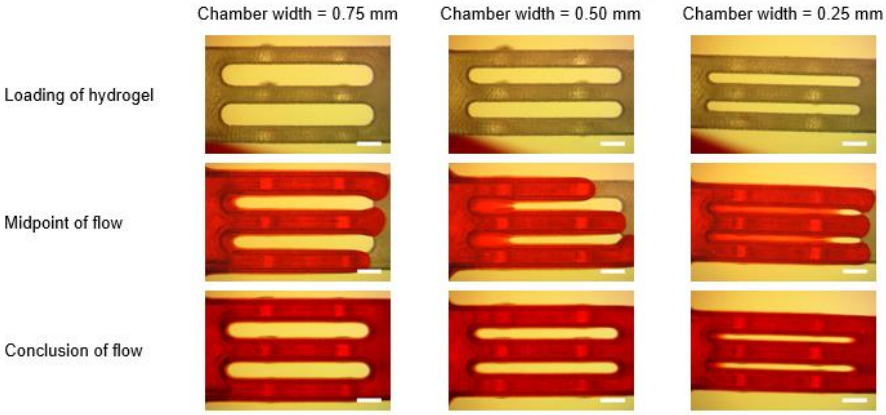

c)

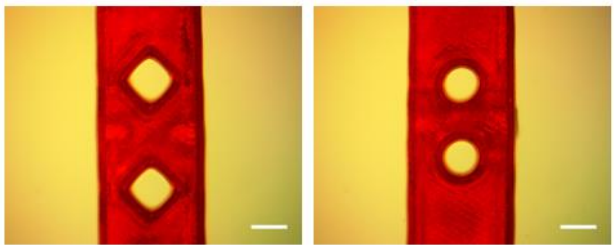

Figure B3. Extent of device patterning capabilities on TCT PS. A) Extent of flooding along a rail. Devices were filled with matrigel dyed with red food dye and imaged from beneath (n = 3 devices). Data presented in the table represent the average width of the wall ± SD for three different device aspect ratios. Height, in addition to width, influences the flooding of the chamber by the wall. B) Limit of culture chamber area due to flooding. Our platform enables fabrication of culture chambers down to a resolution of 0.25 mm width, below which we observed complete flooding of the culture chambers during the flow. At the conclusion of flow, the gel receded from the chamber leaving gel residue on the chamber floor. Images are representative of flow in n = 3 devices on TCT PS at different time points. Scale bar = 1 mm. C) Geometric patterning capabilities of our platforms. Scale bars = 1 mm.

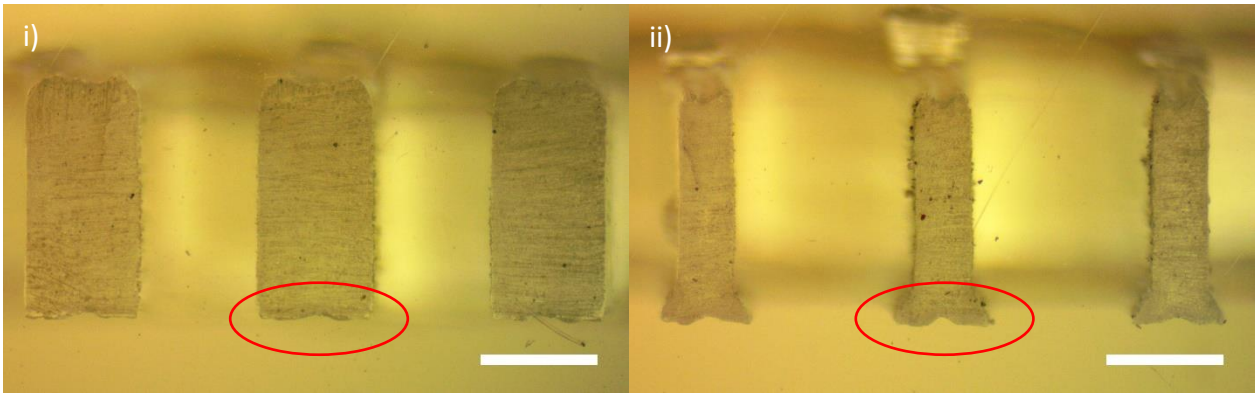

Figure B4. Images represent the trapezoidal rail cross section. Cross sections presented here illustrate the rail without (i) and with (ii) a trapezoidal pinning feature at the scale used in each device. 3D-printed defects can be observed along the base of the rail, which were consistent throughout all devices. Scale bar = 1 mm.

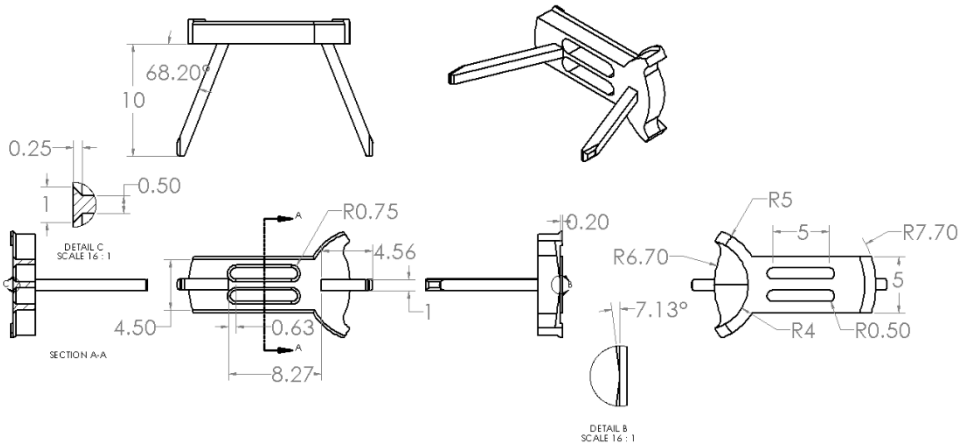

Figure B5. Schematic diagrams illustrating the dimensions of our platform. All dimensions are in mm.

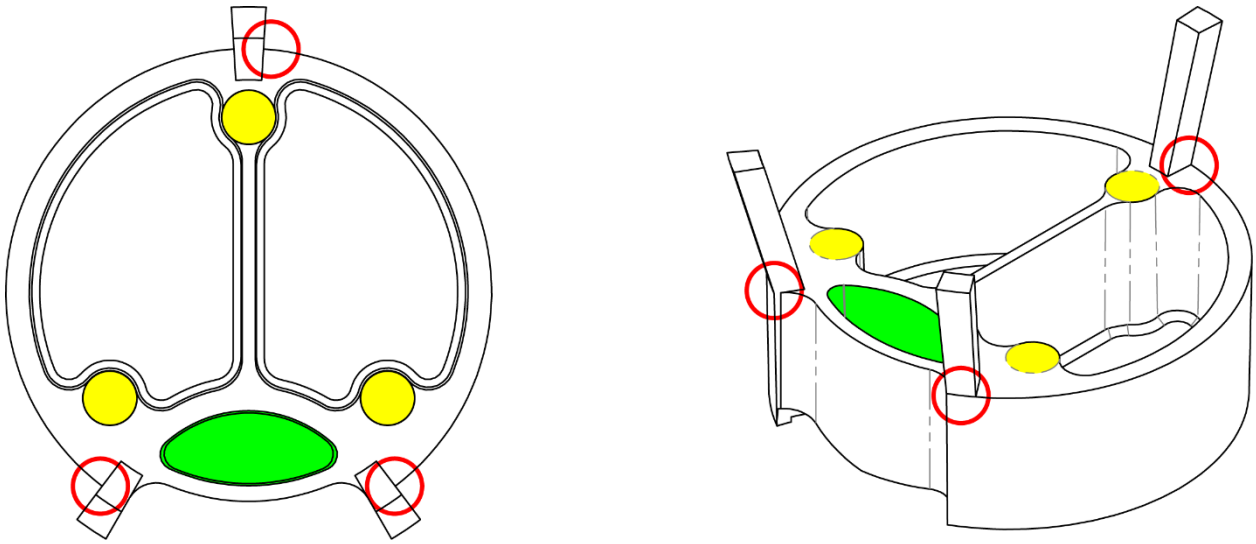

Figure B6. Schematic images of an injection-moldable version of the Monorail Device. The Monorail design was modified for manufacturing by injection molding through the addition or modification of features of importance to the injection molding process. These features include: mold ejection zones (yellow) that provide an increased surface area for ejection pin/device contact; a cavity (green) to maintain a homogenous device thickness and avoid device deformation during cooling and setting steps; and re-positioned pressure struts (red) to avoid overhang, allowing fabrication with a two-piece mold. Further, the entire piece is drafted to a 1^{o} angle to aid in device removal from the mold.

Table B-1. Optimized matrigel loading volumes associated with each device aspect ratio and geometry

Device	Height (mm)	Width (mm)	Loading Volume (μL)
Figure 3.2b	0.15	0.50	25
	0.15	0.60	25
	0.15	0.75	20
	0.15	1.00	20
	0.25	0.50	35
	0.25	0.60	35
	0.25	0.75	30
	0.25	1.00	25
	0.35	0.50	35
	0.35	0.60	35
	0.35	0.75	30
	0.35	1.00	30
Figure 3.2c	0.25	1.00	25
Figure 3.3	0.20	1.00	25
Figure 3.4a	0.20	1.00 - 2.00	35
Figure 3.4b	0.20	1.00	85
Figure 3.5	0.20	1.00	40
Figure 3.6	0.20	1.00	50

Reference:

1. J. Berthier, K.A. Brakke, E. Berthier, “Open Microfluidics”. Wiley; 2016.

Appendix C

Reproduced in part with permission from Berry, S.B.; Haack, A.; Theberge, A.B.; Brighenti, S.; Svensson, M.; "Host and pathogen communication in the respiratory tract: mechanisms and models of a complex signaling microenvironment". *Front. Med.* Submitted.

***In Vitro* Model Type**	**Advantages/Disadvantages**	**Specific Examples**	**Applications for investigating cross-talk in infections**
Transwell/cell culture inserts	+ Simple and robust + Compatible with standard cell culture equipment + Standard air-liquid interface protocol + No external equipment requirement (*e.g.* pumps or vacuum for controlled fluid or air flow) + Compatible with established readouts (*e.g.* microscopy, RNA analysis) + Access to cultures for direct manipulation – Limited customization – Mechanically static – Poorly quantified diffusion gradients	Nguyen Hoang *et al.* 2012 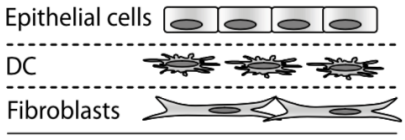	• Direct contact signaling • Soluble factor signaling • Co-culture with various cell types (*e.g.*, DCs, stromal cells) • Air-liquid interface on 3D culture • Cell-permeable inserts can be used for neutrophil/immune cell migration modeling through epithelium
Mechanically "breathing" microfluidic model	+ Cyclic airflow and mechanical stretching possible + Continuous nutrient/media flow + Customizable + ALI compatible + Compatible with established readouts (*e.g.* microscopy, RNA analysis) + Control over diffusion gradients – External equipment required (*e.g.* syringe pump for fluid flow control and vacuum pump for pressure control). – Microfabrication technology may be necessary for additional customization	Huh *et al.* 2010, Benam *et al.* 2016 "Lung-on-a-Chip" 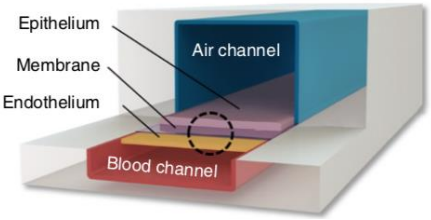	• Direct contact signaling • Soluble factor signaling • Investigations involving mechanical stretch • Investigations requiring controlled air or liquid flow • Coculture with multiple cell types (*e.g.*, endothelium) • Porous membrane allows for neutrophil/immune cell migration modeling through epithelium • Control over airflow in ALI model

	– Difficult to access cultures for direct manipulation	Stucki *et al.* 2015 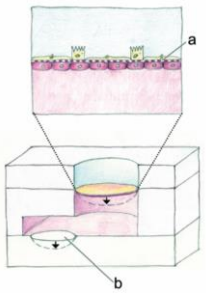 	• Direct contact signaling • Soluble factor signaling • Investigations involving mechanical stretch • Investigations requiring controlled air or liquid flow • Coculture with multiple cell types (*e.g.*, endothelium) • Porous membrane allows for neutrophil/immune cell migration modeling through epithelium • Open well for easier access of culture for downstream analysis
Hydrogel-based microfabricated models	+ Customizable + Complexity in tissue components and shape + Multiple signaling modes (*i.e.*, volatile, direct contact, soluble factor, *etc.*) + ALI compatible + Open systems enable access to cultures for direct manipulation – External equipment may be required if controlled fluid flow or airflow is desired – Microfabrication technology may be necessary for additional customization	Barkal *et al.* 2017 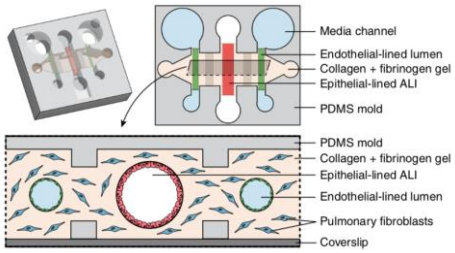 	• Volatile signaling coculture experiments • Direct contact signaling • Soluble factor signaling • Investigations involving endothelial, mesenchyme and epithelial cells • Modular cell culture experiments • Co-infection experiments
		Humayun *et al.* 2019 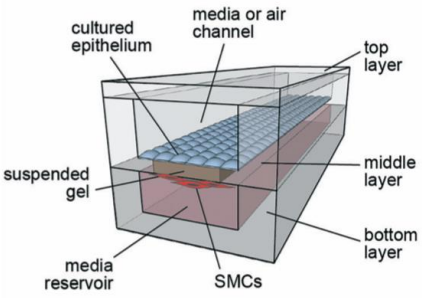 	• Co-culture with epithelial and smooth muscle cells • Native ECM interactions (*i.e.* collagen/matrigel) • Continuous media flow • Air liquid interface • Soluble factor signaling • Direct contact signaling

Table C1: *In vitro* lung models to study communication in the pulmonary microenvironment. Models are broadly grouped into three separate classifications: Transwells/cell culture inserts, mechanically "breathing" microfluidic models, and hydrogel-based microfabricated models. Advantages and disadvantages of each is described, as well as representative examples of each type.

Appendix D

Reproduced in part with permission from van Neel, T.L.*; Berry, S.B.*; Berthier, E.; Theberge, A.B. "Localized Cell-Surface Sampling of Secreted Factors Using Cell-Targeting Beads". In preparation. *denotes co-authorship

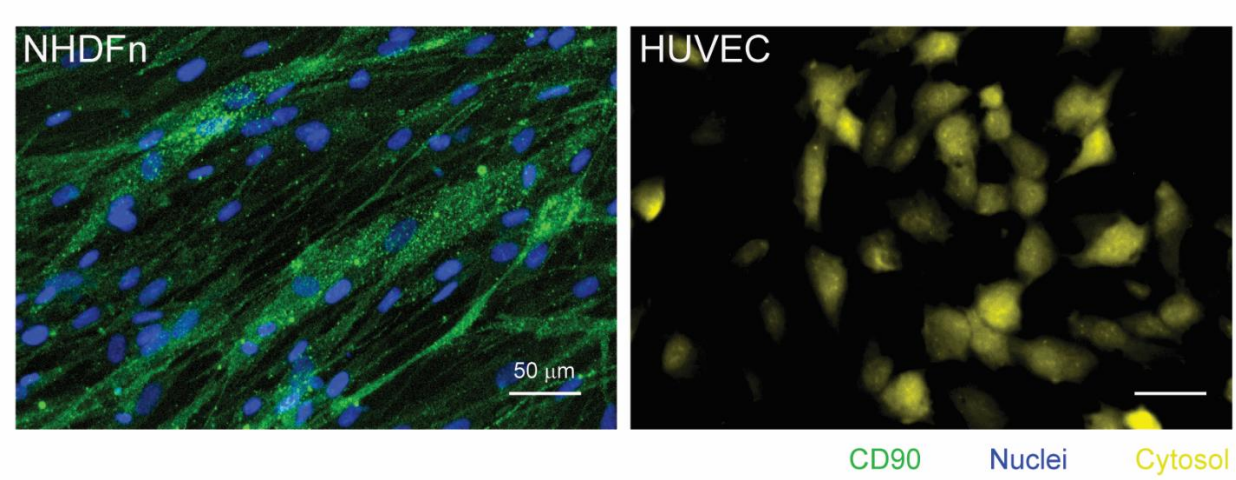

Figure D1: Validation of CD90 expression by NHDFn cells using immunocytochemistry. CD90 expression (green) was confirmed in NHDFn ($CD90^+$ cells) using standard immunocytochemistry techniques. HUVECs ($CD90^-$ cells) were used as a negative control and stained with CellTracker Blue (pseudocolored yellow). CD90 was not expressed by HUVECS. Scale bar is 50 µm.

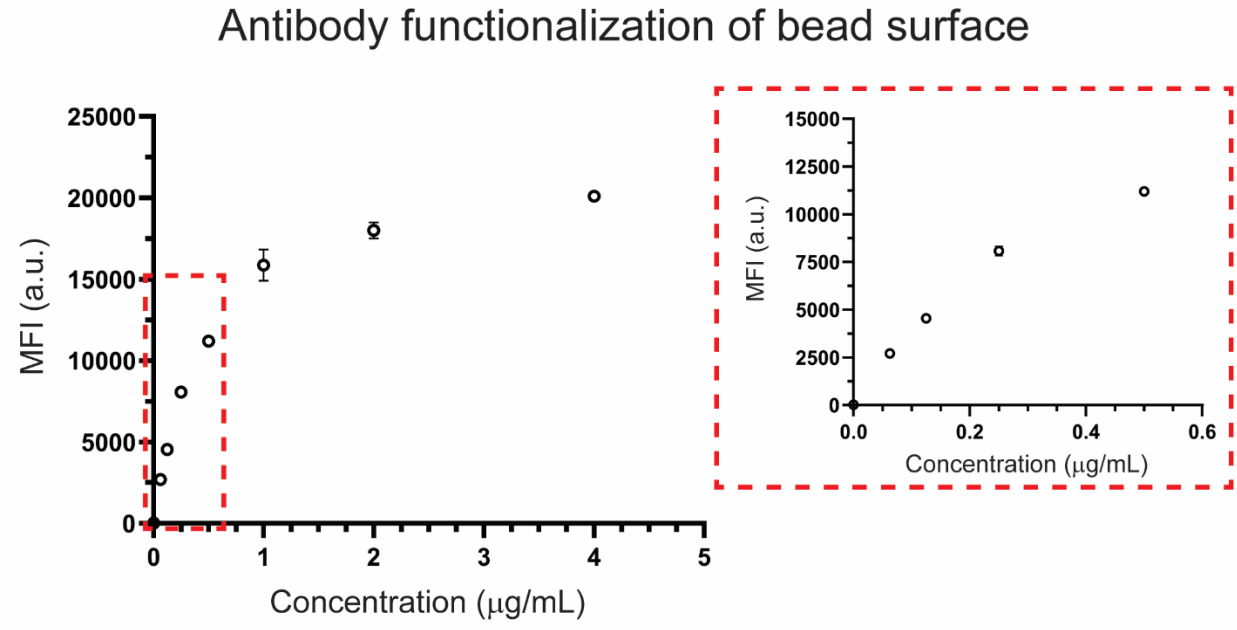

Figure D2: Validation of antibody functionalization on MagPlex bead surface. Antibodies (CD90 and HGF) were covalently coupled to the bead surface and then incubated with a range of fluorescent secondary antibody concentrations to demonstrate successful coupling of antibodies to bead surface (see

Materials and Methods for details). Data points are the average of duplicate measurements with error bars representing standard deviation. The graph on the right is an inset of the 0-0.5 µg/mL concentration range.

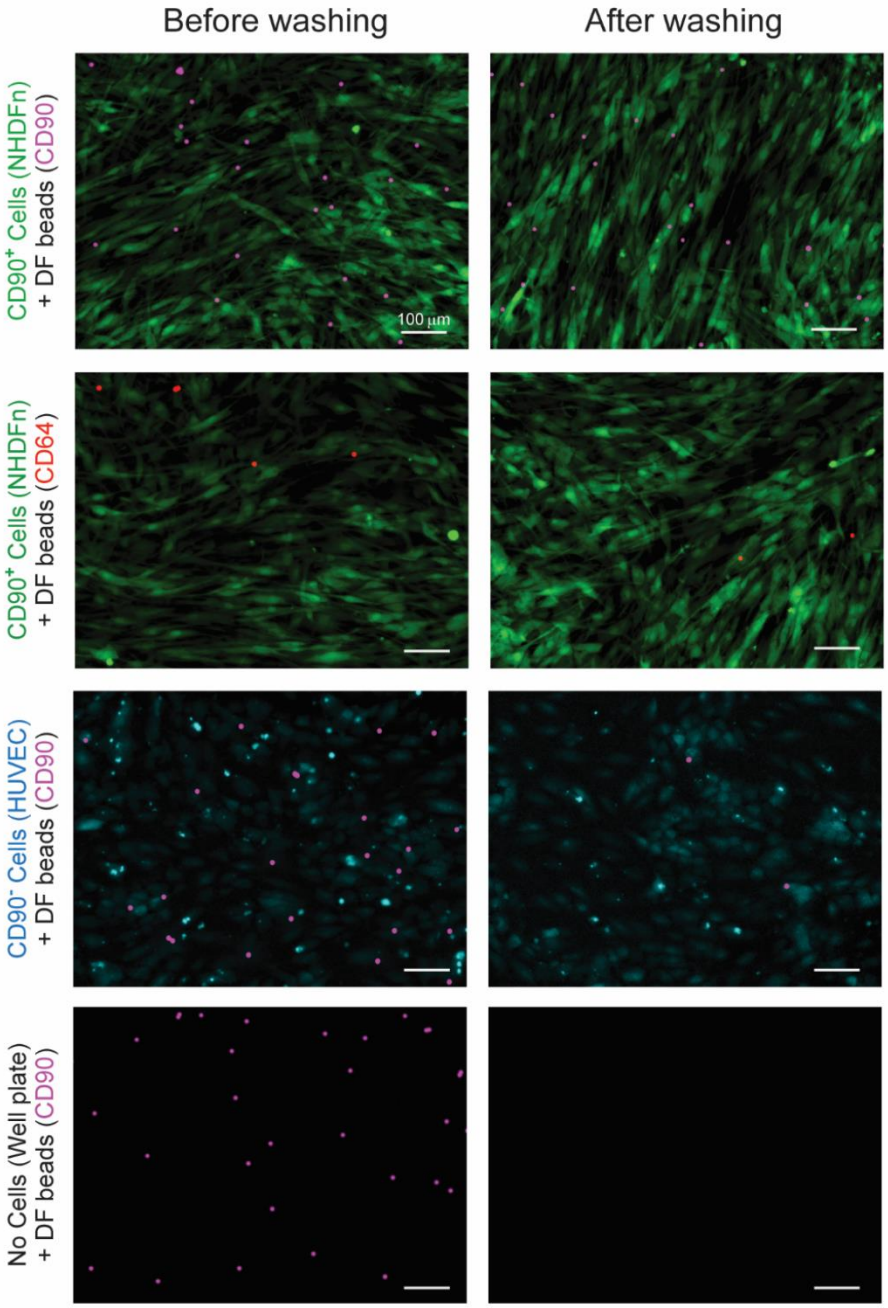

Figure D3: Validation of dual-functionalized (DF) bead binding to the surface of targeted CD90^{+} cells (NHDFn). Representative images from n=4 independent experiments demonstrating DF bead [(anti-CD90, anti-HGF) (pink)] tethering to NHDFn cells (green) after multiple washing steps. Bead retention was also quantified in three negative control conditions where bead retention after washing is not expected: anti-CD64, anti-MMP12 DF beads (red) with NHDFn; anti-CD90, anti-HGF DF beads with CD90^{-} cells [(HUVECs) (blue)]; anti-CD90, anti-HGF DF beads in a well plate with no cells. All negative

conditions showed negligible bead retention on the cell/well plate surface. Images were processed individually for better DF bead visualization as described in the methods section. Images are representative of xxx fields of view across xxx independent experiments. Bead retention data is quantified in Figure 2C. Scale bar is 100 µm.

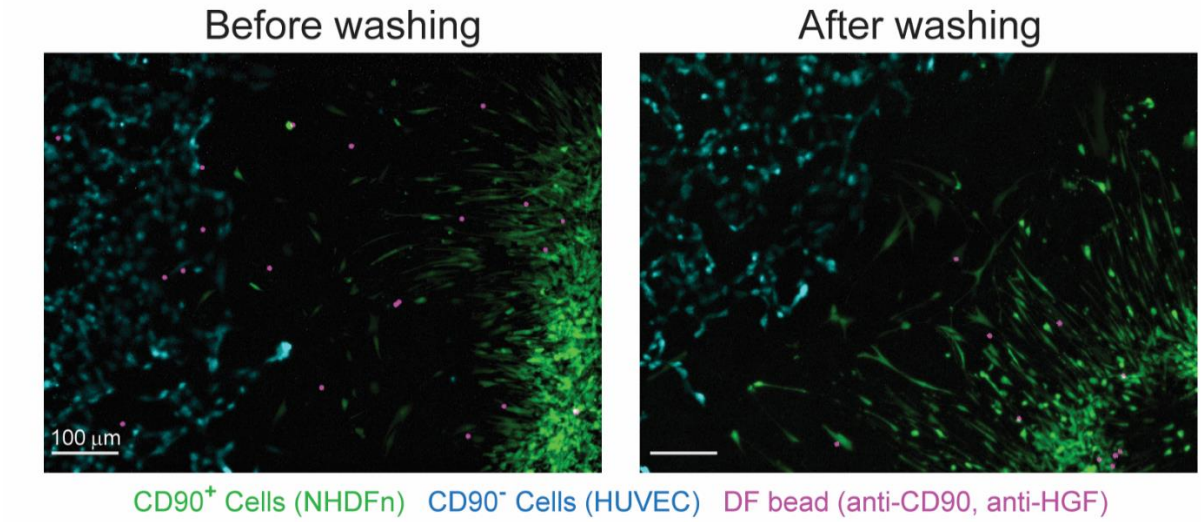

Figure D4: Dual-functionalized (DF) beads (anti-CD90, anti-HGF) remain tethered to targeted $CD90^+$ cells (NHDFn) in coculture with $CD90^-$ cells (HUVEC). DF beads (pink) were added to a patterned coculture of NHDFn (green) and HUVEC (blue) cells for a 2-hour incubation followed by multiple wash steps. Beads remain tethered to $CD90^+$ cells (green), while being removed from $CD90^-$ cells (blue) after washing. Scale bar is 100 µm.

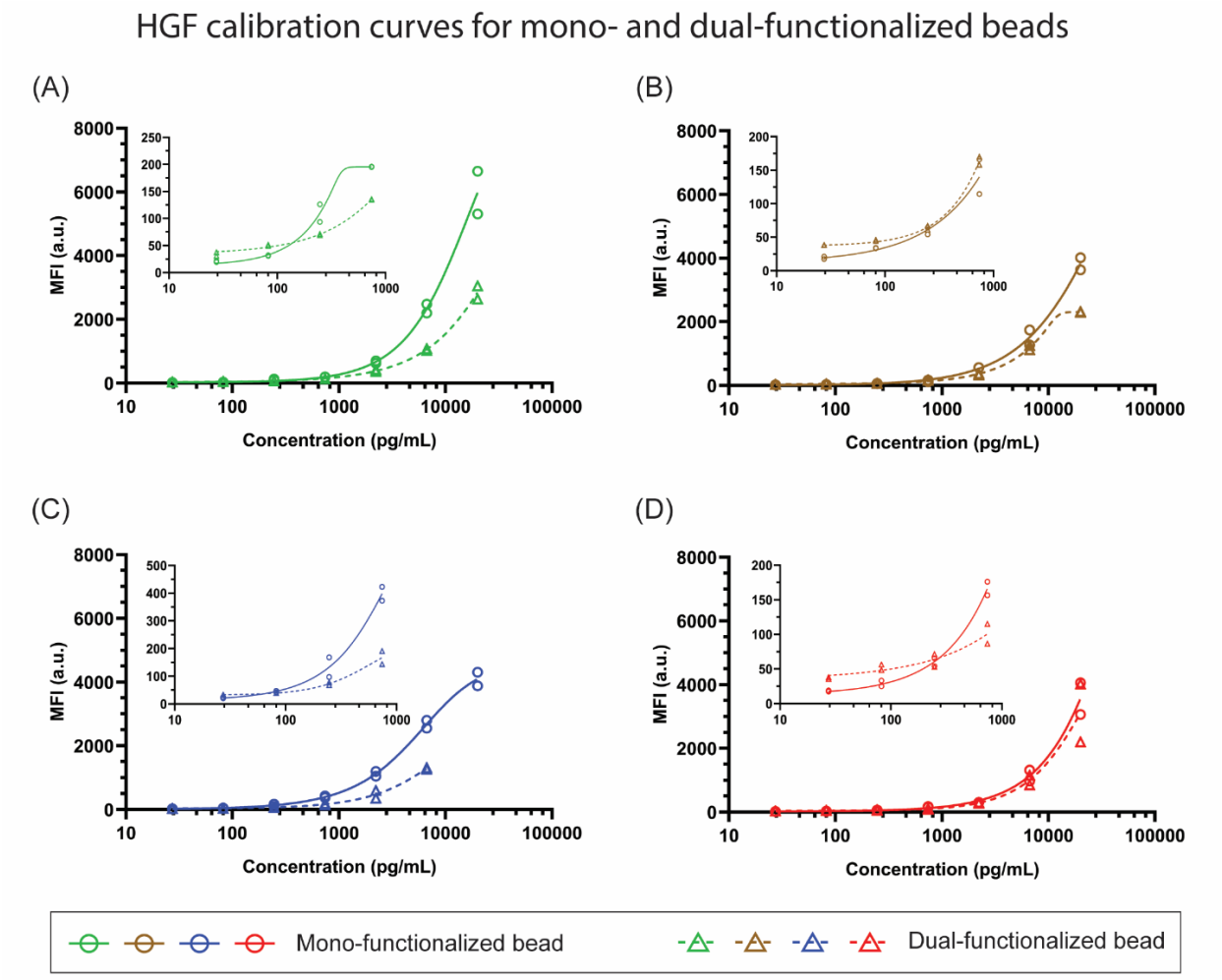

Figure D5: Calibration curves for mono- (MF) and dual-functionalized (DF) beads demonstrates ability of both beads to capture HGF. Per MagPlex manufacturer's recommendation, a five-parameter logistic fit was used to fit calibration curves and demonstrate the HGF-bead binding ability for each independent experiment (A: Experiment 1; B: Experiment 2; C: Experiment 3; D: Experiment 4) in duplicate (duplicates are shown as two plotted circles or triangles). Decreased signal is observed for DF beads as the surface has roughly half the binding sites for HGF compared to MF beads. Highest concentration for DF beads in Experiment 3 (C) did not contain beads for analysis and was therefore excluded from the curve. Insets are of first four points of the calibration curves. All curves are plotted on a logarithmic scale for visualization.

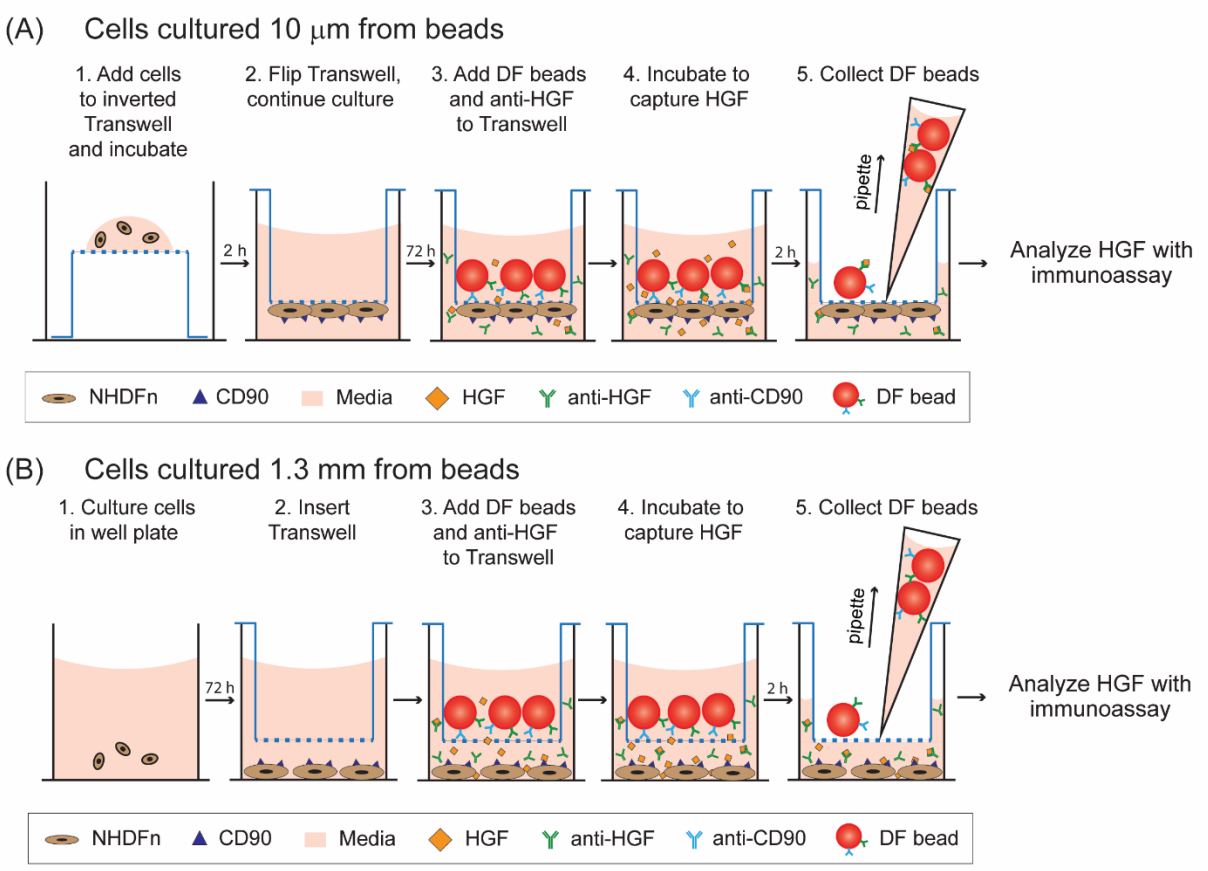

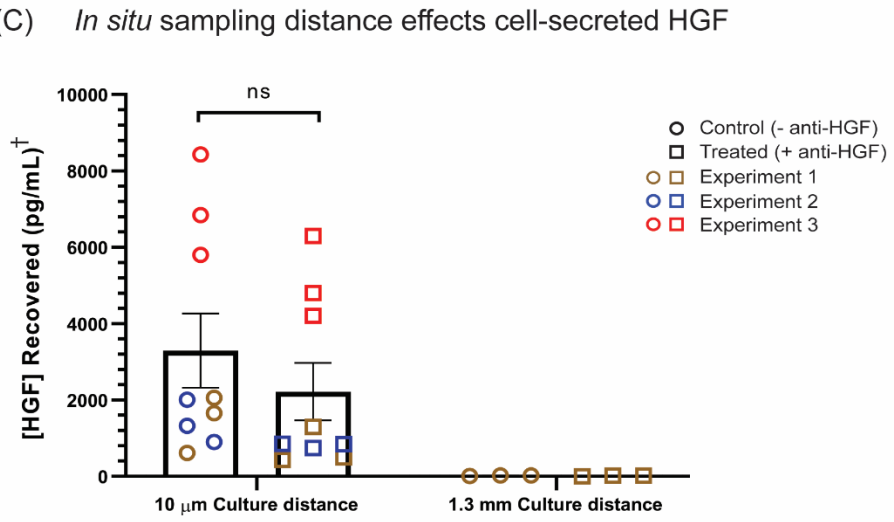

Figure D6: Increased *in situ* HGF recovered concentration results from bead proximity to cells. Schematic showing steps for culturing cells (A) 10 μm from beads and (B) 1.3 mm from beads. These two distances were chosen to probe the effect of bead sampling distance on HGF capture. When beads were cultured 10 μm from cells there was (C) no statistical significance between the control (- free anti-HGF) and treated (+free anti-HGF) groups. This same trend was observed when beads were tethered to the cell surface *via* CD90 (see Figure 3 in the manuscript). In contrast, beads cultured 1.3 mm from the cells resulted in signals below the assay limit of detection (LOD) in both conditions. Three independent experiments with three replicates were performed for each experiment. Error bars are SEM. Unpaired,

parametric t-test. († HGF recovered using DF beads was captured 10 µm away from cultured cells, rather than the bulk, leading to increased overall HGF capture.)

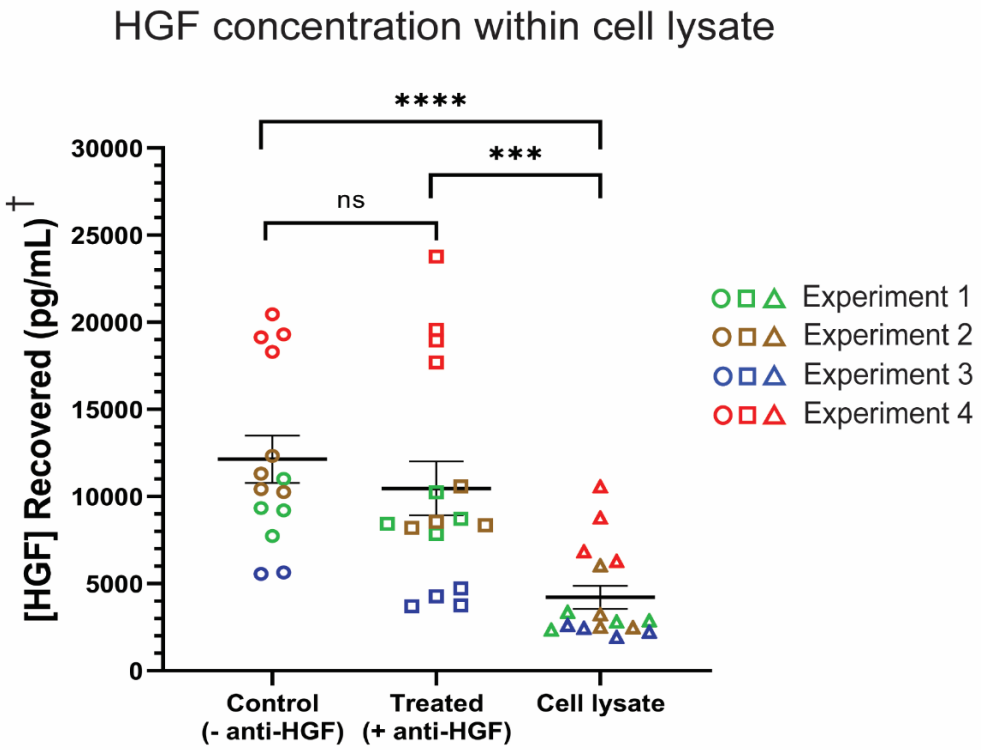

Figure D7: Quantification of HGF in cell lysate from the cell lysis step to remove DF beads tethered on cell surface. To determine the contribution of intracellular HGF to total recovered HGF signal, we quantified the amount of HGF present during the 15-minute lysing period used in the localized cell-surface sampling workflow by simultaneously adding DF beads and lysis buffer to cells. While signal is observed in the cell lysate, the HGF concentration is significantly less than the recovered HGF from either localized cell-surface sampling condition (control and treated). Each data point plotted represents one technical replicate, with typically 4 replicates per independent experiment. Error bars are SEM. Two replicates in the control condition from Experiment 3 were excluded due to absence of DF beads in well. († HGF recovered using DF beads is captured at the surface of the cell, rather than the bulk, leading to increased overall HGF capture. Traditional immunoassay calculations use bulk solution sampling; here, we are sampling a small volume on or near the cell surface.) Unpaired, parametric t-test. *** $p < 0.001$, **** $p < 0.0001$.

Appendix E

Reproduced in part with permission from Berry, S.B.; Gower, M.S.; Su, X.; Seshadri, C.; Theberge, A.B. "A modular microscale granuloma model for immune-microenvironment signaling studies *in vitro*". *Front. Bioeng. Biotech.* Submitted.

A. 3D Injection Molded Device for Model Granuloma Layer

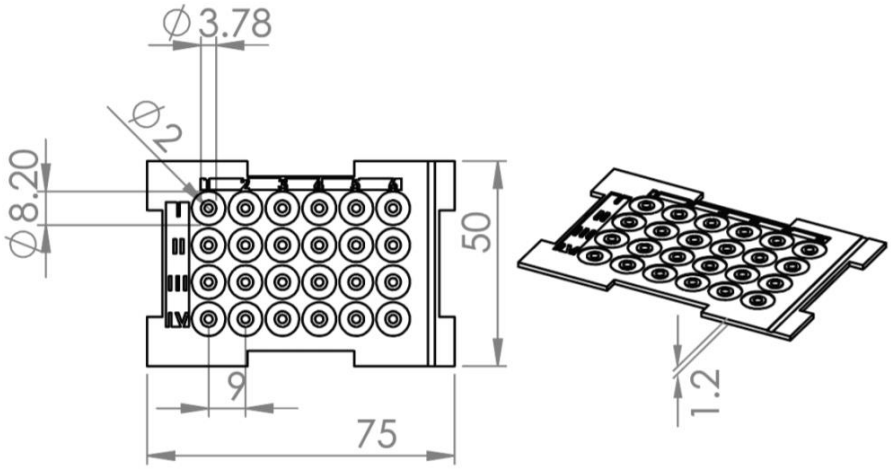

B. CNC-Milled Device for Endothelial Layer

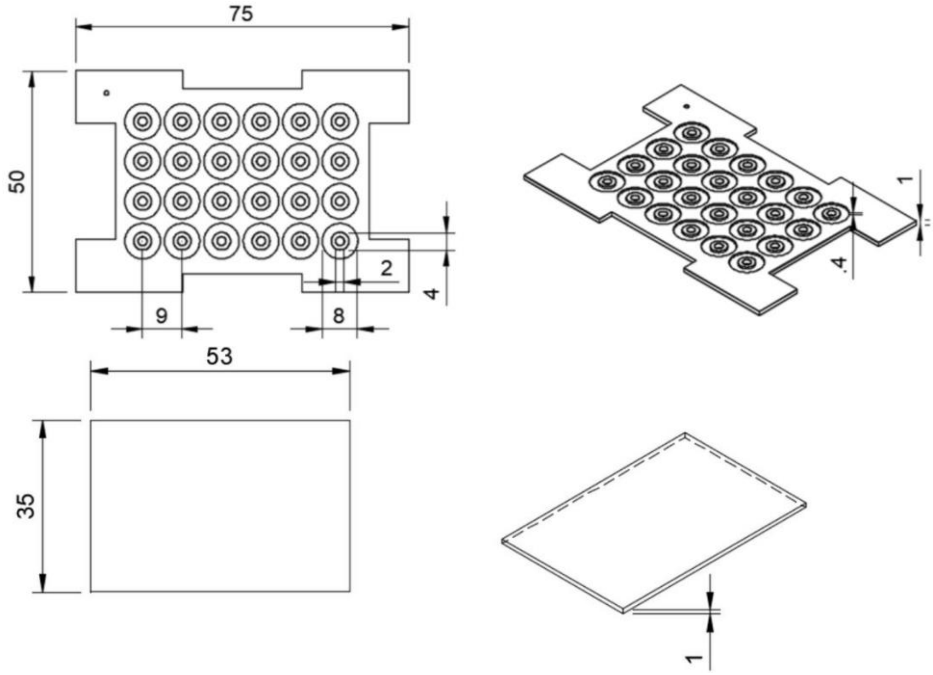

Figure E1. Detailed Device Schematics and Dimensions. A) The injection molded layer used in Figures 6.1-6.4 for the model granuloma. Dimensions and figure reproduced from Yu *et al.*[1], Supplemental Figure 3. B) The endothelial layers containing a floor used in Figure 6.4 was milled using CNC bonding with a solvent-bonded floor. Dimensions labeled in millimeters.

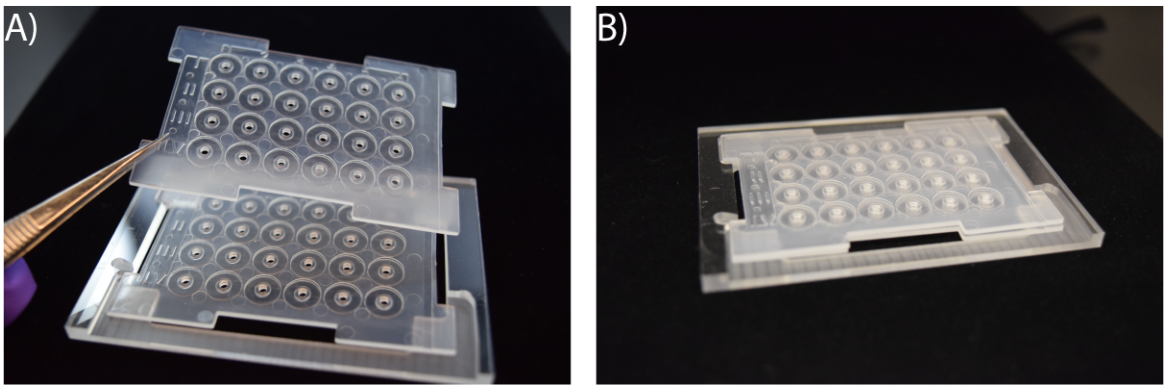

Figure E2. Stacks devices placed inside of CNC-milled device holders. A-B) Layers can be placed directly into the holders to prevent contact between the open suspended culture wells and the floor, as well as to keep the devices in place during culture and aligned once vertically stacked.

E1: Polypropylene (PP) Device Flattening Protocol

Protocol is for use with a Carver Bench Top Standard Heated Press (Model #4386). This protocol can be adapted for use with alternative heated presses with model-specific changes.

1. Preheat platens to 110°C (this takes ≈ 20 min to heat up and stabilize, as the temperature fluctuates).
2. Prepare a stack of devices (4-5 devices) and carefully align the stack to avoid deformation.
3. Place Kapton® polyimide film (#2271K2, McMaster Carr) on the top and bottom platens and place the stack of devices between the films (to avoid direct contact between the devices and the platens).
4. Turn on the pressure sensor.
5. Pump the hot press handle until contact is just made and the devices are flattened.
    - The devices stacks should not be compressed at all (*i.e.*, the pressure sensor should read "0 psi" or fluctuate between “0-10” psi), but the devices should be in contact with the platens and flattened.
6. Let the stacks flatten for 60 min at the above temperature and pressure.
7. After 60 min, turn off the platen temperature and let the temperature drop down to ≈30°C.
    - Do not use coolant to lower the temperature as this causes the temperature to drop too rapidly and can cause deformation. This cooling process takes 1.5-2 h.
8. Once the temperature has dropped below 30°C, turn on the coolant circulator and run the coolant for 5 min to completely cool the platens.
9. Turn off the coolant, release the pressure, and remove the devices from the platens.

E2: Culture Optimization for Miniaturization of Mycobacterial Infection

Condition	Conventional Macroscale Protocol	Optimized Microscale Protocol	Reason for Optimization
Fetal Bovine Serum Concentration[2]	10%	15%	Adaptation for microculture leads to decreased volume of media per cell; increased [FBS] provides greater amount of serum to culture.
Media Buffer Concentration[2]	Variable (0-25 mM HEPES)	25 mM HEPES	Adaptation for microculture leads to decreased volume of media per cell; increased [HEPES] provides greater buffering capacity of media to counter waste accumulation.
Culture Feeding Frequency[2]	Every 2nd or 3rd day	Daily	Adaptation for microculture leads to decreased volume of media per cell; increased media changing frequency prevents nutrient depletion and waste buildup.
Multiplicity of Infection (MOI)	0.1[3,4]	0.05	Adaptation to microscale decreases the total volume of space in the culture well and increases probability of BCG-recognition by monocyte-derived macrophages; decreased MOI results in reproducible and consistent aggregate formation in each well with sufficient uninfected MDMs remaining to aggregate around the infected cells.
Tween-80 Concentration	0.05%	0.003%	Adaptation for the Stacks platform requires a Tween-80 concentration below the critical micelle concentration to maintain capillary pinning and functionality of Stacks devices (see below).
Device Material	Polystyrene (PS)	Polypropylene (PP)	Adaptation for use with immune cell and mycobacterial media requires an increase in the contact angle to maintain capillary pinning of media for cultures.

Optimization of the Tween-80 concentration for culture of *M. bovis* BCG was required for compatibility with the Stacks platform. Traditionally, mycobacteria are cultured in varying concentrations of surfactant (commonly Tween-80) to prevent clumping of mycobacteria during culture. However, the presence of surfactant within the Stacks platform interferes with the capillary pinning necessary for maintenance of cell cultures and stacking of multiple layers. This is due to the decrease in interfacial tension between the culture media and the device surface caused by the presence of surfactant, effectively decreasing the contact angle of the media on the surface. In order to alleviate the effects of surfactant on the capillary pinning, the concentration of surfactant must be well below the critical micelle concentration (CMC), which is 0.0013% w/v[5], in the final media. Therefore, we cultured the BCG at a concentration of 0.003% w/v Tween-80, which yields a final concentration (after all dilutions and mixing) of 0.0000025% w/v Tween-80 in the collagen plug; this concentration was selected as it was the highest concentration of Tween-80 we could use without loss of capillary pinning on the surface. However, to decrease the aggregation of BCG within our model system, the BCG were vortexed, vigorously pipetted, passed through a 27G needle to disperse aggregates, and then allowed to settle for ≈ 1 min before aliquoting from the top of the culture for use.

E3: Culture Optimization of Endothelial Layer

To miniaturize the *in vitro* angiogenesis model[6-8] we adapted for this layer and to ensure functionality, we optimized certain components of the culture system within the Stacks platform. The first condition optimized was the seeding density; too high of a seeding density results in formation of a confluent monolayer or islands of cells on the surface of the Matrigel, whereas too low of a seeding density results in a dispersed culture that does not form endothelial connections. Therefore, the seeding density was calculated from previously established protocols using 48 well plates[7] to obtain a similar ratio of cells to area in the Stacks well (1,650 cells/well of the Stacks layer). We observed that concentrations greater or less than 1,650 cells/well resulted in inconsistent tubule or network formation.

Additionally, the volume of Matrigel within each well was optimized. The final volume of 3 μL was selected to allow complete and reproducible coating of the bottom of each well and to limit the effect of the meniscus on cell localization (*i.e.*, cells aggregating towards the middle of the well/bottom of the meniscus) and cell visualization. Lower volumes of Matrigel (< 3 μL) resulted in uneven coating of the surface of the well floor, causing a non-uniform surface wherein cells adhered to both Matrigel and exposed polystyrene on the floor of the well, leading to altered morphology. Higher volumes of Matrigel (> 3 μL) caused an exaggerated meniscus effect, resulting in cell aggregation in the center of the well. In cases where the volume of the well was completely filled with Matrigel (> 3.6 μL), we observed cell growth both on the Matrigel and on the polystyrene pinning ridge surrounding the well, resulting in varying surface-dependent morphologies (*i.e.*, cells displayed different morphologies on the polystyrene and the Matrigel).

References:

1. Yu, J. *et al.* "Reconfigurable open microfluidics for studying the spatiotemporal dynamics of paracrine signaling". *Nat. Biomed. Eng.*, 2019, 3, 830-841.
2. Su, X. *et al.* "Effect of microculture on cell metabolism and biochemistry: do cells get stressed in microchannels?" *Anal. Chem.*, 2013, 85, 3, 1562-70.
3. Kapoor, N. *et al.* "Human granuloma *in vitro* model, for TB dormancy and resuscitation". *PLoS ONE*, 2013, 8, 1, e53657.
4. Puissegur, M.P. *et al.* "An *in vitro* dual model of mycobacterial granulomas to investigate the molecular interactions between mycobacteria and human host cells", *Cell. Microbio.*, 2004, 6, 5, 423-433.
5. Sigma-Aldrich, "Tween® 80 Sigma Ultra Product Information Sheet", P8074. Accessed 2020/04/01.
6. Koh, W. *et al.* "In vitro 3D collagen matrix models of endothelial lumen formation during vasculogenesis and angiogenesis". *Methods in Enzymology*, 2008, 443.
7. Lonza, Inc. "Clonetics™ Endothelial Cell System Technical Information and Instructions," Walkersville, MD. 2018.
8. Sarkanen *et al.* "Intra-laboratory pre-validation of a human cell based in vitro angiogenesis assay for testing angiogenesis modulators". *Front. Pharmacol*. 2010; 1:147.